PROCESSING AND ELECTROMAGNETIC PROPERTIES OF LOW AC LOSS, MULTIFILAMENTARY RARE EARTH-BARIUM-COPPER-OXIDE SUPERCONDUCTOR TAPES

A Dissertation

Presented to

the Faculty of the Department of Mechanical Engineering

University of Houston

In Partial Fulfillment

of the Requirements for the Degree

Doctor of Philosophy

in Mechanical Engineering

by

Ibrahim Kesgin

December 2013

PROCESSING AND ELECTROMAGNETIC PROPERTIES OF LOW AC LOSS, MULTIFILAMENTARY RARE EARTH-BARIUM-COPPER-OXIDE SUPERCONDUCTOR TAPES

Ibrahim Kesgin

Approved:

Chair of the Committee
Venkat Selvamanickam, Professor,
Mechanical Engineering

Committee Members:

John C. Wolfe, Professor,
Electrical and Computer Engineering

Dong Liu, Associate Professor,
Mechanical Engineering

Philippe Masson, Assistant Professor,
Mechanical Engineering

Haleh Ardebili, Assistant Professor,
Mechanical Engineering

Suresh K. Khator, Associate Dean,
Cullen College of Engineering

Pradeep Sharma, Professor and Chair,
Mechanical Engineering

Acknowledgement

I would like to express my sincere gratitude to my advisor, Prof. Venkat Selvamanickam, for his continuous support, his patience, motivation, enthusiasm, and immense knowledge. He patiently provided the vision, encouragement and advice necessary for me to proceed and complete my dissertation. I could not have imagined a better advisor and mentor for this study.

I would like to thank my rest of the committee members, Dr. John C. Wolfe, Dr. Dong Liu, Dr. Philippe Masson, and Dr. Haleh Ardebili for their evaluations and insightful comments. I own a great gratitude to other colleagues in our research group. I address my thanks to Dr. Goran Majkic for his endless help and excellent guidance. I would like to thank all other researchers and students in our group: Dr. Senthil Sambandam, Dr. Xuming Xiong, Dr. Yunfei Qiao, Dr. Edward Galstyan, Dr. Xiao-Fen Li, Jeong Kim, Albert P. Guevara, Aarthi Sundaram, Xinwei Cai, Narayan Das Khatri, Jian Cao, Yue Zhang, Xin Tao, Yao Yao, Yuhao Liu, Louis Delgado, Meysam and so on. I do appreciate their endless help, care, and support during my PhD. I am thankful to Dr. George Levin for his advices and collaborations and Dr. Milan Majoros for helping me in calibrations. I would also thank the staffs at TcSUH, Bernadette Williams and Helen Espinoza; Graduate Assistant Trina Johnson at Mechanical Engineering department. In addition, I appreciate the funding for this research provided by Superpower Inc. and the U.S. Department of Energy.

I want to express my deepest appreciation to my sisters and brother, Muradiye Saglam, Memnune Efe, and Sukru Kesgin. I would like to dedicate this work to my mother and father, Emsel and Cemil Kesgin. I hope this work makes you proud.

PROCESSING AND ELECTROMAGNETIC PROPERTIES OF LOW AC LOSS, MULTIFILAMENTARY RARE EARTH-BARIUM-COPPER-OXIDE SUPERCONDUCTOR TAPES

An Abstract

of a

Dissertation

Presented to

the Faculty of the Department of Mechanical Engineering

University of Houston

In Partial Fulfillment

of the Requirements for the Degree

Doctor of Philosophy

in Mechanical Engineering

by

Ibrahim Kesgin

December 2013

Abstract

Extensive AC losses are a major impediment for the use of second generation (2G) high temperature superconducting (HTS) rare earth-Ba-Cu-O (REBCO) coated conductors (CC) in AC applications. Filamentization has been shown to be a viable method to reduce magnetization AC losses. Different techniques have been developed including the removal of the thick copper stabilizer layer. Non-uniform ablation, re-deposition of the removed metal, excessive degradation of the critical current, and limited throughput are some of the drawbacks associated with these techniques. In this dissertation, striation methods were developed to address these issues. For the first time, a thick copper stabilizer layer has been selectively-electroplated onto the superconducting filaments. By oxidizing the striated grooves, the striations remain copper-free due to the formation of a resistive oxide layer in between the filaments. The influence of stabilizer thickness on fully-filamentized CCs has also been investigated. The results showed no significant loss contribution from increasing the stabilizer thickness up to 30 μm in fully-filamentized tapes. This thickness should be sufficient for most of the targeted AC applications of coated conductors. Filament widths as small as 180 μm have been fabricated successfully for the first time without compromising the beneficial effect of striations on the AC losses. The loss measurements were performed in a frequency range of 40 to 500 Hz at 77K and compared with theoretical models. The experimental data agrees well with these models above the penetration fields. The adhesion strength of the conductors has also been enhanced approximately three-fold due to the reduced number of defects after modification of the composition of the REBCO film. The techniques developed in this dissertation could potentially be transferred to large-scale manufacturing of stabilized, low loss, multifilament coated conductors.

Table of Content

List of Figures

List of Tables

Nomenclature

a : Half width of a filament or tape

a_0 : Spacing between the vortices

B : Magnetic flux density

B_a : Externally applied field

B_c : Critical field

B_{self} : Self-field

B_i : Internal field

B_p : Full-flux penetration field from a virgin state

B_{p0} : Full-flux penetration field from a non-virgin state

B_0 : Amplitude of applied field

β : Peeling angle, normalized loss

d_s : Thickness of the metal stabilizer

d_n : Thickness of the metal substrate

d_{sc} : Thickness of superconducting film

E : Electrical field, energy

E_c : Critical electric field

f : Frequency

F_p : Pinning force

F_L : Lorentz fore

$f(Y)$: Eddy current loss function

g_n : Free energy of normal state

g_s : Free energy of superconducting state

$g(\Upsilon)$: Hysteretic loss function

H : Magnetic field strength

H_a : Externally applied field

H_c : Critical field

H_{c1} : Lower critical field

H_{c2} : Upper critical field

H_{irr} : Irreversibility field

H_0 : Characteristic field

I_c : Critical current

IBAD : Ion beam assisted deposition

J : Current density

J_c : Electrical current density

$J_{M,y}$: Moment of inertia for a rectangular tape

J_d : De-pairing current density

κ : Ginzburg-Landau parameter

L_c : Critical coupling length

L_p : Twist pitch

M : Bending moment

M : Magnetic moment

MOCVD : Metal organic chemical vapor deposition

Nd:YAG : Neodymium-doped yttrium aluminum

Nd:YVO : Neodymium-doped yttrium orthovanodate

n_f : Number of filaments

η : Viscous drag coefficient

P : Peeling force

P_m : Magnetization AC loss

P_t : Transport AC loss

P_{tsf} : Self-field transport loss

P_{tff} : Flow-flow transport loss

P_{me} : Eddy current loss

P_{total} : Total loss

$P_{me\text{-}Mul}$: Eddy current loss from the Muller model

$P_{mh\text{-}BI}$: Hysteretic loss from the B-I model

$P_{mh\text{-}Mawatari}$: Hysteretic loss from the Mawatari model

$P_{tsf\text{-}Norris}$: Self-field transport loss from the Norris model

$P_{average}$: Average power

P_{peak} : Peak power

$P_{mBrickwall}$: Magnetization AC loss from Brickwall patterning

$P_{mFishnet}$: Magnetization AC loss from Fishnet patterning

P_{joule} : Joule heating loss in a copper wire

R : Flux-creep rate

R : Radius

REBCO : Rear-earth barium copper oxide

R_0 : Frequency of hope attempts of fluxon

$\mathcal{R}$: Break-even sweep rate

ρ : Effective transverse resistivity

ρ_{ff} : Flux flow resistivity

ρ_m : Resistivity of the metal stabilizer

Γ : Normalized loss

T : Temperature

T_c : Critical Temperature

U : Effective energy barrier

U_0 : Potential depth for a pinning center

v : Velocity

W : Width of the tape

w_f : Filament width

Yb:KYW : Ytterbium-doped potassium yttrium tungsten

Yb:YAG : Ytterbium-doped yttrium aluminum

YBCO : Yttrium barium copper oxide

γ : Debonding force

Ψ : Work expenditure rate

λ : London penetration depth

Λ : Specific loss

ξ : Coherence length

Φ : Magnetic quantum flux

Δ : Bridge width

δ : Plating thickness

Λ : Specific loss

Chapter 1. Introduction

Electric current is carried by conduction electrons. When the conduction electrons pass through a metal, they are affected by impurities and thermal vibrations of atoms in the lattice, which leads to resistivity. By decreasing the temperature, thermal vibrations in the lattice can be reduced and resistance to conduction electron motion decreases. When the temperature is lowered to zero, resistivity also should be zero. However, every substance has impurities and scattering from these impurities are more or less independent from temperature. As a result, a residual resistivity caused by these impurities will be observed even at the lowest achievable temperature (Figure 1-1).

Certain materials behave in an unusual manner when cooled. A sudden loss of resistivity is observed when they are cooled below a certain temperature and are transformed to a superconducting state. The temperature of phase transition from normal state to superconductive state is called critical temperature, T_c. The field of superconductivity was established after Kamerlingh Onnes discovered the first superconductor in 1911 in his laboratory in Leiden University [1]. He observed that when the temperature dropped below 4.15 K, the resistance of mercury disappeared. Later, superconductivity was discovered in variety of metals, alloys and compounds. Three quarters of a century of research resulted in the discovery of new superconducting materials with higher T_cs, up to a level of 23.2 K in Nb_3Ge [2]. These superconductive materials with T_c values lower than 30 K are called low-temperature superconductors (LTS) and usually are cooled with liquid helium, which is expensive and rare.

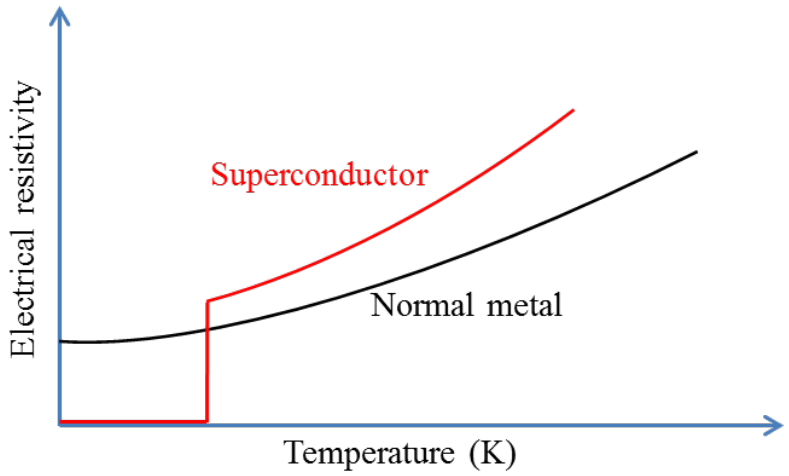

Figure 1-1. Resistivity of a normal metal and a superconductor with respect to temperature.

After Bednorz and Muller discovered superconductivity in La-(Lanthanum) based cuprate perovskite material with T_c of 35 K [3], an era of high-temperature superconductors (HTS) started, where T_c values are higher than 30 K. The T_c was further increased to 92 K with the discovery of $YBa_2Cu_3O_7$ [4]. With these discoveries, the transition temperature exceeded the boiling point of liquid nitrogen.

Using liquid nitrogen as a refrigerant is advantageous because it is inexpensive and easily available. Later, bismuth-based superconductors, were discovered with higher transition temperatures [5-7]. New classes of superconductors namely, magnesium-diboride and iron-based superconductors have also been discovered [8, 9]. Figure 1-2 summarizes important milestones in the discovery of superconductive materials.

Crystal structure of Yttrium barium copper oxide, Y-Ba-Cu-O, (YBCO) and Bismuth strontium calcium copper oxide (BSCCO), Bi-2223 are shown in Figure 1-3. YBCO has a layered orthorhombic perovskite structure composed of two layers of Cu-O and Ba-O_2 sandwiching two CuO_2 planes. These CuO_2 planes are responsible for superconductive current transportation. Bi-2223 has a tetragonal, layered, orthorhombic

perovskite structure containing two layers of Bi(Ca)-O and Sr-O, sandwiching three strongly superconductive CuO_2 planes.

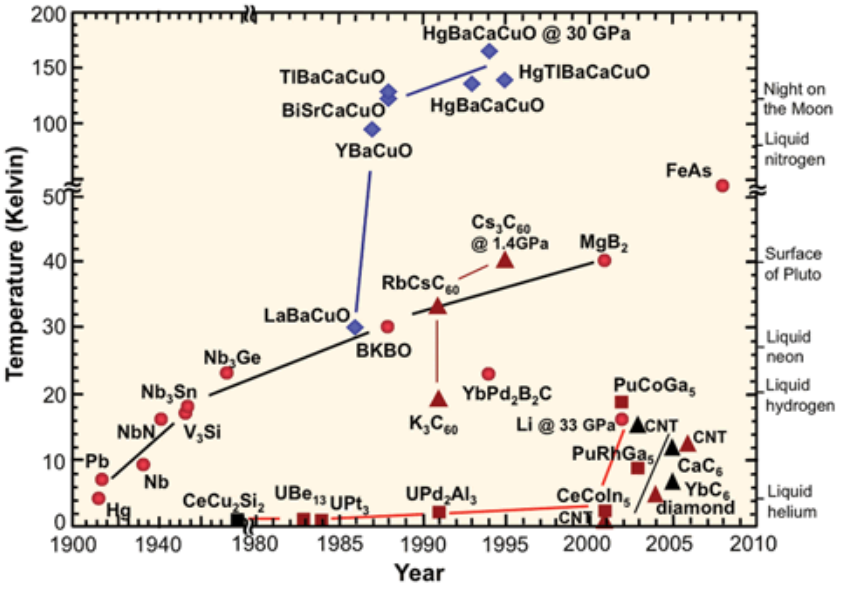

Figure 1-2. Discovery of superconductors with increasing T_c [10].

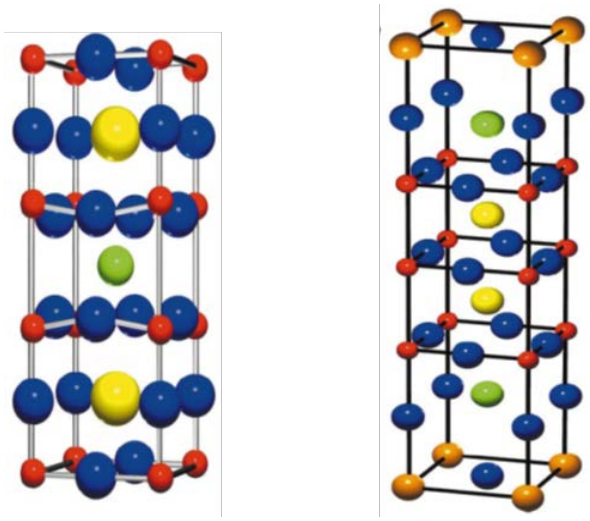

Figure 1-3. Unit cell of yttrium barium copper oxide (YBCO) (left) and bismuth strontium calcium copper oxide (Bi-2223) [11].

1.1. Properties of superconductors

Superconductors exhibits two properties that are different from other materials. Zero resistance and diamagnetism are the most distinguishing properties of

superconductors. When the temperature of a superconductor is lower than T_c, no resistance is presented to impede electron motion.

The German physicists Walter Meissner and Robert Ochsenfeld discovered in 1933 that when superconductors are cooled below their T_c in the presence of an applied field, nearly all the interior magnetic field is cancelled [12, 13]. This experiment demonstrated that superconductors are not only different than hypothetical perfect conductors, but they also have a unique property of magnetic flux not existing in their interiors. This property is known as the Meissner effect. If a conductor is cooled to a low temperature when it becomes perfect ($\rho=0$) and is exposed to externally applied field, B, magnetic flux will be expelled from its interior because $\partial B / \partial t = 0$ must hold. If a perfect conductor is exposed to an external field before the cooling, the magnetic flux inside it will be the same as the external field because the value of relative magnetic permeability is very close to unity in non-ferromagnetic metals. Upon cooling the metal down to a lower temperature, magnetization will not be affected. If the applied field is removed, $\partial B / \partial t = 0$ must hold again. This indicates that current will be induced in the interior of the perfect conductor to resist the flux change inside. Meissner and Ochsenfeld, however, found out that a material in the superconducting state never allows a magnetic flux to exist in its interior and the equality $B=0$ always holds.

In terms of their magnetic properties, superconductors can be categorized into two main groups, type−I and type−II. In a type−I superconductor, magnetic field does not penetrate beyond a small penetration depth at temperatures below T_c, and it shows property of perfect diamagnetism. The free energy of superconducting state is lower than that of the normal state. When a superconductor is exposed to an external field, H_a, its free energy

changes by $1/2\left(\mu_o H_a^2\right)$ where μ_0 is permeability of free space. Conversely, the effect of applied field on free energy of the normal state is negligible. Therefore, a maximum limit exists for an external magnetic field to be exerted on a superconductor to maintain the superconductivity and it is given by [14]

$$H_c = \sqrt{\frac{2}{\mu_0}[g_n(T) - g_s(T)]}, \tag{1-1}$$

where g_s and g_n are the free energy of normal state and superconducting state respectively. An externally-applied magnetic field that is greater than H_c destroys the superconductivity and transition from superconductive to normal state occurs. H_c varies with temperature and this dependence can be represented in H−T (Applied Magnetic Field vs. Temperature) phase diagrams as shown in Figure 1-4 [14, 15]. The superconductors are in the Meissner state when the applied field strength is less than $H_c(T)$. Magnetization curves of ideal superconductors in Figure 1-4 reveals that below $H_c(T)$, the interior of a superconductor is free of magnetic flux and beyond $H_c(T)$, flux penetrates into the superconductor.

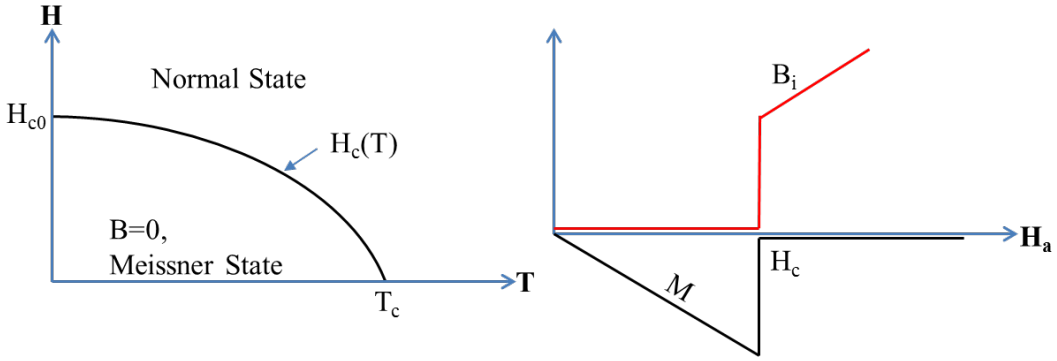

Figure 1-4. H−T phase diagram (left) and magnetization curves (right) for type−I superconductors. B_i is the internal field and M is the magnetization.

A state quite different from the Meissner state, called the mixed state, was observed by Abrikosov in 1957. Due to this additional state, the H−T phase diagram of the type−II superconductor mainly consists of three phases (Figure 1-5). Initially, as in Type−I

superconductors, all magnetic flux is excluded and the superconductor is in the Meissner state. The field value, $H_{c1}(T)$, below which the superconductors are in the Meissner state is called the lower critical field. In this state, perfect diamagnetism is present. When the applied field reaches H_{c1}, magnetic flux begins to penetrate into the superconductor. Normal cores start to form and the superconductor is in the mixed state. In this state, the superconductor carries current without resistance but is no longer perfectly diamagnetic. Magnetic flux penetrates into the superconductor in the form of flux lines that consist of quantized vortices [14], which are not superconductive. These normal cores repel each other and arrange themselves in a form of hexagonal fluxon lattice [15, 16]. Upon increasing the magnetic field values, quantized vortices overlap and the entire region becomes non-superconductive. Then, the magnetic field can penetrate freely into the material with no resistance. As a result, transition from a superconductive state to a normal state occurs. The field value, $H_{c2}(T)$, below which the superconductor is in the mixed state are called the upper critical field. Magnetization curves for an ideal type−II superconductor are shown in Figure 1-5. In field values up to H_{c1}, no magnetic flux penetrates inside the superconductors while it increases with respect to applied magnetic field after H_{c1} is exceeded. Beyond H_{c2}, superconductivity is destroyed.

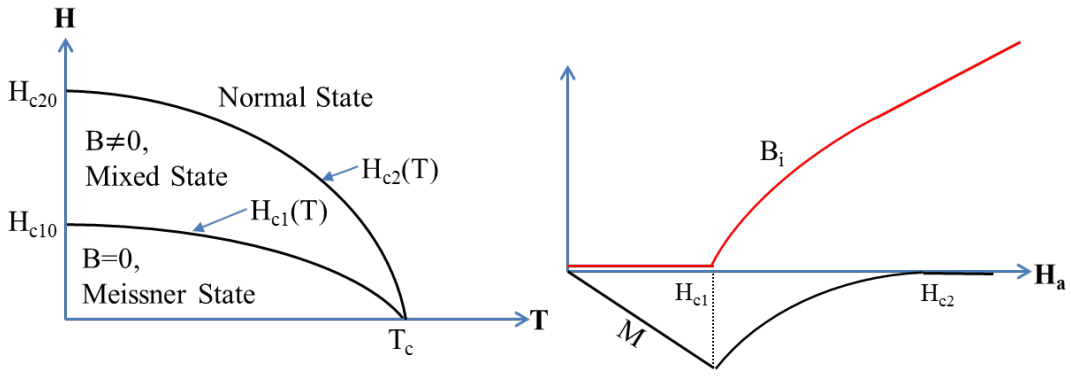

Figure 1-5 H−T phase diagram (left) and magnetization curves (right) for type−II superconductors.

Superconductors have three important parameters. These parameters are critical current density, (J_c), critical field (H_c, for type-II H_{c1} and H_{c2}) and critical temperature (T_c). When one of these critical values is exceeded, transition from superconductive to normal state occurs. In literature, these parameters are gathered in one 3D plot known as T−H−J plots (Figure 1-6).

The first crucial property of superconductors is the critical current density, J_c. Superconductors with high-current densities (J_c >10^5 A/cm^2) were demonstrated in 1961 [17].

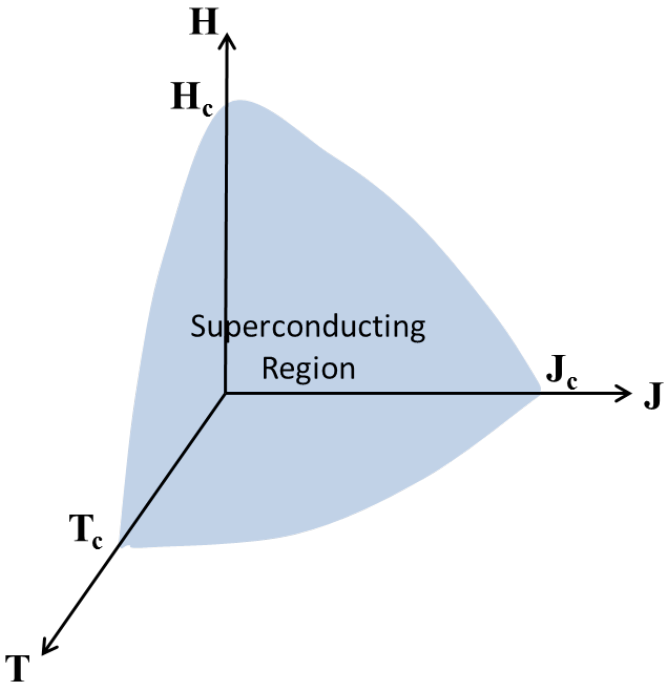

Figure 1-6. Boundaries that limit the superconductivity

Bulk superconductivity exists up to the upper critical field $H_{c2}(T)$, which can exceed 100 T for Bi-2223 and YBCO [11]. However, applications are limited by a lower characteristic field, the irreversibility field, $H_{irr}(T)$, at which J_c vanishes. J_c is nearly zero in the superconductor at applied field values higher than $H_{irr}(T)$. This is due to the interaction between Lorentz force and non-superconductive normal cores. When a super-

current (**J**) flows through type−II superconductor materials, the created self-field, $\mathbf{B_{self}}$, penetrates into the superconductors and generates non-superconductive cores. A force called Lorentz, $\mathbf{F_L}$, is applied to these cores according to Equation (1.2)

$$\mathbf{F_L} = \mathbf{J} \times \mathbf{B}_{\text{self}} . \tag{1.2}$$

Energy needs to be provided to convert the superconducting volume into a normal state in the mixed state. If the flux line enters into normal state region such as a defect, then this energy penalty can be saved and these defects create pinning effect when the Lorentz force is exerted. If the Lorentz force is less than the pinning force, the normal cores and the magnetic flux lines inside do not move and are pinned in the material. However, when the current is increased, the $\mathbf{B_{self}}$ increases, and the Lorentz force increases too and eventually exceeds the pinning force $\mathbf{F_p}$. From this point onwards, the flux lattice begins to move. Finally, the whole superconductor becomes normal due to the free-moving flux lines. As a results of this interaction, superconductors cannot be used practically up to the upper critical field values. In Figure 1-7, $H_{c2}(T)$, at which the bulk superconductivity is destroyed, is indicated by thin black solid lines, and $H_{irr}(T)$, at which the bulk J_c goes zero, is indicated by thick red solid lines. The difference between $H_{c2}(T)$ and $H_{irr}(T)$ is pronounced for some materials such as Bi-2223. Only a slight difference between the two values can be seen for materials such as Nb-Ti. The difference in YBCO is not as severe as in Bi-2223, and therefore YBCO can be used in much higher fields and temperature (~7T @77K) as compared to the other superconductive materials. This became a key motivation for developing YBCO conductors.

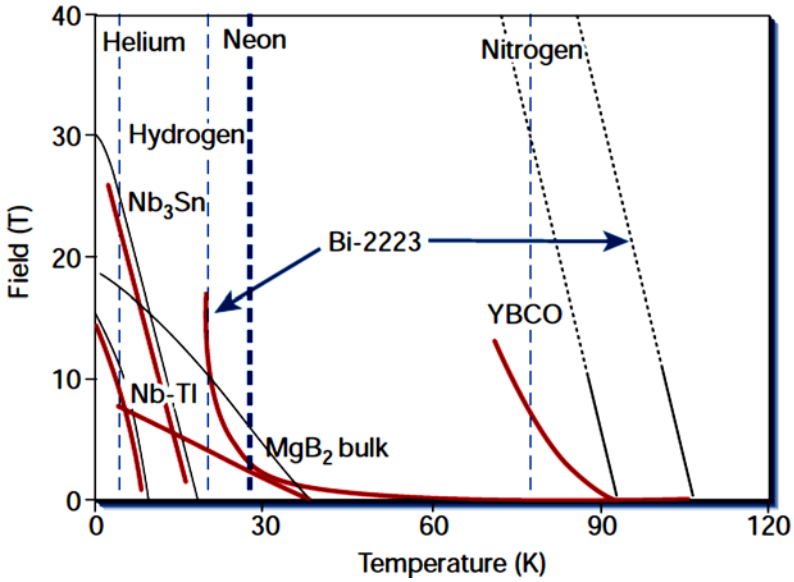

Figure 1-7. The upper critical field $H_{c2}(T)$ (indicated in black) and irreversibility field $H_{irr}(T)$ (indicated in red) for some superconductive materials [11].

The last property is critical temperature, T_c, which is important because with decreasing the operating temperature of the superconductors, other critical parameters such as critical magnetic field or critical currents can be increased significantly. If the T_c in a superconductor is high, better performances can be achieved more economically at elevated temperatures. The main obstacle for HTS conductors is that their current carrying capability rapidly deteriorates with increasing temperature and magnetic field.

1.2. Fabrication of 2G-HTS superconductors

After the discovery of superconductivity above 77 K, extensive efforts were invested for fabrication of these materials. A variety of techniques was developed for fabrication of different superconductive materials. Early attempts include powder-in-tube [18], that was used successfully in the manufacturing of Bi−2223, hot extrusion and hot pressing [19], sputtering [20], electron beam evaporation [21] and molecular beam epitaxy [22]. The three most common fabrication techniques for YBCO thin films are pulsed laser deposition, metalorganic deposition [23, 24] and metal organic chemical vapor deposition

[25, 26]. MOCVD will be the only method discussed in this dissertation as it was the only method used for sample fabrication.

1.2.1. Buffer layers and substrates

Single crystal growth of YBCO was demonstrated successfully on several substrates such as MgO [21], ZrO_2 [23], Al_2O_3, Y_2O_2 stabilized ZrO_2 (YSZ) [27], $SrTiO_3$ (STO), and $LaAlO_3$ [28]. However, a long length of single crystal YBCO is impossible for commercial applications. In polycrystalline YBCO superconductors, grain boundaries were found to act as weak links that degraded superconductive properties [29]. For this reason, in long-scale polycrystalline growth of YBCO, a good grain-to-grain alignment is required to obtain high J_cs. To achieve the desired structure of YBCO, a biaxially-textured buffer layer is needed. For this purpose, two methods were developed. In one, the substrate was textured using a method called Rolling-Assisted-Biaxially-Textured-Substrates (RABiTS) [30]. In the other, a buffer layer was textured using Ion-Beam-Assisted Deposition (IBAD) [31, 32]. The architectures of these two methods are shown in Figure 1-8. In RABiT substrates, a barrier layer was used because poisonous elements can diffuse from Ni-W substrate and deteriorate the superconductive properties.

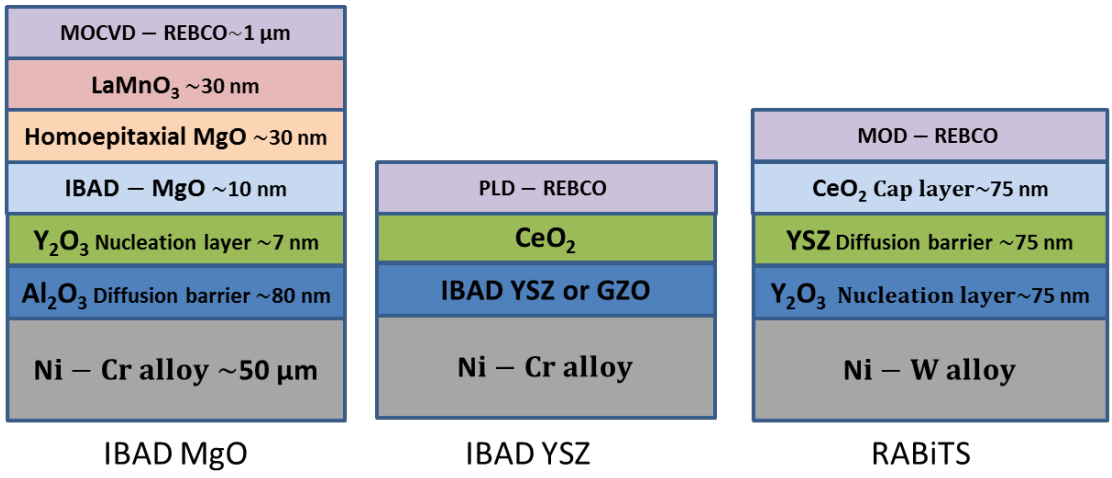

Figure 1-8. Architectures of textured buffers and substrates with different methods.

Although excellent current densities have been achieved using an IBAD yttria-stabilized-zirconium-oxide (YSZ) textured template with pulsed laser deposition (PLD), very slow deposition became a problem because the required thickness of YSZ is approximately 1 μm to achieve a good texture. An excellent in-plane texture was obtained successfully using IBAD-MgO which required a much shorter deposition time compared to IBAD-YSZ [33, 34]. As in other methods, in IBAD-MgO, a multi-layered buffer structure for diffusion barrier and texture formation. IBAD-MgO is typically deposited on Hastelloy C−276 substrate (Figure 1-8). This Ni−based substrate has excellent flexibility that is crucially necessary for applications requiring twisting or bending. More importantly it is non-magnetic and does not create ferromagnetic loss. Its high melting point is suitable for processing conditions of the layers deposited on top of the Hastelloy.

After polishing, the surface of Hastelloy becomes very smooth (surface roughness is about 1 nm). An 80 nm thick amorphous alumina (Al_2O_3) layer is deposited on top of the Hastelloy substrate using a magnetron sputtering technique. This layer serves as a barrier layer to elements that might diffuse from Hastelloy to RE-Ba-Cu-O (REBCO, RE=rare earth) and destroy superconductivity. A seed layer of 7 nm yttrium oxide (Y_2O_3) is deposited for the nucleation of subsequent IBAD-MgO layer. To achieve excellent biaxial texture in the <100> orientation of normal to the tape surface, a 10 nm IBAD-MgO layer is deposited. To improve the texture further, 30 nm homo-epitaxial MgO layer is deposited. The lattice constant of MgO is 0.422 nm that does not match compared to the YBCO lattice constant of 0.385 nm in it's a-b plane. For this reason, $LaMnO_3$ layer is deposited epitaxially as an intermediate layer by magnetron sputtering to obtain a good

lattice match with YBCO. On top of this layer (LMO), a MOCVD- REBCO layer is deposited.

1.2.2. MOCVD

As stated earlier, MOCVD is a thin film deposition technique vapor-phase metal organic precursors are used. This method has been long used in semiconductor industry and has been adapted for REBCO growth. An excellent crystal quality of REBCO with very good properties at a high deposition rate has been reported using MOCVD technique [35, 36]. Excellent uniformity in in-field performance [37] and high critical current densities [38] over long lengths have been reported using this method. Some of the major advantages of MOCVD−REBCO growth technique are long deposition times because the precursor is kept outside of the deposition chamber, large-area deposition and high deposition rates.

A schematic representation of a reel-to-reel MOCVD system used for REBCO deposition is presented in Figure 1-9. A liquid precursor is delivered to the evaporator by using an inert gas carrier such as Ar. In the MOCVD process, THD precursors (2, 2, 6, 6-tetramethyl-3, 5-heptanedionate) of Zr, Gd, Y, Ba and Cu are used as metal organic source materials and are dissolved in tetrahydrofuran (THF), an organic solvent. The solution is flash vaporized and the resulting vapor is mixed with heated oxygen gas. The mixture of vapor-phase precursor and oxygen is delivered into the reactor that consists of a heated susceptor, showerhead and tape-handling system (Figure 1-9). Vacuum in the chamber and evaporator is provided by a screw pump that can achieve a pressure as low as 10 mTorr before each run.

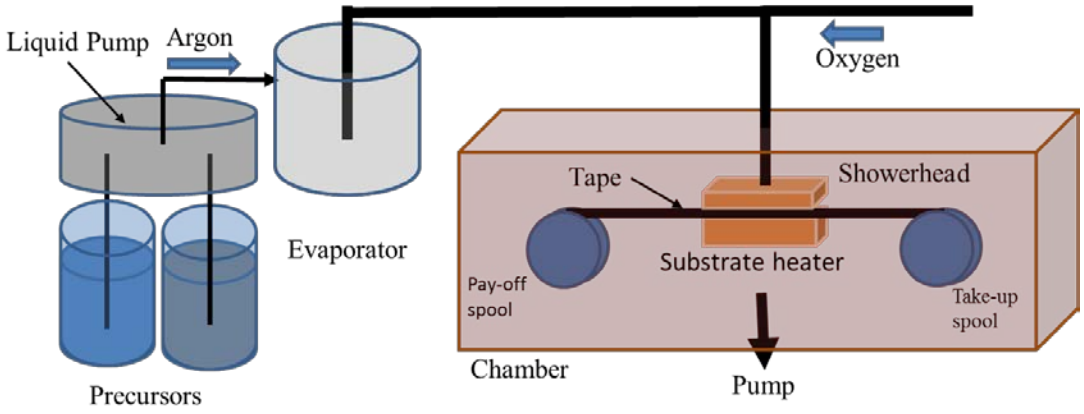

Figure 1-9. A schematic of major components of MOCVD.

1.3. Applications of HTS and link to AC losses

LTS applications are concentrated primarily on Nb based alloys and some of those include Magnetic Resonance Imaging (MRI), Nuclear Magnetic Resonance Spectroscopy (NMR) and High Energy Physics (HEP) accelerators and superconducting quantum interface devices (SQUIDS). First generation 1G-HTS wires have been used in prototypes for electric power applications, such as the 5 MW high-torque ship propulsion motor [39] and transformers [40], etc. Major problems with 1G-HTS are that they use a lot of silver that substantially increases the cost of wire, and their low currents in magnetic fields at high temperatures. Because of superior properties of 2G-HTS, applications of superconductors have been shifted to these superconductors.

Two main companies that supply commercial 2G-HTS in long length are SuperPower, Inc. (SP) and American Superconductor (AMSC) [35, 41]. Benefits of using 2G-HTS wires include energy savings, reduced pollution or less environmental hazards compared to conventional materials and enhanced grid stability [42]. Superconducting devices are significantly smaller and lighter than conventional equipment of same power rating.

Cables have been widely demonstrated using HTS conductors. One of the early demonstrations of an in-grid cable was in Albany, where a 30 m section of the cable was made using 2G-HTS wire by SuperPower, Inc [38]. Superconductor cable projects were extended later to larger power handling capabilities [43].

Fault current limiters (FCL) are another application of superconductors and a conceptual design and implications of usage of superconductors in a fault current limiter are provided in reference [44]. One of the earliest attempts for FCL with 2G-HTS was made on an individual conductor 10−20 m long with $I_c \sim 200$ A where a good fault current limiting performance obtained [45, 46]. Initiatives regarding FCLs have been developed [47, 48], and the application has been demonstrated [49].

Rockwell Automation demonstrated a simple generator using only YBCO coils in 2004 [50]. Superconducting motors and generators are under active development for naval applications as well [51]. Experiments and simulations on SMES have been made with 2G-HTS [52, 53]. Magnets made with REBCO conductors have generated 35.4 T [54] and 32 T [55] fields and developments to achieve higher fields for particle colliders are underway [56]. However, degradation in critical current under thermal cycling has become a crucial problem in coil applications [56-58]. This degradation originated from the weak mechanical properties in the c-axis direction in 2G-HTS CCs [59].

Numerous demonstrations have shown that it is feasible to build and operate devices fabricated with HTS REBCO CCs. In applications, requiring AC field and AC currents or a combination of both, however, the major impediments are AC losses, particularly magnetization AC losses, due to the tape geometry (due to the high aspect ratio), as well as the weak mechanical properties of tapes along the c-axis. AC losses

potentially increase the cryogenic costs to unaffordable levels and the weak mechanical properties could cause inevitable failures. For example, to remove 1 W heat generation at liquid helium and nitrogen temperature, a ~700 W and ~15 W refrigerator is needed respectively [60]. Hence, reduction of heat dissipation of 1 W at low temperatures will reduce the need of the high coolant powers. AC losses will necessitate much of the refrigeration that the HTS equipment will entail and that refrigeration adds substantial capital and operational costs [61]. Improving c-axis mechanical properties is another necessity and is another objective of this dissertation along with the AC loss reductions.

1.4. Losses in superconductors

Superconductors are generally materials without electrical resistance and are free of power dissipation. The fact is that superconductors used in applications dissipate a little electric power when electrical current passes through them or when they are exposed to externally applied fields even below the critical values I_c, H_c and T_c. In direct current (DC) and magnetic field, this dissipation may be negligible when the transport current and field are less than their critical values, I_c and H_c respectively. An MRI is an example of this kind of application in which electrical current circulates without perceptible diminution. The situation differs when the superconductors exposed to AC magnetic fields or AC current or both even if the electrical current and magnetic fields are below their critical values. AC losses generated by transport current are called as transport losses and those from AC magnetic field are called magnetization AC losses. AC magnetic field losses are at least a few orders of magnitude higher than the losses originated from AC transport current. So they require special attention to reduce refrigerant needs. Reduction of magnetization loss is required and is a very significant problem in 2G-HTS tapes. As a result of this fact, the

main focus of this dissertation will be magnetization AC losses and their reduction. Other aspects will be briefly explained.

1.5. Objective and outline of the dissertation

The first goal of this dissertation is to present the development of striation techniques that address the magnetization AC-loss-related issues in 2G-HTS. The optimization of critical current and AC losses in the striated conductors is targeted.

The second goal is to develop an innovative electroplating technique that allows selective electroplating of stabilizer layer on only superconducting filaments of filamentized 2G-HTS conductors rather than undergo a cumbersome process of striating the conductor through a thick stabilizer layer. Commercially available copper deposition uses acidic solutions. However, such solutions cannot be used in multifilamentary tape because acid in the solution degrades the properties of superconductors. To accomplish selective electroplating on superconductor filaments, an acid-free copper electrolytic solution has been employed.

The third goal is to determine the AC loss behaviors of such fully-filamentized tapes with different thickness values of the selectively-electroplated stabilizer layer with different number of filaments and to compare the results with the existing theoretical models to verify the success of the techniques developed in this dissertation. Determination of the limitations of the developed techniques in terms of plating thickness and filament widths is another goal of this dissertation. The last goal is to develop method(s) to investigate and improve the mechanical properties of 2G-HTS along the c-axis.

This dissertation is structured as follows:

- Chapter 1 provides an introduction to superconductivity, its applications, related problems and goals of the dissertation.
- Chapter 2 provides an overview of theoretical framework to superconductivity and AC losses. Analytical models to calculate hysteretic, eddy, and coupling losses are discussed in this chapter.
- Chapter 3 explains the experimental framework with which samples are studied and presents the techniques of measurements. Self-field critical current, critical temperature measurements and systems are explained in detail. Principles for both transport and magnetic AC loss measurements are explored and the experimental set-up for magnetization losses is discussed.
- Chapter 4 provides details on filamentization techniques of REBCO conductors, selective-electroplating and delamination. Related microstructures of filamentized, oxygenated, selectively-electroplated and delaminated tapes are individually discussed.
- Chapter 5 provides the results of magnetization AC losses, critical current, critical temperature measurements and delamination tests. The experimental findings and analytical results are compared. Finally, in the conclusion, a summary is provided with recommended future works.

Chapter 2. Theoretical overview and fundamentals of AC losses

This chapter presents a brief introduction to superconductivity and AC losses. The background theory and concepts are described using simple geometries and real conductor configurations. These theoretical calculations and formulae form the basis for comparing experimental results and will be utilized in later sections.

2.1. Theories on superconductivity

2.1.1. The London theory

A phenomenological theory for superconductivity was provided by the brothers, F. and H. London, in 1935 [62]. Their proposed equations are consistent with the Meissner effect and can be used with Maxwell's equations to predict how the magnetic field and surface current vary with distance from the superconductor surface. A detailed derivation of the magnetic field distribution inside a superconductor and a solution to the London equations in 1D geometry is provided in Appendix A. The magnetic field distribution formula inside a superconductor can be re-written as

$$B(x) = B_a e^{-x/\sqrt{\alpha}}. \tag{2-1}$$

This equation indicates that the applied field fades away exponentially inside a superconductor. This exponential reduction falls to 1/e of its value (Figure 2-1) at a distance from the surface of

$$x = \sqrt{\alpha} = \sqrt{(m / \mu_0 n_s e^2)}. \tag{2-2}$$

This distance is called the London penetration depth, λ_L. The behavior of most type−I superconductors can be approximated by these simple equations with good accuracy. Later on an alternative to the London theory, the Ginzburg-Landau theory was established.

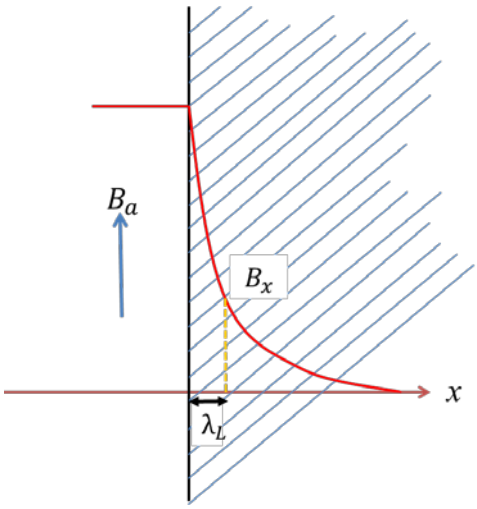

Figure 2-1. Magnetic field density variation by the distance from the surface.

2.1.2. The Ginzburg-Landau theory

London theory was derived using a classical electromagnetism framework while the Ginzburg-Landau theory used a pseudo quantum method to describe the effect of a magnetic field. Ginsburg and Landau defined a complex order parameter field, ψ, which can be used to express the free energy. Below the transition temperature, this parameter is non-zero and related to the density of super-electrons. A state consisting of both superconducting and normal phases forms an intermediate state which occurs in type−I superconductors. One important implication of this theory is that the intermediate state can be analyzed when the applied field is equal to the critical field, $B_a = B_c$.

The G-L theory introduced a characteristic parameter called coherence length, ξ, the distance over which the super-electron density raises from zero to its superconducting state density. Coherence length, ξ, and penetration depth, λ, can be used to distinguish type−I and type−II superconductors. The ratio $\kappa = \lambda(T)/\xi(T)$ is known as the Ginzburg-Landau parameter. Type−I superconductors are defined as those with $0 < \kappa < 1/\sqrt{2}$ and type−II superconductors are those with $\kappa > 1/\sqrt{2}$ (illustrated in Figure 2-2). If the

magnetic flux penetration distance is smaller than the super-electron density their contributions do not cancel near the boundary. This results in a positive surface energy as shown in Figure 2-2a. It is not favorable to form a mixed state in these superconductors because it increases the free energy. Superconductors with these parameters are referred to as type–I. If λ is larger than ξ, a negative surface energy is present producing the favored mixed state over normal or fully-superconducting states and such superconductors are referred to as type–II.

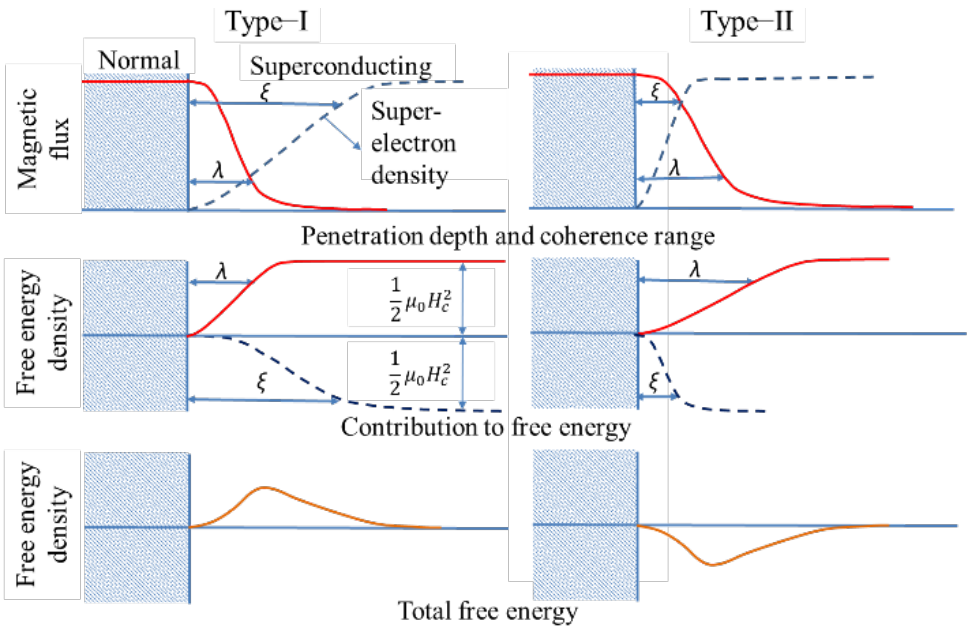

Figure 2-2. Classification of superconductors according to λ and ξ. Type–I (left) and type–II (right) [14].

2.1.3. Flux-creep and flux-flow

When an applied field is larger than the lower critical field ($H_a > H_{c1}$), the normal and superconductive phases exist at the same time producing a mixed state. Non-superconductive normal cores penetrate the superconductor and consist of vortices that have a quantum flux of $\Phi_0 = h/2e = 2.6678\times10^{(-15)}$ Wb, where h is Planck's constant. The formation of vortices continues until H_{c2} is reached. This increase in the number of

vortices results in a decrease in the spacing between them which is given by $a_0 = 1.075\sqrt{\Phi_0 / B_a}$.

The motion of flux lines in the mixed state causes energy dissipation in type−II superconductors. This phenomenon is referred to as flux-flow resistivity. The Lorentz force applied to a single flux quantum is responsible to such a motion $\mathbf{F}_L = \mathbf{J} \times \Phi_0$. The electric field induced by the flux motion with a velocity, **v**, is described as $\mathbf{E} = \mathbf{B} \times \mathbf{v}$. When the current densities are larger than the J_c, the vortices are not influenced by the pinning barriers and their motion in the presence of a driving force is only affected by the viscous drag force. In a steady state, the mean velocity of the system is determined by the equilibrium between the Lorentz force and the drag force $\mathbf{J}\Phi_0 = \eta \mathbf{v}$, where η is the viscous drag coefficient. By combining these two equations related to electric field, *E*, and current density, *J*, the flux-flow resistivity, ρ_{ff}, can be written as

$$\rho_{\mathrm{ff}} = \frac{E}{J} = B\frac{\Phi_0}{\eta} . \qquad (2\text{-}3)$$

At absolute zero, there is no thermal activation and the flux is either pinned or moved into the flux-flow regime (shown with the red solid line in Figure 2-3). In the flux-flow regime, there is a simple linear correlation between *E* and *J*. However, finite temperatures have two effects on vortices pinning. The first effect is that the flux lines vibrate about their equilibrium positions and are sometimes de-pinned at very low current densities where $J<J_c$. This is called the thermally-activated flux flow (TAFF) [63, 64]. The second effect is that at sufficiently high temperatures the thermal energy may allow flux lines to jump from one pinning center to another. This occurs when the pinning potential barrier is overcome even if the current density is not larger than $J_c<J<J_{c0}$. This thermal

motion of flux vortices, known as flux-creep [65], becomes more pronounced at high temperatures i.e., 77 K. Both of these finite temperature effects are shown in Figure 2.3 with a dashed black line.

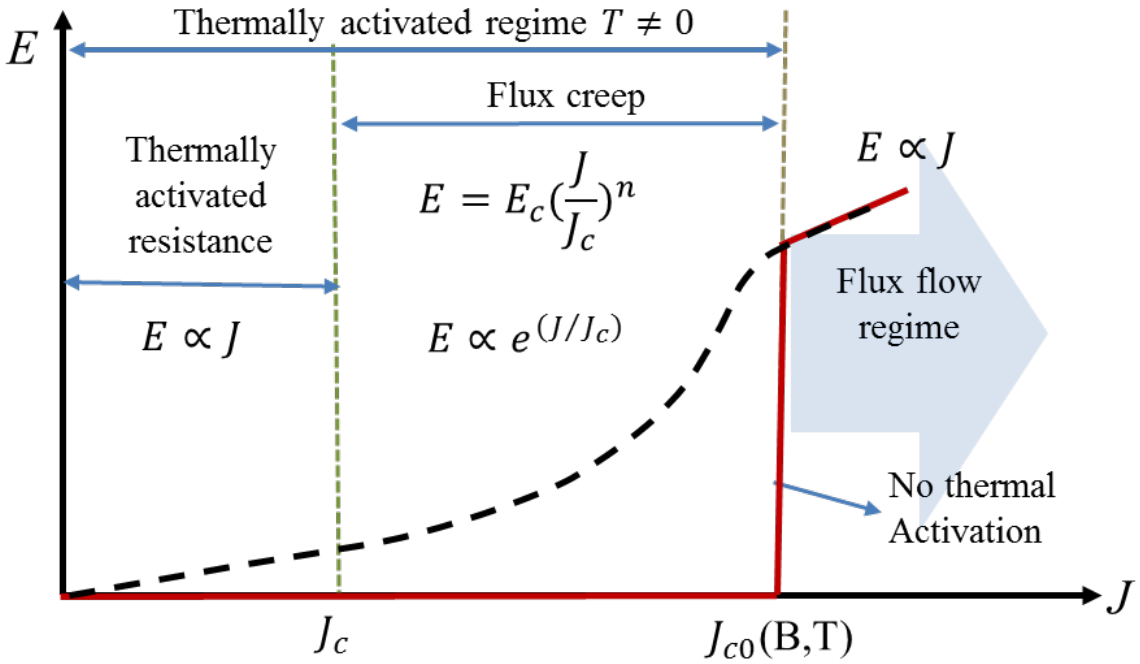

Figure 2-3. *E-J* characteristics with and without the presence of flux-creep. The solid red line is without the thermal effect while the dashed black line is with the thermal effect.

The jump rate out of a pinning center follows an Arrhenius type equation and can be written as $R = R_0 e^{(-U_o/kT)}$ with a potential well depth of U_0. R_0 is the frequency of hop attempts, k is the Boltzmann constant, and T is temperature. The Lorentz force causes the potential barrier to decrease by U_L in the direction of the force and increase by U_L in the reverse direction. Using this information the flux-creep rate can be written as

$$R = 2R_0 e^{-U_0/kT} \sinh\left(U_L / kT\right). \tag{2-4}$$

The magnetization relaxation process was investigated assuming that the effective creep activation barrier (U) grows logarithmically with decreasing current, $U = U_0 \ln\left(J / J_c\right)$ [66]. Since the flux-flow dissipates energy, the electric field induced by

flux-creep can be written as $E(J) = E_c e^{-U/kT}$ [66, 67], where U is the effective energy barrier. By combining these two equations and substituting $n = -U_o / kT, E$ can be represented as

$$E = E_c (J / J_c)^n, \tag{2-5}$$

where E_c is the electrical field criterion, which is typically equal to 1 μV/cm.

2.1.4. Critical current density in HTS conductors

Equation (2-5) is a non-linear model that fits very well to the experimental $I-V$ curves for many HTS superconductors. n is a specific characteristic parameter of the HTS. For instance the cases of $n = 1$ and $n = \infty$ correspond to the linear Ohm's law and Bean's model ($J=0$ or J_c) respectively. The variation of $I-V$ curves with different n values is shown in Figure 2-4. When a superconductor has a strong flux-creep, it should also have small n values. When n > 20 (the dashed red line shown in Figure 2-4), the curve becomes already good approximation to the Bean's critical state (CS) model [68]. The destruction of superconductivity and transition from a superconductive to normal state occurs when sufficient electromagnetic energy or if the temperature or the magnetic field are raised above their critical values. Superconductivity is also destroyed if the kinetic energy of the superconducting current density exceeds the equivalent binding energy of the Cooper-pairs. The current density for breaking the Cooper-pairs is called the de-pairing current density. De-pairing current density can be calculated as $J_d \approx \Phi_0 / 2\pi\mu_0\lambda^2(T)\xi(T)$ ≈ 50 MA/cm^2 at 77 K, with T_c=90 K, λ=260 nm, ξ=3.5 nm for REBCO CCs. Currently the highest experimentally achieved J_c at 77 K using a 1 μV/cm is less than 10 MA/cm^2. This shows that there is significant room for current density improvement.

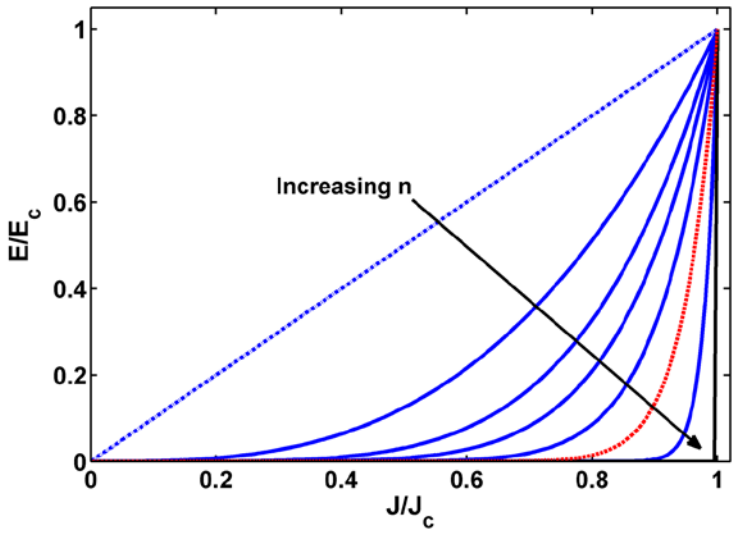

Figure 2-4. Normalized E-J curves with different *n* values (the red dashed line is for n=20).

2.1.5. Critical state

The CS model, also called the Bean model, is a macroscopic description of the type−II superconductor magnetization which employs the spatially averaged electromagnetic properties of the superconductors [69]. This model is not only a simple phenomenological approach, but is also useful for finding current and magnetic field distributions inside a superconductor. Magnetic field sweeping, dB_a/d_t, induces screening current according to Faraday's law. This opposes changing magnetic field and reacts with Lorentz force to distribute the current starting from the edge of the conductor. When the applied magnetic field, B_a, is raised after cooling the sample in a zero field, some magnetic flux is allowed to penetrate the slab (conductor). However, the pinning centers near the surface capture the flux vortices and hinder homogeneous flux diffusion. By increasing the field these vortices are redistributed resulting in dissipation. In this model, the current is assumed to be either zero or its critical value, J_c. Combining these assumptions with Ampere's law, Bean's critical state model can be written as

$$\nabla \times \mathbf{B_i} = \pm \mu_0 \mathbf{J},\ |\mathbf{J}| = J_c \text{ or } 0. \tag{2-6}$$

For a 1D case, the critical state model can be simplified. Since the field only has a y component and the current flows in the z direction, the curl of *B* is reduced to one term

$$\frac{dB_i}{dx} = \mu_0 J_c, \tag{2-7}$$

where B_i is the internal field of the superconductor. Using the boundary condition of $B_i = B_a$ at $x = a$, the internal field can be solved as

$$B_i = B_a + \mu_0 J_c (x - a), \quad \text{for } x > 0. \tag{2-8}$$

The boundary of flux penetration just before it reaches the center of the slab can be located by setting $B_i = 0$, thus

$$x_p = a - \frac{B_a}{\mu_0 J_c}. \tag{2-9}$$

The macroscopic magnetic field and the current distributions of an infinite slab under the effect of a magnetic field takes the values shown in Figure 2-5a. When there is a positive slope, the current density is $+J_c$ according to Equation (2-7). When the slope is negative the current density becomes $-J_c$. If the magnetic field reaches the center, the slab is said to be fully-penetrated and this can be found by taking x_p to be zero yielding $B_p = \mu_0 J_c a$. This is the penetration field from the virgin state (Figure 2-5b). When the external field has an amplitude higher than B_p it will not oppose any further to the field increase inside the superconductor since the screening current density cannot exceed J_c. The penetration pattern simply shifts upwards. The difference between the field at the edge and the center of the specimen remains constant. However, if the external field starts to diminish the screening currents should oppose this decrease resulting in a reversed current

appearing near the edges of the slab. In the rest of the slab, the field and the current density remains unchanged. This is shown in Figure 2-5b with dashed red lines. When the external field has decreased $2B_p$ from its peak value, the field and current patterns will completely reverse. This penetration field, B_{po}, from a non-virgin state is simply double the virgin penetration field.

Two main concerns about the Bean model are the sharpness of the current density distribution boundary and the negligence of thermally-weakened pinning centers. In the first case, the current density decays exponentially according to the London penetration field and the size of the specimen has to be significantly larger than the decaying distance in order for the model to be valid [70].

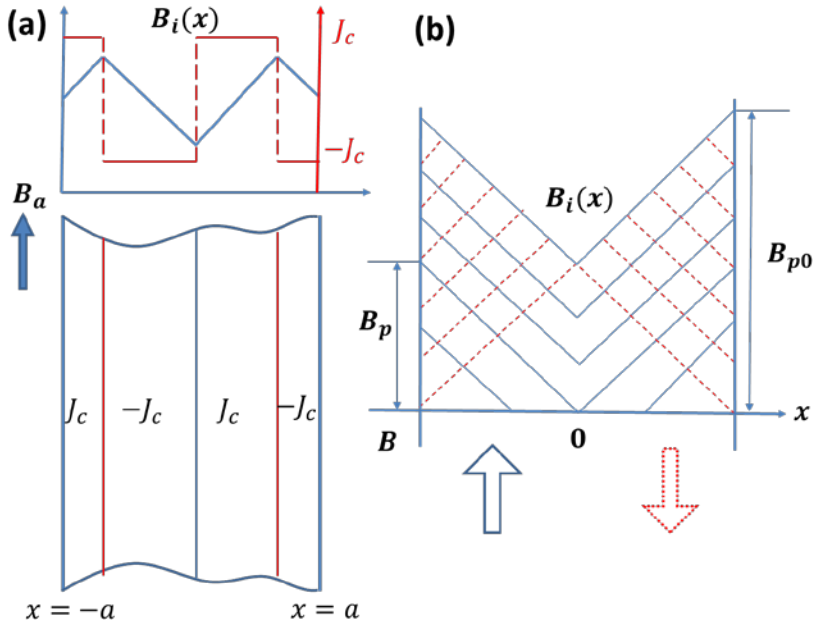

Figure 2-5. Field and current distribution in (a) a 1D slab and (b) a virgin and full-flux penetration field.

2.2. AC losses

One important implication of using HTS is that it greatly reduces the heat removal problem because of a low cooling penalty at relatively high temperatures i.e., 77 K.

However, this does not completely eliminate the problems related to operational costs. For this reason, investigating AC loss is important as this directly affects operational costs and stability. In general, AC losses of short samples can be divided into two categories: transport and magnetization.

Magnetization loss, P_m, is the power dissipated in the superconductor when an alternating magnetic field, B_a (t), is applied. Transport current loss, P_t, is the power dissipation that occurs when an external power supply enables a transport current, I, to flow through the superconductor. The voltage, V, along the sample is a measure of the dissipated power.

2.2.1. Transport loss

Self-field loss, P_{tsf}, is one type of transport current loss and is caused by the interaction of the transport current and the transverse field induced by the transport current itself [13]. Usually the self-field is much smaller than the externally applied field for a single tape and this loss is negligible compared to other loss types. Self-field losses can also be reduced by filamentization.

When the transport current increases, flux-flow loss occurs causing progressively more flux lines to de-pin. The energy dissipation associated with this process is called flux-flow loss, P_{tff}. Initially the self-field loss dominates but with increasing transport current the flux-flow loss contribution becomes significant.

2.2.2. Magnetization loss

Magnetization losses can be categorized in three groups − hysteretic, coupling and eddy current losses. Since magnetization AC losses are comparatively larger than the

transport losses, this dissertation focuses mainly on them, although some aspects of transport losses are also briefly discussed.

2.2.2.1. Hysteresis loss

Hysteresis loss, P_{mh}, occurs when the superconductor is in the mixed state. In type−II superconductors, this type of loss is caused by irreversible magnetic flux motion driven by an externally changing field at any frequency. Hysteresis loss is related to flux pinning and flux motion; therefore, is related to critical current density and the size of the superconductor.

Energy dissipation happens due to the electrical resistance and changing magnetic field. The electrical resistance is not a problem for superconductors since they have zero resistance. However, $\nabla \times \mathbf{E} = -\partial B / \partial t$ is still relevant. A time-varying magnetic field is always accompanied by a spatially-varying electrical field. Hysteresis in type−II superconductors causes energy dissipation and to sustain the current, a driving force, voltage, is needed. In DC applications, $\partial B / \partial \mathrm{t} = 0$ and flux is pinned. In AC applications the loop formed by hysteresis determines the energy loss in the superconductor. A larger loop results in larger losses and the dissipated energy is released as heat. An example of a hysteretic loop is shown in Figure 2-6 with the field penetration profiles on the sides.

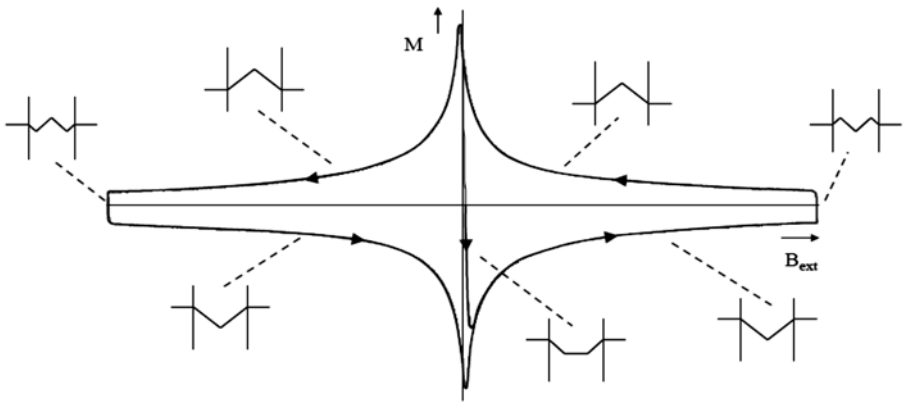

Figure 2-6 Magnetization loop for a full cycle of an applied field [71].

2.2.2.2. Eddy current loss

As stated earlier, a time-varying magnetic field penetrates into a conductor and induces a spatially-varying electric field that drives circulating currents creating a magnetic field opposing the initial one. These currents are known as eddy currents. This loss component is usually the smallest one in 2G-HTS CCs; however, this ohmic energy dissipation needs to be considered when the external magnetic field is perpendicular to the tape. Calculations of eddy current losses have been studied and an analytic expression for the loss per length for an isolated metal was provided [72-74]

$$P_{\mathrm{me}} = \frac{2\pi^2 f^2 B_0^2 J_{M,y}}{\rho_m} n_f, \tag{2-10}$$

where B_0 is the amplitude of the transverse applied field, n_f is the number of filaments and ρ_m is the resistivity of the metal. $J_{M,y}$ is the moment of inertia and for a rectangular tape is given by

$$J_{\mathrm{M,y}} = \frac{w_f^3 d_s}{12}, \tag{2-11}$$

where d_s is the thickness of the stabilizer layer, w_f is the filament width. This formula does not take into account the superconductor layer. A more detailed analysis for eddy current loss that accounts for the field and current distribution on the superconductor was calculated by Muller [75]. In order for this equation to be valid, $w_f / 2$ must be smaller than the skin depth, which is given by

$$\delta = \sqrt{\frac{\rho}{\pi \mu_0 f}}. \tag{2-12}$$

The resistivity measured from thin-layer, electroplated copper was found to be, $\rho_{\text{room\_Cu}} = R\,A/l = 2.976\times10^{(-8)}$ Ωm and $\rho_{77\text{K\_Cu}} = 4.512\times10^{(-9)}$ Ωm at room and 77 K respectively. *R* is the resistance of copper measured using the sample (dimensions shown in Figure 2-7). *A* is the cross-sectional area, and *l* is the distance between the voltage taps. Skin depth calculated using Equation (2-12) is 5.34 mm at 40 Hz and 1.52 mm at 500 Hz. The maximum width of a filament is 2 mm. This calculation validates the use of Equation (2-10).

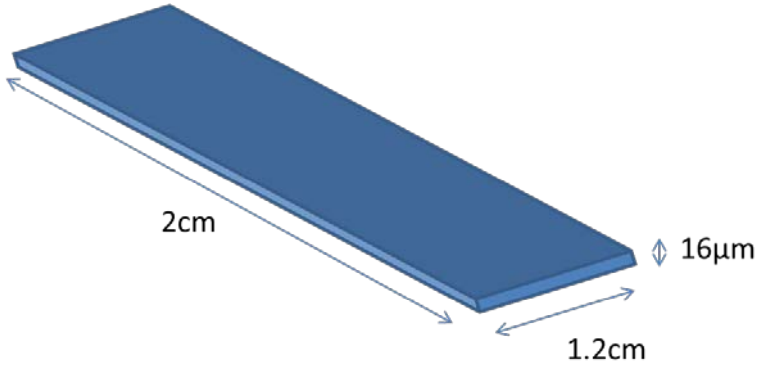

Figure 2-7. Sample dimensions for the resistance measurement of electroplated copper.

In practice the eddy current loss can be reduced by increasing the effective resistivity of the matrix. As it can be seen from the Equation (2-10), eddy current losses are proportional to the width cubed. Filamentization is a potential solution to decrease the eddy current loss contribution to negligible levels.

2.2.2.3. Coupling loss

There are two types of coupling; magnetic and electrical. Magnetic coupling results from distortion of the magnetic field near the grooves at relatively low field. It can be prevented by increasing the distance between the filaments [76]; however, this increase is undesirable because it reduces the superconductive material fraction. For this reason the

inter-filament width needs to be optimized for the width of filament and magnetic coupling effects on AC losses.

Although filamentization is aimed to reduce hysteresis losses, it produces another undesirable loss mechanism called electrical coupling loss. When filamentization is achieved by the selective removal of associated layers the conductive barrier between filaments typically consists of a metal substrate. The electrical coupling losses are governed by the resistivity of this metal substrate. Electrical coupling is a significant problem for striated REBCO CCs since it increases the losses to undesirable levels or even eliminates the benefit of filamentization altogether [77, 78]. This phenomenon was recognized in multifilamentary superconducting wires in late 1960. The source of loss is Joule heating caused by the resistive current transferred between neighboring filaments through a metallic path. When the external AC field is applied, voltage will be induced according to Faraday's law and that voltage will drive the current in a loop along individual filaments if the resistivity of the barrier material is sufficiently high (Figure 2-8a). In this case, there is no current transfer between the superconducting filaments. This configuration is called a completely-decoupled configuration and only hysteresis loss is presented. However, if the resistivity of the barrier material is not high enough the electrical current runs from one filament to another and a fully-coupled configuration occurs. In this configuration the tape magnetization behaves identically to a non-filamentized tape of the same width (Figure 2-8b). The total losses in this configuration can even exceed the losses on tape with no-filamentization. Theoretical models have been proposed to describe electrical coupling loss. One of them is the anisotropic continuum model [79]. The REBCO layer in the anisotropic continuum model is treated as a homogenous medium. The sample

configuration for these calculations is provided in Figure 2-9. Calculations were made for a tape with no-transport current.

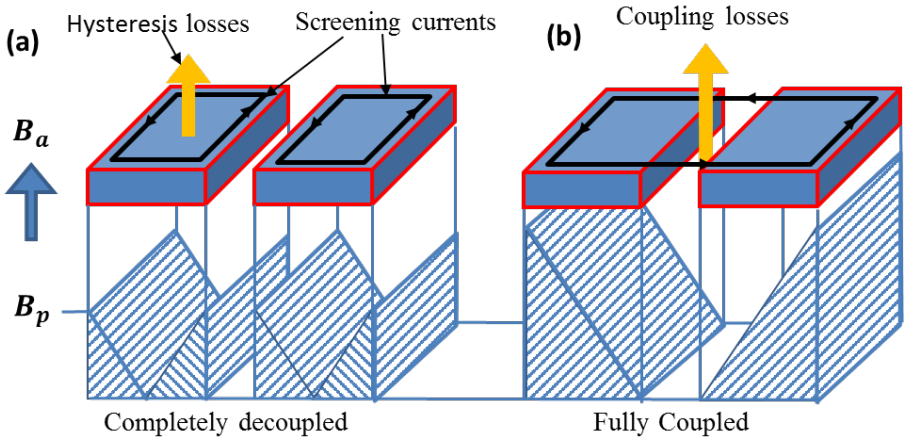

Figure 2-8. (a) Completely decoupled and (b) fully coupled filament configurations and their magnetizations.

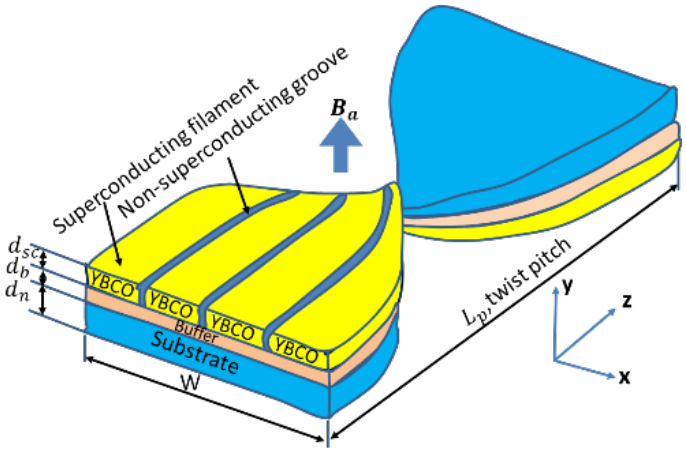

Figure 2-9. Sample configurations for the electrical coupling loss calculation.

The electrical coupling is given by the transverse resistivity term as

$$P_{\text{mc}} = \int \mathbf{E} \cdot \mathbf{J} dV = \int \rho^{-1} E_{\perp}^{2} dV. \tag{2-13}$$

The electric field driving the current from one filament to a neighboring one through the resistive matrix can be described by $\mathbf{E} = -\frac{f B_0 L_p}{2\pi} \sin(\frac{2\pi z}{L_p}) \hat{R}$ [79]. Using Equation (2-13) integration of the electric field squared yields $\int_{z=0}^{z=L_p} \frac{E^2 d(2\pi z / L_p)}{\rho L_p} (\frac{L_p}{2\pi})$. Averaging it over z

yields $\frac{q^2}{2\pi\rho}\int_{z=0}^{z=L_p}\frac{1-\cos^2(2\pi z/L_p)}{2}d(\frac{2\pi z}{L_p})(\frac{L_p}{2\pi})\Big/L_p=\frac{q^2}{2\rho}$ where $q=(fB_0L_p)$. The electrical coupling loss per length can be obtained as

$$P_{\mathrm{mc}}=\frac{(fB_0L_p)^2}{2\rho}d_nW, \tag{2-14}$$

where L_p is the twist pitch, f is the frequency, W is the width of the tape, d_n is thickness of metal substrate, and ρ is the experimentally determined effective resistivity. The correlation between single groove resistance, R_{sg}, and ρ is provided in [80] as

$$R_{\mathrm{sg}}=\frac{k\rho}{L_z}. \tag{2-15}$$

L_z is the conductor length which can substituted for the twist pitch and k is the parameter that depends on the striation method. The effective resistance for multifilamentary tape is $R_{\mathrm{ef}}=kn_f\rho/L_z$.

Superconducting filaments have no-resistance and current can flow very long lengths along these filaments. If this length exceeds some threshold, called the critical length, full coupling occurs as shown in Figure 2-8b. The tape should be transposed meaning that each filament needs to swap their places along the length in order to reduce mutual flux linkage. If the magnetic flux cannot penetrate into the grooves, the multifilamented tape behaves as mono-filamentary tape. The critical length to prevent this coupling is formulated to be [13]

$$L_{\mathrm{c}}=4\sqrt{a\rho J_c/\frac{dB_a}{dt}}, \tag{2-16}$$

where *a* is half the superconductive film width or half the filament width in multifilamented tape. Using the half width of $a = 400\times10^{-6}/2 = 200\times10^{-6}$ m, resistivity $\rho = 0.53\times10^{-6}$ Ωm, $Jc = (110/20)/(1.4\times10^{-6}\times400\times10^{-6}) = 9.8\times10^{9}$ A m^{-2} and magnetic field sweep rate of $dB/dt = f\ B_m$, $B_m = 50\times10$ mT the coupling length is calculated to be 2.2, 0.86, and 0.56 m at f = 10, 70 and 170 Hz, respectively. There is no practical material with the resistivity to prevent coupling at the required length. Transposing by twisting the tape is a smart way to deal with this problem. By twisting the wire, as shown in Figure 2-9, the screening current loop can be confined and prevent the occurrence of critical coupling.

Calculations for the different types of losses using analytic formulae are provided in Figure 2-10 for a12 mm wide REBCO tape at 45 Hz and 30 mT. A pie chart of magnetization loss distribution in a tape without striation is provided in Figure 2-10a. In a wire without striation, the losses dominantly originate from hysteresis with only a 2 % contributed by eddy current loss. If the losses are calculated for a sample after striation and fully-coupled, most of the losses originate from electrical coupling with a little from hysteretic and negligible amounts from the eddy current (Figure 2-10b). The loss reduction is about two-fold compared to the non-striated reference sample. In Figure 2-10c, the losses are calculated for a sample after striation and fully-decoupled. Almost all the losses are hysteretic in nature with a substantial decrease in magnetization AC losses, ~15 times out of 11 striations. These calculations suggest that coupling is highly undesirable in a striated tape and needs to be addressed wisely to avoid any deterioration of structural integrity.

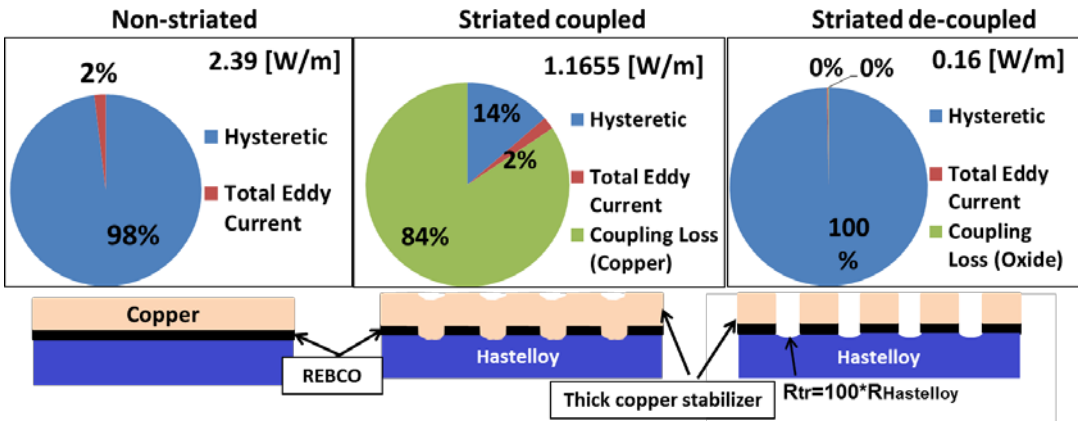

Figure 2-10. Comparisons of losses (a) before striation, (b) after striation and coupling, and (c) after striation and de-coupling.

2.3. AC loss models for the superconductor layer

2.3.1. CS Model for a slab parallel to the applied field

A detailed derivation of the magnetization AC loss calculation for a slab geometry is provided in Appendix B The loss function or normalized loss (loss per cycle per Tesla squared per volume) in terms of normalized field, $\beta = B_0 / B_{p0} = B_0 / 2\mu_0 J_c a$, can be written for the penetration fields, both above and below, as follows

$$\Gamma(\beta) = \begin{cases} \dfrac{\beta}{3}, & \beta < 1 \\ \dfrac{1}{\beta} - \dfrac{2}{3\beta^2}, & \beta > 1 \end{cases} . \qquad (2\text{-}17)$$

One important conclusion is that the loss is proportional to B_0^3 below the penetration field while it is proportional to B_0 above the penetration field.

2.3.2. AC loss for a thin strip CCs

The previous derivation was based under the assumption of an infinite slab. However REBCO CCs are very thin materials with a high aspect ratio (10^4). In real superconductor applications, coated conductors can be simulated by infinitely long thin strips carrying a transport current or in an externally-applied magnetic field. In other words,

the problem is still one dimensional. The geometry for calculations of a superconducting strip filling the space, $|x| \le a, |y| \le d/2, |z| < \infty$ with $d_{sc} \ll a$ is shown in Figure 2-11. Taking into account that the width is considerably larger than the thickness the real current distribution in the strip cross-section is reduced to sheet current densities (current per unit width of conductors $J_c = I_c / 2a$).

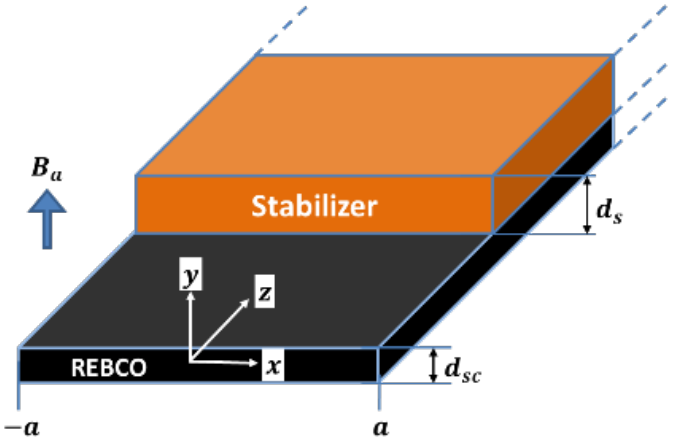

Figure 2-11. Geometry provided for thin film calculations.

2.3.3. Brandt-Indenbom model

Brandt-Indenbom (B-I) [81] has developed theoretical formulae for analyzing AC losses which has very good agreement with experimental results [76, 82-85]. The Bean model fits to long-superconductors where demagnetization effects are negligible. B-I realized that in practice, experiments use flat superconductors for which demagnetizing effects are crucial and need to be taken into account. Very detailed analysis of the current and field distribution of a superconductive strip in a perpendicular field is provided in [81]. In the B-I model for a virgin state the current and field profiles in a perpendicular applied field of $B_a(t) = B_0 \sin(wt)$ with zero transport current can be summarized when $B_a(t)$ increases from its zero value to peak as

$$J(x)=\begin{cases}\dfrac{2J_c}{\pi}\arctan\dfrac{cx}{\left((b^2-x^2\right)^{(1/2)}}, & |x|<b \\ \dfrac{J_c x}{|x|}, & b<|x|<a\end{cases} \quad \text{and} \tag{2-18}$$

$$B(x)=\begin{cases}0, & |x|<b \\ B_c\operatorname{arctanh}\dfrac{\left(x^2-b^2\right)^{\frac{1}{2}}}{c|x|}, & b<|y|<a \\ B_c\operatorname{arctanh}\dfrac{c|x|}{\left(x^2-b^2\right)^{\frac{1}{2}}}, & |x|>a,\end{cases} \tag{2-19}$$

where $b=a/\cosh(B_a(t)/B_c)$ and $c=\left(a^2-b^2\right)^{1/2}/a=\tanh(B_a(t)/B_c)$. To find a solution for the whole cycle linear superposition can be used when the applied field B_a decreases from its zero to negative peak value as

$$J_{\downarrow}(x,B_a(t),J_c)=J(x,B_0,J_c)-J(x,B_0-B_a(t),2J_c) \text{ and} \tag{2-20}$$

$$B_{\downarrow}(x,B_a(t),J_c)=B(x,B_0,J_c)-B(x,B_0-B_a(t),2J_c). \tag{2-21}$$

The hysteresis loss per length per cycle (the area under the hysteresis loop) can be written with $M(t)=\int_{-a}^{a}xJ(x,t)\,dx$ as

$$P_{\text{mh-BI}}=\int M(B_a)\,dB_a=W^2J_cB_o g(\Upsilon), \tag{2-22}$$

where $W=2a$, $\Upsilon=B_0/B_c$, $B_c=\mu_0 J_c/\pi$ and $g(\beta)=\left[(2/\Upsilon)\ln(\cosh(\Upsilon))-\tanh(\Upsilon)\right]$. For small and large amplitudes, this can be modified to

$$P_{\text{mh-BI}} = \begin{cases} \dfrac{\pi W^2}{6B_c^{\,2}} B_0^{\,4} \ , \ B_0 < B_c \\ W^2 J_c \left(B_0 - B_c \right) \ , \ B_0 > B_c . \end{cases} \tag{2-23}$$

In the B-I approach, the main idea of Bean is still intact. The flux-line starts to move when the current density reaches a critical value. There are several differences between the two models. Comparing the virgin state profiles in Figure 2-12 and Figure 2-5, it is apparent that when the flux has partially penetrated and a critical state with $J = J_c$ is established near the edges of the specimen the current flows over the entire width of the strip shielding the central flux-free region. In the Bean model, the flux-free region is current-free. Additionally, the screening current is continuous in B-I model while it is piecewise constant in the Bean model. As soon as the direction of I or B changes, the current density in thin films falls below J_c everywhere while in the Bean model $J = J_c$.

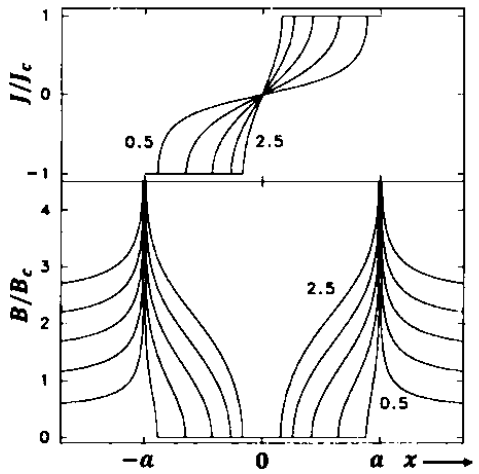

Figure 2-12. Current and field distribution in thin film calculated by B−I model for the virgin state [81].

Comparisions of calculated plots for an infinite slab and a thin film are shown in Figure 2-13. AC losses initially grow to the fourth power of the applied field in B-I whereas it grows to the third power in the Bean model. Above the penetration field, they follow almost the same trend.

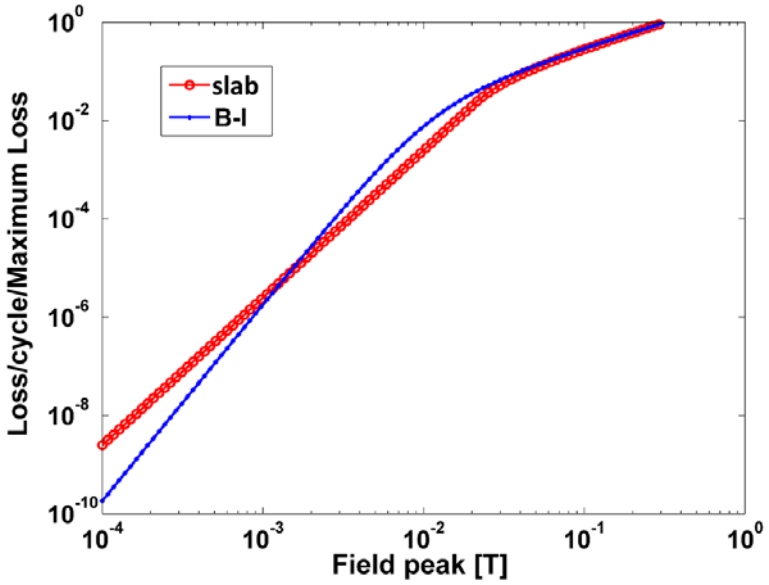

Figure 2-13. Comparisons of loss per cycle normalized to the maximum loss, calculated by the Bean model and B-I model.

The loss function or normalized loss versus applied field plot is presented in Figure 2-14 for an infinite slab and a thin film calculated from Equation (2-17) and (2-22) respectively. For better comparison, the normalized loss is divided by the maximum loss. These calculations are very helpful for finding the penetration fields. There is a difference in the penetration field from B-I and slab model in that the B-I model is relatively smaller.

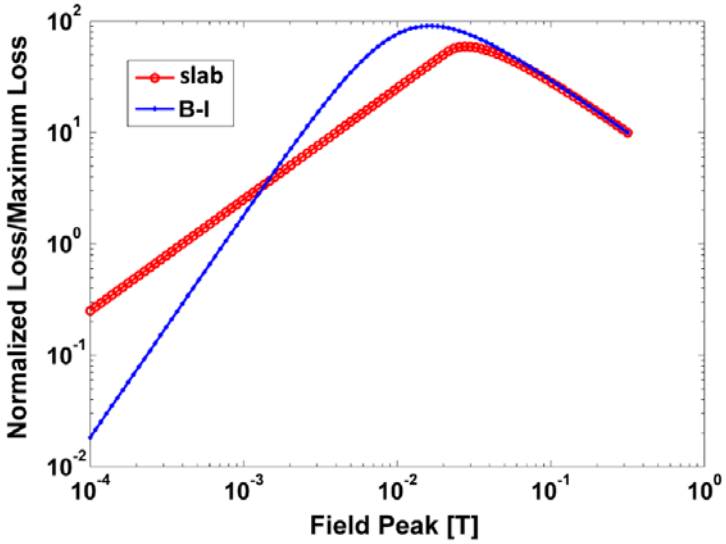

Figure 2-14. Loss function or normalized loss divided by maximum loss with respect to applied field.

Muller [75] has re-estimated the eddy current losses by taking into consideration the current and magnetic field calculated by B-I as

$$P_{\text{me-mul}} = \frac{4 d_s W^3 f^2 \pi}{3\rho} B_c^{\,2} f\left(\frac{B_0}{B_c}\right) \text{ and} \tag{2-24}$$

$$f(\Upsilon) = \int_0^{\Upsilon} \sqrt{\Upsilon\xi - \xi^2}\left(1 - \frac{3}{\cosh^2 \xi} + \frac{2}{\cosh^3 \xi}\right) d\xi. \tag{2-25}$$

Plots for reduced loss functions are given in Figure 2-15. *g* is for hysteretic loss from the B-I model and *f* is for the eddy current loss from Equation (2-25). When HTS is exposed to an external field, $g(\Upsilon)$ initially increase if Υ increases. However, after some point it starts to decrease with increasing Υ. $f(\Upsilon)$ increases all the time with increasing Υ by decreasing slope.

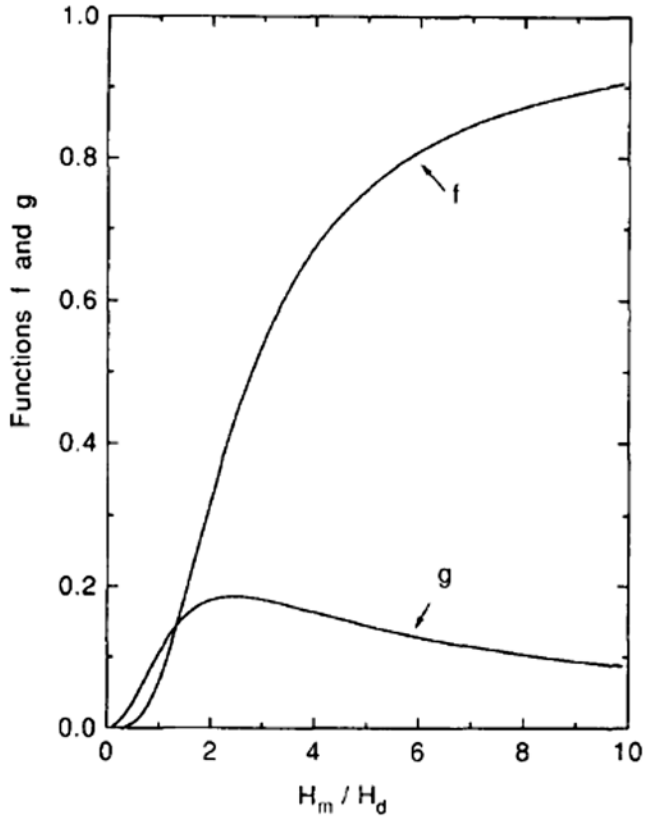

Figure 2-15. Reduced loss functions $f(\Upsilon)$ and $g(\Upsilon)$ [75].

Equation (2-24) for eddy current loss per cycle per length can be reduced as follows:

$$P_{\text{me-mul}} = \frac{21\pi^2 d_s W^3 f^2}{512\times 2\rho_m}\left(\frac{B_0^6}{B_c^4}\right) \quad \text{for } B_0 \ll B_c \text{ and}$$

$$P_{\text{me-mul}} = \frac{\pi^2 d_s W^3 f^2 B_0^2}{6\rho_m} \qquad \text{for } B_0 \gg B_c. \tag{2-26}$$

For the condition $B_0 \gg B_c$, Equation (2-26) is identical to Equation (2-10). Eddy current loss can be calculated from Equation (2-26) using the parameters of $d_s = 20\times10^{-6}$ m, $W = 12\times10^{-3}$ m, $I_c = 200$ A, $f = 40$ Hz, $\rho_m = 4.5\times10^{-9}$ Ωm for the stabilizer layer. The results from the calculations of eddy current and hysteretic losses are compared in Figure 2-16. Note that eddy current loss is orders of magnitudes lower than the hysteretic loss and neglecting eddy current loss in the calculations does not distort interpretations.

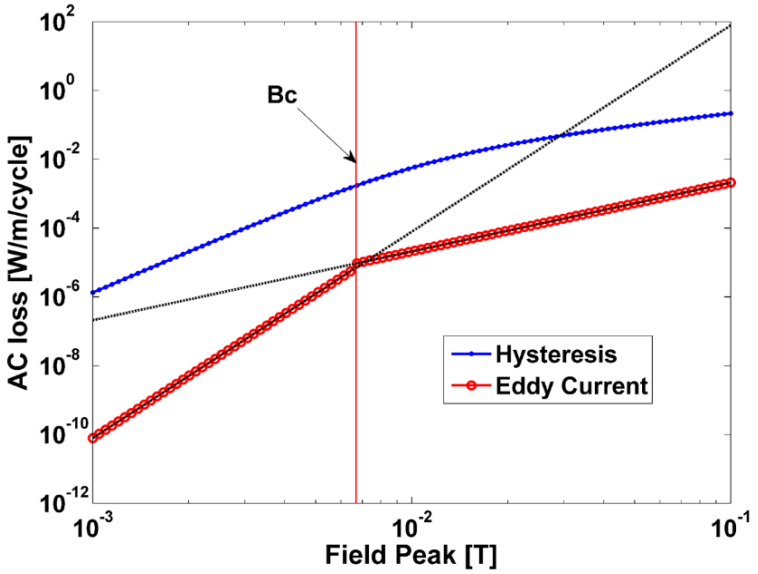

Figure 2-16. Comparisons of eddy current loss and hysteretic loss.

2.3.4. Mawatari model

Both the Bean and B-I derivations suggest that hysteresis loss can be reduced proportionally by dividing the tapes into filaments or smaller segments. Although the B-I

expression has fairly good agreement with measurements in an isolated strip, it does not describe multifilamentary tape well. In the B-I expression the effect of the neighboring filaments is neglected. In a striated conductor, the magnetic field distribution is affected by the field concentration in the non-superconducting grooves. This leads to a change in magnetization AC loss performance of striated samples at relatively low field amplitudes (below penetration field). This is due to the magnetic coupling which is not dependent on the electrical resistivity of the groove material. For this reason, the magnetization AC loss calculated using the B-I model includes an error when the applied field magnitude is small due to neglecting the influence of the neighboring filaments. Mawatari [86] has derived another expression by considering an infinite array of superconducting filaments in order to take into account the neighboring filaments effect on AC loss performance.

The field and current distribution calculated by the Mawatari model is shown in Figure 2-17 and compared with the isolated strip model where $\varepsilon / w \to \infty$. At the edges, the Mawatari model diverges from the one calculated by B-I. This leads an increase in magnetization loss when the applied field amplitudes are relatively low.

The geometrical configuration for the Mawatari model is provided in Figure 2-18. The loss per unit length for one field cycle $P(H_m)$ can be calculated by

$$\frac{P_{\text{mh-Mawatari}}(H_m)}{L_p} = -\frac{4\mu_0\varepsilon^2}{\pi}\int_0^{H_m}(H_m - 2H_a)\,ln\left[1-\frac{\sin^2(\pi a/\varepsilon)}{\cosh^2(H_a/H_0)}\right]dH_a, \qquad (2\text{-}27)$$

where H_a is the applied field, H_m is the peak value of the applied field, ε is the distance from the middle of one filament to middle of the neighboring one, W is the width of the filament and H_0 is the characteristic field given by $H_0=J_c d/\pi$.

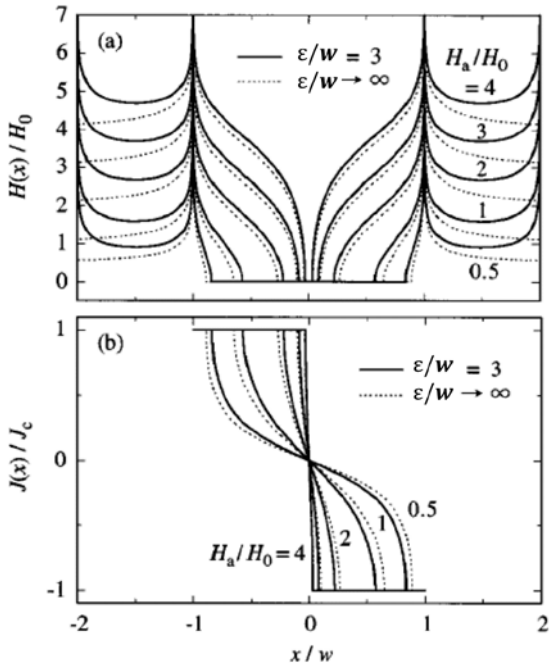

Figure 2-17. Profiles of magnetic field (a) $H(x)$ and (b) $J(x)$ *in* an arrays where $\varepsilon / w = 3$ (solid lines) and in an isolated strip line where $\varepsilon / w \to \infty$ (dashed lines) at H_a/H_0=0.5, 1, 2, 3 and 4 [86].

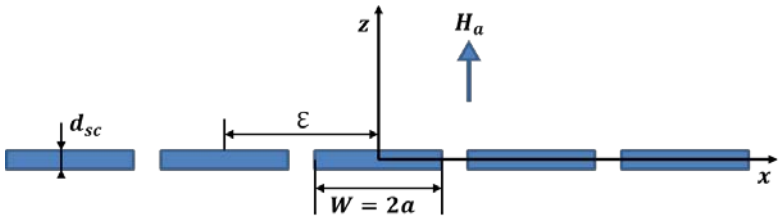

Figure 2-18. Arrangement of strip lines in an array. An infinite number of strip lines are aligned along the x axis at a period of ε. Each strip line has width $W = 2a$ and thickness d_{sc} and is infinitely long along the y axis.

Comparisons of the loss per cycle per unit length behaviors of the B-I model for isolated strips and the Mawatari model for infinitely long strip arrays are provided in Figure 2-19. Calculations were made for a 12 mm tape oriented side by side with a distance of 0.5 mm. At relatively high field amplitudes, the results coincide whereas there is considerable deviation at relatively low fields. This deviation has been regularly reported in other studies [87, 88] and attributed to the magnetic coupling effect [76].

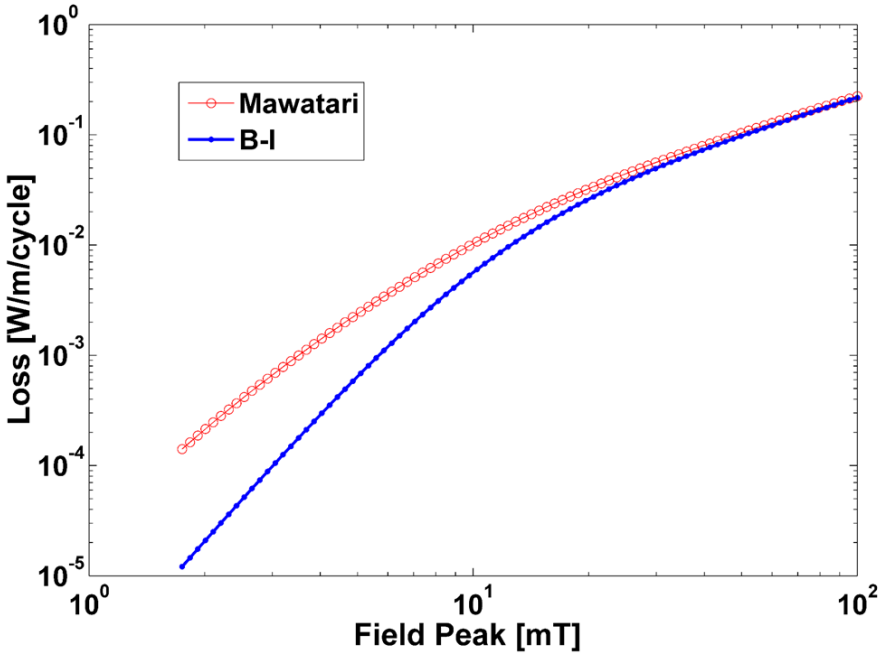

Figure 2-19. Comparisons of the B-I and Mawatari models.

The obvious difference at low fields can be seen when the gap between two adjacent filaments is increased from *W*/10 (width of the filament divided by 10) to *W*/2 (width of the filament divided by 2).

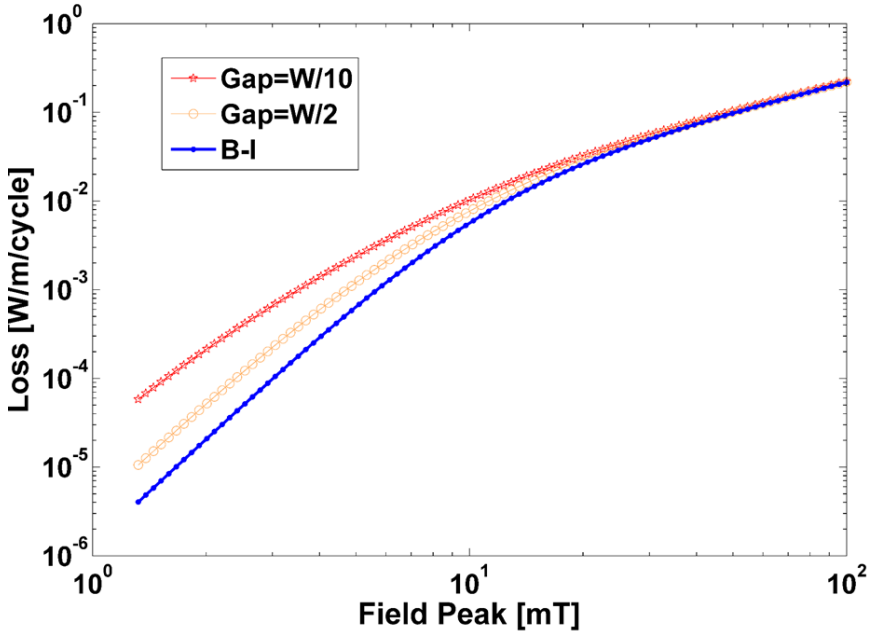

Figure 2-20. AC loss dependence on groove width and comparisons with the B-I model.

2.3.5. Norris model

Norris [89] derived an analytical expression to estimate the AC loss for a self-field based on the London model. He postulated that the resistance rises very suddenly when the current increases above the critical value and the resistance produces an ohmic voltage drop that is balanced by the driving emf while the current density remains constant. In real materials the resistance rises to a finite value gradually. An error is introduced in this model by neglecting this gradual resistance increase. However, it is not significant and the error introduced can be safely neglected at frequencies up to 1 kHz [89]. The maximum frequency used in this dissertation is 500 Hz so this formula can accurately be used for comparison calculations. Similar to the B-I and slab models the current density is assumed to be independent of the applied magnetic field although it is well known that critical currents depend on both the magnitude and direction of the field [90].

For a superconducting tape carrying a transport current with a magnitude I_0, the transport AC loss per length can be formulated

$$P_{\text{tsf-Norris}} = \frac{\mu_0 I_c^2 f}{\pi}\left[\left(1-\frac{I_0}{I_c}\right)\ln\left(1-\frac{I_0}{I_c}\right)+\left(1+\frac{I_0}{I_c}\right)\ln\left(1+\frac{I_0}{I_c}\right)-\left(\frac{I_0}{I_c}\right)^2\right]. \qquad (2\text{-}28)$$

Calculated results for the self-field loss are provided in Figure 2-21. Using an I_c of 200 A and a sample width of 12 mm. Self-field loss has a linear frequency dependence. Self-field loss at 500 Hz with I_o/I_c=0.95 is about 2 W/m; however, this is an extreme condition and no practical applications run with 95% of the critical current. However, the self-field loss is 0.09 W/m at 500 with I_o/I_c=0.5. The hysteresis loss calculated from the B-I model is about 40 W/m at 40 mT and 500 Hz, and 7.7 W/m at 40 mT and 100 Hz. If a real application is considered, a comparison of 0.09 W/m versus 7.7 W/m is more realistic.

The ratio of self-field loss to hysteresis loss is about 1/80. This is why hysteresis loss attracts more attention over self-field transport loss. The reduction in hysteresis loss is very important and is almost equivalent to a reduction in total AC losses.

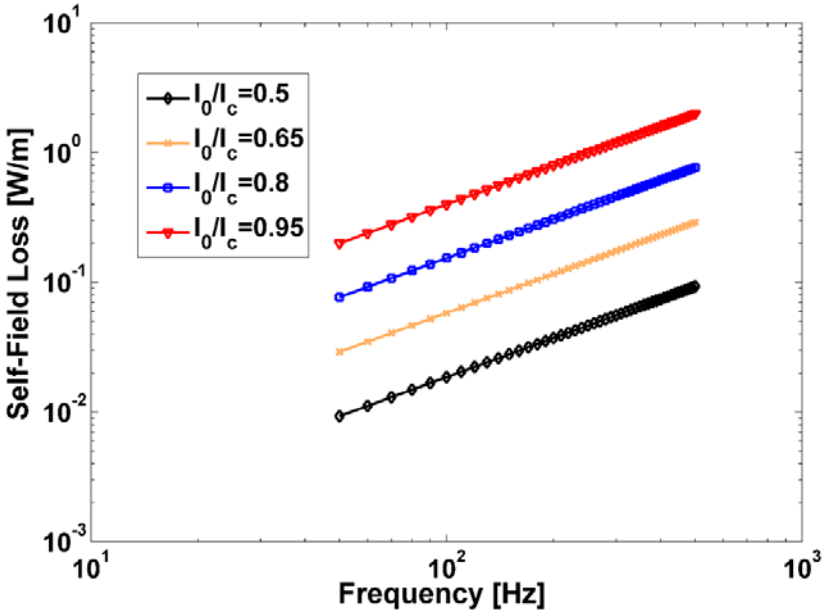

Figure 2-21. Calculated self-field loss using the Norris model.

2.4. Effective width calculations

Quality of the striation process is one of the most important parameters in a novel striation technique. For this purpose, Levin, et al., [84] defined a term called the break-even sweep rate to determine the quality of striation and the contribution of coupling and hysteretic losses to total magnetization AC losses.

$$\mathcal{R} = \lambda_1 / \lambda_2, \tag{2-29}$$

where $\lambda_1 \approx w_f$ and $\lambda_2 = 2L^2 d_n W / (\rho I_c)$, where w_f is the filament width, W is sample width, L is sample length, d_n is metal layer thickness and ρ is the effective resistivity. The coefficients λ_1 and λ_2 are independent of sweep rate and only relate to the sample properties. The first term, λ_1, represents the hysteretic loss while the second, λ_2, represents

the electrical coupling loss. In this analysis the eddy current component is negligible due to its significant reduction by the stabilizer layer filamentization. The point where the coupling loss is equal to the magnetization loss (break-even sweep rate, $\mathcal{R}$) can be calculated using these two constants. If the break-even sweep rate is high the coupling contribution to total magnetization AC loss is low. When $B_0 \gg B_c$ the total loss per length in terms of the hysteretic loss, P_{mh} from the Equation (2-23), and the coupling loss, P_{mc} from the Equation (2-14), be expressed as

$$P_t = P_{mh} + P_{mc} = \Lambda I_c B_0 f, \tag{2-30}$$

where $\Lambda = \lambda_1 + \lambda_2 B_0 f$ is called the "specific loss" (loss per cycle per unit length normalized by $I_c B_0$, in units of length) and f is the frequency. Λ can also be interpreted as either the effective filament width or as an indicator of the striation quality of the procedure.

2.5. Parameters affecting AC losses

When the field dependent hysteresis loss is investigated, the field values below and above the penetration field need to be investigated separately. It can be seen from Equation (2-23) that hysteretic AC loss has a fourth power dependence on applied field values below the penetration field and is linear for those above the penetration field. The magnetic field also has a substantial effect on coupling and eddy current losses since these losses depend quadratically on the applied magnetic field according to Equations (2-14) and (2-10) respectively.

Frequency is another important factor that affects losses. According to Equation (2-22), the hysteresis loss per cycle is independent of the frequency while the eddy current and coupling loss per cycle depends linearly on frequency according to Equations (2-14) and (2-10) respectively. Frequency-dependent AC losses are used to differentiate the

coupling loss component, especially at low frequencies. Practically slope on the frequency versus the loss line should be related to the electrical coupling loss component if the eddy current component is negligible. However, it was found that hysteresis loss also depends on frequency. The penetration field changes with respect to frequency. For instance, B_p at 3 mHz, 30 mHz and 120 mHz is 21.5 mT, 24.9 mT and 27.7 mT, respectively [91]. This behavior clearly shows that for field values smaller than B_p the sample volume occupied by magnetization currents decreases with increasing frequency, and consequently the losses decrease.

AC losses are linearly dependent on current densities according to Equation (2-22). Critical current densities depend on the temperature. If the temperature rises current densities drop drastically and the losses decrease.

There are a number of ways to reduce the coupling loss. Sometimes it is necessary to reduce the sample length or twist-pitch (Figure 2-9). The twist-pitch is important because the electrical coupling loss is quadratically depends on L_p. It is known that L_p should be less than L_c , the critical length for full-coupling to occur. Another parameter that can alter the coupling loss is the resistivity of the coupling material. By increasing the resistivity of the coupling material the twist-pitch can also be increased. Oberly, et al., [92] have reported numerical calculations for generators with a working power of 1 MW for high-frequency aircraft applications. If the resistance value in these applications is 0.2 Ω/cm then the twist-pitch should be about 300 mm. For an aircraft generator working at 200 Hz this could be commercially viable from the viewpoint of AC loss reduction. If the frequency of the generator increases to 400 Hz, this would not be practically viable due to an increase in the electrical coupling loss term. When this is compared to transformer applications, the

required resistance value would be more than 103 Ω/cm [83]. In 2G-HTS achieving these resistance values is not a simple task since multifilamented tape has Hastelloy coupling material. With current striation techniques the only viable way to obtain the necessary resistance values is to oxygenate the Hastelloy coupling material. This allows the creation of a highly resistive oxide layer, increasing the resistance.

AC losses in 2G HTS CCs are very complex and important matter in AC applications of superconductors. The fundamental principles are now defined and using those principles there are number of things can be done to optimize the REBCO CCs for AC loss reduction. In this chapter, AC losses are formulated. The most pronounced loss contribution was found to be hysteretic in non-striated tape; however, in striated tapes, another loss mechanism, called electrical coupling, was found to be more significant. The AC loss models for slab and thin films were explained and compared. Also the methods to evaluate effectiveness of filamentization was investigated. These evaluations and calculation will be extensively revised in later chapters (Chapter 4 and 5). In the next chapter, the experimental methods through which the samples were characterized are explained in detail.

Chapter 3. Experimental Methods

Empirical studies on superconductivity have been always challenging due to extremely cold experimental environments. For example, exposure to low temperatures can cause thermal contraction in the samples or experimental housing. Measurement system parts including wires become brittle. They might break or produce noise due to shape distortion, interfering with measurement accuracy. For this reason, each component needs to be chosen and designed carefully. An additional impediment to superconductor measurements is that many of the sample and cryogenic parts need to be non-magnetic since magnetic properties of superconductors need to be measured. This restricts the material selections for building the instrumentation. Energy dissipation also needs to be considered because it affects the consumption of coolant and the resulting sample stability. Fortunately, there is abundant literature characterizing the challenges related to measurement at cryogenic temperatures such as proper material selection, cryostat designing, etc. [13, 93, 94].

3.1. Critical temperature measurements

Critical temperature measurements were performed using an inductive susceptibility technique. Using a home-built system (Figure 3-1a) the input signal was applied to an excitation coil to generate a magnetic field. The time-varying field induces a voltage at the pick-up coil and the induced signal is analyzed by a lock-in amplifier (*signal recovery 7265*). The sample was placed between a pick-up and an excitation coil. A silicon diode temperature sensor (DT-470, *Lake Shore Cryotronics, Inc.*) with a controller (*330 temperature controller, Lake Shore Cryotronics, Inc.*) was used to measure the sample temperature. The temperature was varied by allowing the samples to slowly heat up from

77 K in the neck of a liquid nitrogen dewar. The samples, coils and temperature sensor were mounted on a copper block to provide uniform temperature distribution (Figure 3-1b). Stycast was used as a bonding material (shown in black Figure 3-1b) to mount to a G10 plate. Matlab software was used for programming and data acquisition through IEEE-488 communication.

At temperatures below T_c, superconductive samples induce less electromotive force (EMF) to the pick-up coil as compared to the induced EMF of a non-superconductive sample. This variation determines the transition temperature. The variation in induced voltage (EMF) is relatively abrupt for most samples and is an indicator of superconductor quality. An example of a result from T_c measurement is shown in Figure 3-2. The T_c is defined as the mid-point between the temperature values that are 10% less and more than the maximum and minimum temperatures in the transition regime respectively. Typically, the sample width is 12 mm and the length of the sample is between 0.5 and 30 cm.

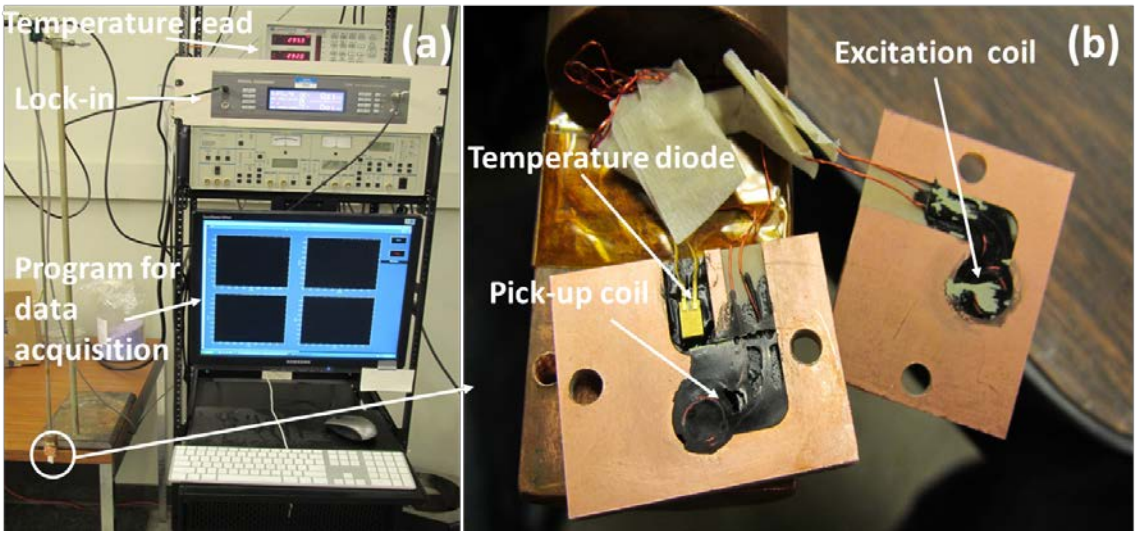

Figure 3-1. Critical temperature measurement set-up (a), details of the location of the coils and sensor (b).

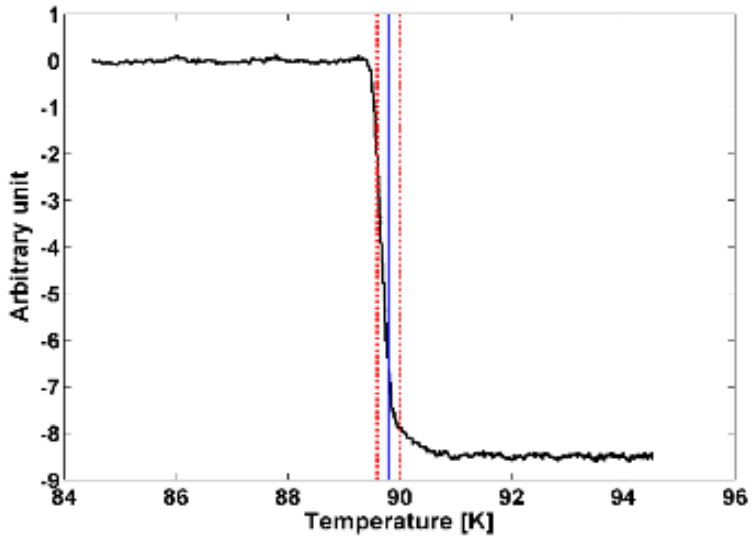

Figure 3-2. An example of a T_c plot. Dashed red lines show the maximum and minimum temperature values in the transition regime and the solid blue line shows the T_c.

3.2. Critical current measurements

A standard four-probe method at 77 K was employed for I_c measurements using a 1μV/cm voltage criterion (Figure 3-3). Current was supplied by a power supply (GEN-3300*W* 600*A*, *Lambda*) and the voltage on the sample was detected by a two-channel nanovoltmeter (*2182A*, *Keithley*). LabVIEW software was used for programming and data acquisition through IEEE-488 communication. A schematic configuration of the voltage and current taps for total I_c measurement is shown in Figure 3-4. Two thin silver strips were soldered to each individual filament along the width of the tap using eutectic In-Sn solder. This allows the simultaneously detection of voltage drops from all filaments. A different configuration was implemented to measure individual I_c of each filament (Figure 3-5). In this configuration, the total I_c of the tape including all the filaments was measured (Figure 3-5a), after which the current tap was systematically cut and re-soldered eliminating one filament at a time. The length of each filament differed by 0.5 cm on each side therefore a new current tap could be soldered to eliminate the longer filaments (Figure

3-5b). After re-soldering the new current taps, the I_c of the remaining filaments was measured while keeping the voltage taps intact. This process was continued until the I_c of the last (shortest) filament was measured.

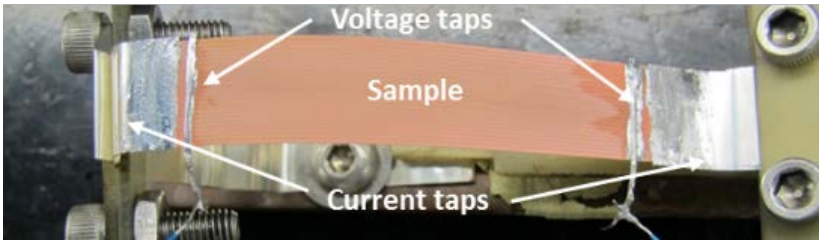

Figure 3-3. Actual sample mount showing voltage and current taps.

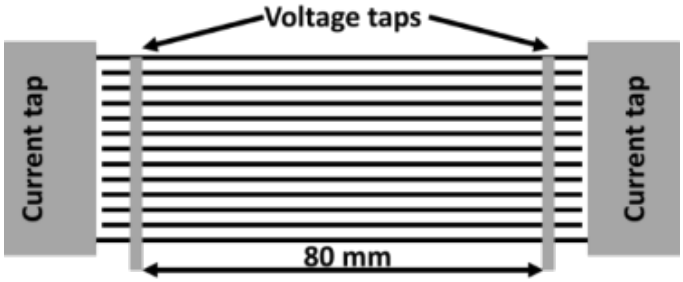

Figure 3-4. Configuration of voltage and current taps used for overall I_c measurements .

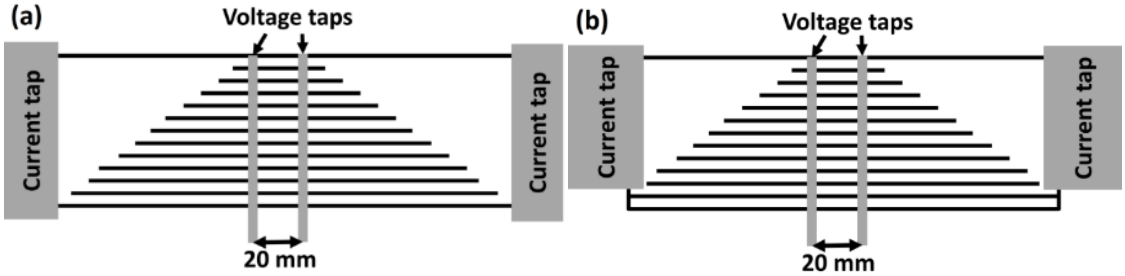

Figure 3-5. Locations of voltage and current taps used for filament I_c measurements. Measurement of total I_c for all filaments (a), the example (b) shows the configuration with one filament excluded from I_c measurement .

3.3. Structural characterization

The microstructures were analyzed using a LEO−1525 scanning electron microscope (SEM), a JEOL JSM 6330F Field Emission SEM with Energy dispersive X-ray spectroscopy (EDS) capability, and a JEOL 2000 FX transmission electron microscope (TEM). Cross-sections and Energy-dispersive X-ray spectroscopy (EDX) data were taken

by a FEI 235 Dual-Beam Focused Ion Beam (FIB) SEM equipped with EDAX EDS system. Additional microstructural analysis and filament profiles were investigated by a Keyence optical microscope.

3.4. AC losses and transport AC loss principles

The rationale for measuring the AC loss is to better understand the mechanisms of the loss and to investigate loss reduction in the wire as well as the devices. Another reason would be to investigate the thermal stability of cables, coils and devices. Most importantly, ac loss measurements help determine the required cooling power which is important to design proper cooling system. Measurement techniques are well established for measuring transport and magnetization AC loss in short samples of wire and for power applications. Use of a pick-up coil and Hall probe, similar to the pick-up coil technique, is the most suitable method for measuring magnetization AC loss. A four-point measurement technique using voltage taps is commonly used to measure the transport AC loss. AC losses are measured mainly by two methods – electrical [95-98] and thermal [96, 99-101]. The electrical measurements require a complicated experimental set-up and high precision equipment. Some of the advantages and drawbacks of these methods are provided in Table 3-1 [102].

Transport AC loss can be found experimentally by integrating the Poynting's vector on a closed surface, *S*, over the period *T*

$$P_{\text{tsf}} = -\frac{1}{L_p}\int_0^T dt \int_S \mathbf{E}\times\mathbf{H}ds, \tag{3-1}$$

where L_p is the sample length between the voltage leads inside a surface *S*. **E** and **H** are respectively the electrical field and magnetic field inside the surface.

Table 3-1. Comparison of electrical and calorimetric methods to measure AC losses.

Electrical method	Calorimetric method
Advantages	**Advantages**
➢ Transport and magnetization losses can be investigated separately. ➢ More sensitive and relatively fast. ➢ Covers wide range of frequency, field and transport current. ➢ Suitable for short samples.	➢ Applicable for any phase difference of transport and field at any frequency. ➢ Suitable for both long and short samples. ➢ Measurements can be done in an actual system such as coil, transformers.
Drawbacks	**Drawbacks**
➢ Transport and field must be in-phase. ➢ Good compensation and phase control are required.	➢ Less sensitive and time consuming. ➢ It does not allow investigate transport and magnetization losses separately. ➢ Temperature rise might affect the sample properties. ➢ Temperature measurement must be very sensitive to accurately measure AC losses.

Magnetic and electrical field can be related to current and voltage respectively, which converts the integration in the following form [103, 104]

$$P_{\text{tsf}} = \frac{1}{L_p}\int_T I(t)V(t)dt = \frac{IV_{in}(r)}{L_p f}, \tag{3-2}$$

where I, and V_{in} are the rms of the transport current and the rms value of the in-phase voltage component measured by the voltage leads respectively. This component can be measured by a lock-in amplifier with a reference signal that is in-phase with the transport current. Equation (3-2) is the final form that relates the in-phase voltage to AC loss per cycle and per length with current applied through the sample.

3.5. Magnetization AC loss principles

Early experimental studies on AC losses were started in the 1980s for LTS [105, 106] while investigations of AC losses for HTSs were started in 1990s [107-112]. Cost-effective, reliable measurement design was a significant issue for researchers. However, recently, development in fast acquisition and computing systems with compatible equipment have allowed the design of reliable measurement systems with better accuracy.

The signal of a pick-up coil depends on the rate of magnetization change $\partial M(t)/\partial t$ which depends on an externally applied AC magnetic field $B_a(t)$. The magnetization AC losses per length and cycle, P_m, [W/m/cycle], can be calculated by the formula [13, 113]

$$P_m = \int_T B_a(t)\dot{M}dt. \tag{3-3}$$

A conventional pick up coil method is utilized to measure magnetization AC losses. The time derivative of magnetization can be determined from the induced voltage in the pick-up coil as [98, 112]

$$\frac{\partial M(t)}{\partial t} = C\pi W_c \frac{V_{in}}{\mu_0 N L_{pick}}, \tag{3-4}$$

where W_c is the half-width of the coil, V_{in} is the pick-up voltage in-phase with the excitation current of the solenoid. L_{pick} is the length of the pick-up coil. μ_0 is the permeability of free space, N is the number of turns in the pick-up coil and C is a calibration factor that accounts for the conversion of the measured voltage to the magnetic moment. One way to measure the calibration constant is a technique where a wire loop is placed inside the pick-up coil and fed by an alternating current [114]. The voltage induced in the pick-up coil was measured with the lock-in amplifier. The calibration factor C was calculated using the following formula

$$C = \frac{\dot{m}_{rms}}{U_{rms}} = \frac{2\pi f I_{rms} A}{U_{rms}}, \tag{3-5}$$

where A is the area of the calibration loop inside the pick-up coil, U_{rms} is the rms voltage and I_{rms} is the rms current from power supply with frequency f.

A material with known magnetic properties can be also used for calculation of this constant. Usually a ferromagnetic material with well-known properties is chosen for this purpose. AC losses of the material can be calculated and compared to the measurements to find the constant.

The most common method is to use a metal with known resistivity to find the calibration constant. In this method, the resistivity of the metal can be calculated and compared to the AC loss value obtained from the measurements [115]. This is the method employed for the magnetization calibration of the AC loss system. Eddy current loss was calculated numerically using a 3D−FEM model with the COMSOL program. The sample (dimensions provided in Figure 3-6) was used for four-probe resistivity measurements and a segment of $11.85 \times 44 \times 2.05\ \mathrm{mm}^3$ was cut for the magnetization AC loss measurements. Eddy current loss of the sample was calculated using the resistivity values obtained from the measurement and dimensions of the sample.

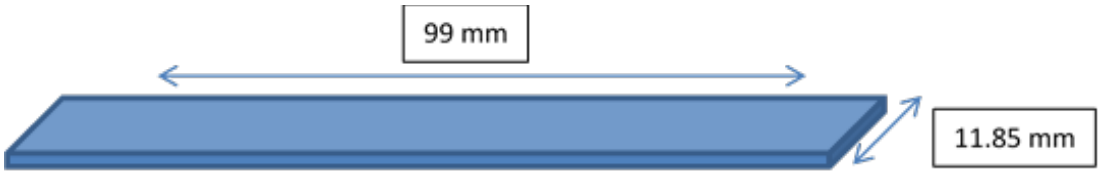

Figure 3-6. Sample dimensions used in the calibration of the system

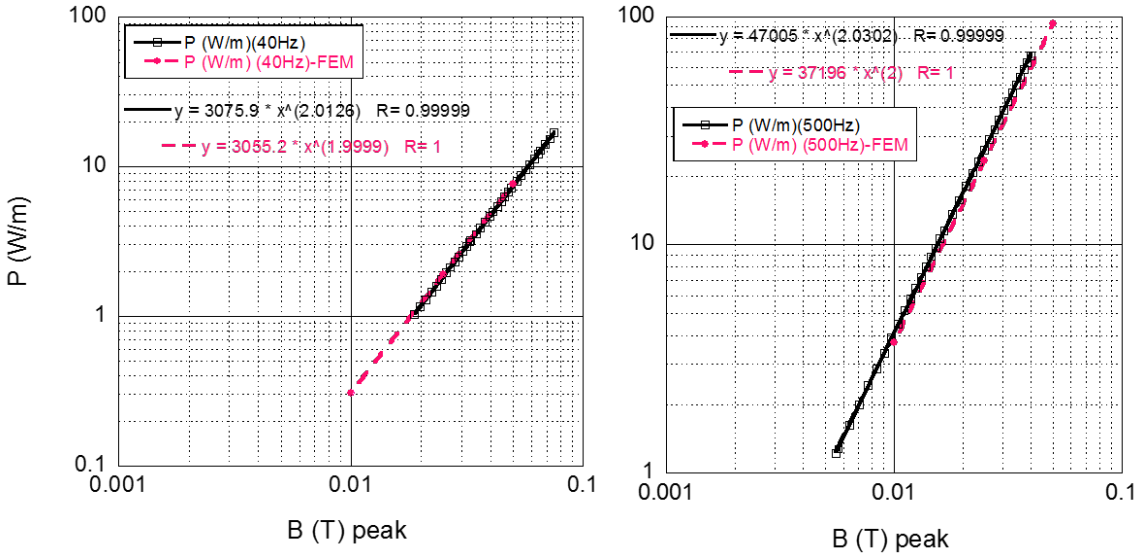

Figure 3-7. Calculated eddy current loss and comparisons with the measurements at 40 and 500 Hz respectively.

Comparisons of the FEM calculations and the measurements are shown for two different frequencies (Figure 3-7). Six different frequencies were investigated in this analysis and a ratio of the measured losses to the calculated losses at respective frequencies is given in Figure 3-8. These frequencies were selected because these are the frequencies most frequently used in this dissertation. A computer program was written to incorporate these ratios to improve AC loss measurement accuracy.

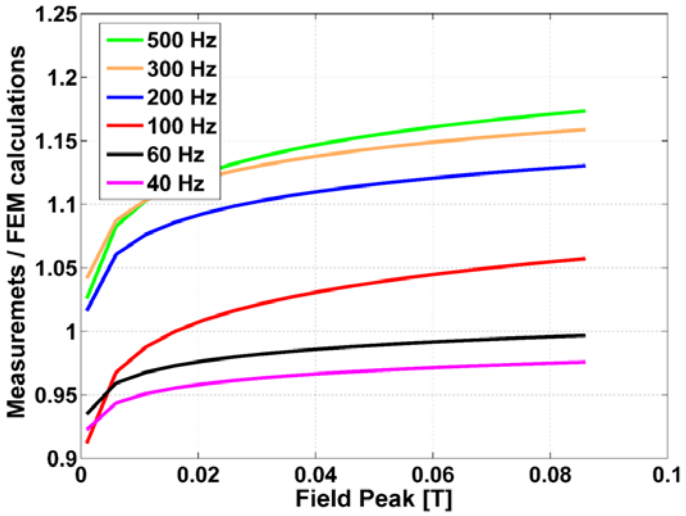

Figure 3-8. Ratio of measured eddy current losses to calculated ones at the six most commonly-used frequencies.

Finally, by substituting Equation (3-4) in (3-3) and time averaging, the formula for magnetization AC losses per length per cycle can be written as

$$P_m = C\pi W_c \frac{B_{rms} V_{in}}{\mu_o N L_{pick} f}, \tag{3-6}$$

where $B_{rms} = (I_{rms} - C_o)C_1$. C_0 and C_1 are experimentally determined constants. Again, several methods can be employed to determine these constants. Separate probe-coil and hall-probe methods are used for this purpose. A probe coil is inserted inside the solenoid to measure the field in the sample location and the field distribution inside the solenoid. A hall probe is used to confirm these results (Figure 3-9). The hall probe was configured in the sample holder where the sample would be during actual measurements. AC current from the power supply was applied to the excitation solenoid and the voltage on the hall probe was measured with the nano-voltmeter. Using the formula provided by the manufacturer and calibration curves, the magnetic field inside the solenoid was measured at the sample location. AC magnetic field distribution inside the excitation solenoid was also measured by the probe coil and was found to be fairly uniform; therefore the spatial-variation had a negligible effect on the measurement results. The field profile in the solenoid is shown in Figure 3-10. The maximum variation on the field at the edge and middle is about ~0.5 percent.

By inserting the field term inside the Equation (3-6), the final formula for the magnetization AC loss per length can rewritten as

$$P_m = C\pi W_c \frac{(I_{rms} - C_0)C_1 V_{in}}{\mu_o N L_{pick}}. \tag{3-7}$$

This formula is the final form that relates the in-phase voltage to magnetization AC loss per length.

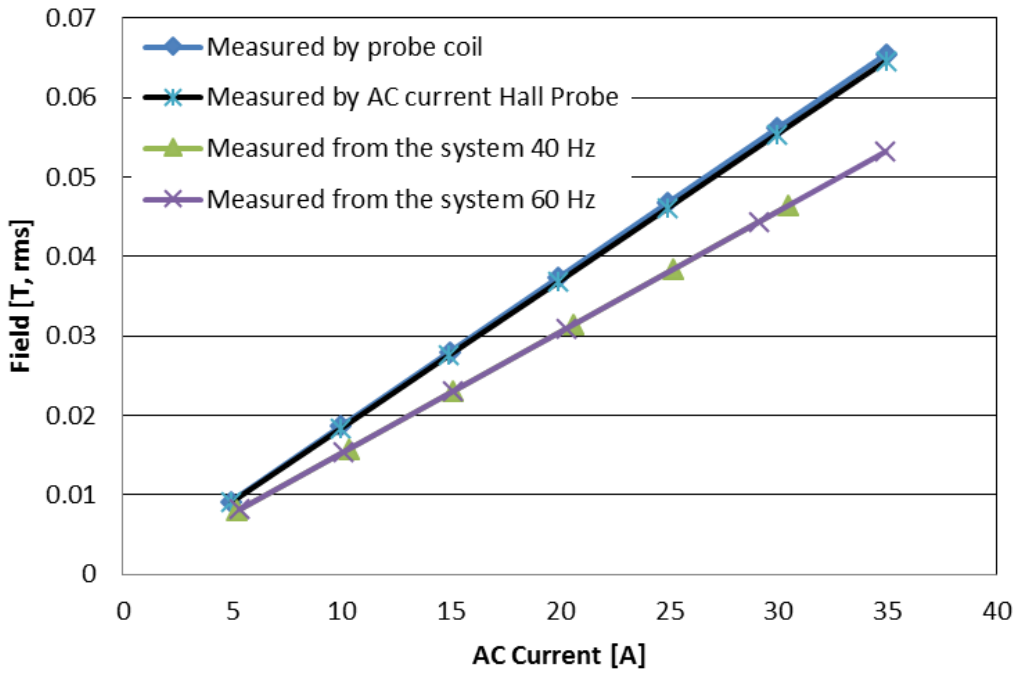

Figure 3-9. Current versus rms field measurement in the excitation solenoid by several methods.

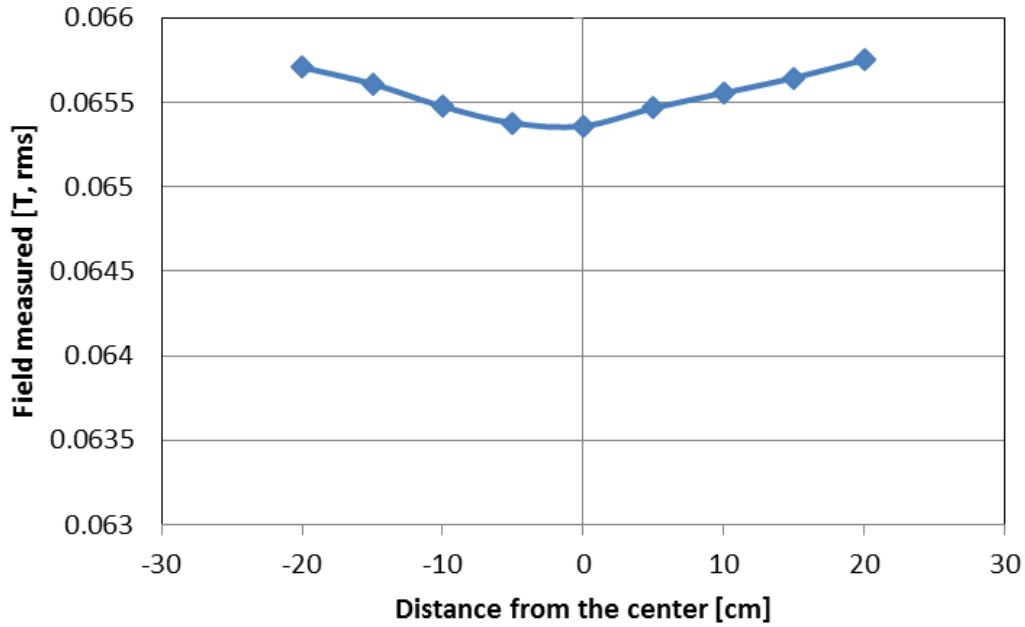

Figure 3-10. Field profile inside the solenoid excitation coil.

3.6. AC Loss measurements

Various methods for magnetization AC loss measurements were employed such as pick-up coils, Hall probes, and vibrating sample magnetometers (VSM). The VSM

technique is too slow for measurements at power frequencies. Pick-up and Hall probe measurement are very similar to each other and relatively fast. The calorimetric method is also widely used for measurement of total AC losses. The most common techniques will be discussed below including the pick-up method that was used for sample measurements in this dissertation.

3.6.1. VSM

In a vibrating sample magnetometer, the sample should vibrate sinusoidally in the presence of a stable, uniform magnetic field. VSM, invented by Simon Foner at MIT, measures the magnetic properties of a material [116]. A schematic describing the main components of a VSM is shown in Figure 3-11. It consists of detection and compensating coils with the sample located in the middle. These components are exposed to a uniform magnetic field generated by either a water-cooled resistive or a superconducting magnet. Depending upon the system, the cryostat can be cooled to temperatures as low as a few Kelvin. VSM can also be used for determination of T_c. A static magnetic field is applied to the samples, the sample itself vibrates, and the magnetic moment of the sample is observed by a detection coil and lock-in amplifier. The induced voltage in the pick-up coil is proportional to the sample's magnetic moment. The resolution is increased with an increased strength of the applied field, however the induced voltage does not depend on the strength of that field. The voltage signal from the pick-up coil is integrated with respect to time, a $M-H$ loop is generated and the magnetization losses are calculated. One of the major disadvantages of a VSM is that the maximum measurable sample length is typically very small due to the size of the pick-up coil and limited space. However this system offers wide range of measurements in terms of temperature, and applied field values.

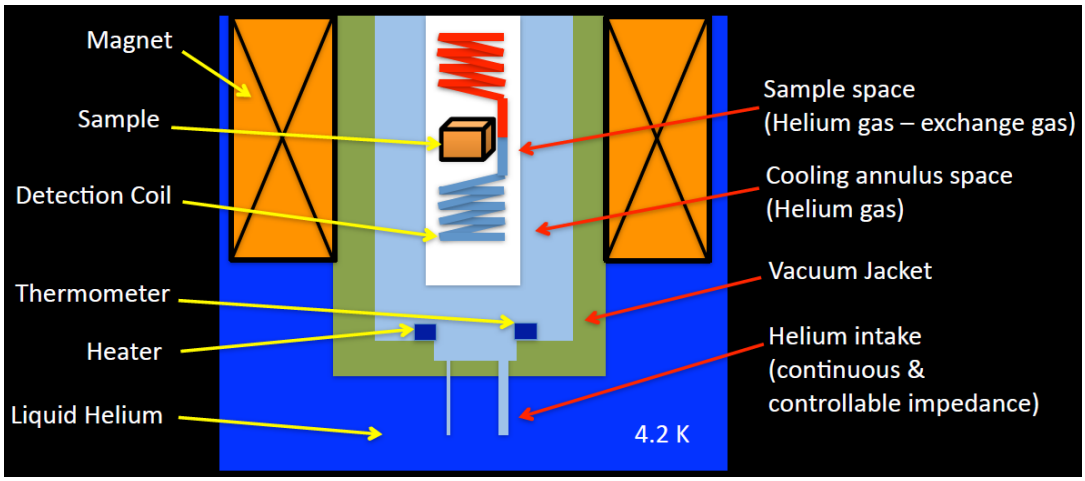

Figure 3-11. A schematic representation of the main components of a VSM [117].

3.6.2. Calorimetric AC loss measurements

Sometimes electrical methods for AC loss measurements are not adequate. The electrical method is very sensitive, but limited to the in-phase components of transport current and magnetic field. The influence of material shape or pick-up coil position on the measurement is the primary issue in electrical methods [99]. These conditions make the calorimetric measurements advantageous over electrical ones, especially in the case of transformers or motor generators where the magnetic field and transport current is not in-phase. This method measures the contribution of both transport and magnetization AC losses at the same time and at any phase difference.

The calorimetric method can be employed in two ways; by measuring the cryogen boil-off or the change in sample temperature [118]. The boil-off method is very useful at liquid helium temperature, however it is less useful at liquid nitrogen temperature due to the large latent heat. Thermal insulators and thermal sensing material are extremely important in this technique and need to be carefully selected and designed. The second method relies on the temperature difference in the sample, measured by thermocouples. If a DC current higher than the critical current is applied to a superconductor over a specific

time period, this will result in a sample temperature increase. This temperature increase can be accurately measured with the four-probe technique and a calibration curve can be obtained. Similarly if AC current applied to the sample over the same time period as the DC case, this will also result in a temperature increase. This increase is compared to the one obtained from the calibration curve and the total AC loss is obtained.

In calorimetric methods, the temperature increase should be kept low to prevent any degradation in the superconductor properties. Formation of the bubbles due to a significant temperature increase could potentially decrease I_c drastically and influence the measurement stability. Samples with high critical currents pose an additional problem; the heat source coming from the current leads. This can be eliminated by measuring the temperature rise primarily from the current leads. When a DC current below the critical current of any superconductor is applied, the temperature rise originates from the resistive contact and this background can be subtracted from the actual measurements to obtain better accuracy.

3.6.3. Pick-up coil method

All of the AC loss measurements in this dissertation were conducted by the pick-up coil method. The pick-up coil method is the most widely-used experimental technique to determine the magnetization AC losses due to its accuracy and efficiency.

3.6.3.1. Experimental set-up

Magnetization AC loss measurements were performed using an axial solenoid excitation coil coupled to an AC power source and a compensated pick-up coil at liquid nitrogen temperature (77K). A SolidWorks drawing of the assembled AC loss measurement rig is provided in Figure 3-12. The pickup coil was located

inside the excitation solenoid as shown in the detailed cross-section (Figure 3-13). Only the parts shown in the figure are exposed to liquid nitrogen. A thin 2G-HTS tape located inside the sample holder is shown in black. All the parts including the screws are machined from non-magnetic G10 materials. A picture of the whole system in a rack can be seen in Figure 3-14. AC loss measurements were performed on 44 mm long sections cut from the middle of the samples used for I_c measurements.

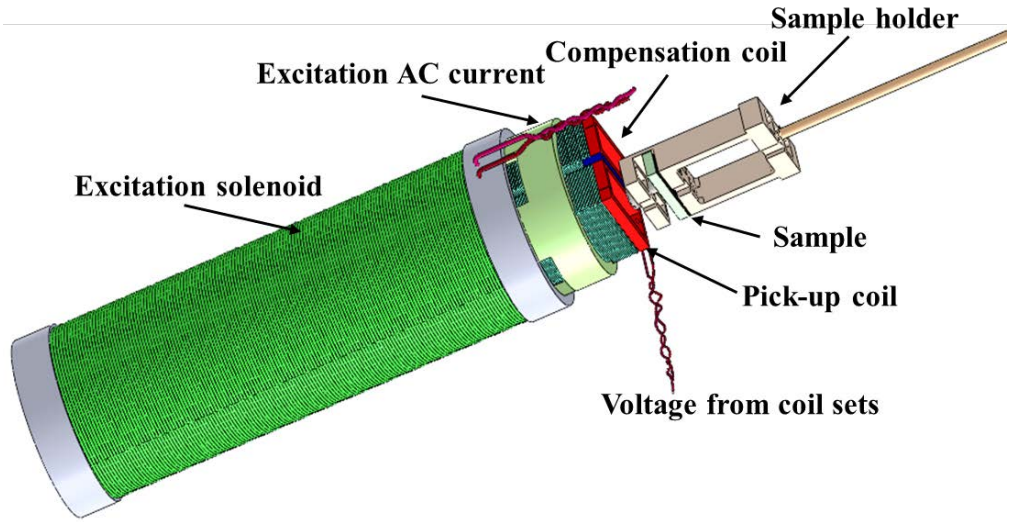

Figure 3-12. A SolidWorks drawing of the magnetization AC loss measurement rig.

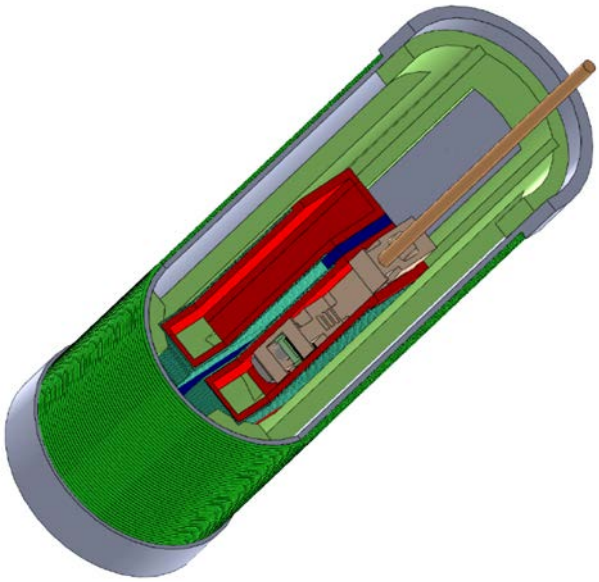

Figure 3-13. Cross-section of the measurement rig with all the components inserted in their actual positions.

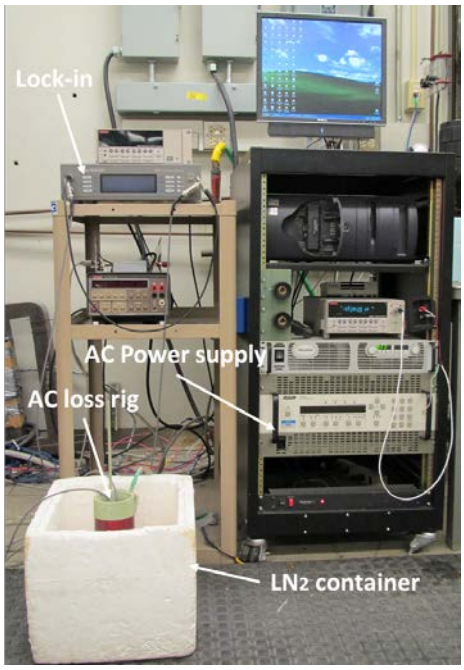

Figure 3-14. Magnetization AC loss system shown in a rack.

3.6.3.2. Electrical set-up

A sketch of the electrical set-up is shown in Figure 3-15. AC power supply provides AC current to the excitation solenoid. As shown in Figure 3-15, a set of pick-up and excitation coils compensate for each other when there is no sample present. However when the sample is present, the voltage associated with sample magnetization appears. The in-phase component of this voltage is extracted by the lock-in amplifier. Two different signals are used as a reference and the magnetization AC losses are obtained by using these two reference signals. In one measurement, a transistor-transistor logic (TTL) reference signal from the AC power supply is employed as a reference signal. This signal is widely used for industrial controls, test equipment and instrumentation applications. In the second measurement, a reference signal from the probe-coil is used to extract the in-phase component of the induced voltage in the pick-up coil. The TTL reference signal is more sensitive at relatively low field amplitudes while the signal from the probe-coil is not

adequate at these field amplitudes (Figure 3-16). All electrical connections are tightly twisted to prevent any voltage loop formation that could disrupt the accuracy and sensitivity introducing noise to the measurements.

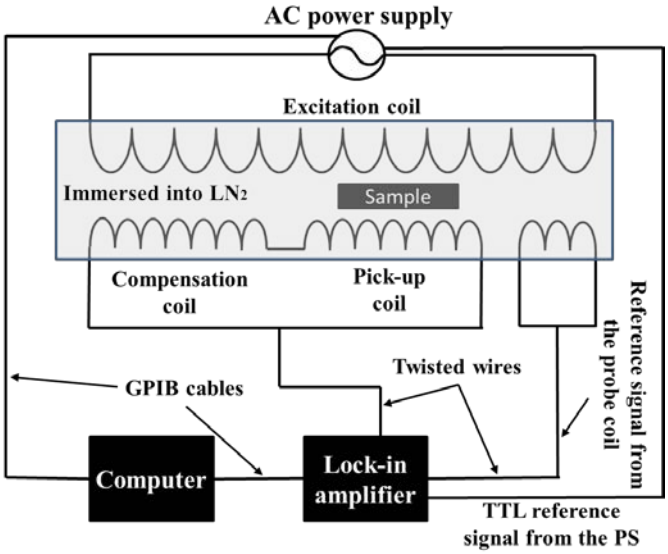

Figure 3-15. Electrical set-up for the magnetization AC loss measurement system.

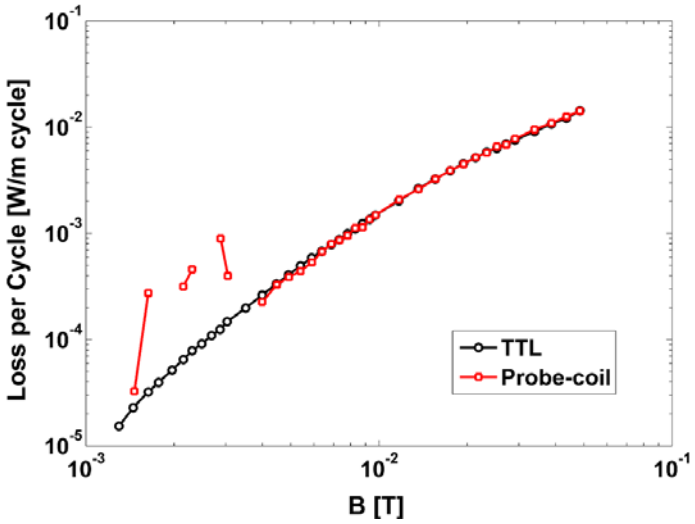

Figure 3-16. Comparisons of magnetization AC losses measured using TTL and probe coil signals. The discrepancy between two signals is obvious at low field.

3.6.3.3. Data acquisition

Measurement systems have to be equipped with reliable data acquisition. Data acquisition is a process that collects the physical signals from its instruments and

transforms the measurement system-controlled environment into useable information. The inter-instrument communications were made using a GPIB bus. GPIB is a byte serial, bit parallel bus that uses a three wire handshake and is capable of connecting 15 devices to one computer. The software used for the data acquisition is LabVIEW, a programming language from National Instruments. LabVIEW is very effective for laboratory usage, especially data acquisition, and many instruments have driver software for the LabVIEW program.

3.6.3.4. AC solenoid

For all the magnetization AC loss experiments presented in this dissertation, the magnetic field is provided by a copper wire solenoid with an inner radius and height of 76 and 220 mm respectively. A central 90 mm region along the length is used for the measurements. This is roughly equal to the length of the pick-up coil. The solenoid has 146 turns. The magnetic field throughout the central region is homogeneous within 0.5 % certainty. The solenoid is located inside a non-magnetic foam ice chest which produces no eddy current effect and the solenoid is cooled with liquid nitrogen. The magnet is capable of producing a central field peak amplitude close to 100 mT at frequency of 40 Hz. During the measurements, liquid nitrogen is provided continuously to account for LN_2 evaporation, keeping the environment stable.

3.6.3.5. Sample holder

Although the sample holder is considered to be the least important component in AC loss measurement system, it has a direct effect on the measurement results. The sample holder must gently secure the sample in a stable position and effectively provide heat transfer between the sample and the cryogen. The sample holder was innovatively designed

to allow liquid nitrogen circulation. LN_2 circulation is very important to prevent any possible sample temperature increase during measurement. A SolidWorks drawing of the sample holder is shown in Figure 3-17. Previously, the sample holder did not have a channel on it and was machined in the form of two parallel flat plates. Since this design did not allow proper Ln_2 circulation, the extensive loss generation increases the temperature by several Kelvin and leads to a drastic decrease in current densities and magnetization of the measured sample. This results in an abrupt decrease or fluctuation in AC loss performance which generates misleading information about the loss behavior of the sample. This strong effect is especially obvious in the high field region where the magnetization AC losses are prominent (Figure 3-18). AC loss resulting from a regular sample holder showed a saturation during the measurements whereas the improved holder measurements have no saturation in AC loss performance. This saturation also depends on frequency. The losses become larger at higher frequencies and the saturation starts at relatively lower field amplitudes. The influence of frequency on magnetization AC losses is shown in Figure 3-19.

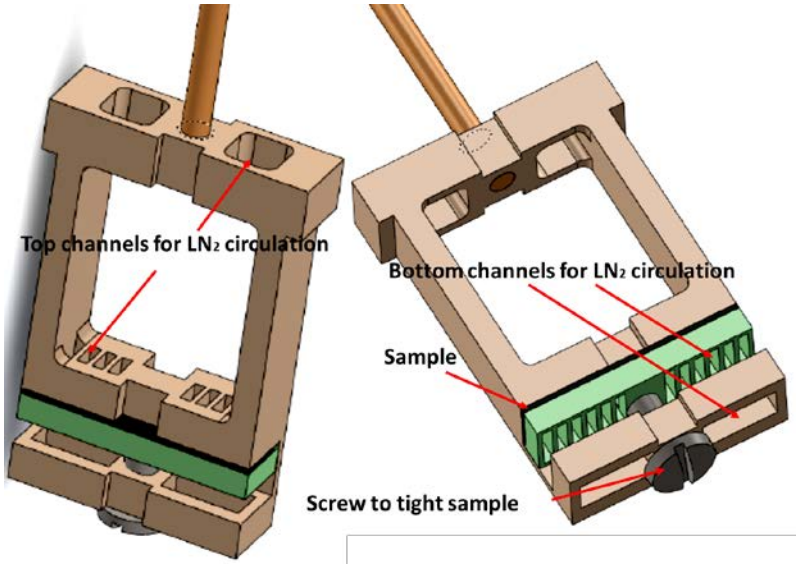

Figure 3-17. A SolidWorks drawing of the engineered sample holder.

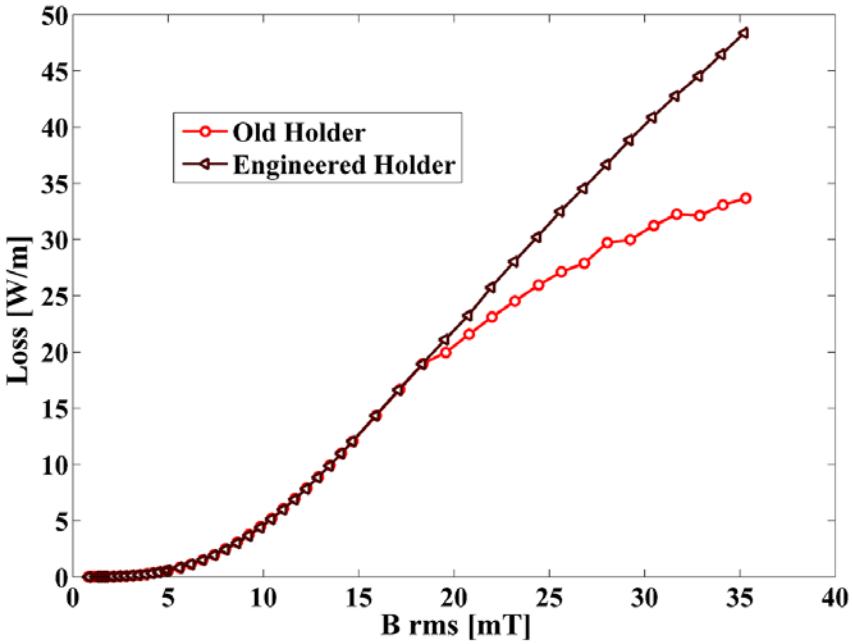

Figure 3-18. Heating effect on measured ac loss before and after the holder modification.

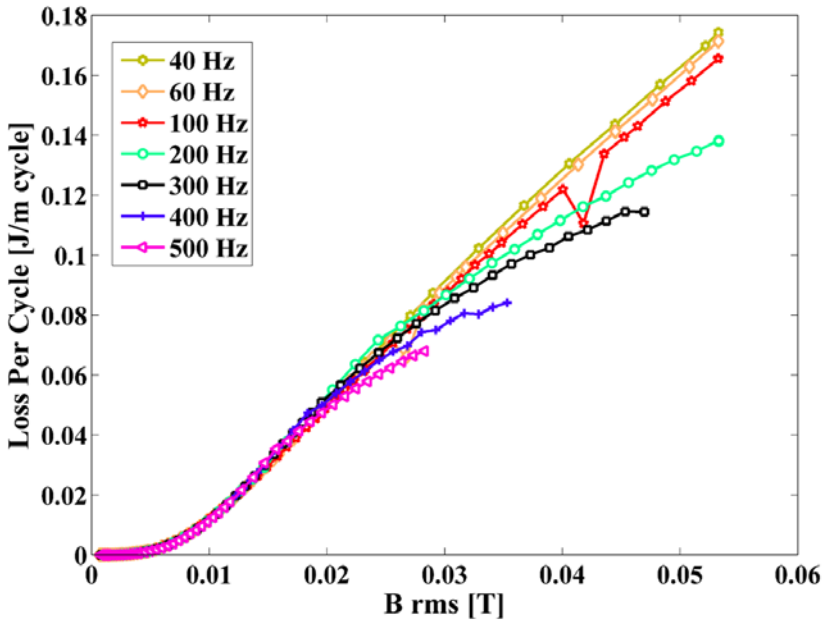

Figure 3-19. Frequency dependence of the heating effect on magnetization AC loss.

3.6.3.6. Pick-up coils

The pick-up coil not only senses the screening field from the superconductor; it also senses the applied field, which is orders of magnitude larger. A compensation coil is set in anti-series to the pickup coil and is also placed inside the excitation solenoid. Ideally, when

there is no sample the induced voltage should be zero and when there is a sample the induced voltage should be proportional to the rate of magnetic moment change in the sample. In this case, the only signal should arise from the sample. However, there are several effects that contribute to voltage generation in the pick-up coil, even if there is no sample (described in Section 3.6.4). Both the pick-up and compensation coils are extended above and below the actual sample space for uniformity. Dimensions of each pick-up and compensation coil are displayed in Figure 3-20. Each turn of the pick-up and compensation coil is machined in a groove form and wound in an 8-figure. This design is slightly different from that typically seen in the literature [96, 112, 119]. The winding wire precisely fits in the groove and does not cause any vibration during measurements. This allows us to avoid using any epoxy bonding material which causes wire breaks after several rounds of thermal cycling due to the thermal contraction and expansion. Additionally, a figure-8 shaped winding provides better compensation since signal compensation occurs in each turn. A thin copper wire is used for windings and the total number of turns is 110.

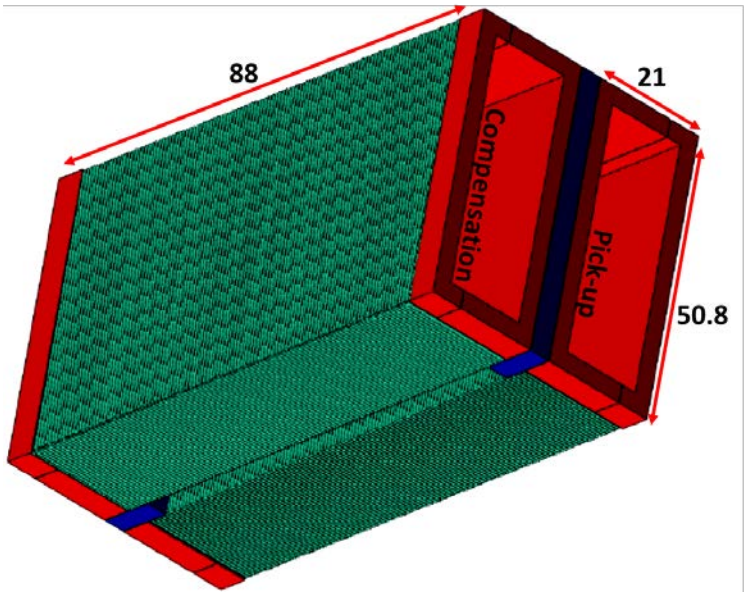

Figure 3-20. Pick-up and compensation coil set with their respective dimensions in mm.

3.6.3.7. Lock-in amplifier

In its most basic form, the lock-in amplifier is an instrument with dual capability. It can recover signals in the presence of overpowering background noise or it can provide high resolution measurements of relatively clean signals over several orders of magnitudes and frequency ranges. This dissertation utilizes the first capability. A signal recovery 7265 type lock-in amplifier is used for the measurements. Voltage from the pick-up and compensation coil set is measured from the signal channel. The signal channel offers operational modes of A only, -B only, and differential (A-B). The -B only operational mode was employed in the magnetization AC loss measurements. This channel has a sensitivity from 2 nV to 1 V. It can also be run in current mode with a sensitivity range of 2 fA to 10 nA. The signal from the reference or the TTL is measured from the reference channel. This channel offers a frequency range of 1 mHz to 250 kHz in TTL mode and 1 to 250 kHz using the analog input. The BNC shield can be grounded or floated via 1 kΩ to ground. For the experiments, the floating mode was used. The two signals obtained from the reference and signal channels are compared and the in-phase component is extracted in the lock-in using the single reference mode. Dual mode allows the simultaneously measurement of two signals at different reference frequencies up to 20 kHz. This lock-in amplifier has also a line frequency rejection filter. This allows us to measure the frequency value matching the line frequency with no noise contributions. A standard IEEE-488 digital interface is used for communication although it also has a RS232 serial interface.

3.6.3.8. AC-power supply

An Elgar TrueWave AC programmable power source is employed as an AC current source to excite the solenoid. This power supply is multifunctional and can run in both AC

and DC modes. The AC output voltage ranges from 0 to 156 VRMS while the DC output voltage ranges from 0 to 223V. The AC voltage is controlled during measurements. The voltage accuracy is very good with an error of ±0.1% and a resolution of 0.03% of full-scale. Frequencies as small as 0.1 Hz can be resolved within 0.25% using this power supply. The in-line current is checked by an AC current clamp meter to make sure readings are correct and it was observed that the digital display current shown was identical to the readings from the clamp meter.

3.6.4. Measurement error

In the AC loss measurements, the signal measured is very small and is extracted from a noisy environment. In principle, this is simple, but in practice, these measurements are extremely difficult to collect and are not error free. For this reason, these errors have to be considered carefully and eliminated where possible or included carefully into the actual measurements. Depending upon the error source, their contribution may vary. Some errors significantly affect the results and some are negligible. The errors seen in the magnetization AC loss measurements and their preventions are discussed below.

Resistive signal from the pick-up coil cannot be well-compensated in the coil configurations. Small variations in the pick-up and compensation coil symmetry will occur during the winding process. This is called the empty coil effect. Since this is an error in eddy current nature, the eddy current contribution from neighboring metals and the copper solenoid can also be included in the empty coil effect. Magnetic fields created by the eddy currents in surrounding metals can also induce in-phase or resistive signal to the measurements. The compensation coil signal has to be purely inductive in order to prevent any resistive signal contribution to the sample signal. The empty coil effect is insignificant

in the non-striated reference tape measurements because the measured resistive signal from the sample is significantly higher than the signal from the empty coil effect. However, it is crucial when the signal obtained from the coil sets is comparable to the sample signal. All measurements were performed twice, once with a sample and once without a sample in order to include this error. The measured loss without a sample is subtracted from the measured loss with a sample. The empty coil effect also becomes more pronounced with increasing frequency. An example of loss measurements without a sample at 7 different frequencies is shown in Figure 3-21. At a relatively low field regime, the AC loss gets too noisy. Empty coil measurements are performed for each frequency and sample to account for any possible variation.

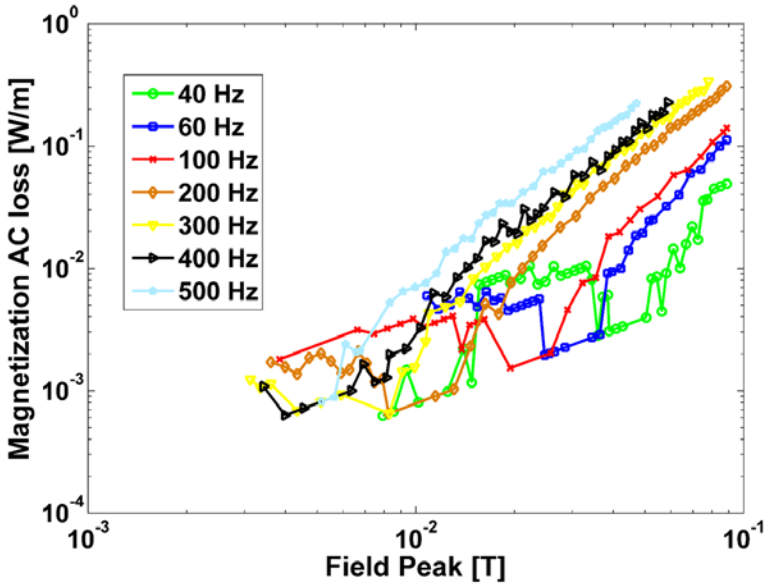

Figure 3-21. Magnetization AC loss without sample present to demonstrate the empty coil effect.

Chapter 4. AC Loss Reductions

4.1. Introduction

To obtain low-magnetization AC loss in niobium-based superconductors, researchers pursued finer filament fabrication and alternate matrix materials [120-123]. Low AC loss in 1G-HTS bismuth-based materials required modification of the effective transverse resistance. The effective resistance depends on matrix material, shape, and filament structure. The matrix material must not react with the superconductive filaments or oxidize during heat treatment. The material has to be oxygen permeable allowing oxygenation of the superconductive filaments [124-126]. The shape and structures of the filaments have also been altered to obtain better AC loss performance [127-129].

Magnetization AC losses of superconductors, particularly 2G-HTS CCs, are dependent on the dimensions and the cross-section of conductors (primarily an aspect ratio of ~10^4). Reduction of the high aspect ratio by increasing the thickness of the HTS layer is impractical from a manufacturing standpoint due to the well-known deterioration of critical current density (J_c) with thickness [130]. To reduce the high aspect ratio, two methods were proposed. One is to deposit REBCO in a circularly shaped template; however, this is not practical with current fabrication techniques. The other, more practical, method is to divide HTS tape into narrower filaments [79].

4.1.1. Early patterning techniques of YBCO

Patterning of YBCO superconductor is not a new procedure. Patterning of YBCO superconductors became interest for many applications including current-controlled switches [131], SQUIDS [132], micro-bolometers, and sub-micrometer weak-link bridges [133]. One of the first patterning methods was ion implantation [132, 134-136]. Weak-link

widths as small as 17 μm were fabricated following mask patterning and ion implantation. These methods rely on the destruction of a superconductive structure rather than removing it. After a critical level of ion exposure, the film underwent a crystalline to amorphous transition. By ion implantation the crystal structure was modified and the transformed phases were determined to be Y_2BaCuO_x or $BaCuO_2$. After re-annealing, the superconductive properties were restored [134]. Similarly, inhibition or reactive patterning techniques were used to create non-superconductive tracks for YBCO patterning. In these methods the superconductivity was destroyed by diffusion of Si atoms into the YBCO matrix inhibiting superconductivity upon Si-YBaCuO intermixing [137]. Sometimes, a resist was deposited on the desired protection areas and the rest of the YBCO was bombarded by Si ion [131, 138]. In another technique, silicon nitride template was selectively patterned by electron beam lithography onto $SrTiO_3$ (STO) [133] prior to YBCO deposition. The YBCO film grew epitaxially on STO, while the film deposited on the nitride forms insulating clusters.

A conventional lithographic processing and etching method was implemented to pattern YBCO superconductors in nitric or acetic acid solutions [139]. A phosphoric acid solution or its dilution form was used to pattern 2 μm wide segments of superconductor without photoresist usage. This method is very difficult to keep stable throughout the etching process [140, 141]. This chemical etching does not degrade the superconductivity; however, such a small patterning solution can erode the grain boundaries. Phosphoric acid vapor was used as an alternative. Laser ablation with an appropriate mask or direct removal of unwanted materials was employed successfully to create structures as narrow as a 30 μm strip and a 1 μm bridge [142-145]. Similarly, a Ga focused ion beam was implemented

to create 0.5 μm superconductive strands. However, even low levels of Ga implantation was enough to poison YBCO [146]. Lift-off techniques with photolithography were also evaluated and produced good superconducting properties down to 5 μm line widths and 50 μm lengths [147, 148].

4.1.2. Patterning of YBCO for AC loss reduction

Although these early patterning techniques were successful in YBCO coated conductor applications, implementing these techniques for long-scale filamentization purposes was almost impossible due to their complexity and high costs. Either the techniques needed to be modified or a new method needed to be developed for CC filamentization. Two categories of filamentization methods were investigated for 2G-HTS. One is top-down and the other is bottom-up. The top-down method used striation starting from the top layer of 2G tape through to the bottom layers. In the bottom-up method, the striation starts from bottom layer of 2G tape and continues to all the way to the top layers. Laser ablation was used, a well-known top-down method, to demonstrate filamentization of CCs [149, 150]. A bottom-up approach has recently been developed using direct laser-writing of a TFA-based precursor onto a buffered substrate [151]. Mechanical striations as a bottom-up [88] and top-down [152] approach were pursued. Top-down approaches such as photolithography followed by dry [76, 153], and wet [154] etching have been evaluated. Inkjet printing of YBCO filaments [155, 156] and high resistive oxide filaments [82] on a buffer layer has been demonstrated as a viable methods for AC loss reduction. The common goal of these methods is to create a high resistive material between the superconductive filaments.

Most of the early applications of filamentization were proof of concept and performed on samples with a thin silver protective layer [84, 87, 157-160]. Later, the viability of AC loss reduction by striation of a long filamentized tape coil with only a thin silver protective layer was investigated and the related AC loss results were presented [161]. Direct laser ablation or etching were applied for samples with a thicker Ag stabilizer layer [83, 153]. A thick Cu stabilizer layer was also directly laser ablated in a top-down approach; however, the beneficial effect of striation is lost at filament widths smaller than one millimeter [162].

While all of these techniques achieve AC loss reduction, they differ in the level of complexity. This has a direct impact on throughput, cost, and other aspects including the degree of critical current degradation, the amount of coupling losses, and the mechanical integrity of the tape. For example, techniques such as wet or dry etching using a photoresist mask are relatively difficult to control and can cause undercuts in the YBCO layer degrading the I_c as well as the mechanical properties [153]. Conversely, filamentization can lead to high coupling losses if the resistivity of the substrate or any material between the filaments is low [163]. For all applications requiring a copper stabilizer, low resistivity copper deposited on the filaments can lead to high levels of coupling losses, degrading or even eliminating the beneficial effect of 2G-HTS filamentization [78]. This necessitates filamentization of the thick stabilizer layer as well, an issue that was unanswered. In addition, filamentization of the shunt/stabilizer layer can greatly reduce the eddy current loss contribution to the total AC loss.

In this chapter, striation techniques that address the HTS striation issue are presented. Stabilizer filamentization, groove resistivity, and cost/scalability of the

approaches were investigated. One bottom-up and two top-down filamentization methods were developed for scribing REBCO conductors. Top-down techniques developed could be called semi top-down since the filamentization procedure is followed by groove resistivity control through the formation of an oxide layer on the striations and a bottom-up electroplating step. The resulting tape is fully-filamentized with respect to both the HTS and stabilizer layers and includes highly resistive grooves separating the filaments. The details of each striation technique (laser and mechanical), differences of between these techniques, electroplating, and annealing/oxygenation procedures are explained in the following sections.

4.2. Mechanical scribing

Mechanical scribing is one of the simplest techniques for the filamentization of 2G-HTS. Although many bottom-up approaches were investigated for 2G tape filamentization, only a few studies were conducted with a mechanical striation technique. Only one reference cited a similar technique which was implemented with a scalpel [152]. In the method developed here, the striation was performed using a custom-made system consisting of a diamond-tip scriber manipulated by Z motion of the translational stage to maintain the load exerted by the scriber on the tape. In the initial proof of concept, the striations were made by hand using a ruler. However an X-Y translational stage was later used to provide accurate tape motion. After the load was adjusted to completely remove just the buffer stack for the bottom-up approach, and the Ag, HTS, and buffer stack for top-down approach, the X-Y stage was moved to the desired location for filamentization. A schematic representation of the striation and filaments after material removal is provided in Figure 4-1.

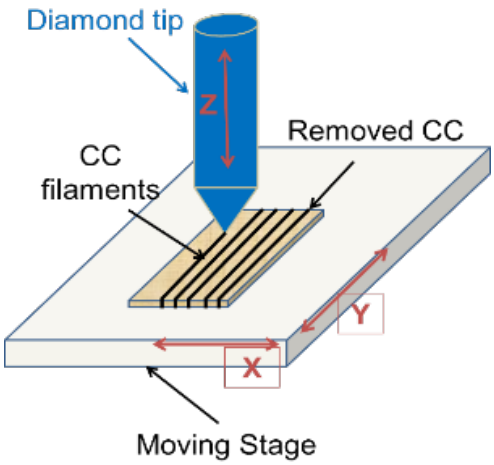

Figure 4-1. Schematic representation of the mechanical scribing process.

A Matlab computer program controls the X-Y-Z translational stage motion with micrometer precision. This method eliminates some of the problems associated with filamentization. This technique is cost effective and has high throughput because no additional processing after the scribing is needed. There are no undercuts to degrade mechanical integrity. This system does not require complex operational procedures or chemical processing. It simplifies the associated processes at all levels, including the AC loss striation, fulfilling one of the important criteria for manufacturing.

4.2.1. Buffer scribing

Buffer scribing is one of the methods discussed in this dissertation as a bottom-up approach for striation of 2G-HTS films and is aimed at developing a simple and cost-effective filamentization technique for AC loss reduction with performance similar to established techniques. In a bottom-up approach, striation is applied before the deposition of REBCO and a shunt layer, unlike other methods such as the photolithography/etching top-down approach. A standard 12 mm wide SuperPower buffer tape, consisting of a buffer stack deposited on a Hastelloy substrate, is striated by mechanically removing the buffer stack in narrow lines with a diamond tip. This process is followed by REBCO-MOCVD

deposition. The MOCVD deposition in the damaged region forms a non-superconducting, ill-textured structure with poor electric and magnetic properties that is suitable to decouple the filaments.

A 35 µm diameter diamond tip is used to remove parallel lines of material along the length of the tape. In total, ten filaments were made consisting of eight 1 mm and two 2 mm wide buffer filaments (Figure 4-2). The REBCO layer was deposited using an MOCVD system at the University of Houston.

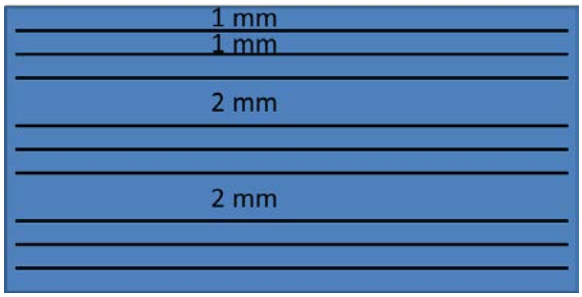

Figure 4-2. Filamentization configuration for buffer striation producing eight 1 mm and two 2 mm filament.

An SEM micrograph of a striation track with the buffer stack removed is shown in Figure 4-3. The image in Figure 4-3a is a low-magnification image revealing a groove width of approximately 25 µm and depth of 1.8 µm. The rectangular feature is a FIB cross section to reveal further detail. Figure 4-3b is a higher magnification image of the transition from the buffer layer to the striation track. The light region is the buffer stack in the cross-section. The transition from striation to buffer occurs within about 2 µm and consists of a lifted buffer stack section. Optical microscopy confirms the track width is not constant across the length because the station was performed manually. However, the track width reveals that this approach could produce fairly narrow tracks. This striation technique does not create any undercuts or incomplete etching compared to the typical photolithography/etching (Figure 4-4).

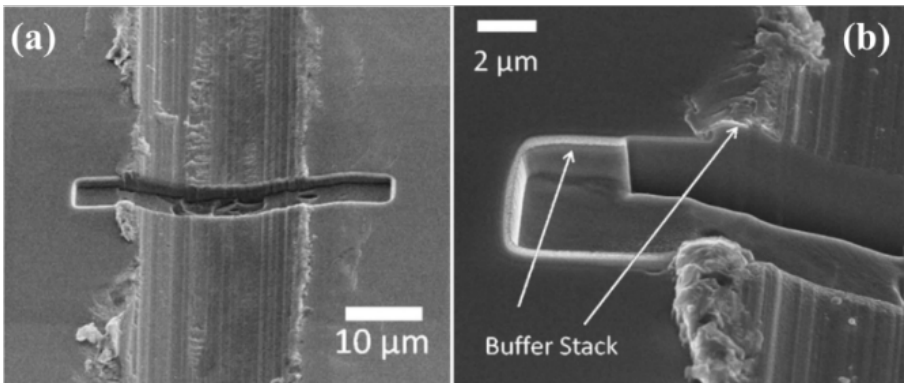

Figure 4-3. (a) SEM Micrograph of a striation track with the buffer stack removed, shown at 52º inclination. (b) Low magnification FIB cross-section reveals a track width of 25 µm and depth of 1.8 µm.

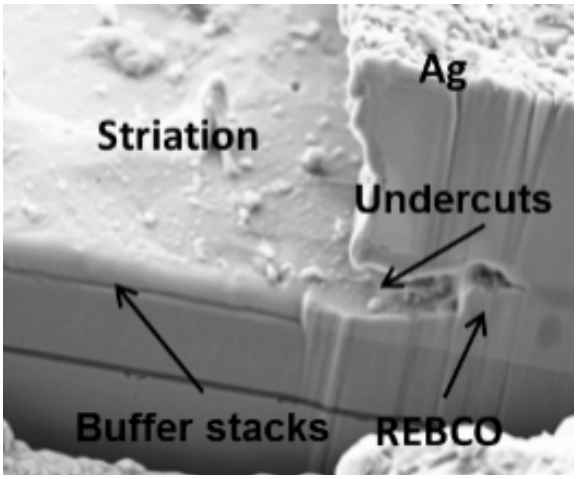

Figure 4-4. Striated sample with photolithography/etching revealing undercuts and incomplete etching. The buffer layer is clearly visible [153].

A REBCO layer was deposited by MOCVD following the striation. Optical and SEM images of the as-deposited REBCO layer are shown in Figure 4-5. Figure 4-5a is a SEM micrograph of a single groove. A typical REBCO texture is present to either side of the striation, while the striation itself has a polycrystalline-like, rough surface texture. Furthermore, the width of the ill-textured deposition does not disperse appreciably after MOCVD deposition. Figure 4-5b is a photograph where the striation grooves are clearly visible with a contrast different from the superconducting filaments.

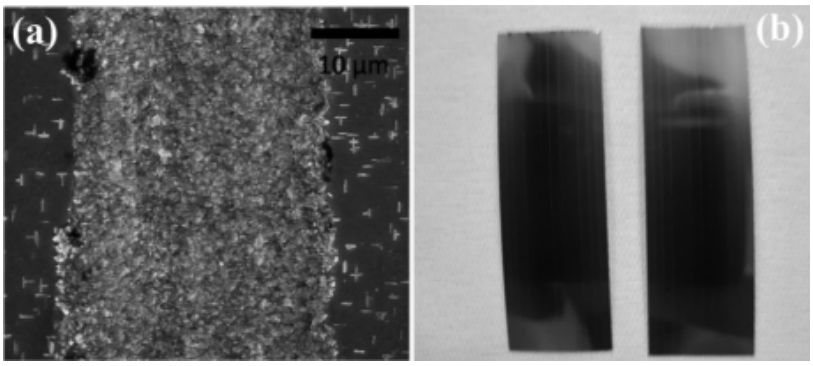

Figure 4-5. Optical and SEM images of samples after REBCO deposition by MOCVD. (a) An SEM micrograph of a striation track and (b) a photograph revealing clearly visible striation tracks.

A TEM cross-section was cut from the transition region of a groove for further investigation. The low magnification TEM micrograph of the transition region is shown in Figure 4-6. The top layer is a protective platinum strip deposited during the FIB-TEM sample preparation. The REBCO layer thickness is approximately 650 nm. In the figure, the buffer stack and its termination near the transition section are visible. The micrograph also reveals that the ill-textured section extends from the buffer end into the textured REBCO region for approximately 1.8 µm, which is only a fraction of the total striation groove width.

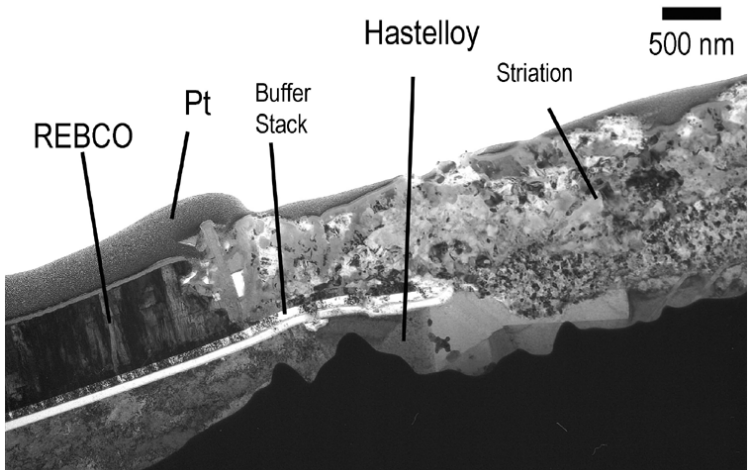

Figure 4-6. A TEM micrograph of the transition area between the buffered and striated parts of the sample after REBCO deposition.

A higher magnification TEM analysis was performed on the textured REBCO layer 1.8 µm adjacent to the buffer section with the ill-textured deposit. A TEM micrograph and a corresponding selected area diffraction pattern (SAED) at the imaging conditions are shown in Figure 4-7. The figure shows a typical REBCO texture.

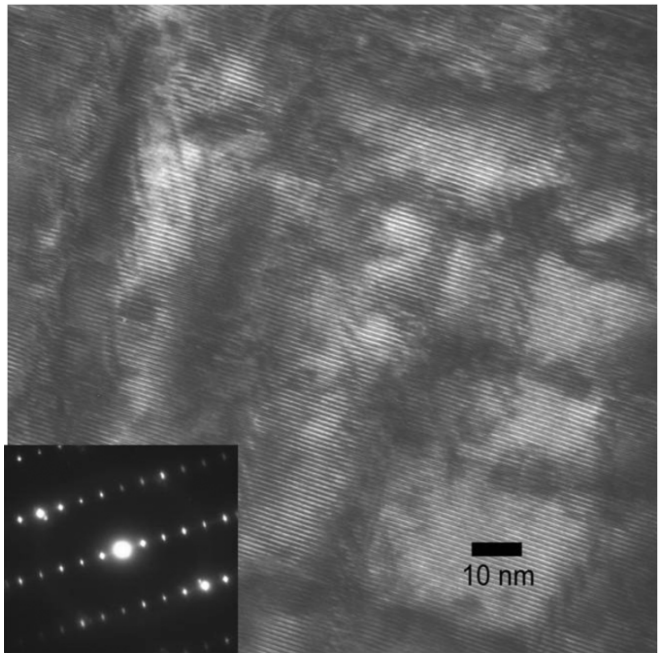

Figure 4-7. TEM micrograph of the REBCO layer adjacent to the ill−textured area of the striation. The micrograph and SAED reveal texturing typical of REBCO films.

The importance of the stabilizer layer and electroplating of copper stabilizer are explained in detail in section 4.5. However, silver stabilizer electroplating should be mentioned briefly. Following the MOCVD deposition, an alternative, low-cost technique for silver shunt layer deposition was introduced. Instead of sputtering, silver electrodeposition was used [164]. Silver sputtering is a relatively costly process and does not provide a means for the selective deposition on the superconducting stripes that is necessary to electrically-decouple the filaments for AC loss reduction. With electrodeposition, high throughput and preferential deposition on either layer can be obtained depending on the room temperature resistance ratio between the superconductor

and groove. The samples were electroplated with silver after the MOCVD process. One sample was electroplated directly after the MOCVD deposition. Another sample was electroplated after the MOCVD coated sample was oxygenated at 500°C. Optical images of the electroplated samples, before and after oxygen annealing are shown in Figure 4-8. Before oxygen annealing, the silver electroplated only on the striation grooves, whereas following oxygen annealing, both the superconducting and striation grooves are electroplated with silver. This indicates a lower electric resistance of the striation groove compared to the superconducting layer at room temperature before annealing.

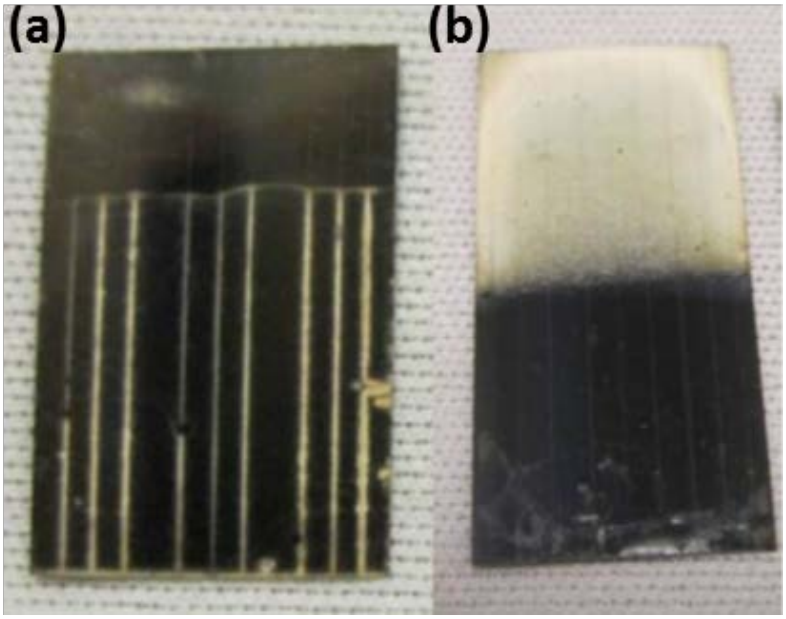

Figure 4-8. Optical camera images of samples after electrodeposition. (a) Sample electroplated after MOCVD deposition but prior to oxygen annealing treatment. (b) Sample electroplated following oxygen annealing.

Although this method meets the requirement for non-superconductive groove formation by forming ill-textured REBCO, the electroplating process coupled the filaments by deposition on both the ill-textured REBCO and superconducting filaments. This is not a fully-decoupled structure and is highly undesirable in a filamentization process. For this approach to work, several technical issues need to be addressed. First, coupling of the

filaments through the divider tracks or striations may result in inefficient loss reduction. Second, as the buffer stack including the alumina diffusion barrier is removed, the diffusion of Hastelloy constituents into the REBCO layer or vice versa may degrade the superconductor performance. For these reasons, an alternative semi top-down mechanical striation technique was developed to solve these problems. This technique is explained in detail in the following section.

4.2.2. Scribing through Ag protective layer

The starting coated conductor (SuperPower Inc.) consists of alumina, yttria, MgO and $LaMnO_3$ (LMO) buffer layers deposited on 12 mm wide, non-magnetic, electro-polished Hastelloy substrate followed by deposition of REBCO by MOCVD. The superconducting film was capped by a 1-2 µm annealed sputtered Ag stabilizer for protection. All samples used in this section were cut from the same tape reel. Six samples, labeled S1 through S6 were investigated for mechanical striation through an Ag protective layer. Details of the samples used in this section are provided in Table 4-1. Samples S1, S2, S5 and S6 were striated identically using the mechanical striation automated station. In each sample, eleven straight grooves were created, resulting in 12 1-mm wide superconducting filaments. Samples S3 and S4 were control samples with no striations, S3 was an untreated sample, and S4 was electroplated with 11 µm of copper. To examine the effect of oxidation alone on AC loss, samples S5 and S6 were prepared identically (filamentization with no electroplating), except for an oxidation step applied to sample S6. To evaluate the effect of copper plating, S1 and S2 were prepared with filamentization and oxidation, but only sample S2 was electroplated. A schematic representation of the top-down mechanical striation is shown in Figure 4-9.

Table 4-1. Measured I_c and T_c values and treatment information on the samples studied.

Sample ID	Critical Current [A]	Critical Temperature [K]	Electroplating	Filamentization	Oxygen Annealing
S1	196	91.3	No	Yes	Yes
S2	194	91.9	11 µm Cu	Yes	Yes
S3	210	92.0	No	No	No
S4	220	91.1	11 µm Cu	No	No
S5	200	90.9	No	Yes	No
S6	193	91.4	No	Yes	Yes

Figure 4-9. Schematic representation of the tape architecture achieved using Ag mechanical striation.

Shown in Figure 4-10 are optical and SEM images of the striations on sample S5. An optical image of the 1 mm wide filaments and the surrounding grooves is shown in Figure 4-10a. The cross-cut in Figure 4-10b was performed using FIB to reveal the cross-section of the groove and the surrounding filaments. The width and depth of the striations was varied from 35 to 55 µm and 7 to 12 µm, respectively depending on the load applied to the diamond tip. The groove shown in Figure 4-10b has width and depth of about 45 and 10 µm respectively. The length of each sample is about 130 mm. The details of the groove cross-section reveal the layered structure of the filaments with the substrate, buffer, REBCO and silver layers identified (Figure 4-10c). The thickness of the REBCO layer was measured to be 0.85 µm. Figure 4-10b and c shows that the silver was pushed to the edge during scribing. Furthermore, the figures reveal that the silver and Hastelloy are not smeared to the buffer edge or onto the surface of the groove, a feature reported in samples striated by laser ablation [83, 85, 161].

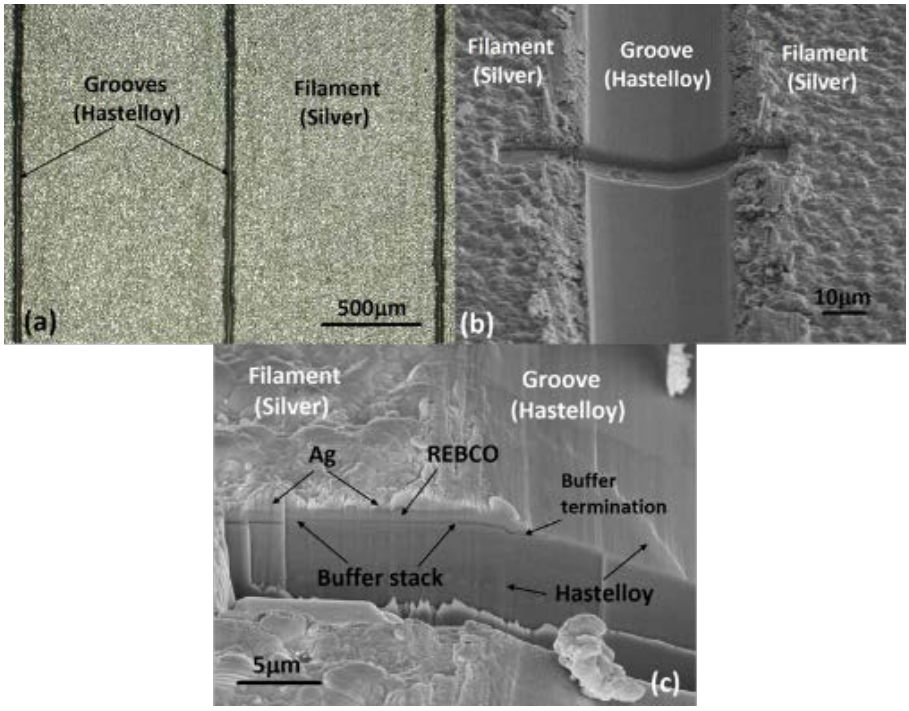

Figure 4-10. Optical microscope and SEM micographs after striation of the coated conductor revealing (a) a 1 mm filament width, (b) a 45 µm groove width and (c) the layered structure cross-section.

An important distinction in the technique is that instead of etching or ablating a thick stabilizer, copper was electroplated selectively onto the filaments using a copper nitrate ($Cu(NO_3)_2$) solution. A detailed explanation on the underlying mechanism for selective electroplating and electroplating process is provided in section 4.5. Optical microscopy, FIB-SEM, and camera images of the filamentized conductor are presented in Figure 4-11 and Figure 4-12. Optical images of samples before and after copper electroplating (S1 and S2, respectively) are shown in Figure 4-11a and b. The grooves are clearly visible both before and after electroplating. A FIB cross-section, shown in Figure 4-11c, reveals only minor discontinuous, island-like formations of small Cu particles on the grooves. After electroplating, the groove width decreased from 48 µm to 25 µm due to copper deposition on the sides in a direction perpendicular to the filaments. The copper thickness in this sample was 11 µm and highly uniform along the filament width and length.

The control sample (S4) was copper plated under the same conditions as sample S2 and exhibited the same thickness and uniformity. A complete cross-sectional profile of sample S2 is presented in Figure 4-12. The top layer is electroplated copper, the intermediate black layer represents the REBCO/buffer films, and the bottom layer is the 50 µm Hastelloy substrate. The groove between the filaments extends all the way into the substrate after the removal of the REBCO and silver stabilizer layers. The depth of the groove is about 20 µm measured from the top copper surface.

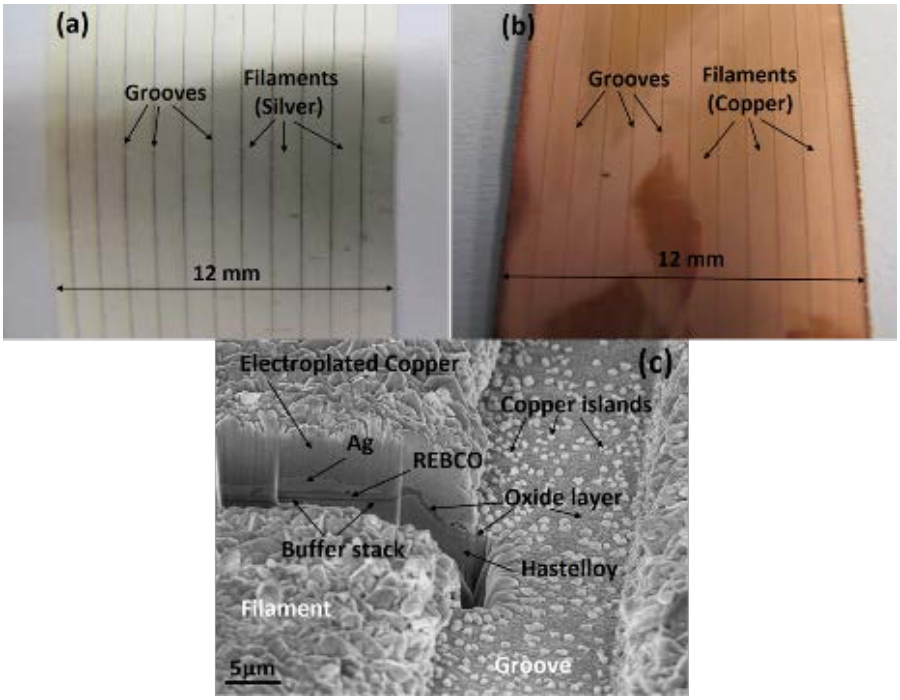

Figure 4-11. Photographs of samples (a) S1 and (b) S2, showing the general appearance of samples after (a) striation/oxidation, and (b) copper electroplating. (c) SEM micrograph of the FIB cross section of the sample S2 filament-groove edge.

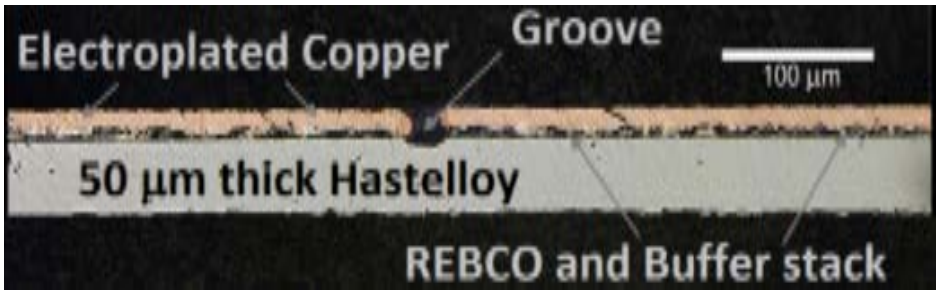

Figure 4-12. Optical micrograph of a fully-filamentized coated conductor cross-section revealing the substrate, copper stabilizer, buffer and REBCO layers.

As the thickness of electroplated copper is increased, it is expected that the lateral growth will eventually cause the deposits to merge and bridge the grooves, which would correspond to the upper limit for copper thickness with this method. Such bridging conditions should be avoided because they drastically increases coupling loss. To determine the limits for stabilizer thickness and AC loss performance, another set of samples were constructed. All samples were cut from the same parent tape and 11 total parallel striations were made with 1 mm spacing using conditions identical to the previous samples. All samples, except the reference sample, consisted of 12 filaments. A reference sample (M7) was not striated, but electroplated with 30 µm copper. Table 4-2 details the sample properties. In these samples, consecutive rounds of electroplating with copper nitrate ($Cu(NO_3)_2$) and groove cleaning with sulphuric acid (H_2SO_4) solutions were performed to obtain different thicknesses of copper stabilizer layer. A cleaning step was employed to remove the copper islands formed during the electroplating process. One sample, M5, was sputtered with a thick silver layer without copper for comparison with the electroplated sample, M6. Camera images of the samples are displayed in Figure 4-13. With increasing thickness, the tracks get blurry and it is not easy to see striations due to the decreased groove width.

Table 4-2. Experimental details and treatment conditions of the stabilizer thickness samples.

Sample ID	Critical Current (A/12 mm)	Oxygenation	Electroplating Condition
M1	200	yes	10 µm Cu
M2	195	yes	20 µm Cu
M3	205	yes	30 µm Cu
M4	208	yes	44 µm Cu
M5	210	no	30 µm sputtered Ag
M6	220	no	36 µm Cu
M7	228	no	33 µm Cu

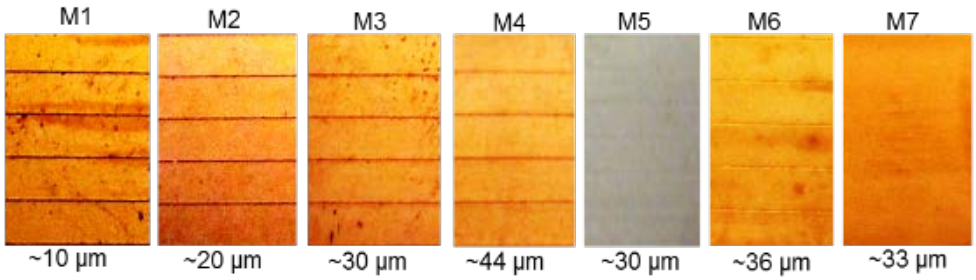

Figure 4-13. Photographs of the stabilizer thickness samples. Values (µm) represent the thickness of Cu or Ag deposited.

FIB/SEM images for sample M1, M3, M4 and M6 are shown in Figure 4-14. The grooves and filaments are clearly visible in Figure 4-14a and b. No electroplated Cu is seen on the grooves in samples M1, M2 and M3. For this reason, these samples are referred to as completely-decoupled to be consistent with the discussions in Chapter 2. The groove width decreases with increasing Cu thickness. It is about 40 µm in M1 and decreases to 15 µm in M3. This could be due to non-uniform distribution of current density during the electroplating procedure. At the edge of the filaments, the current density is relatively higher than in the middle leading to lateral growth of Cu across the groove. This growth limits the thickness of the electroplated Cu because it results in the undesired formation of highly conductive copper bridges. Figure 4-14c reveals that the lateral growth after electroplating ~44 µm Cu onto sample M4 resulting in copper merging and filaments bridging. This configuration is referred as partially-coupled. This thickness level can be considered an upper limit for copper thickness electroplated on samples with a groove width of about 50 µm. Considering the width reduction from M1 to M3, selectively-electroplated copper thickness up to 35-40 µm is estimated to be achievable with this technique and this can be increased further by increasing the width of the groove. The achieved thickness using this method appears to be sufficient for most targeted coated conductor AC applications. Since the electroplating of Cu in M4 was partial, another

sample was prepared, M6, to analyze effect of complete-coupling. M6 was not oxygenated after striation to let electroplated Cu grow on the groove uninterrupted and this sample is referred to as completely-coupled. An SEM image of M6 in Figure 4-14d reveals that the copper on the groove has larger grains than the copper on the filaments. Hastelloy has different morphology and current distribution during electroplating as compared to the thin silver layer that could account for the difference in grain size between the copper on Hastelloy between filaments and that on silver on the filaments.

Although mechanical scribing through Ag provides excellent results in terms of fully-filamentized wire structures, one of the most important problems associated with the mechanical striation is the agglomeration of the material at the tip front making long-scale scribing challenging. This agglomeration results in diamond tip breakage or discontinuous striation due to staggering. Implementing any kind of high-frequency vibrational load might resolve the problem. Alternatively, laser ablation, which has been investigated in the literature, can be used for filamentization. This can be integrated with the selective electroplating method to address the agglomeration issue.

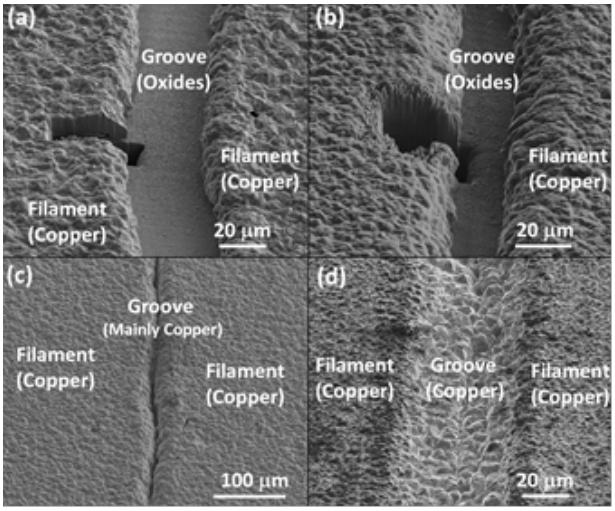

Figure 4-14. SEM/FIB images for decoupled samples with selectively-electroplated copper. (a) 10 μm thickness, (b) 30 μm thickness, (c) partially-coupled, and (d) completely-coupled configurations.

4.3. Laser scribing

LASER stands for Light Amplification by Stimulated Emission of Radiation. A laser is a light amplifier. Lasers consist of coherent monochromic beams of photons moving in the same direction. This is in contrast to light sources that usually produce incoherent beams of light at a variety of wavelength and moving in different directions.

4.3.1. Pulse and continuous laser

For continuous wave operation, a laser is pumped continuously and continuously emits light. The power obtained is constant in this type of system. Some medium would require pumping the laser at a high, continuous power level, which would be impractical or would destroy the laser by producing excessive heat. These lasers cannot be run in continuous wave (CW) mode. Pulsed operation of lasers refers to any laser not classified as continuous wave. The optical power appears in pulses of some duration and at some repetition rate. The pulse reputation frequency (prf) is a measurement of the number of pulses the laser emits per second. The main difference between a continuous laser and pulsed laser in terms of output power is explained Figure 4-15.

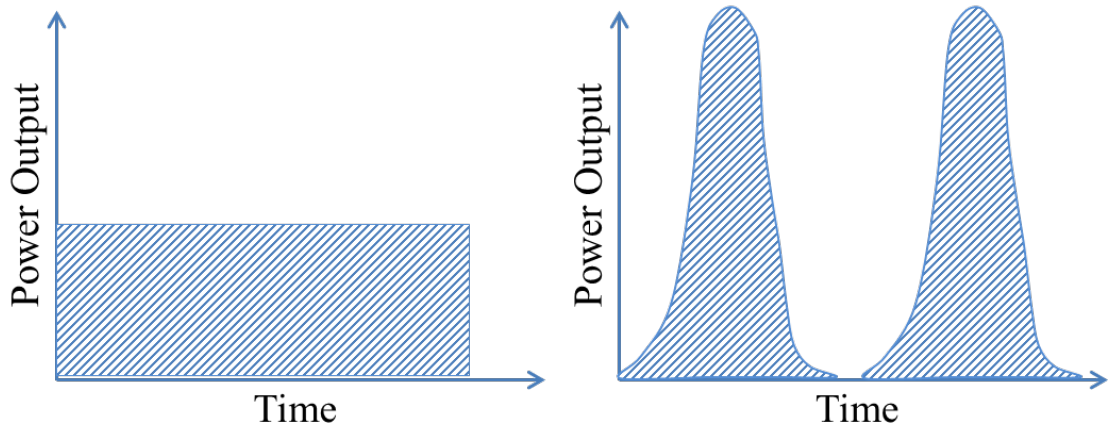

Figure 4-15. The power output of a continuous laser (left) and a pulse laser (right).

The average power can be calculated with a laser that produces 200 mJ, 40 ns pulses at a prf of 5 Hz as

$$P_{\text{average}} = \frac{\text{Energy/pulse}}{\text{Period}} = \frac{200 \times 0.001}{1/5} = 1\frac{J}{s} = 1\text{W}. \quad (4\text{-}1)$$

However, the peak power can be calculated for the same laser as

$$P_{\text{peak}} = \frac{\text{Energy/Pulse}}{\text{Pulse length}} = \frac{2 \times 10^{-1}}{4 \times 10^{-8}} = 5 \times 10^{6}\frac{J}{s} = 5\text{MW}. \quad (4\text{-}2)$$

In applications such as laser ablation, a small volume of material at the surface of a work piece can be evaporated if it is heated over a short time period. A pulsed laser can do this easily because of the peak power (5 MW in the example).

4.3.2. Laser ablation

Laser ablation is the process that removes material from a surface by irradiating to obtain desired structures. With appropriate laser intensity, the material absorbs the laser energy and is evaporated. Usually in laser ablation, the material removal is performed with a pulsed laser, although it is possible with a continuous wave laser beam if the laser intensity is high enough. Ablation depth is limited by the material energy absorption, which also depends on pulse duration, beam energy density and laser wavelength. Laser energy per unit area is measured by the energy fluence (intensity) that is given by laser pulse energy (J) / focal spot area (cm^2).

A key parameter to be considered when choosing a laser is the selection of wavelength with a minimum absorption depth. This results in small volume depositions with focused energy and fast ablation. According to Equation (4-2), the duration of the pulse should be short to obtain maximum peak power yielding small thermal dispersion on the surrounding metal. Repetition rate is also important. Small rates cause the energy to

dissipate and the ablation does not occur. The heat should be confined to a small region for the ablation to be efficient. For the purpose of this study, more of energy will be input into the ablation process reducing dissipation into the surrounding metal. Material removal depends on the optical properties, pulse length and wavelength, which will determine the amount of material removed from the ablation zone. Beam focusing has to be perfect to obtain homogenous removal with maximum efficiency.

A laser ablation process has several advantages. The process is quick and wet etching can be eliminated, although some of the laser applications might still require an etching process for filamentization. This minimizes the degradation from chemical reactions. It does not require a vacuum and the entire process of patterning can be done at ambient pressure.

- No solvents are used and the materials are not exposed to chemicals.
- Operation is relatively straightforward and simple.
- Although capital investments are high ($300k for an average femtosecond laser), the operational costs are relatively low.
- The process is relatively gentle, the damaged region relatively small, and no undercuts introduced.
- Heating, especially in the case of pulsed laser, is extremely localized minimizing damaged areas.

4.3.3. Laser ablation on 2G-HTS CC filamentization

Laser ablation is widely used in 2G-HTS conductor striation. One of the first laser used was the YAG laser for film ablation at room temperature and atmospheric pressure [149]. Later this method was investigated more thoroughly [87, 157, 165]. An image of a

laser-striated sample is shown in Figure 4-16 where a 12 mm wide tape is divided into 48 filaments. The width of the groove is about 70 µm while the width of the filament is about 180 µm. Reel-to-reel fabrication tape in long scale is very important. Filamentization of a short sample using a laser is a relatively simple task but it needs to be adapted for the long-scale production of filamentized structures in 2G-HTS conductors (Figure 4-17). A YAG laser using Nd:YAG crystals for the active medium and a laser diode for light source pumping was used in this system. The system was claimed to be capable of producing a 500 m tape and initially, a 50 m tape was produced [83]. It is capable of providing a 5 W energy maximum with a wavelength of 1064 nm and a repetition rate of 10−30 kHz. Tape moving speed and laser spot size vary from 2-20 mm/s and 20-60 µm respectively. Related processing parameters and comparisons with other lasers are provided in Table 4-3.

Table 4-3. Comparisons of various lasers and their respective processing parameters.

Source	Lasing Material	Average Power [W]	Repetition rate [kHz]	Speed [mm/s]	Pulse length [FWHM]	Laser spot [µm]	Wavelength [nm]
Ref. [83]	Nd:YAG	2.4	30	6	10−20 nm	20	1064
Ref. [158]	$Nd:YVO_4$	3.5	10	20	30 ns	-	355
Jenoptik	Yb:KYW	2.6	100	25	350 fs	40	1025
TRUMPF	Yb:YAG	5	400	214	5 ps	< 20	1030

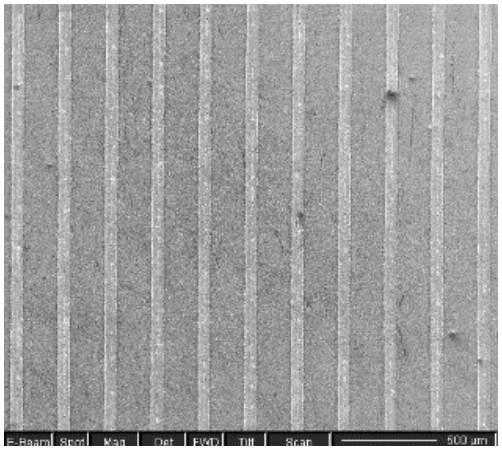

Figure 4-16. General SEM view of a 10 µm copper electroplated multifilamentary tape divided into 48-filaments. The widths of the groove and filament are 70 and 180 µm respectively.

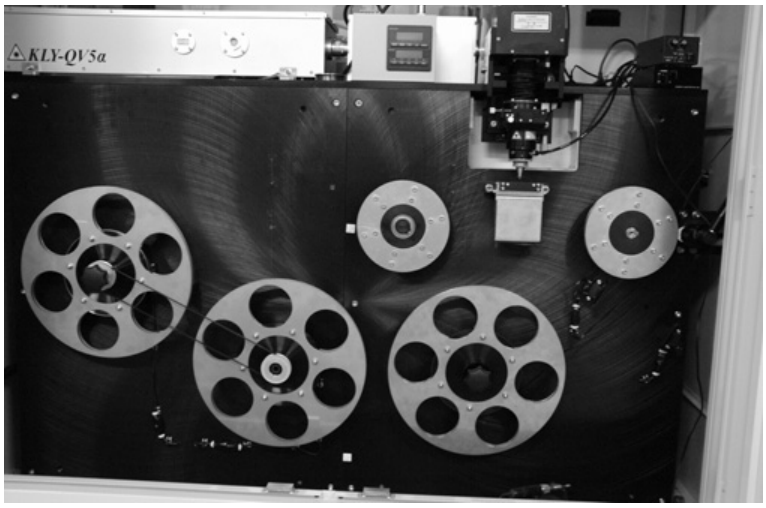

Figure 4-17. A reel to reel YAG laser scribing system [83].

Fabrications of coils made with striated tapes were demonstrated and AC losses of such coils were measured experimentally by the boil-off method [161, 166]. By creating three filaments, a threefold reduction in AC losses was demonstrated (Figure 4-18). The tape length used was 23.6 m with 60 mm inner diameter windings and the stabilizer layer thickness was about 5 µm. The striation was made by laser ablation followed by a chemical etching process.

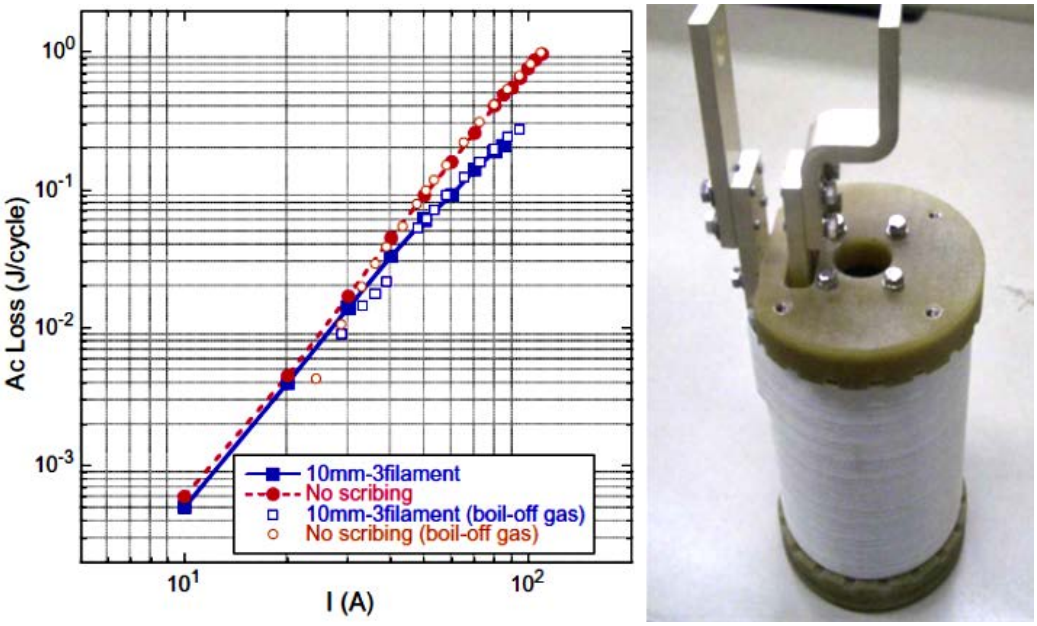

Figure 4-18. AC loss measurement to show threefold reduction in AC losses (left) and the coil (right) [166].

Another study of a striated filamentary tape in a long coil was conducted [167]. Two types of model coils were fabricated with 70 m long tape. 5 mm wide YBCO wire divided into 5 filaments by laser ablation is used in one of the coil while the model coil was fabricated using 5 mm wide tape with no-division. Short tapes with 5 filaments and a non-filamentized reference were also investigated for comparison. The AC loss measurements of the coils, filamentized tape structures, and non-filament references are shown in Figure 4-19. There is a nearly one-to-one correlation of tape to coil loss performance. This indicates that decreasing magnetization loss has a direct effect on the total AC loss reduction in coil configuration. AC transport current losses are relatively lower than the magnetization losses and can be considered negligible.

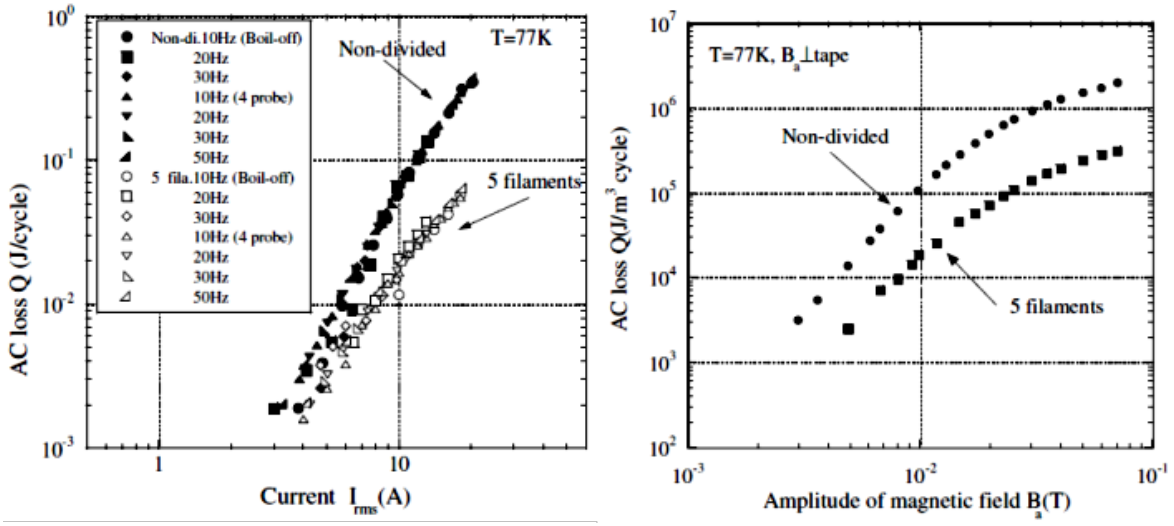

Figure 4-19. AC loss performance of a coil (left) and tape (right) structures compared with their undivided references [167].

An alternative to Nd:YAG tape striation was accomplished utilizing a frequency tripled, diode-pumped, solid-state Nd:YVO_4 (Neodymium-doped yttrium orthovanadate) laser [158]. The system is capable of providing 30-45 ns laser pulses with repetition rate of 1 to 100 kHz. Related processing parameters and cross-sections are shown in Table 4-3 and Figure 4-20, respectively.

In this dissertation, a diode-pumped laser was implemented to obtain the multifilamentary tapes (Jenoptik JenLas® *D2.fs* Yb:KYW, ytterbium-doped potassium yttrium tungstate). This system is capable of providing laser pulses of less than 400 fs with a repetition rate of 30 to 200 kHz. The laser energy is 40 µJ at 100 kHz and 20 µJ at 200 kHz. Related processing parameters and cross-sections are in Table 4-3 and Figure 4-20, respectively. One pass was sufficient to cut a groove through silver and YBCO, although some of the samples required more than one pass to achieve wider grooves. The width of the groove fabricated with this method is relatively wider than those seen in references [83, 161]. Usually, wider grooves are undesirable. However, the sideways growth of electroplated copper forces a wider groove to prevent coupling. Extremely short pulses vaporize nearly every material without a heat-affected zone, melt or burr. These femtosecond lasers allow micro-processing with an optimum combination of quality, productivity and cost-effectiveness. It is productive without heating, has a high average power, and the best beam quality.

A TruMicro 5050 TRUMPF© Yb:YAG (Ytterbium-doped) laser was also investigated. The system is capable of providing a max average power of 50 W with a repetition rate of 200 to 800 kHz. The pulse energy is less than 250 µJ and pulse length is less than 10 picoseconds (ps). The laser system processing parameters and cross sections are in Table 4-3 and Figure 4-20 respectively.

Jenoptik femtosecond and Trump picosecond lasers behave similarly and provide a relatively smoother surface while a nanosecond laser results in a rough surface (Figure 4-20). With the laser scribing technique, a groove width as low as 20 micrometer can be achieved although wider widths enable electroplating of a thicker stabilizer.

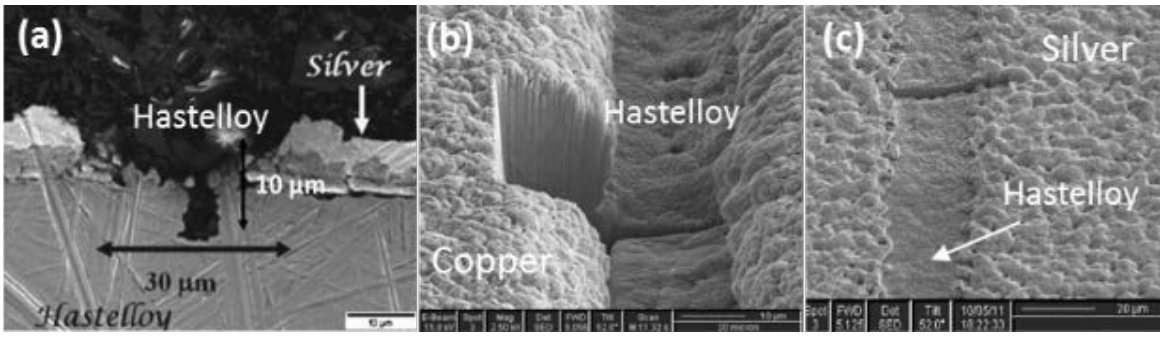

Figure 4-20. SEM images of a groove from (a) a nanosecond laser [158], (b) from a Jenoptik femtosecond laser, and (c) from a TRUMPF picosecond laser.

Figure 4-21. Laser striated samples. The top images are before copper electroplating and the bottom are after copper electroplating with different number of striations (12, 24 and 48, from left to right).

Details about the laser ablation sample preparation are provided in Table 4-4. A total of 12 samples were prepared including a reference sample (L12) to investigate the effectiveness of laser striation and to compare with the mechanical striation technique. Samples with increased numbers of filaments and various copper stabilizer thicknesses were investigated as well.

The ps laser striated samples (L9, L10 and L11) were prepared to investigate how small a groove width can be achieved. A width of ~25 µm was obtained with this laser. SEM and optical images of sample L11 are shown in Figure 4-22 and Figure 4-23, respectively. The groove is copper free after electroplating, as expected. These images

prove that the method developed for mechanical scribing can be successfully incorporated into a laser filamentization technique.

Table 4-4. Experimental details of laser-striated samples.

Sample ID	**Groove width (μm)**	**Annealing Temperature (°C)**	**I_c (A)/12 mm**	**# of filament**	**Plating (μm)**	**Laser used**
L1	~ 65	500	~ 345	12	~ 19	Fs
L2	~ 65	550	~ 310	12	~ 20	Fs
L3	~ 70	650	~ 245	12	~ 30	Fs
L4	~ 55	Not annealed	~ 316	12	~ 15	Fs
L5	~ 75	550	~ 222	24	~ 15	Fs
L6	~ 70	550	~ 230	48	~ 10	Fs
L7	~ 75	650	~ 218	24	~ 25	Fs
L8	~ 60	650	~ 88	48	~ 25	Fs
L9	~ 25	Not annealed	~ 216	12	–	Ps
L10	~ 25	Not annealed	~ 188	24	–	Ps
L11	~ 25	650	~ 140	24	~ 11	Ps
L12	–	Not annealed	~ 338	–	~ 20	–

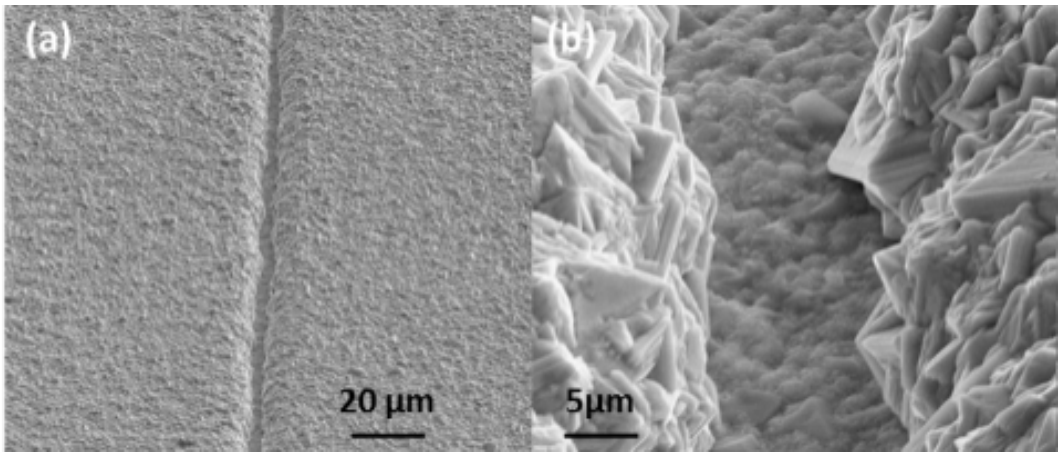

Figure 4-22. Inclined (52°) FIB/SEM images. (a) Lower and (b) higher magnification

After copper plating, the groove width decreased from 25 μm to 13 μm. The groove widths are more uniform and flat in these samples compared to that in mechanically-

striated samples. The decrease in width after electroplating is slightly less than that seen in mechanical striation and similar to the femtosecond laser-striated samples. This indicates that groove edges are an important parameter for sideway growths.

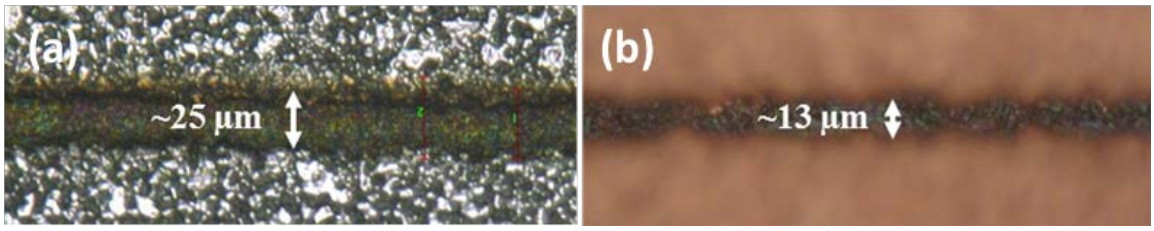

Figure 4-23. Optical microscope images of a sample before (a) and after (b) Cu electroplating, revealing that the groove width is about ~25 µm before electroplating and decreased to ~13 µm after electroplating of ~11 µm thick copper.

The femtosecond laser-striated samples (L1 through L8) were prepared with wider groove widths to achieve thicker electroplated copper. Figure 4-24a shows the SEM microstructure of L6 revealing the copper and groove with oxide layer. Figure 4-24b is the groove from a mechanically striated sample. In comparison, the mechanically striated tape has a relatively smother groove surface though traces of the diamond tip motion can be seen easily. It was assumed that a smother groove would provide better selective electroplating; however, this is not the case. Although the laser striated sample surface is relatively rougher, no electroplating particles are present on the groove surface.

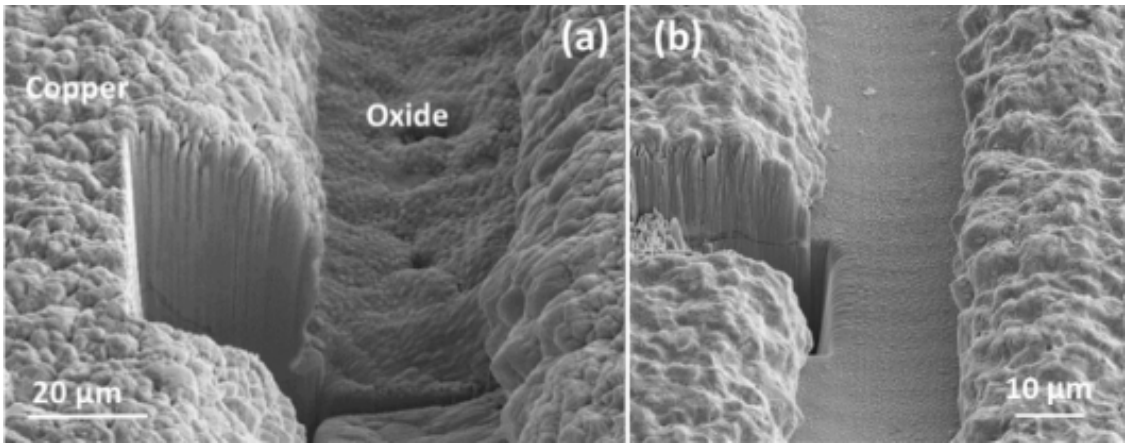

Figure 4-24. General view of a groove from a sample prepared by (a) femtosecond laser and (b) prepared by mechanical scribing.

Microstructural optical images of L3 are provided in Figure 4-25. After 30 µm copper electroplating, the groove width decreased to 20 µm. This is slightly less than the width decrease observed by the mechanical striation after copper electroplating.

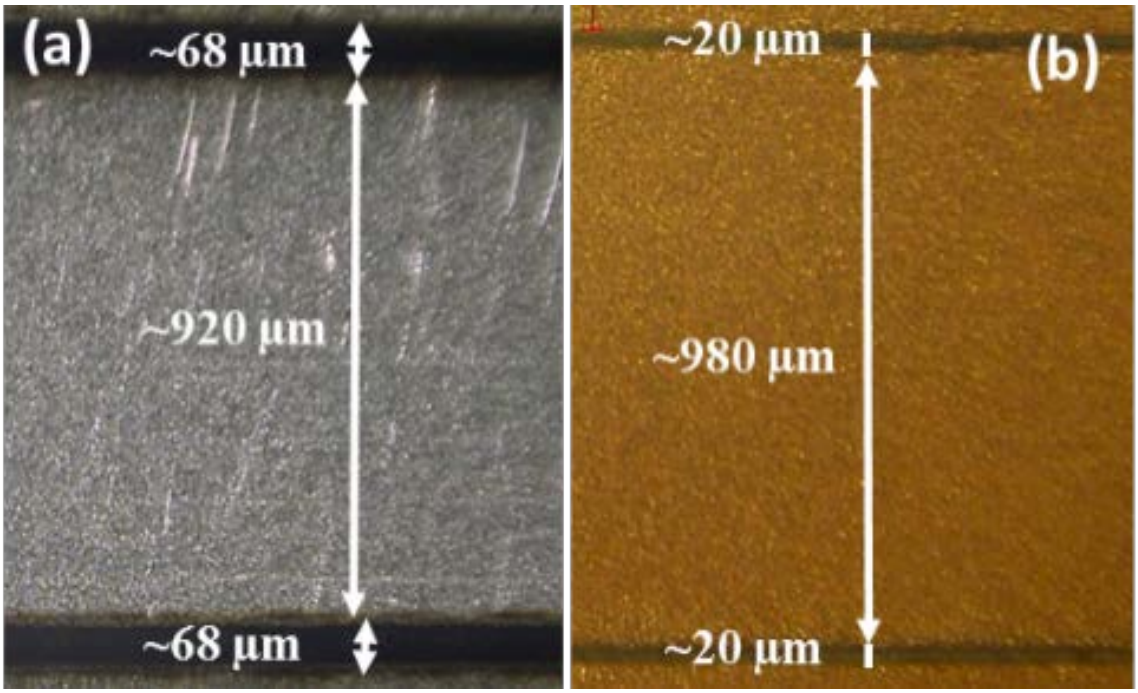

Figure 4-25. Optical images of a sample (a) before and (b) after Cu electroplating. After 30 µm Cu electroplating, the groove width has decreased to 20 µm from 68 µm.

4.4. Annealing/Oxygenation

The creation of a highly resistive barrier between filaments without degrading the superconducting properties is important for the reduction of coupling losses generated by current transfer between superconductive filaments.

Coupling loss is generated by the current flow between superconductive filaments through a resistive path [84, 87, 158, 161], in this case the Hastelloy substrate. Increasing the cross-resistivity between filaments reduces the coupling loss. Filamentized tapes were post-annealed/oxidized at high temperature in an oxygen atmosphere to create a highly resistive oxide layer on the groove. This process is referred to as oxidation. This approach

has been investigated previously [83, 158]. In this dissertation, the benefits of oxidation extend beyond AC loss reduction. The high resistivity of the striations can prevent electrodeposition of the copper stabilizer on the grooves. Utilizing this opportunity, an electroplating approach was developed (explained in section 4.5.) to selectively deposit copper stabilizer only on the filaments. This avoids any re-coupling of the filaments due to copper deposition on the grooves. FIB/SEM images of the groove created by laser scribing before and after oxygenation are shown in Figure 4-26. After oxygenation, the groove became smoother and the oxide layer can be seen clearly.

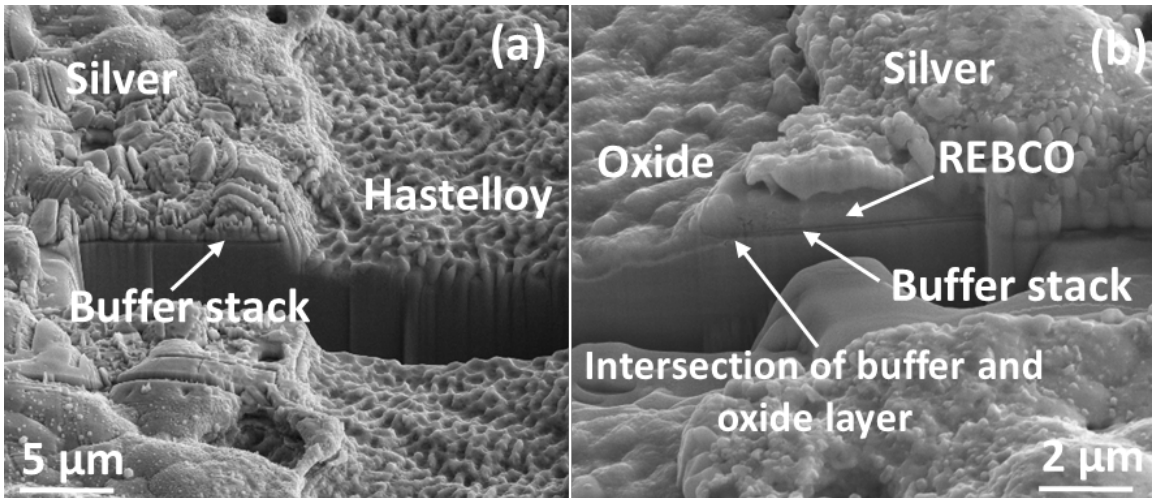

Figure 4-26. FIB/SEM image of a groove. Half of the groove is shown (a) before oxygenation and (b) after oxygenation.

Higher magnification FIB/SEM images are shown in Figure 4-27. Figure 4-27a is a high magnification image prior to oxygenation and Figure 4-27b is a similar image following oxygenation. Figure 4-27c is a detailed cross-section of Figure 4-32b revealing the top protective Pt layer that was deposited before the FIB cross-section to protect underlying layers. After oxygenation, the groove becomes smother and oxide layer between Pt and Hastelloy substrate can be clearly seen in Figure 4-27c.

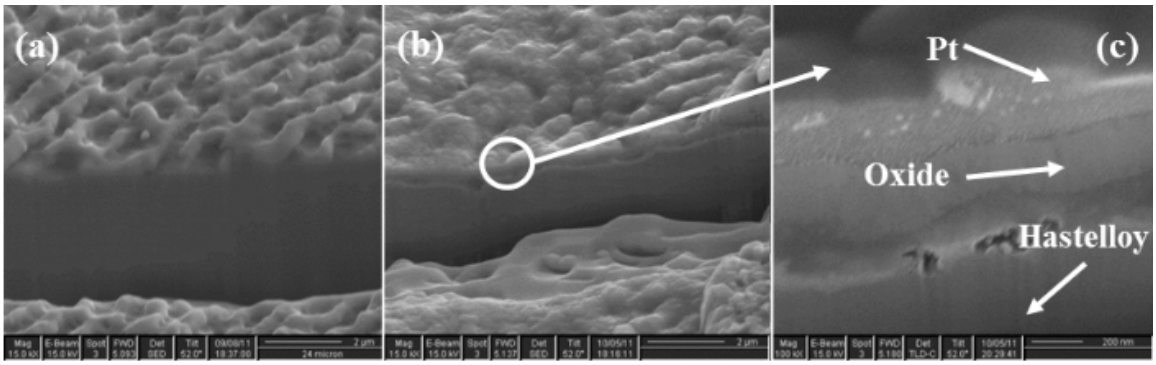

Figure 4-27. Higher magnification FIB/SEM images (a) before oxygenation and (b) after oxygenation. (c) is a detailed cross-section of (b).

The whole structure and clean cross-section are shown in Figure 4-28. This figure reveals the stablizer copper, protective silver, REBCO, buffer stacks, oxide layer, Hastelloy, and protective Pt layers. The hump on the edge between the filament and the groove results from a plastically deformed region of the Hastelloy substrate, which extends ~10−15 μm on the filament side. The figure shows that the oxide layer formation starts right from the termination of the buffer layer and extends across the entire groove area.

To further analyze the oxide layer, a corresponding TEM image to the right side of the hump region was taken, confirming the presence of a polycrystalline oxide layer on the groove surface (Figure 4-29). The thickness of this oxide layer was measured to be between 300 and 350 nm. The nominal chemical composition of Hastelloy consists of 15 wt% Mo, 15 wt% Cr, 4 wt% Fe, 3 wt% W, and 2.5 wt% Mn, and Ni as the remainder [168]. Therefore, it is likely that this layer consists of oxides such as NiO, Cr_2O_3 and Mo_2O_3, and possibly compound oxides such as spinels, $NiO{\cdot}Cr_2O_3$ [158].

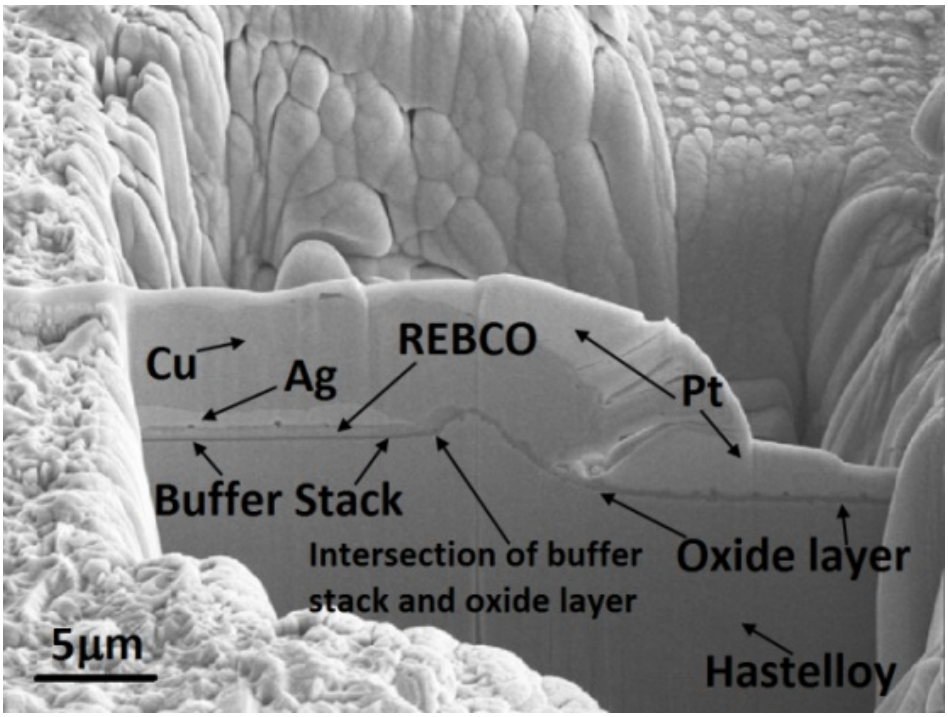

Figure 4-28. An SEM micrograph of a FIB cross-section of sample S2, revealing the oxide layer formed on the groove, extending right to the buffer layer termination. All of the layers are labeled including the protective Pt layer deposited prior to FIB milling.

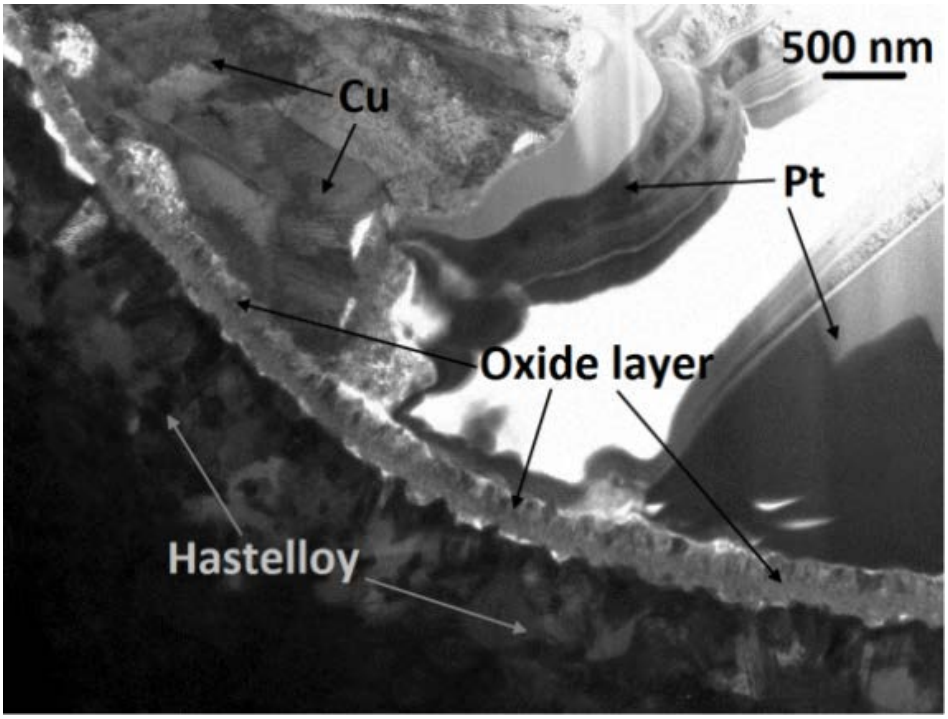

Figure 4-29. A TEM micrograph of the edge between the filament and groove of sample S2 after high-temperature oxidation. The oxide layer formed during oxidation is evident on the groove surface. The thickness of this layer is 300-350 nm.

4.4.1. Optimization of oxygenation temperature in terms of microstructures

Three samples (L1 through L3) were prepared at different oxygenation temperatures. Identical striations were done with the femtosecond laser. In total, 12 filaments were made and the spacing between the filaments was slightly less than 1 mm. The groove widths of each sample are shown in Table 4-4. This study was performed to determine the optimized oxygenation conditions for the femtosecond-laser-striated samples and the related microstructural analyses are presented. Oxygenation time and temperature graphs for each sample are shown in Figure 4-30.

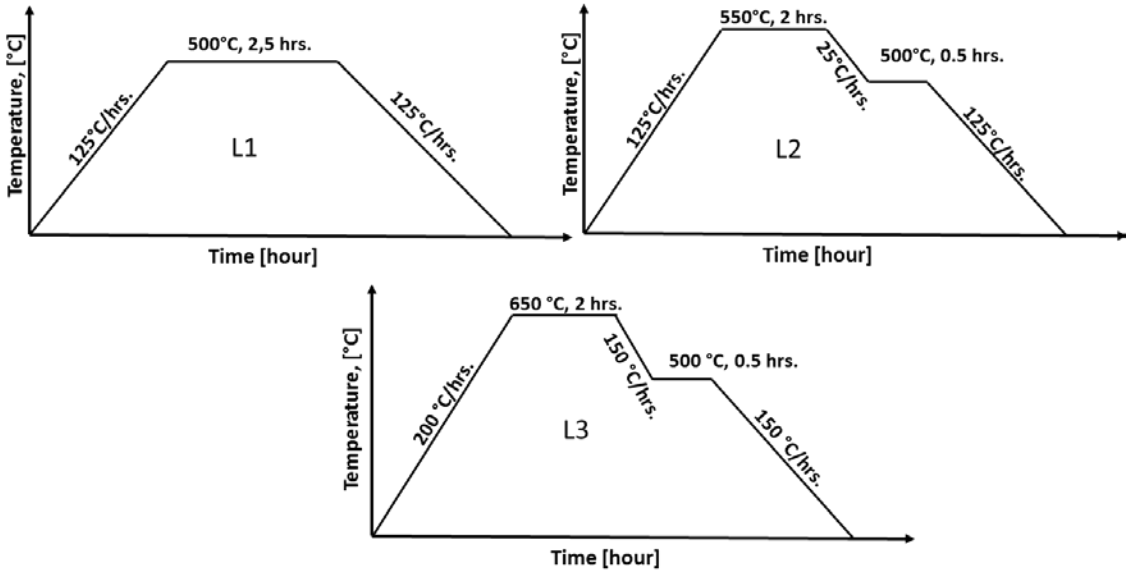

Figure 4-30. Plots of oxygenation time and temperature for sample L1, L2, and L3.

The SEM microstructures of samples L1, L2 and L3 are shown in Figure 4-31. It was previously assumed that the smoother surface would prevent the surface from being electroplated well. From the figures, it is apparent that the oxygenation temperature had a more severe effect on the selective electroplating. The sample oxygenated at a relatively low temperature of 500°C had significant copper island deposition on the groove (Figure 4-31a). These depositions decreased by increasing the temperature. Eventually, no deposition was observed (Figure 4-31c).

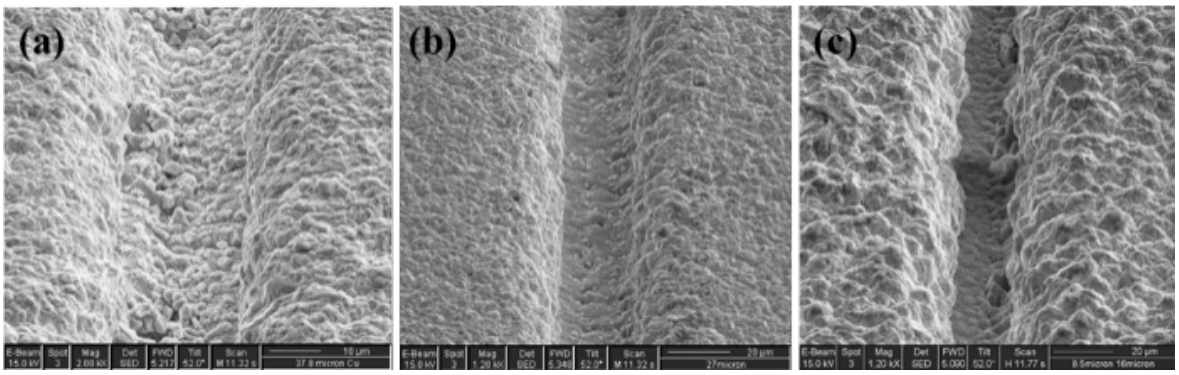

Figure 4-31. SEM images of the samples oxygenated at different temperature. The figures provided in (a), (b) and (c) are taken from L1, L2 and L3 respectively.

In terms of microstructures, the sample annealed at 650°C has the best selectively electroplated structure and the grooves are completely copper free. However, I_c and AC loss performance had to be investigated. I_c degradation and AC loss behavior of these samples needed to be investigated to fully-optimize the oxygenation temperature and these results are presented in Chapter 5.

4.5. Selective electroplating

Usually the most challenging step in a filamentization procedure is the striation of a relatively thick stabilizer layer. A thick stabilizer layer along with the HTS film has been striated by some of the aforementioned techniques. Many difficulties were observed. The ablated material was seen to re-deposited in the grooves. Discontinuous cuts due to the stabilizer layer thickness can increase the coupling loss contribution and reduce or even completely suppress the efficiency of striation. A reduction in I_c was observed due to various reasons including the diffusion of etchant into the REBCO layer and the creation of an oxygen deficiency near the filament edges because of the high power laser exposure necessary to ablate the thick layer of stabilizer [83, 87, 153, 154, 156, 158]. To eliminate these problems, a selective-electroplating method was developed in this work.

Electroplating is a current-dependent process. Electroplating uses electrical current to reduce dissolved metal cations, coating the desired surface. One can expect that current free regions are not coated during electroplating. This is the underlying mechanism for the selective electroplating. Creating an oxide layer not only helps to reduce coupling current but also create a means to selectively electroplate the stabilizer layer only on the filaments. This is necessary to obtain fully filamentized tape structures. If the material resistance is sufficiently high, a selective electroplating of thick copper stabilizer can be accomplished. Currently, no well-established approaches exist to make a long length, multifilamentary, coated conductor with a filamentized thick copper stabilizer. With selective electroplating, the obtained stabilizer layer thickness is sufficient for most applications in a fully-decoupled configuration.

4.5.1. Basics of electroplating

Figure 4-32 shows a copper electrodeposition cell. An anode and cathode are connected to an external DC power supply with the anode to the positive side and cathode to the negative. When this is powered, the copper on the anode is oxidized into copper ions and dissolve into the electrolyte (150 g copper nitrate in 1 L methanol or water). On the cathode, the copper ions are reduced at the desired surface and plated.

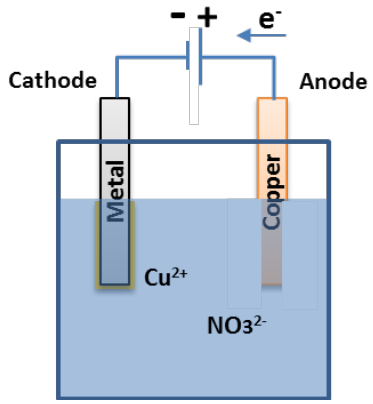

Figure 4-32. Sketch of an electroplating cell.

In general, metal ions (M^{n+}) are supplied by the bath solution and these ions are moved towards the cathode where the electric current is supplied (ne^-). The reaction can be written as

$$M^{n+} + ne^- \Leftrightarrow M. \tag{4-3}$$

Electroplating involves the electron-transfer reactions of metal ions from aqueous, organic or salt electrolytes. The cathode reaction for the copper plating is as follows

$$Cu^{2+} + 2e^- \rightarrow Cu(s). \tag{4-4}$$

The anodic reaction depends upon the anode material whether it is inert or sacrificial. It can be the metal to be deposited. In this case, metal ions are continuously supplied to the electrolyte. The anode material can also be an inert material. In this case, the anodic reaction is oxygen evolution. In second case, the ions in the solution are depleted and the deposition rate is altered accordingly. The reaction at the anode can be written for a copper plating as

$$Cu(s) \rightarrow Cu^{2+} + 2e^-. \tag{4-5}$$

In 2G-HTS, the cathode is silver and a copper electrode is used as a sacrificial anode. Therefore, the necessary copper ions are dissolved from this sacrificial layer; the concentration is kept constant and uniform deposition is provided throughout the process.

4.5.2. Electroplating parameters

The composition of the plating solution plays an important role in obtaining good quality plated structures. Changing the temperature, current density, or providing agitation and filtration can alter the quality of electroplating. All samples were plated in a beaker; however, this would need to be scaled-up for longer lengths. In this section, scaling-up requirements are discussed along with the parameters that effect the electroplating.

The temperature in an electrolytic cell is an effective parameter to vary the plating conditions. Usually in industrial-scale electroplating, the temperature is kept a little higher than room temperature for easier control of the electrolytic cell. It is very difficult to maintain temperature at room level because these systems typically lack a temperature controller and rely on ambient temperature. Many contributions can interfere with the electrolytic bath temperature. Because the electroplating was performed in a beaker for these studies, the temperature did not affect the plating process. Electroplating in a beaker takes a relatively short time and is easily controlled. In a reel-to-reel process, room temperature deposition is usually not preferred. In this case slightly elevated, easily controllable temperatures are ideal. Temperatures for Cu electroplating are typically varied from room to 55°C. Temperature variation can drastically alter the bath conductivity. By increasing the temperature, a higher plating solution conductivity can be obtained producing a higher deposition rate; however, the temperature needs to be optimized based on the required thickness.

Agitation is provided by stirring the solution in a beaker. Without stirring, the deposition is not stable and the growth is more dendritic. Agitation during Cu electroplating can be used for reducing the porosity in the electroplating cell and it can result in an increased current density. In a reel-to-reel system, the solution is pumped into the cell and the agitation is provided by a suitable pumping condition that produces uniform plating. Rapid solution flow around the cathode provides an agitation effect for plating rate and improves deposition.

Current density during electroplating has a significant impact on the deposition rate. Insufficient current will result in poor coating and low plating rate. The presence of

excessive current does not necessarily increase the plating rate. High current densities might be detrimental for electroplating and can create dull, burnt plating.

Filtration of the solution is required when the solution contains contaminant that can affect the plating.

4.5.3. Shielding

Electric current distribution of an electroplating system can have effects on the uniformity of the plated film thickness. This distribution can be controlled using several methods including using a dummy surface to act as a shield, current thief electrodes, or extra anodes. Usually current density is higher at the edge and causes more electroplating. In a 12 mm tape, without shielding, the thickness of electroplated copper at the edge could be as high as 20 µm while the middle of the sample is only approximately 5 µm. A sample holder was designed to redistribute the accessible copper ion concentration throughout the sample and obtain uniform thickness. The sample is mounted inside the shield (Figure 4-33c). The shield protects the edge from direct contact with electrolyte solution and reduces the copper ion concentrations at the edges. Different shield designs were investigated and the resulting film thickness profiles were measured. With inclined walls, the electroplating thickness at the tape edge and center was found to be ~5 to ~20 µm, respectively (Figure 4-33a). This indicates that electroplating was limited extensively at the edges. Later, the edges and top of the shield were slightly shaved to allow more ions access at the edges (Figure 4-33b). The thickness profile of the shaved shield starting from the edge through the middle of the sample is shown in Figure 4-34. The total width of the sample was 12 mm and due to the symmetry, only half of the sample thickness profile was measured. FIB cross sections were obtained at certain intervals to measure the thickness at

the various positions along the sample width. Although fairly good uniformity was obtained with the shaved shield over a majority of the sample width, a drastic decrease in copper thickness was observed 1 mm from the edge. To make it perfect, the inclined walls were straightened (Figure 4-33c). This new shield configuration provided uniform thickness along the entire tape width. The thickness at the edge and the middle of the sample were found to be 22 and 20 µm, respectively. Electroplating of a 15 cm long tape, which is sufficient for I_c and magnetization AC loss measurements, is possible by employing the developed shield. While this shield configuration works in beaker electroplating, the shield design has to be reconsidered and perhaps modified for a reel-to-reel copper electroplating.

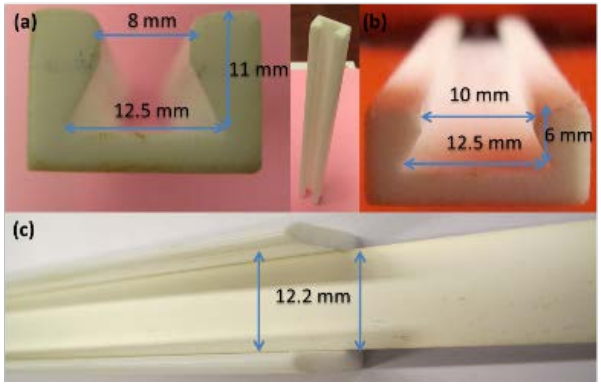

Figure 4-33. Different shielding configurations for electroplating copper to obtain uniform deposition thickness.

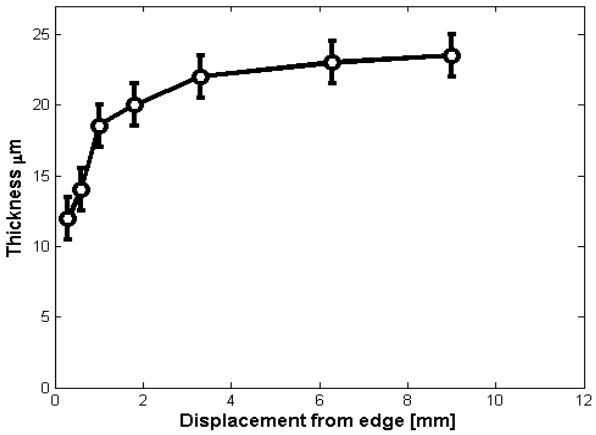

Figure 4-34. Copper thickness profile electroplated with the inclined walled shield.

A complete architecture of 2G-HTS is provided in Figure 4-35 with the stabilizer layer at the top. Conventional plating uses an acid-based solution that is reactive to superconducting layer and rapidly destroys the critical current. An organic solvent found to be harmless to the superconductors was used; however, a capping Ag layer of at least 1 μm thickness between the superconductor layer and the Cu-stabilizer layer is necessary to avoid any possible reaction from an electrolyte during electroplating [169].

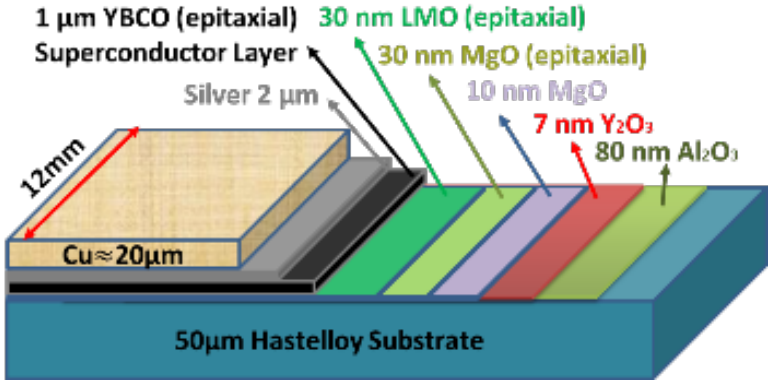

Figure 4-35. Complete structure of 2G-HTS coated conductor after electroplating the copper stabilizer layer.

4.5.4. Plating thickness estimations

A detailed derivation of the formula to estimate the plating thickness is provided in Appendix C. This formula can be rewritten for Cu electroplating with the unit of m,

$$\delta = \frac{t \times \frac{I}{A} \times 6.242 \times 10^{18}}{140700 \times 6.022 \times 10^{23} \times 2} [\mathrm{m}]. \tag{4-6}$$

In the experiments, a current density of $\frac{0.94}{0.13 \times 0.012} = 602 \ \frac{\mathrm{A}}{\mathrm{m}^2}$ was used with a 20 minute deposition time. Plugging these numbers into Equation (4-6), the thickness was estimated to be ~26.63 μm. The thickness also was measured by FIB/SEM (Figure 4-36) and found to be ~25 μm, close to the calculated value. The 3% difference might result from the rough surface of the electroplated copper.

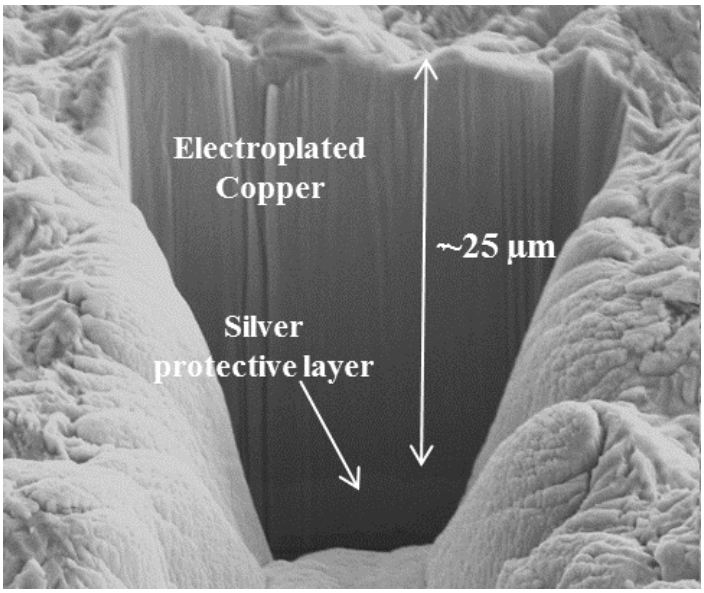

Figure 4-36. A FIB/SEM cross-section for the determination of the thickness of copper plating after a 20 minute deposition.

4.5.5. Stabilizer selection and purpose of stabilizer

The stabilizer concept in superconductors is not new and has been broadly applied to 1G-HTS superconductors. Usually silver is chosen as a sheath material because of its superior properties such as high conductivity, high permeability, etc., [164]. In 2G-HTS conductors, it is widely used for several reasons.

If a short-circuit accident happens in an application, a fault current can reach a value ten times larger than an operation current for a short period of time. This may cause the superconductor to transition from the superconducting to the normal state, known as quench, and result in irreversible damage to the superconducting device. This excess current has to be carried out through supportive layers to prevent burn out. One example of sample burn out due to excess current is shown in Figure 4-37. The sample is completely burnt and the silver protective layer melted. This is not a desired scenario and needs to be prevented at an earlier stage. A parallel path, called stabilizer layer, must be designed so the current can flow temporarily. A stabilizer layer is necessary for HTS CCs to provide

thermal, mechanical, and electrical protection. The purpose of the stabilizer layer is to temporarily carry a major part of the current in the conductor sections with hot spots. In a superconducting device quench has to be detected. A stabilizer layer with high conductivity can make this detection more difficult and cause catastrophic failure. Sometimes a less conductive material might be chosen for easier detection; however, device stability will be in jeopardy. An optimum condition needs to be determined by trading off these two parameters depending upon the application.

Figure 4-37. Burn out of the tape due to the over current.

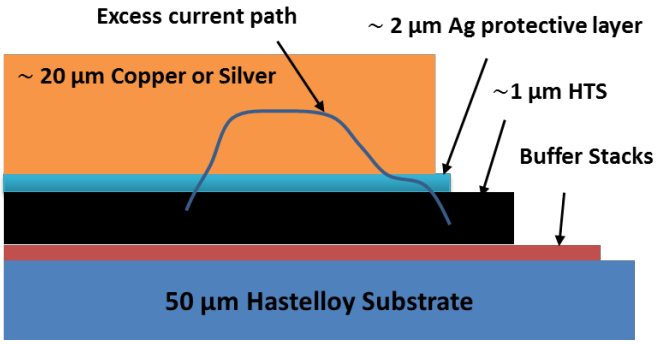

Figure 4-38. Excess current path through the stabilizer layer when a fault current is present.

4.6. Concerns about filamentization

The solution to AC loss reduction by striation is not straightforward and it has serious drawbacks. The ability of superconducting stripes to share the current due to the lack of connectivity could cause serious problems. For example one filament could be blocked temporarily or permanently by a defect or a hot spot. The problems related to defects in 2G-HTS is more important in a striated tape because if there is no current sharing

between the filaments and the problem becomes more severe with increasing numbers of filaments. A stabilizer layer can temporarily carry the electrical current for a short time, but not permanently. For this reason, a current sharing between the filaments should be provided. Usually devices such as generators, motors or transformers are operated well below the critical current. In these operational conditions, facilitating the current sharing through a resistive connection is not possible because all the filaments are in equal potential. For this reason the practical approach for current sharing is to achieve a degree of connectivity by providing properly engineered bridges or connections between filaments [85]. In this case, these bridges become an additional source of AC losses and need to be investigated carefully to not compromise the benefit of striation.

For the current to be redistributed, Brickwall and Fishnet patterning are two suggested techniques for obtaining better current sharing between the filaments. The related sketches are provided in Figure 4-39 [85]. Shown in Figure 4-39a is the twisted tape configuration; Figure 4-39b, the brickwall pattern; and Figure 4-39c, a fishnet pattern. In these patterning configurations, AC losses are considered to be a significant problem and the contribution of these patterns was investigated. In the brickwall pattern, total magnetization AC losses are found to be

$$P_{\mathrm{mBricwall}} \approx I_c \, BfW_n + I_c \, Bf \, x\Delta / L. \tag{4-7}$$

By taking $\Delta = W_n / 2$, formula can be rewritten in the following form

$$P_{\mathrm{mBricwall}} \approx I_c \, BfW_n \left(1 + x / 2L\right). \tag{4-8}$$

Where L is the length of the twist pitch x is the distance from the center as shown in Figure 4-39b and Δ is the bridge width.

In fishnet patterning, the total magnetization AC losses can be written as

$$P_{\text{mfishnet}} \approx I_c\ BfW_n + I_c\ W_n Bf\ \frac{\Delta^2}{W_n L} \approx I_c\ BfW_n\left(1+W_n/4L\right). \qquad (4\text{-}9)$$

The contribution of brickwall patterning to the magnetization AC loses is $I_c Bf\ (x/2L)$ while the contribution of fishnet is $I_c BfW_n\left(W_n/4L\right)$. For easier interpretation, the terms in the parenthesis are the only comparative contribution from each patterning. In the samples The length of the samples is about 44 mm, which is approximately equal to 2*x* in the brickwall patterning. Plugging in these numbers, the loss contribution is calculated approximately 25%. However, the loss contribution in fishnet patterning is significantly lower because it is divided by 4L and because W_n is much smaller than *x* in the fishnet patterning. The width of the bridge, Δ, can be increased to be equal or greater than W_n without paying a significant penalty in terms of increased losses. Such a configuration can be incorporated in the method developed in this dissertation and the problem of current sharing can be eliminated with no compromise on the AC loss reductions.

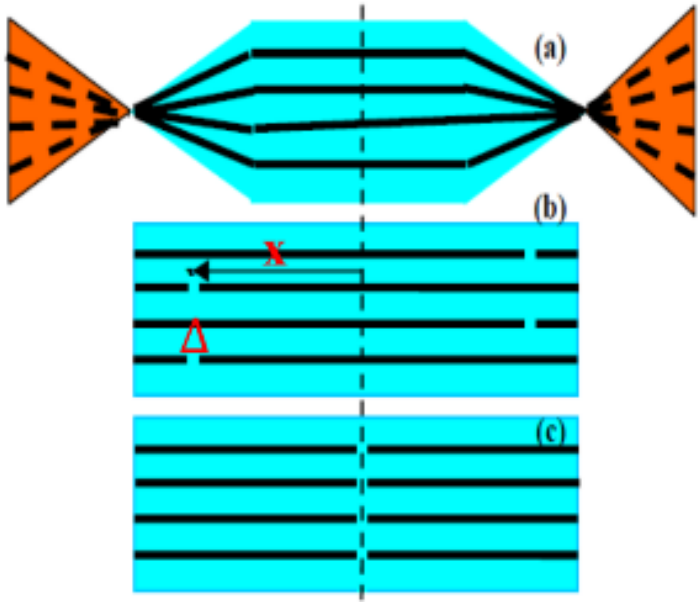

Figure 4-39. "Brickwall" and "fishnet" patterning of conductors suggested for current sharing. (a) twisted wire, (b) brickwall and (c) fishnet patterning [85].

4.7. Additional AC loss reduction techniques

Filamentization is not the only approach to reduce AC losses. However, it can be incorporated into other approaches developed for this purpose to maximize the benefit of filamentization. In the following section, alternative methods to achieve low AC loses are discussed.

4.7.1. ROEBEL transposition

ROEBEL bar transposition was introduced in 1914 by Ludwig Roebel in his patent application to reduce AC losses in copper generators cables [170]. This concept was extended to NbTi superconductor cables [171]. 1G-HTS conductors have benefited as well [172]. The ROEBEL concept has been demonstrated in 2G-HTS CCs [170, 173]. This concept combined with laser scribing for transposing purposes and to further reduce AC losses in 2 μm capped conductors (Figure 4-40) [174].

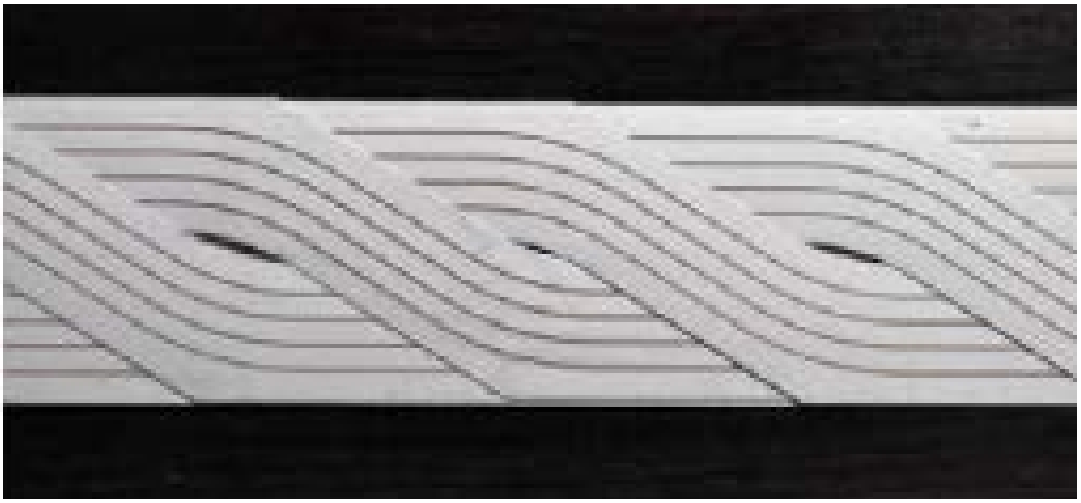

Figure 4-40. ROEBEL with laser striation performed on the 12 mm REBCO CC [174].

The REBCO CCs have to be cut from the CC tapes by a mechanical precision punch tool before assembling. It then needs to be wound as a wire. Shown in Figure 4-41 is an

example of such a winding. ROEBEL cable assembly is a promising approach for reducing the losses in 2G wires [175-178].

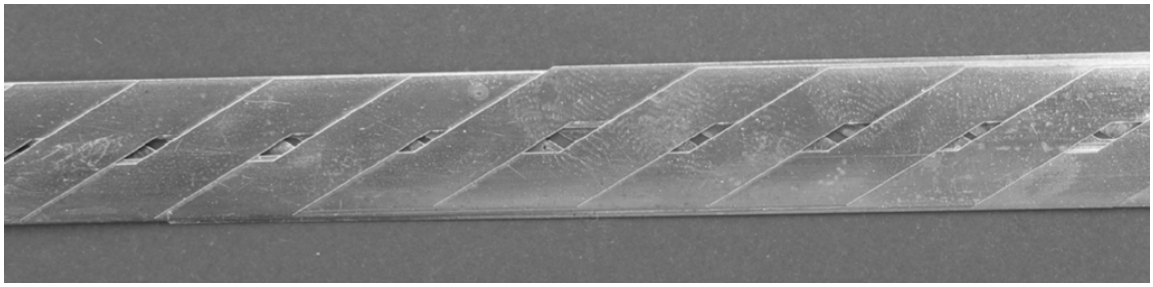

Figure 4-41. View on a section of the REOBEL assembled cable (width 12 mm) [170].

4.7.2. RUTHERFORD cables

Twisting has been extensively investigated in Chapter 2. Here the RUTHERFORD cable configuration of twisted multifilamentary superconductors is emphasized. The first Rutherford cable architecture from NbTi strands has been developed for high-energy physics applications [179]. Various Rutherford cables using 1G-HTS conductors in the form of round wires as strands have been examined [180, 181]; however, the field limits these wires. To obtain higher fields for future high energy physics applications, 2G-HTS CCs have to be incorporated.

The twist-pitch must be impractically short to keep the AC loss under control at high frequencies. To minimize high-frequency loss, a Rutherford cable architecture is proposed for YBCO tapes. Combining filamentization and Roebel and Rutherford twisting for low-AC loss wires is practical and theoretically possible, although an empirical demonstration is not yet available. The conceptual design has been demonstrated for a Rutherford strand made out of Roebel cable punched from 12 mm REBCO tape [182] (Figure 4-42) and the configuration is being investigated experimentally [183].

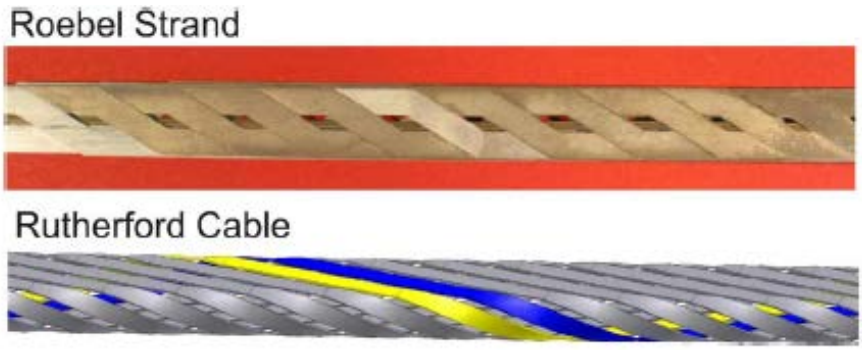

Figure 4-42. Roebel assembled cable fabricated from punched tapes on top and CAD design of a Coated Conductor Rutherford Cable (CCRC) assembled from a Roebel cable at the bottom [182].

4.7.3. Magnetic shielding

Manipulation of magnetic field is an alternative AC loss reduction method for conductors. This method has been effective for the reduction of transport AC losses [184] although it also has been used to reduce magnetization AC loss [185]. A magnetic cover to divert flux has been implemented on multifilamentary tape by embedding the whole structure into magnetic material [186] or with the grooves alone filled with a magnetic material [184]. In both, similar AC loss behavior is observed. Deposition of the grooves with ferromagnetic material seems to be effective for relatively low field AC loss reductions and can be incorporated practically with the striated conductors. Ferromagnetic material has been deposited on the edge of the coated conductors to divert the flux in non-striated conductors [185] with successful reduction in AC losses. This method was investigated in cable applications to favorably distribute the flux [187].

4.7.4. Transverse cut instead of twisting

Full-flux penetration on the grooves is required to reduce AC losses. One suggestion to achieve flux penetration was the twisting explained earlier. It is postulated that sometimes tape twisting is not trivial. A new technique for obtaining decoupled filaments has been suggested by introducing periodic transverse cross-cuts [152, 188]. The

cross-cuts, shown in Figure 4-43a, allow the magnetic flux to penetrate into the grooves and decouples them (Figure 4-43b). The continuity of the current path is maintained by the stabilizer layer across the cross cuts. Although the developed techniques in this dissertation can easily be combined with this method, the practicality of this approach depends on the trade-off between the magnetization AC loss reduction and additional resistive joule heating loss at the bridges. Another question is how feasible is to translate this approach to reel-to-reel, long length production of 2G-HTS conductors.

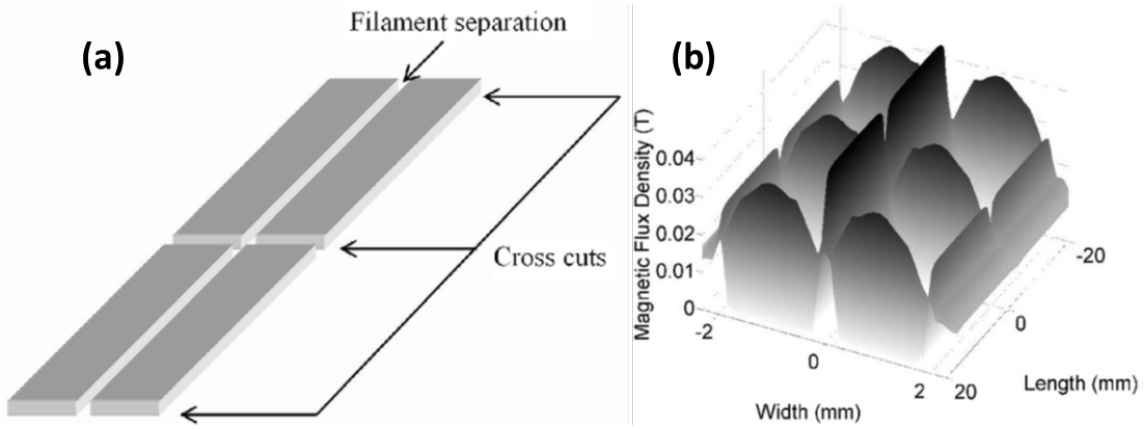

Figure 4-43. (a) Transverse cut of filaments and (b) flux penetration patterns [152].

4.8. Delamination

High-power applications, especially those using low AC loss striated tapes, usually require improved mechanical properties along the c axis. The mechanical integrity of 2G-HTS wires during operation has become one of the most critical problems [57, 189-191]. The structure of CCs in longitudinal direction is robust and can carry super-current up to an irreversible strain limit of 0.5-0.6 % [192, 193]. In the transverse direction along the c-axis, the stress level is lower, which is detrimental to the structure. Coil winding, thermal cycling, Lorentz force, epoxy impregnation, etc., have a significant impact on deformation and failure along the transverse direction during testing and application [57]. The failure is more devastating in the filamentized tape because the adherent fraction is reduced by the

removal of material. This can be seen with some of the thick copper electroplated, multifilamentary tapes (Figure 4-44). Although these problems appear during coil manufacturing or application, they should be addressed at an earlier stage such as the wire manufacturing. Later failure and evaluation is not cost effective. An appropriate testing method prior to device fabrication using short-tapes would be economical and efficient.

Figure 4-44. Camera images of some delaminated multifilamentary samples.

The mechanical property in transverse direction is closely related to the delamination phenomenon, adhesion strength [191]. Many techniques have been evaluated to characterize the adhesion behavior of thin film structures. Specific to REBCO CCs, methods have been developed to investigate adhesion of short samples. The anvil test developed [192] allows the sample to be a stress-free form from room to 77 K. In this method, critical current is measured as a function of transverse stress. The pin-pull test [194-196], the cleavage test [197], the double cantilever beam test (DCB) mode I type delamination behavior [198], and the four point bending test [199] have also been developed. A more complex mixed-mode delamination test procedure was developed that combines double cantilever beam (DCB) mode I loading and end-notch fixture (ENF) mode II loading [200].

The term strength might differ from test to test and can be referred to as c-axis tensile strength, delamination strength, cleavage strength or interfacial fracture toughness. Different testing can result in various loading configurations leading to stress state

variation. In all testing configurations, a transverse tensile stress component is presented. The c-axis tensile stress measured by some of these methods varies across a wide range and the results do not necessarily correlate with the coil performance [191]. Because of this variation and correlation difficulty with coil performance, a peel test was developed in coordination with SuperPower Inc. to investigate adhesion strength of REBCO CCs. It was found that the peel test has a better correlation with coil performance [191].

4.8.1. Peel test

Adhesion is associated with the nature and strength of binding between two materials in contact with each other [201]. Ideally, adhesion should be related to atomic bindings and can be related to the atomic bonding energy multiplied by the number of atomic bindings per unit area [202]. Adhesion strength can be found either by determining the maximum force per unit area exerted when two materials are separated (the pull test) or the work used to separate two materials from one another (the peeling test). Adhesion strength is less than the ideal determinant due to surface contaminations and stress concentrations originating from the high-temperature growth process [203]. The failure that occurs at the interface is called interfacial-debonding or adhesive-debonding. If the failure occurs within the matrix of one of these layers, such as the substrate or thin film, it is referred to as cohesive-debonding [202, 203] (Figure 4-45).

The peel force per unit width can be written as [202]

$$p = \gamma + \psi, \tag{4-10}$$

where γ is debonding energy, ψ is the work expenditure rate per unit advance of the peel propagation caused by plastic deformation in the adherent. The substrate is usually considered to remain elastically deformed. This is generally the case for CCs. Because the

peeling consists of plastic bending the mechanical properties and the thickness of the adherent and substrate are crucial.

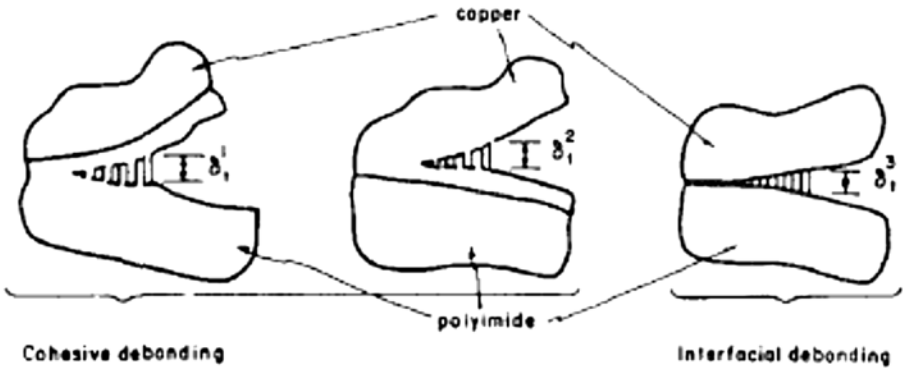

Figure 4-45. Mode of de-cohesion [202].

A peel test is used to characterize the adhesion strength due to its simplicity. Peel strength and interfacial bond strength have a simple relationship as given in Equation (4-10). In general, a portion of the work is consumed by debonding, while the other portion is dissipated through a plastic deformation of the adherent. The peel test offers a minimum cost for the characterization and is relatively quick to perform.

In the most thin-film vacuum deposition techniques, the surface temperature increases during deposition resulting in considerable internal stresses. Typically the top of the film tends to contract relative to its bottom or vice versa as an effect of these stresses. In the peel test, these stresses manifest themselves in terms of a reduced peeling force [203]. Three kinds of peel test configurations, T, 90^o and 180^o, were developed in this dissertation.

4.8.1.2. "T" peel test

The most convenient of these techniques is the T peel test. It is easy and relatively faster than the other test configurations and is more appropriate for adhesion stress characterization of thin films.

A simple sketch and a photograph of a T peel test are displayed in Figure 4-46. In this test, the peeling angle β can be different from sample to sample, even during measurement. This angle can vary depending upon the force exerted on the peeled region and the remaining length of the sample. Variation of β might produce fluctuations in the lengthwise peeling results if the adhesion strength is relatively high. If the adhesion strength is not sufficient, the plastic deformation in the adherent could be neglected and the peel strength represents the debonding-strength. In a T peel test, the dominating stress at the peeling front is shear.

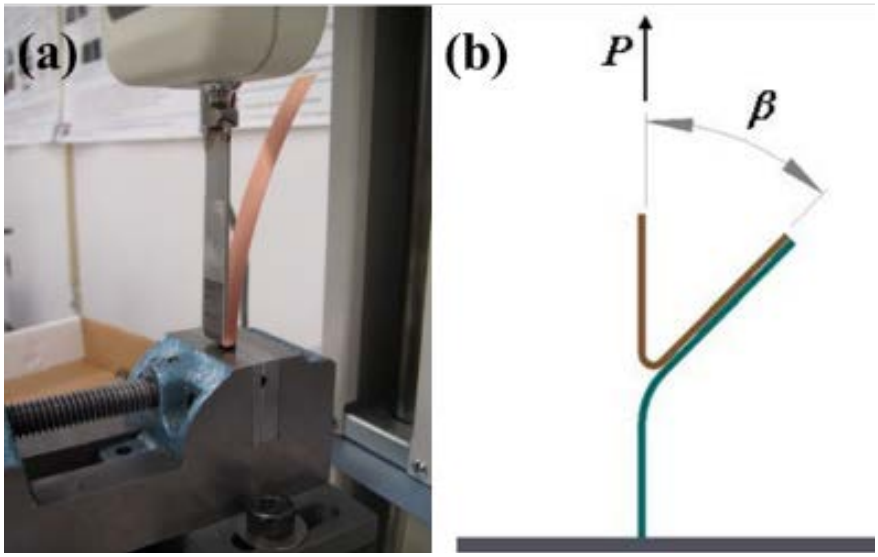

Figure 4-46. T peel test. The photograph is shown in (a) and the drawing in (b).

A digital force gauge recorded the load through a serial connection to a computer. The data acquisition speed was 1 Hz during the tests and all tests were conducted at room temperature. The total length of a peeled sample was measured and ranged from 50 to 80 mm for the T peel test. The test was made at a constant loading displacement speed of 0.833 mm/second. Prior to the experiment, the sample was manually delaminated from the weakest layer and the top layer of delaminated tape was glued to a moving force meter while the bottom layer was kept stationary at the bottom vise using double-sided tape.

The copper stabilizer layer for the peeling sample was electroplated. During electroplating, the front and the back of the wires were connected by sideway growths of electroplated copper stabilizer at the edges. For this study to be a true representation of wire adhesion strength, 1 mm from both edges of each sample was sheared off prior to the tests and the total sample width was 1 cm after the cut, eliminating the contribution of the edge plating.

4.8.1.3. 90° peeling test

A 90° peeling test primarily represents the tensile adhesion strength of the tape, similar to the pull or anvil tests. However, the peeling strength is measured by the force needed to separate the layers per unit width not the area, as is the case for pull and anvil tests. A photograph and sketch of the test configuration is shown in Figure 4-47.

A movable stage is supported by a string attached to the moving cross-head and a spring is used as a counter load to prevent free motion. These two additional forces eliminate any frictional forces that might be introduced during motion. In Figure 4-47b, M is the bending moment formed during peeling, P is the force exerted on the thin film, and R is the radius.

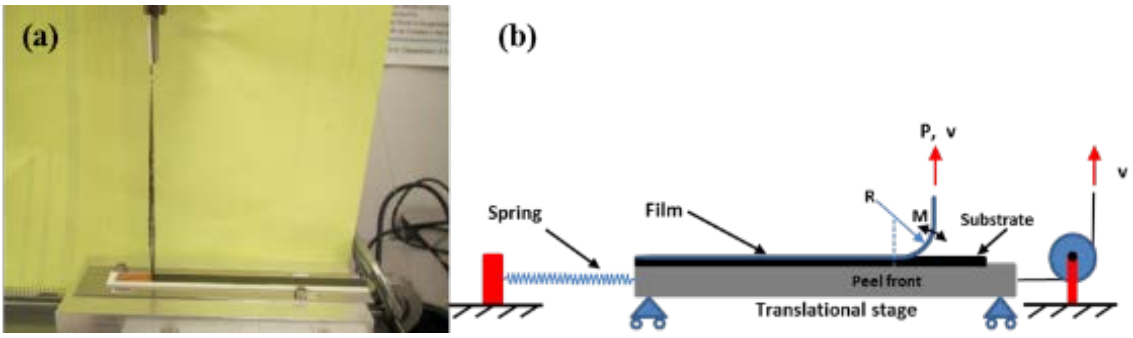

Figure 4-47. A 90° peeling test (a) photograph and (b) sketch.

As seen in the T peel test, the thickness of stabilizer layer is extremely important due to the plastic bending deformation observed at the peel front. A sample length varying

from 150 to 180 mm was tested by the 90° peeling test. This length gives more room to investigate the adhesion strength uniformity lengthwise as compared to 50-80 mm in the case of T peel test.

4.8.1.4. 180° peeling test

A 180° peel test is similar to T test with one difference. In this test configuration, there is a supportive fixed stage to which the sample is glued (Figure 4-48). The goal was to keep the peeling angle consistent during the test and between samples to investigate different stress states. In this test configuration, the dominant component is shearing stress. A photograph and sketch are provided in Figure 4-48.

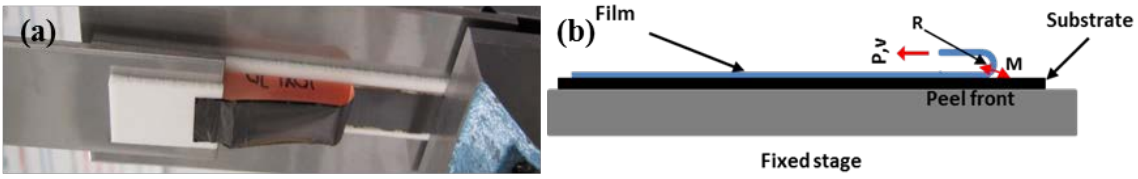

Figure 4-48. A 180° peeling test. A photograph is shown in (a) and a sketch is shown in (b).

As a summary, fabrication of reliable, safe superconductor devices require a sufficient conductive stabilizer layer to protect them from catastrophic failure or damage due to the quench. This layer protects the superconductors from harsh conditions and provides thermal, electrical, and mechanical protection to the superconductors during transportation or applications. However, due to it is thickness, filamentization of stabilizer layer is not easy task. In this chapter of the dissertation, the development of selective electroplating of the stabilizer to achieve a fully-filamentized structure for better AC loss performances in 2G-HTS conductors with thick copper stabilizer was discussed. The material agglomeration at the tip front for mechanical striation was found to be a problem and the concept of selective electroplating was successfully implemented to the laser ablation. Microstructural analysis were conducted for each striation technique and only

semi top down techniques result in fully-filamentized structure; however, only laser ablation was found to be suitable for long-length fabrication. Detailed microstructural explanations and adhesion measurements related to the T peel tests and the AC loss performance of filamentized tapes with different configurations will be discussed in the next chapter.

Chapter 5. Results and Discussion

In this section, the experimental results are discussed within theoretical frameworks. The magnetization AC loss, I_c, of different sample configurations is investigated to understand the AC loss behavior and the contribution of individual AC loss components to the total AC loss. The three sample sets investigated in Chapter 4, are reviewed below. The samples labeled S were mechanically striated and used to investigate the effect of selective electroplating on AC loss reduction. The samples labeled M were also mechanically striated and prepared to investigate the electroplating copper thickness and the electrical coupling contributions to AC losses. The samples labeled L were laser striated and prepared to investigate the method's applicability to well-characterized laser filamentization techniques. The influence of the filament number on AC loss reductions is also investigated with sample set L. Finally adhesion improvements in CCs are discussed.

5.1. Effect of striation on critical current and temperature

The degradation of I_c by the striation process is an extremely complex issue and a crucial parameter that needs careful investigation. If the I_c of the tape is lowered drastically by an AC loss reduction method, these conductors would be considered useless for any application.

I_c reductions resulting from a striation process can occur for several reasons. The first reason is the material removal. This is expected to be around 6-10% depending upon the width of the striation tracks. This reduction increases with increasing numbers of filaments. Another reason for the degradation of I_c is the ablation process itself. Oxygen deficiency near the groove and diffusion of unwanted element from the substrate can occur because the material is heated during the laser ablation process causing I_c reduction as well.

Non-uniformity along the length of a parent tape needs to be taken into account. Some regions of the tape might have a lower I_c compared to other regions. This might present as a reduction in I_c and cause confusion during data interpretation. The etching process can also result in I_c degradation. In the laser and mechanical striation S samples, etching was not applied; however, the etching process was applied in some of the M samples to remove the copper islands on the grooves. Delamination, explained in section 4.5.5. , is another source of I_c reduction that needs to be addressed. The strongest candidate for I_c degradation is the post-oxygenation process. The removal method of striation is also a concern because the diffusion of Hastelloy substrate elements can be poisonous to REBCO layers. This occurs because striation removes the diffusion barrier layer (Al_2O_3). EDX analysis was conducted by varying the distance, starting from the groove edge and moving through the filament width, on two of the mechanically-striated samples oxygenated at 700 and 750°C. The measured I_c for the sample oxygenated at 700°C was very low and the sample annealed at 750°C became non-superconductive. EDX analysis for the sample annealed at 700°C indicated the presence of Cr and Ni diffusion from the Hastelloy to the REBCO filaments (Figure 5-1). This diffusion is probably responsible for the I_c degradation.

The EDX analysis for the sample annealed at 750°C showed even higher element migration, especially Cr from the Hastelloy to the REBCO superconductive layer (Figure 5-2). The nature of the structural damage to the REBCO is still unclear. It is probable that the substitution of element from the REBCO with those that migrated from the Hastelloy substrate resulted in non-superconductive behavior. Additionally, different phases might be formed in the REBCO structure. To make sure the sample is non-superconductive, T_c measurements were performed on the sample annealed at 750°C. The sample had two

regions − one with striation and another without. The T_c measurement results are shown in Figure 5-3. The T_c of the non-striated region showed a very sharp transition while the T_c measurements from the striated region showed no transition at all.

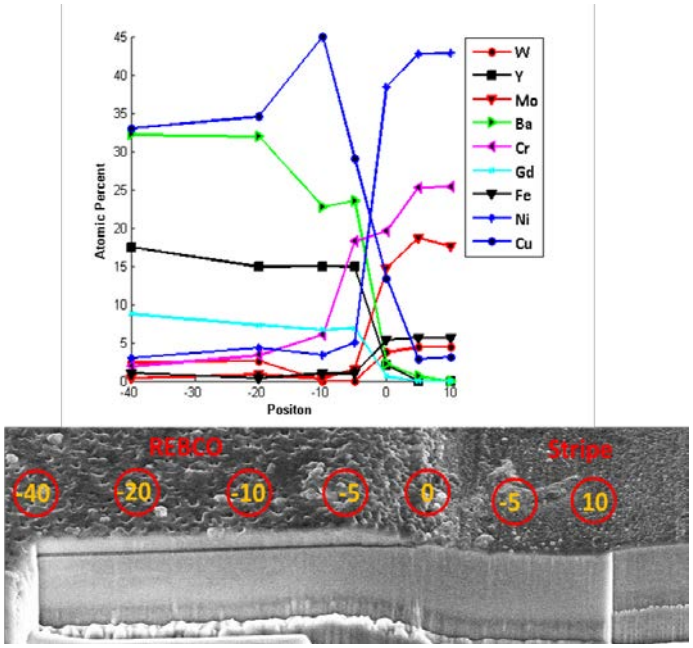

Figure 5-1. EDX results of the sample annealed at 700°C. The bottom figure shows the positions where the EDX analysis was performed.

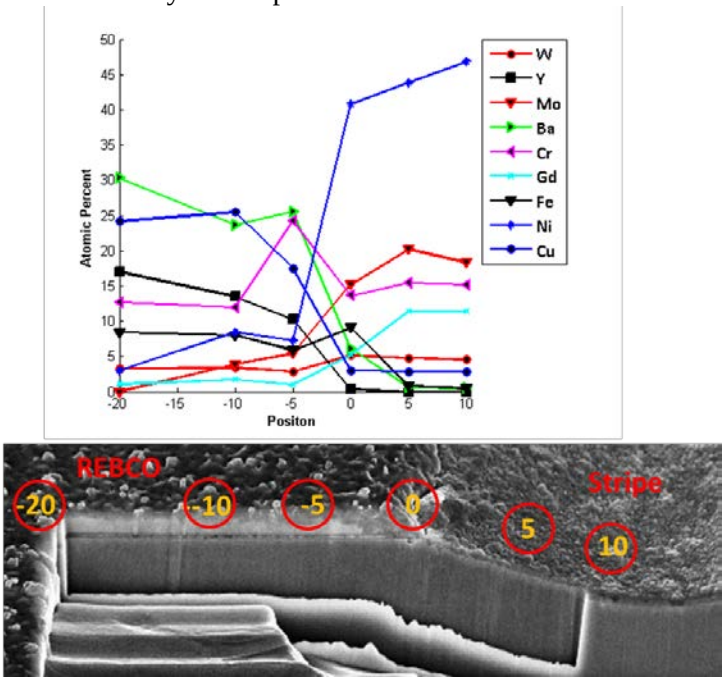

Figure 5-2. EDX results of the sample annealed at 750°C. The bottom figure shows the positions where EDX analysis was performed.

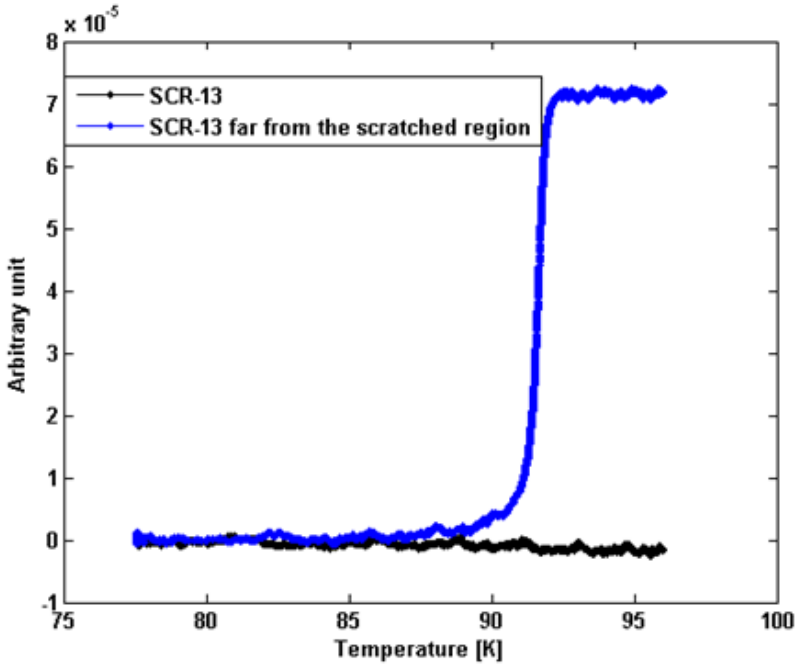

Figure 5-3. T_c from striated and non-striated regions on the sample annealed at 750°C.

Given these results, the investigation focused on oxygenating the samples at temperatures below 700°C and studying I_c performance. The results found in section 4.4.1. demonstrated that the preferable sample oxygenation temperature was 650°C in terms of selective-electroplating behavior; however, the important parameters that affect I_c degradation including the oxygenation temperature, laser ablation, and non-uniformity along the tape length were not discussed. In this section, these parameters are investigated to further optimize the oxygenation temperature.

5.1.1. Oxygenation temperature effect on I_c

These results are specific to the femtosecond (fs) laser striated samples and unfortunately, the findings cannot be directly correlated with other methods because each method has its own unique groove structures. However, it can give some explanation to the degradation of I_c in mechanical striations. Even laser striations with different conditions

might result in a different degree of I_c degradation since the degradation depends on the wavelengths used and the influence of heat on the ablation zone.

Four 12-filamented samples were prepared to investigate the oxygenation temperature effect on I_c reduction along with a untreated reference sample, L12. These are labeled L1 through L4 and oxygenated at different temperatures. Sample property details are provided in Table 4-4. Oxygenation temperature profiles are provided in Figure 4-30 with respect to oxygenation time. Sample L4 was not oxygenated to eliminate the oxygenation effect on I_c and to see effect of striation alone on I_c degradation. The I_cs of these samples are provided in Figure 5-4.

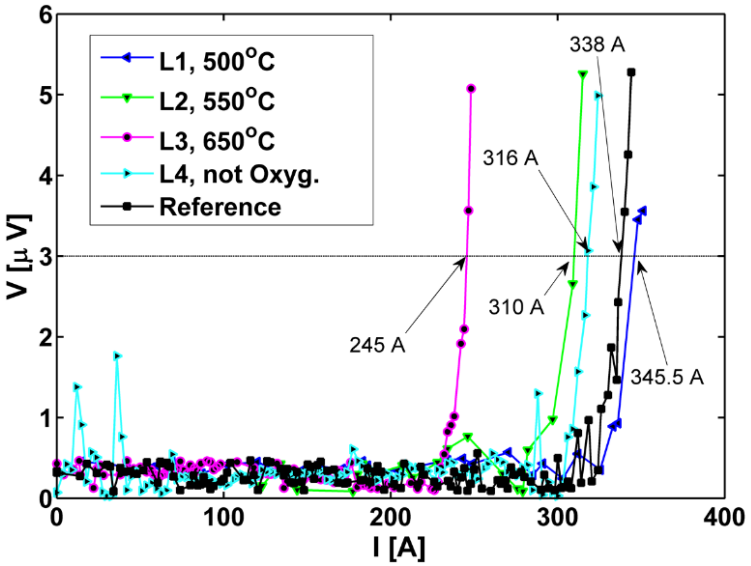

Figure 5-4. Oxygenation temperature effect on I_c.

One important conclusion is that at higher temperatures, I_c degrades drastically. The degradation is 27% and 8% for L3 and L2 respectively. Surprisingly the I_c of L1 is higher than the non-striated reference sample, L12. This clearly indicates that the parent-tape used for the samples is not homogenous in term of I_c performance along the length. The degradation without oxygenation was found to be about 6.5% after comparing L4 and L12. The calculated reduction from material removal for L4 is 5.5%. A 1% increase in

reduction following striation originated from the laser ablation. This conclusion is an estimate and it does not strictly mean that when a sample is laser striated into 12 filaments that the reduction would always be 1%. The reduction depends on the laser parameters and the groove width, which was relatively smaller for this sample. The most important implication of this result is that the laser ablation does not contribute significantly to I_c degradation while oxygenation temperature has strong effect.

I_c reductions by increasing the filament number are also investigated at two particular oxygenation temperatures (550 and 650°C) in Figure 5-5a and b. Unfortunately, in this analysis two of the samples (L5 and L8) were delaminated and that produced increased I_c degradation. For this reason, these two results were discarded. Plots comparing calculated I_c degradation from the material removal and the measured degradation with their respective oxygenation temperature are provided in Figure 5-6. It can clearly be seen that increasing the oxygenation temperature increases I_c reduction to unacceptable levels. Significant deviations were observed between the measured and calculated values on the samples oxygenated at 650°C. However, for the samples oxygenated at 550°C the measured degradation is very close to those estimated for material removal alone.

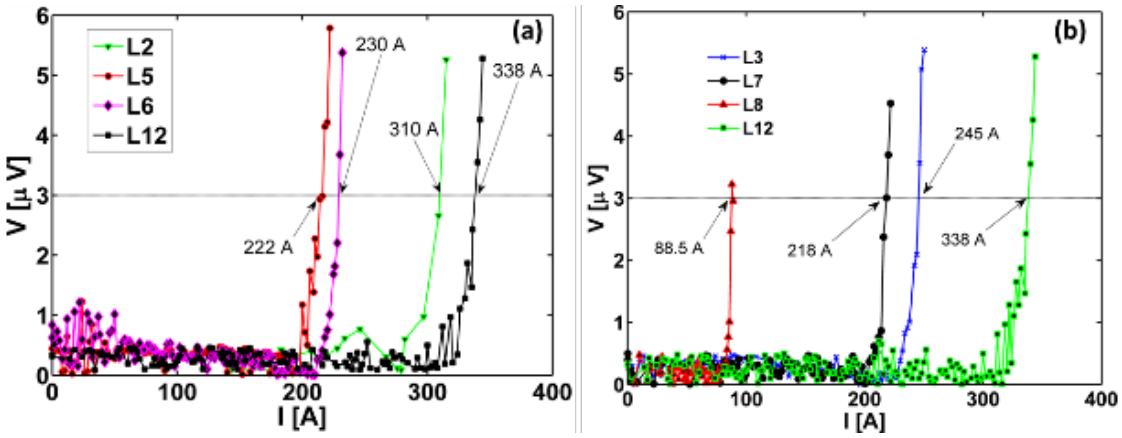

Figure 5-5. I_c degradations with varying number of filaments at (a) 550 and (b) 650°C.

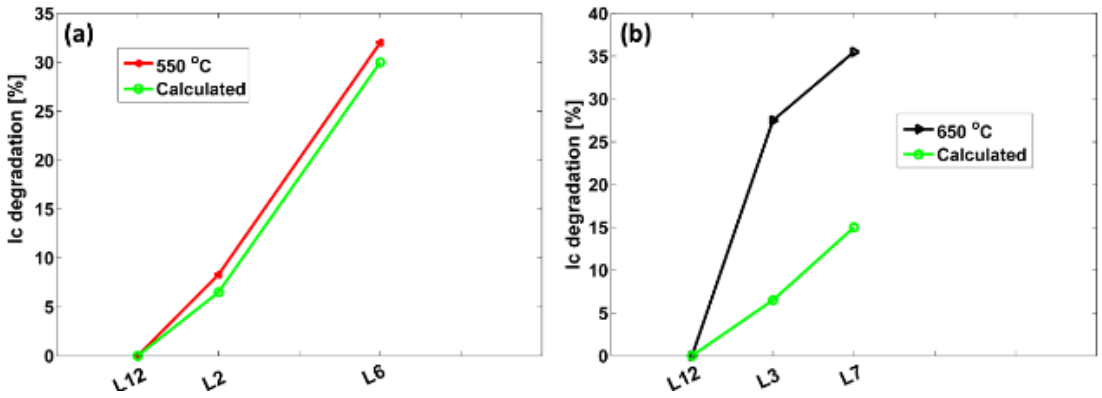

Figure 5-6. Comparisons of I_c reductions with number of filaments and their calculations at (a) 550 and (b) 650°C.

The most suitable oxygenation temperature was found to be 650°C in section 4.4.1; however, I_c analysis showed that oxygenation of the sample at 650°C degrades the I_c significantly. Temperatures at or lower than 550°C do not cause significant degradation. Before fully optimizing the oxygenation temperature the AC loss behavior of these samples has to be evaluated. This is discussed later in section 5.3.

5.1.2. I_c degradations in different striation techniques

In each filamentization technique developed for this dissertation, I_c degradations differ. The most severe degradation (27%) was observed in the laser ablated sample, L3. About 7% can be accounted for by material removal. Striation parameters in the laser-striated samples are comparable with the mechanically-striated samples. In general, the total amount of REBCO removed across the sample width by striation is about 4 to 10%. To be consistent, one untreated reference sample with the same composition as the related set was provided for comparison.

Shown in Figure 5-7 are the I_c values of the mechanically striated S samples. The I_c values were found to be similar to one another. The maximum degradation in I_c is 12%, the minimum is 5%, and the average is about 9%. The I_c degradation due to REBCO layer

removal should be 4-6%. The additional 3-4% degradation might be due to the influence of post-oxidation and/or electroplating.

The I_c performance of the mechanically striated M samples is provided in Figure 5-8. There are minor differences in the I_c values of striated tapes M1, M2, M3 and M4 that is probably due to the chemical groove cleaning process. The I_c values of these samples are lower than M6 and M5, which could potentially be due to performance deterioration resulting from the oxidation procedure used in the first four samples. An average critical current degradation of ~11% was observed after filamentization, oxidation, and electroplating compared to the untreated reference sample M7. This value can be compared with the ~6% expected degradation from material removal.

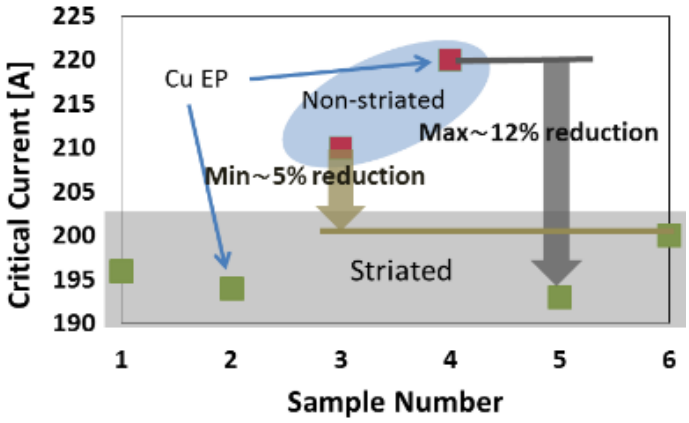

Figure 5-7. I_c of the mechanically striated samples labeled S.

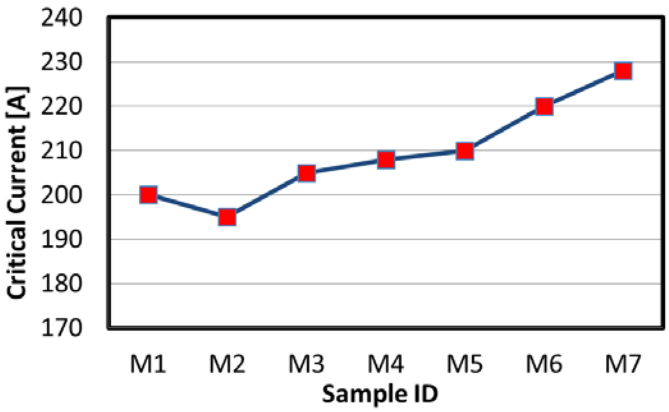

Figure 5-8. I_c values for the samples prepared to obtain thicker copper electroplating labeled M.

Although the oxygenation temperature (650°C) is the same for the laser- and mechanically-striated samples, the reduction is 27% in the laser-striated sample and 9 % for the mechanically-striated S samples and 11% for the mechanically-striated and etched M samples. The reduction in the laser-striated samples is significantly higher than the mechanically-striated samples. One reason could be the lack of plastering material, especially silver, on the sides of the groove in the laser-striated samples. Plastering occurs in the mechanically-striated sample due to the mechanical contact. This plastering materials could act as a barrier for Hastelloy element diffusion. Since the laser ablation removes the material by evaporation, this process might be creating pores on the groove edge that could accelerate the diffusion of the Hastelloy elements. A significant decrease (14.7%) after producing three 1 mm wide filaments was seen using another laser ablation method [204]. Regardless of the problem source, it was found that the issue can be solved by decreasing the oxygenation temperature, assuming that it does not result in a significant AC loss increase due to coupling.

The effect of filamentizations on T_c was found to be insignificant. The critical temperature of the samples was fairly similar indicating that there were no detrimental effects on T_c by copper plating and post-annealing. The lowest T_c was 90.9 K for S5 and the highest was 92.0 K for S3, shown in Figure 5-9.

The previous samples discussed were prepared by semi top-down approach and only one sample prepared by the bottom-up buffer scribing. The critical temperature of the buffer-scribed sample was found to be 89.6 K, slightly lower than semi top-down scribed samples (Ag scribed). The transport critical current was determined to be 106 A for the buffer-scribed sample corresponding to a critical current density of 1.5 MA/cm^2. This is

significantly lower (~25%) than the Ag-scribed samples (~2 MA/cm^2). It was revealed in section 4.2.1 that the epitaxy is well preserved a small distance from the ill-textured polycrystalline material grown on the groove due to the removed buffer stack. Spreading of the ill-textured material presumably should not result in any deterioration. However, diffusion of any possible material could form a secondary phase and cause degradation. The buffer scribing was done manually and this could produce non-parallel striations and reduce the current-carrying width. Due to this current path reduction, the I_c could also decrease. Since the final architecture of the sample was not ideal, detailed experimental work to understand the I_c reduction mechanism was not conducted.

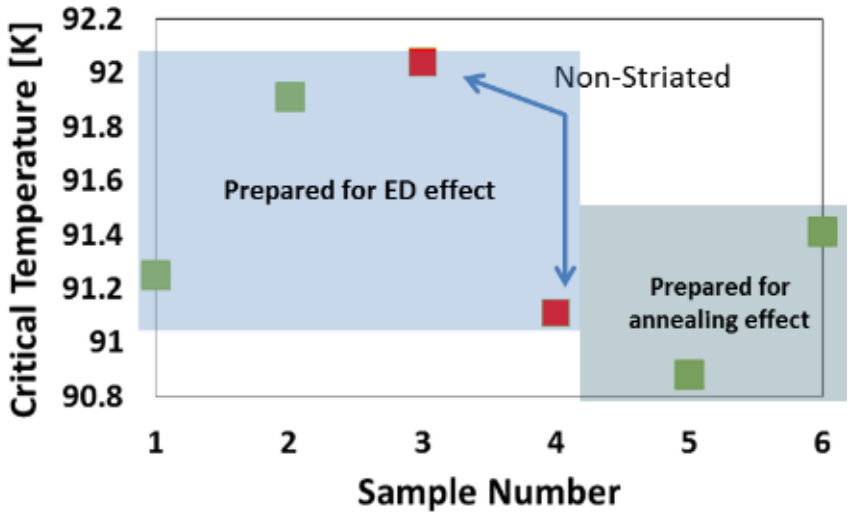

Figure 5-9. The effect of the striation on T_c.

5.1.3. Filament I_c measurements

The distribution of I_c across the filament width is shown in Figure 5-10. The figure indicates that the I_c drops considerably towards the edges of the tape and it is relatively uniform in the middle. This characteristic is most likely intrinsic to the tape itself rather than a result of the filamentization/plating process. A similar behavior has been reported in other studies [154, 161].

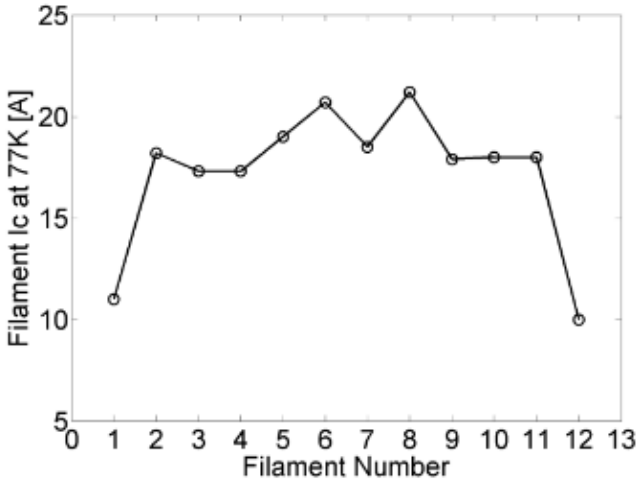

Figure 5-10. Critical current of the individual filaments of a striated conductor as obtained by selective I_c measurements.

5.2. Effectiveness of filamentization and coupling losses

Samples S5 and S6 were prepared to examine the coupling loss effect of the oxide layer created on the groove by oxidation. The specific loss, Λ, with respect to sweep rate, which indicates the effective filament width is shown in Figure 5-11. The linear fit shown by the solid line in Figure 5-11a is calculated at 200 Hz for S5 according to the definition of specific loss as given in section 2.4. A linear fit was also confirmed for other frequencies. The slope of the linear data fit is related to the electrical coupling loss and the intercept of the linear fit with the *y* axis is related to the hysteresis loss. A low slope and the corresponding strong noise effect are present in the samples containing an oxide layer in the grooves making an accurate estimate of the slope, and intercept difficult. However, even with the increased slope/intercept fit uncertainty, it is obvious from Figure 5-11a that after oxidation, the coupling loss is almost completely suppressed compared to the non-oxidized sample, as evidenced by the drastic decrease in slope. The effective widths of the filaments estimated from the linear fits are 1.06 and 0.98 mm for the samples before (S5) and after (S6) oxidation, respectively. This agrees with the filament width measured from

optical or SEM images. These values also indicate good striation quality. The calculated break-even sweep rate, $\mathcal{R}$ (section 2.4.), for the sample before oxygenation (S5) at 200 Hz is found to be about 15 T/s. The plots provided in Figure 5-11b are for S1 and S2 and show the effect of electroplating on striated and oxidized samples. It is apparent that the results before (S1) and after (S2) electroplating of 11 μm copper coincide. This indicates an absence of appreciable electrical coupling loss contributions from the electroplating. The electrical coupling loss is inversely proportional to the resistivity of the normal metal according to Equation (2-14). If there were any significant electroplated copper on the groove in S2, an increase in the electrical coupling loss would be expected due to the low resistivity of copper which would have resulted in an increase in the slope in the linear part of the data (Figure 5-11b). The effective width for the sample shown in Figure 5-11b is about 1 mm. This is consistent with the measured value of the filament width from the SEM and optical images. Furthermore, the similarity in the data for samples S1 and S6, shown in Figure 5-11a and b give an indication of the filamentization/oxidation process reproducibility since the two samples were subjected to identical striation and oxidation conditions.

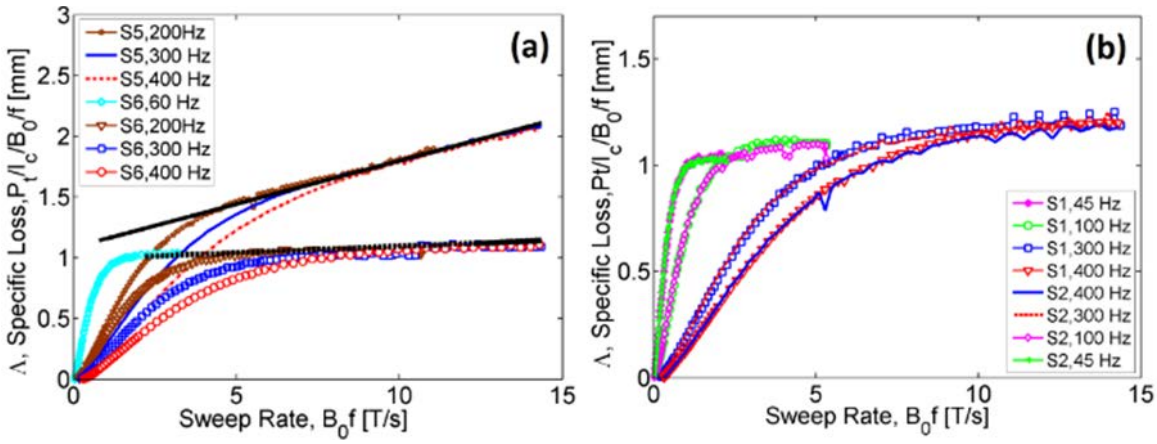

Figure 5-11. Plots of the specific loss vs sweep rate: (a) for S5 and S6, (b) for S1 and S2. The thick solid and dashed lines are linear fits to data.

Effective filament width analysis was also performed on the picosecond laser-striated samples before and after oxygenation, L10 and L11 respectively (Figure 5-12). Again there is a drastic decrease in coupling loss due to decreased slope; however, it is not completely suppressed in this case. The calculated $\mathcal{R}$ before oxygenation (L10) is 17.6 T/s, which is close to that of the mechanically striated sample. The calculated $\mathcal{R}$ after oxygenation (L11) is about 41 T/s. This is still a remarkable increase. The effective width calculated from experiment is about 0.475 and 0.45 before and after annealing, respectively. These numbers agree with the values measured by the SEM and optical microscope. There is a slight reduction in effective width after oxygenation and this could be due to the diffusion of Hastelloy elements into the REBCO material. Some of the REBCO located close to the groove probably became non-superconductive and caused groove width to be more than the width before oxygenation.

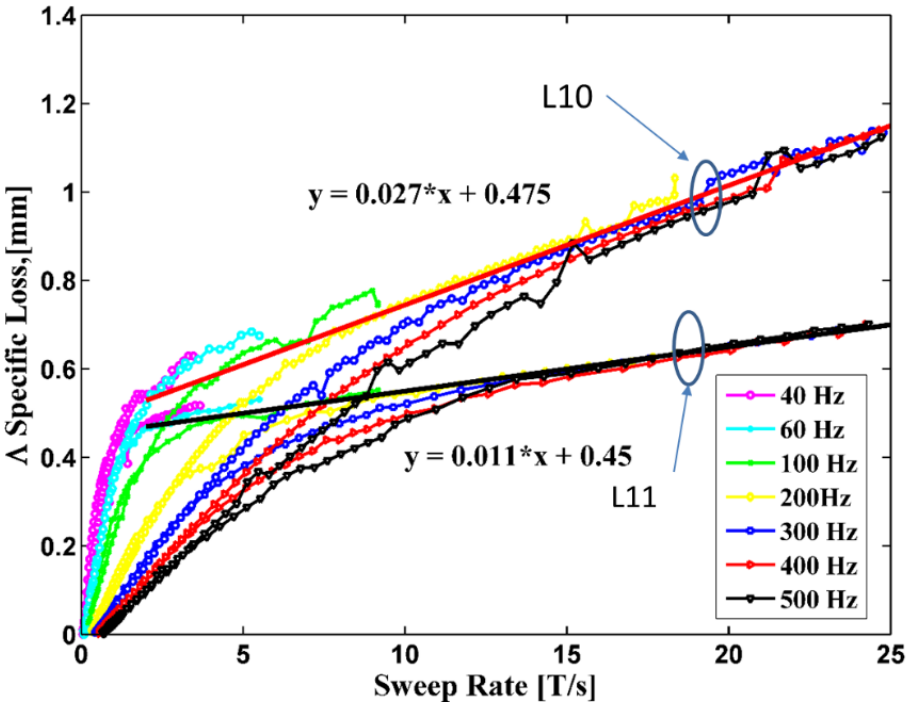

Figure 5-12. Effective width plots for the picosecond laser-striated samples before (L10) and after (L11) oxygenation.

5.3. Effect of oxygenation temperature on AC losses

Investigating the effect of oxygenation temperature on magnetization AC losses is a challenging task. Oxygenation at higher temperatures drastically reduces the I_c and it causes in reduction on the AC losses. Therefore, the I_c effect has to be eliminated from the AC loss measurements to prevent misleading interpretations. From Equation (2-22), it is seen that the AC losses are linearly dependent on I_c so normalizing the losses with I_c eliminates its contribution. Plots for loss per length normalized to current value versus the externally applied field at two different frequencies are shown in Figure 5-13. The loss performance of all of the tapes follows a similar trend. This indicates that the oxygenation temperature does not have a significant effect on the absolute loss performance. However, a small variation at higher field with respect to the frequency should be noted. At 40 Hz and a relatively high field, the highest and lowest loss values are seen in L2 and L1 respectively. At 500 Hz and relatively high field, the loss exhibited in L1 is higher than that of L2. This must be due to coupling at higher frequency (Figure 5-13). An investigation from the absolute loss figures is not practical and more measurements and alternative interpretation methods are needed to probe into this behavior further.

During the discussion of filamentization effectiveness in section 2.4, it was emphasized that the electrical coupling component of the loss can be extracted from the slope of the linear fit to the experimental data. The relative contribution of this component is an important parameter for fully optimizing the oxygenation temperature. The slopes obtained from the sample measurements are shown in Figure 5-14. To see the differences more clearly, the losses are not normalized to I_c. This does not affect the interpretation. The slope for L1 is more pronounced compared to other two samples, indicating that the highest

level of coupling occurs in this sample. The lowest slope is seen in L3, corresponding to the smallest coupling contribution. The electrical coupling loss at 200 Hz in L1 is about 2.1 and 3.4 times higher than in L2 and L3 respectively while the coupling loss in L2 is only 1.6 times higher than L3.

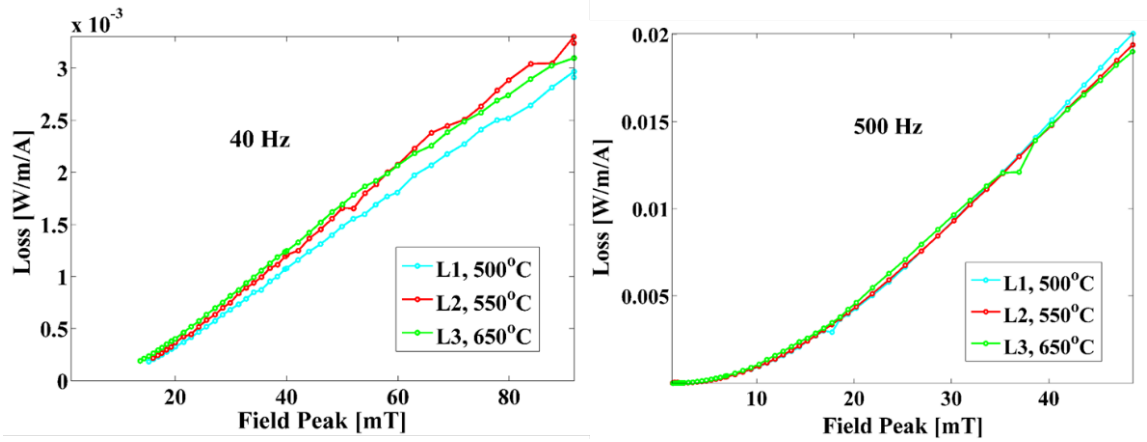

Figure 5-13. AC loss per length per current versus peak applied magnetic field at two different frequencies.

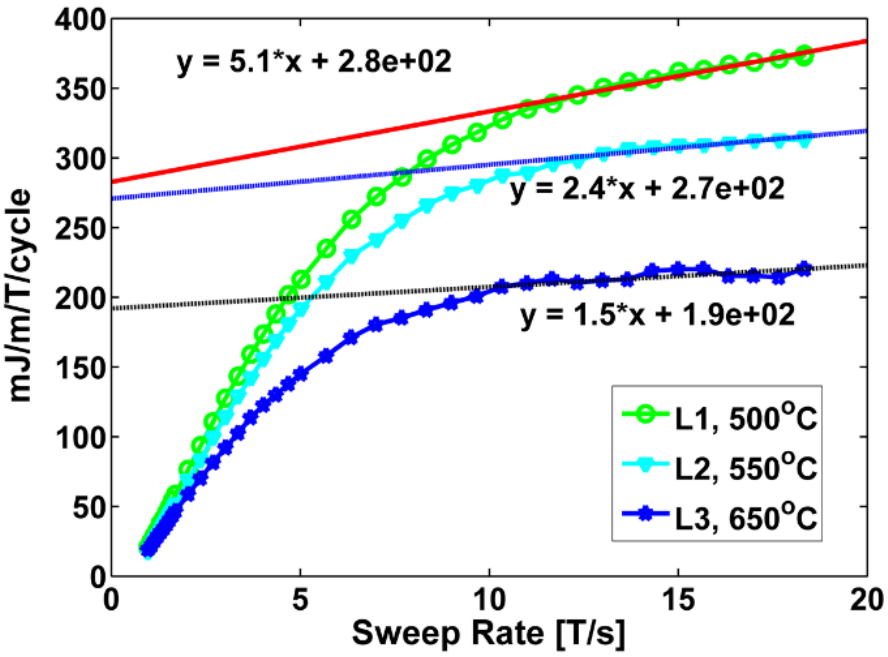

Figure 5-14. Normalized loss versus sweep rate plots at 200 Hz.

The electrical coupling loss component can also be extracted from the frequency dependent AC loses. The losses per cycle should be independent of frequency according to Equation (2-22). The total magnetization AC losses can be found as the sum of the individual contributions, $P_t=P_{mh}+P_{me}+P_{mc}$. $P_{me}=C_2(fB_o)^2$, $P_{mc}=C_1(fB_o)^2/\rho$ and $P_{mh}=C_3(B_of)$. The constants (C_1, C_2 and C_3) can be found from Equations (2-10), (2-14) and (2-22) respectively. The eddy current component of the total loss can be ignored since $P_{me} \propto$ filament width to the third power. P_t can be normalized by frequency $P_t/f=C_2fB_o^2/\rho+C_3B_o$. Since B_o is constant for a specific field the equation can be reduced to $P_t/f=C_4f\rho^{-1}+C_5$, where C_4 and C_5 are constants. This equation indicates that the slopes obtained from the frequency-dependent AC loss per cycle plots represent the electrical coupling loss if the eddy current contribution is neglected and depends only on the effective groove resistance, ρ. Shown in Figure 5-15 are the plots for frequency-dependent AC losses normalized by respective frequencies at four different field amplitudes, 30, 40, 70, and 90 mT. All samples showed frequency-dependent slopes indicating the presence of electrical coupling losses. The smallest slope was seen in L3 while the largest was seen in L1. The losses per cycle are linearly dependent on frequency. If the losses were not normalized by frequency, this dependence would be second order, consistent with Equation (2-14). Further investigation to optimize the oxygenation temperature can be performed by observing the coupling loss ratios: L1/L2=2, L1/L3=3.44, and L2/L3=1.72 at 30 mT; L1/L2=1.96, L1/L3=3.43, and L2/L3=1.75 at 40 mT; L1/L2= 1.91, L1/L3=3.07, and L2/L3=1.6 at 70 mT; and L1/L2=2.3, L1/L3=3.22, and L2/L3=1.4 at 90 mT. There is no clear trend for the frequency-dependent slope of the coupling loss with respect to the applied field. The values are more or less the

same. The averaged ratios were found to be L1/L2=2, L1/L3=3.29, and L2/L3=1.62. These numbers are almost identical to the numbers found in sweep rate analysis.

The frequency-dependence analysis was performed on seven different field values; however, for clarity only four were presented in Figure 5-15. The slopes obtained from Figure 5-15 increase with externally applied field and this increase is not linear (Figure 5-16). It is obvious from the Equation (2-14) that the applied field has a second order contribution to the electrical coupling loss. This has been confirmed by the nearly second order slope increase in Figure 5-16.

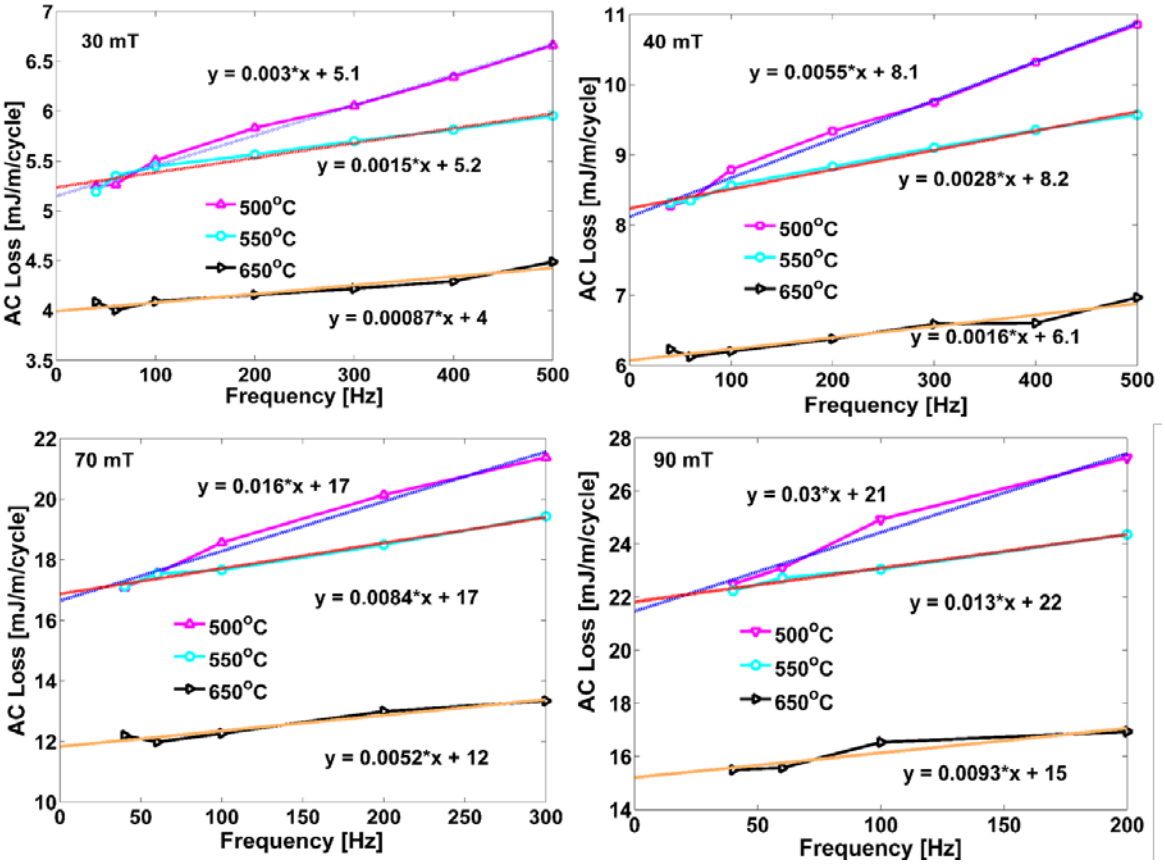

Figure 5-15. Frequency dependent normalized losses to analyze coupling contribution at 30, 40, 70 and 90 mT.

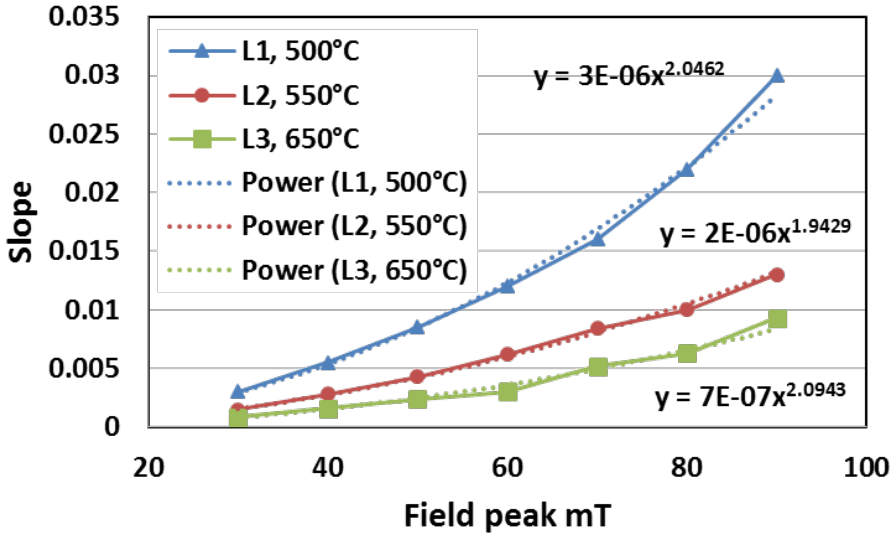

Figure 5-16. Field dependence plot of the slopes extracted from Figure 5-15.

The small electrical coupling contribution to total AC loss is not significant in samples with relatively larger filament widths; however, it needs to be closely investigated in samples with relatively small filament widths where hysteretic loss is comparable to electrical coupling loss. The highest electrical coupling contribution was seen in L1 and the lowest in L3. This probably resulted from the reduced resistivity of the groove due to the changing oxide structure. The copper islands formed on the surface of the groove (discussed in section 4.4.1.) might also create a low resistive path through the islands and underlying oxide layer; however, this effective resistivity of island-oxide structure is not close to the copper resistivity and should be very high compared to the copper resistivity. When there is complete copper deposition on the groove, the electrical coupling increases immensely (see section 5.5.). The electrical coupling contribution in L1 is doubled when compared to L2. The I_c of L1 is even higher than the reference sample, which would give erroneous information if the optimization were decided by the I_c performance alone. Given these results, the optimum temperature is found 550°C (corresponding to sample L2) since

it offers superior properties in terms of the electrical coupling contribution, the I_c degradation, and the electroplating performance.

5.4. Effect of striation and electroplating on AC losses

Before moving into AC loss results it is important to mention the loss behaviors of the striated tapes compared to the B−I and Mawatari models [81, 86]. The Mawatari model will not be referred to in the remainder of this dissertation because few studies use this model for experimental comparisons in the literature. The discussions provided in this section will outline the differences of these two models and experimental results.

In the high-field region, there is good agreement between both the models and the experimental data. However, in the low field region the experimentally measured loss of the striated samples deviates towards the calculated values for the non-striated case. This deviation has been reported in other studies [76, 88, 205] and is attributed to a non-uniform lateral J_c distribution (see Figure 5-10) and a magnetic coupling effect. The validity of the assumption that hysteretic loss is linearly proportional with respect to the width at very low fields has been addressed and analyzed with respect to field line distortions from magnetic coupling loss [76].

The loss versus applied field plots for L2 with B-I and Mawatari calculations are shown in Figure 5-17. It is clear from the figure that Mawatari model fits better at relatively low field while at higher fields they both predict the loss very well. Even the Mawatari model is calculated using the actual separation between the filaments, it diverges at low field. The groove width has to be reduced slightly to fit the experimental data perfectly (the groove width is reduced to 50 μm from 65 μm). This indicates that the magnetic coupling estimated by the Mawatari model is lower than that experimentally observed or that there

is some other loss contribution besides the magnetic coupling of the filaments at relatively lower fields. This extra loss contribution could be due to the additional electrical coupling between the filaments. The variation does not significantly affect the results because the losses are considerably smaller in this region and almost none of applications use magnetic fields this low.

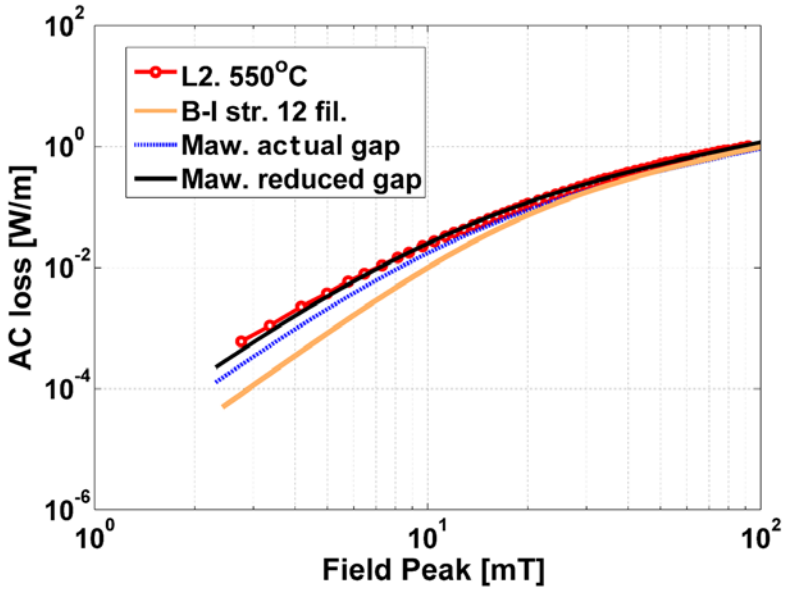

Figure 5-17. Magnetization AC loss versus applied field plots with B-I and Mawatari calculations.

5.4.1. AC losses on mechanically-striated samples

5.4.1.1. Buffer-scribed samples

In this section, the AC loss performance of the buffer scribed sample is explained briefly. The magnetization AC loss behavior of a striated sample without silver plating is shown in Figure 5-18. The B-I model calculations for non-striated and striated tapes having the same I_c are shown in the figure. With increasing field, the AC loss behavior converges towards the striated B-I model. At lower fields the behavior departs from the striated model and converges with the loss levels predicted for a non-striated sample, as described in the previous section.

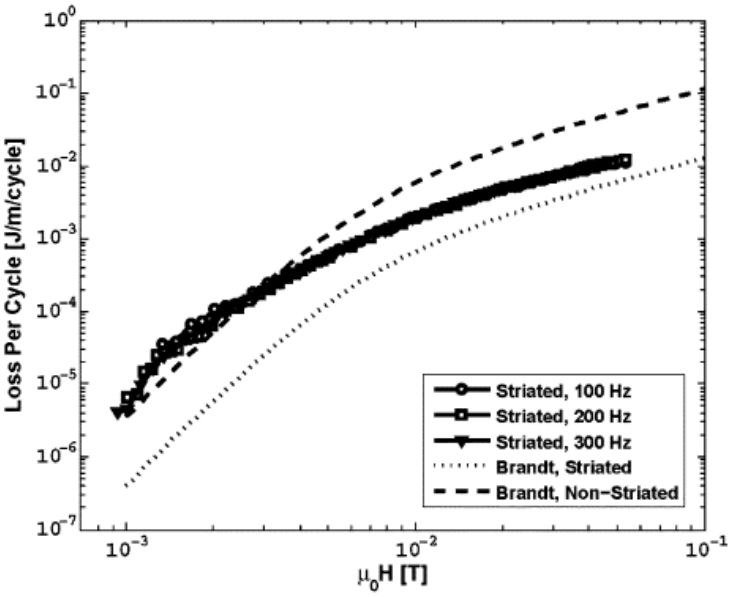

Figure 5-18. Magnetization loss performance of a striated sample. The loss per cycle is independent of frequency. The B-I model behavior of non-striated and striated samples having the same I_c is shown with dashed and dotted lines, respectively.

5.4.1.2. Silver-scribed samples

For the silver-scribed samples (one of the semi top-down methods) a comparison of magnetization AC loss per cycle as a function of field amplitude on a linear scale is shown in Figure 5-19. This summarizes the individual effects of striation and electroplating on samples S1-S4. It is apparent that the electroplating of the striated sample (S2) has no appreciable effect on total AC loss compared to the striated-only sample (S1). The loss curves almost coincide. Conversely, there is a significant contribution from the electroplating on the non-striated sample S4 relative to the completely untreated reference sample S3. The reduction in AC loss due to striation is ~11-fold before copper electroplating (close to the theoretically estimated value) and at least 13-fold after copper electroplating at relatively high field amplitudes. This additional loss reduction is likely due to the reduced eddy current loss achieved by the copper filamentization, given that the

eddy current contribution is proportional to the cube of the tape width according to Equation (2-11).

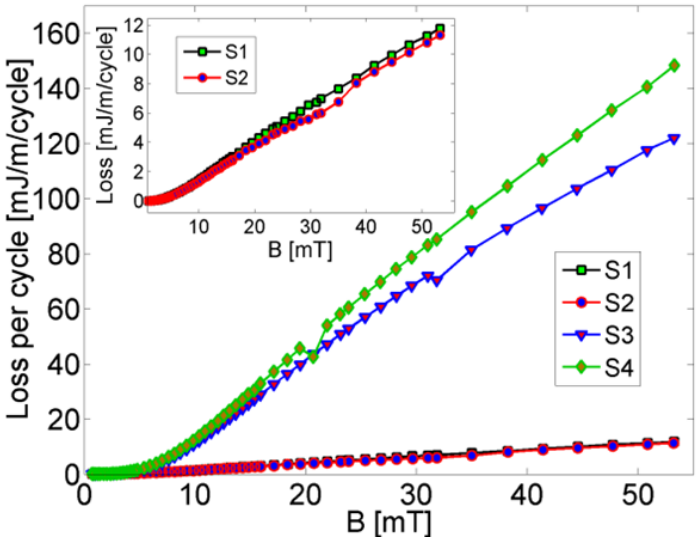

Figure 5-19. Magnetization loss per cycle per unit length vs AC external magnetic field (rms) of striated (S1, S2) and non-striated samples (S3,S4), showing the contribution of copper electroplating on AC loss. The inset shows samples S1 and S2 alone.

In Figure 5-20, the AC losses per length, [*W/m*], of samples S1-S4 are compared as a function of frequency at different AC rms field magnitudes. From Figure 5-20a the magnetization loss is linearly dependent on frequency, which indicates that the electrical coupling contribution is negligible in the striated samples both before and after electroplating. This demonstrates that the present striation/electroplating approach does not result in any appreciable additional losses. However, as can be seen in Figure 5-20b the copper electroplating on the non-striated sample S4 results in additional AC loss. A comparison between control samples S4 and S3 in Figure 5-20b reveals a possible additional eddy current contribution present in the electroplated control sample S4 compared to the completely untreated sample S3.

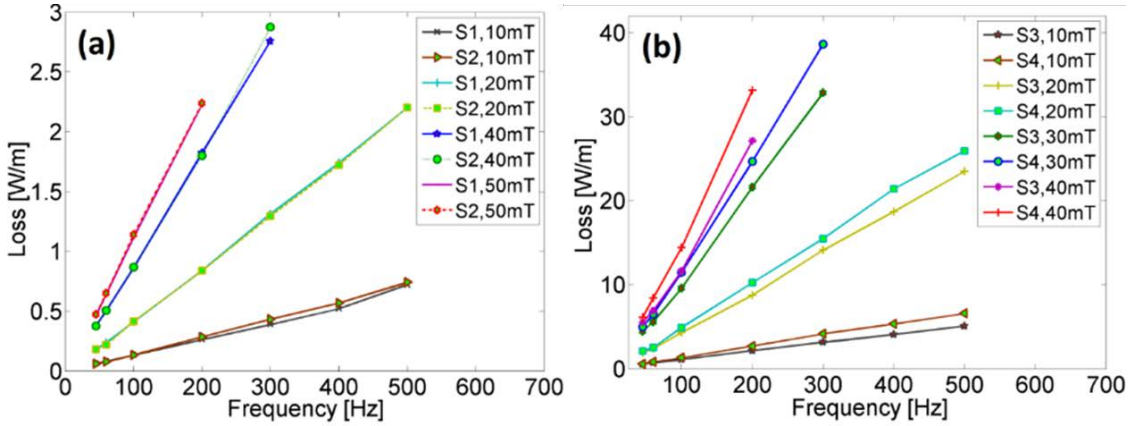

Figure 5-20. Magnetization loss vs frequency at different applied AC field (rms): (a) for S1 and S2, (b) for S3 and S4.

The magnetization AC losses per cycle per length, [*J/m/cycle*], versus the applied AC field for the striated S1 and S2 samples are presented in Figure 5-21, and are compared with the limits predicted by the B-I model on a log scale. The dashed line labeled "B-I, Str." is calculated for a 12-filament sample and the continuous line, labeled "B-I, Non-Str." is calculated for a non-striated reference sample. Both samples have the same AC loss performance indicating that the contribution of the electroplated copper on S2 has no effect. Sample S6 shown in Figure 5-22 also follows the same trend, which is an indication that the striation procedure is reproducible since the processing conditions for S1 and S6 were identical. It is important to note that the magnetization AC losses of striated samples S1, S2 and S6 are linearly dependent on frequency and that the curves in Figure 5-21a and b coincide after normalization to their respective frequencies (loss per cycle). This is an indication that the main contribution to magnetization AC loss is hysteretic.

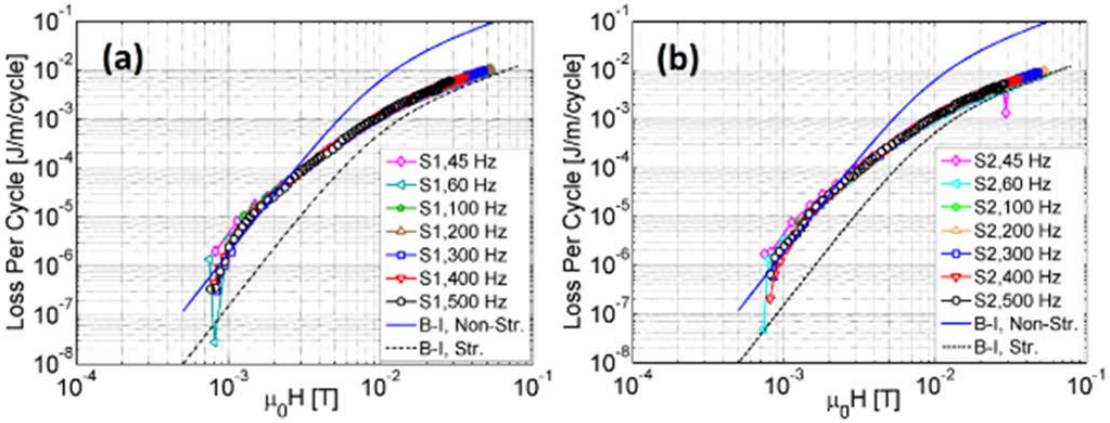

Figure 5-21. Magnetization loss vs AC external magnetic field (rms) of striated samples (a) before and (b) after copper electroplating (samples S1 and S2, respectively).

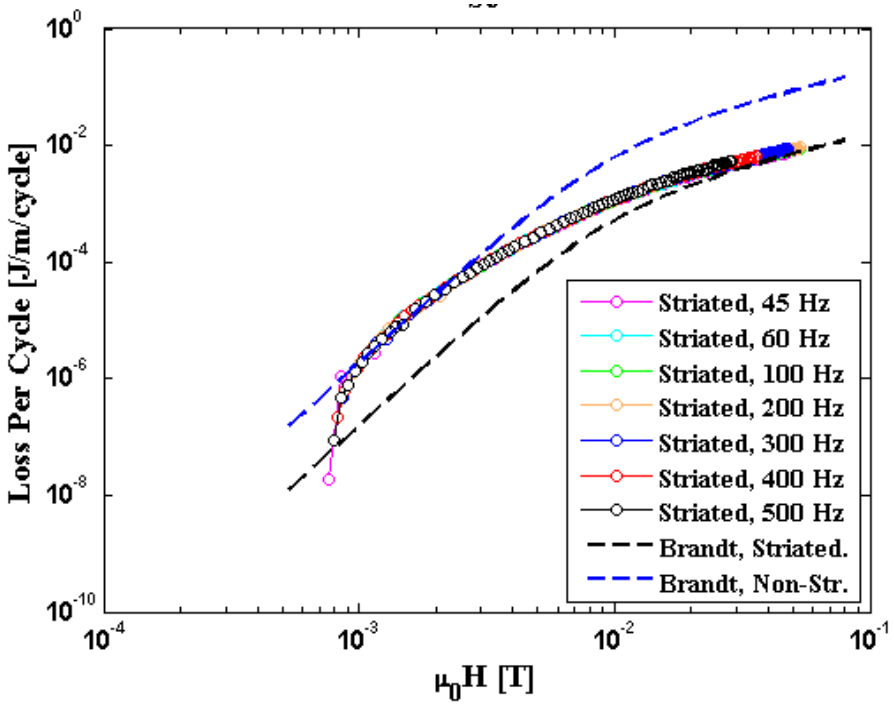

Figure 5-22. Magnetization AC loss versus applied field (rms) for S6.

5.4.2. Femtosecond laser-striated samples

AC losses of the samples striated by the femtosecond laser were measured and the results are compared with B-I model in Figure 5-23 at three different frequencies. In this analysis, the AC loss behavior of different filament numbers were also investigated. L2 was a 12-filament tape while L7 was 24-filament and L6 was 48-filament. Very similar behavior is observed from all of the measurements. The results are in good agreement with

the B-I model at relative high field (above the penetration field) while at a relatively low field, it deviates as discussed in the previous sections. One important conclusion from the figures is that with increasing frequencies, the B-I model describes the loss behavior of L12 well even at relatively low field. This can be attributed to reducing losses by increasing the frequency below the penetration field for non-striated samples as discussed in section 2.5.

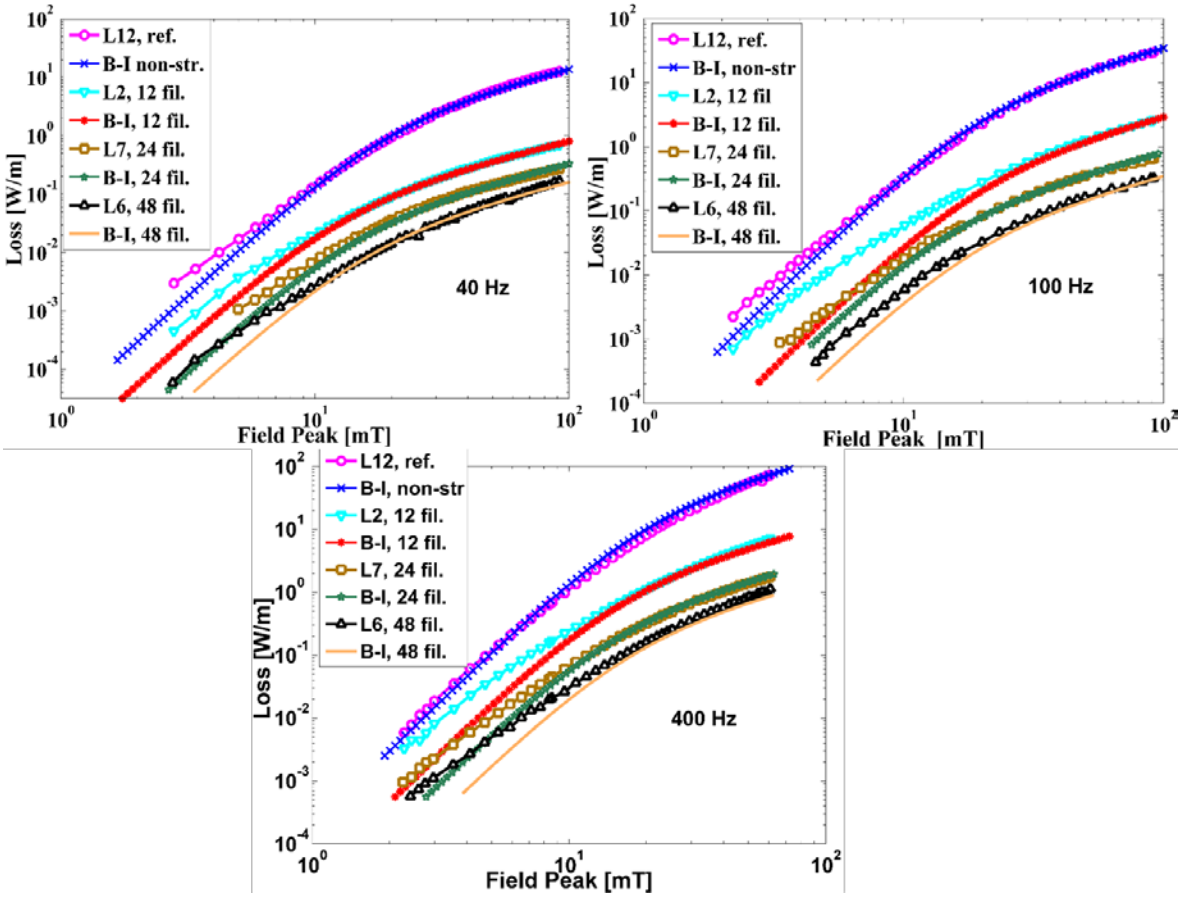

Figure 5-23. Field dependent AC loss measurements of samples L2, L6 and L7 at 40, 100 and 400 Hz respectively and their respective B-I estimations.

In order to evaluate coupling loss, the frequency-dependent loss measurements are provided in Figure 5-24 at two different externally applied field values. The related slopes are also shown for samples with different filament numbers.

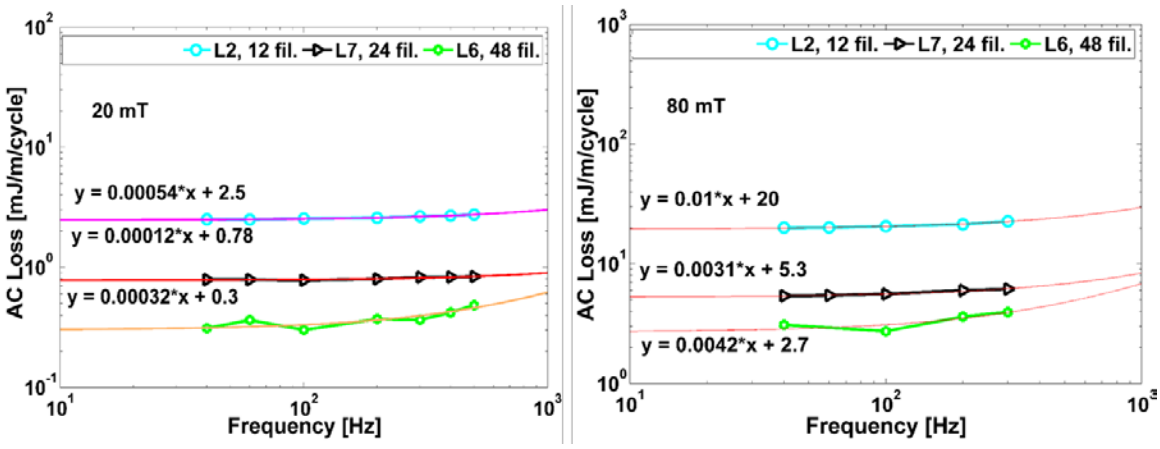

Figure 5-24. Frequency-dependent normalized AC losses to analyze the coupling contribution at 20 and 80 mT.

After the slopes were obtained by linear fitting, the loss ratios were used to calculate the relative electrical coupling loss contribution. The highest electrical coupling contribution is seen in sample L2 while L7 has the lowest electrical coupling component. Since the electrical coupling loss behavior of L2 was discussed, this will give us insight into the electrical coupling loss of samples with higher filament numbers. The electrical coupling loss ratios are: L2/L7=4.5 and L2/L6=1.7 at 20 mT and and L2/L7=3.22 and L2/L6=2.4 at 80 mT. By averaging these loss ratios, the electrical coupling loss in L2 is found to be 3.9 times higher than L7 and 2.05 times higher than L6. By increasing the number of filaments, the electrical coupling losses should increase. This is valid when comparing L6 and L7 despite being oxygenated at different temperatures and might be the reason for the higher electrical coupling loss in L6. However, this is not the case when L2 and L6 are compared. L2 and L6 are oxygenated at the same temperature and there should not be any oxygenation temperature effect on the coupling loss. For this reason, it appears that increasing the filament number does not significantly increase the coupling loss while oxygenation temperature still plays important role in the coupling behavior.

A plot of the loss function $\Gamma = P_h / (\mu_0 H_a)^2 = P_h / fB_0^2$, versus AC field amplitude is given in Figure 5-25 for three samples: L2, L6 and L7. The losses behave differently above and below the penetration field as explained in section 2.3.3. Because of these different loss behaviors, the penetration field can be found by normalizing the loss with B_0^2. The full-flux penetration field was found experimentally to be 32 mT and theoretically to be 29 mT for the non-striated sample L12. For the 12-filament L2 tape, it was found to be 20 mT experimentally and 27 mT theoretically. For the 24-filament L7 tape, it was found to be 21 mT experimentally and 21 mT theoretically while for the 48-filament L6 tape these values were found to be 25 mT experimentally and 26 mT theoretically. These results show that with increasing filament number the theoretical full-flux penetration field has better agreement with the experimental ones. Increasing number of filament affects the magnetic field distribution and magnetization of the filaments and causes a reduction in the magnetic coupling loss contribution. Ideally the full-flux penetration field increases with increasing filament number. However, the I_c effect can change this trend. The penetration field increases with increasing I_c. For instance, the experimental penetration fields for L2 and L7 are almost the same; however there is a significant difference when compared to L6.

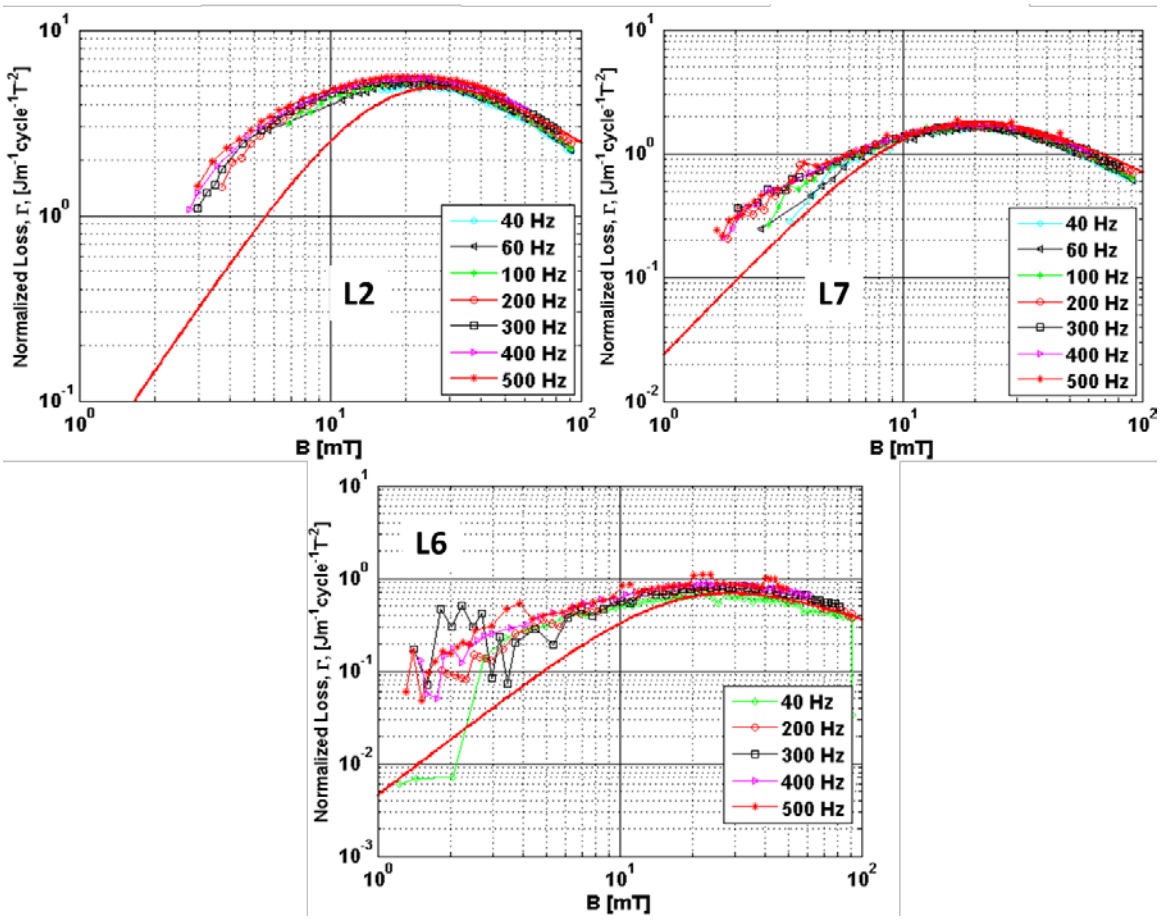

Figure 5-25. Plots for the determination of full-flux penetration fields for L2, L6 and L7.

5.5. Effect of copper stabilizer thickness on AC losses

Figure 5-26 displays a comparison of the field-dependent AC loss measurements at 40 and 300 Hz conducted on the electroplated samples with different configurations and thicknesses (fully-decoupled, partially-coupled and fully-coupled). In the figures, the solid lines represent the B-I model of a non-striated sample with an I_c of 225 A and for a striated 12-filament sample with an I_c of 195 A.

The data from the decoupled samples (M1, M2 and M3) superpose onto each other indicating that the stabilizer thickness effect on AC losses is negligible. There is a significant Cu stabilizer loss contribution in the non-striated tape as discussed in 5.2. An AC loss reduction of almost 15-fold was observed in the fully-penetrated field regime for

the three de-coupled samples (M1, M2 and M3) at all frequencies compared to the non-striated sample M7. This reduction agrees well with the theoretical estimation. Similar to the previous samples, a magnetic coupling effect is present in these samples at relatively low field values. The reference sample has better agreement with the experimental data in the entire field regime at 300 Hz compared to 40 Hz. There is a slight AC loss increase for the decoupled samples at 300 Hz and relatively high field amplitudes when compared with the striated B-I model. The increase at a higher frequency could be the result of electrical coupling.

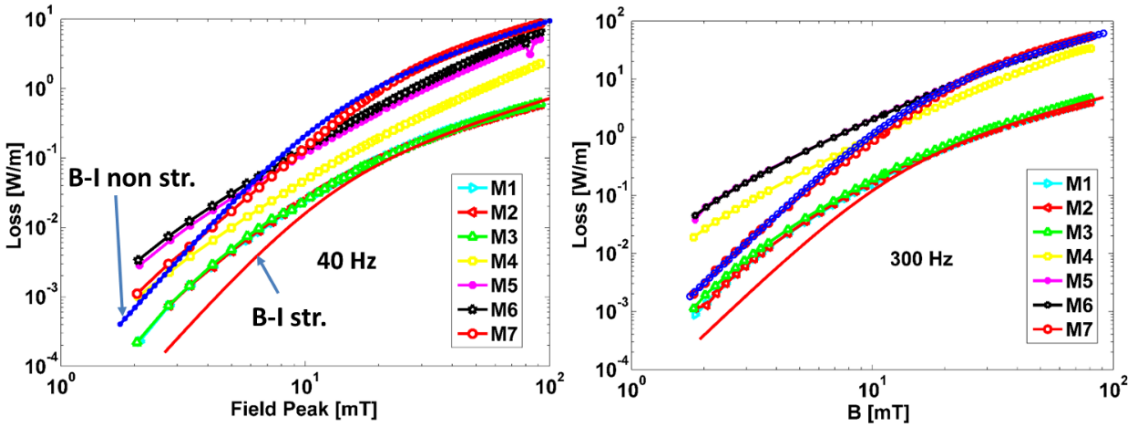

Figure 5-26. Magnetization AC losses versus applied AC field of the electroplated samples at two different frequencies. The solid line is for the striated Brandt-Indenbom (B-I) model using an I_c of 195 A while the dashed line is for a non-striated B-I model using an I_c of 225 A.

The losses in the completely-coupled samples (M5 and M6) are higher than that in the non-striated sample (M7) at low fields. These higher losses are attributed to the absence of a resistive barrier to interrupt the transverse current flow in the completely-coupled samples. This significantly increases both the electrical coupling component in addition to the magnetic coupling. This electrical coupling component is prevented by the highly-resistive barrier in the decoupled samples.

The results for the partially-coupled sample, M4, behaves in a manner between the decoupled and completely-coupled samples. The electrical coupling loss increases the losses closer to a completely-coupled sample at 300 Hz. The losses in M6 are higher than M5 at 40 Hz (Figure 5-26) which could be due to the copper stabilizer in M6 being slightly thicker (~36 μm) than the silver thickness in M5. At 300 Hz, the loss behavior of the two samples coincides in spite of the different material on the grooves (Figure 5-26). This clearly indicates that with increasing frequencies the eddy current and coupling contribution dominates over the thickness contribution to total AC losses.

Plots of the AC loss per cycle as a function of frequency at two different field amplitudes are presented in Figure 5-27. The values of loss per cycle in the partially-coupled sample increase with frequency indicating the presence of an electrical coupling loss influence at all three field amplitudes. The loss values of these samples converge to that of the non-striated reference sample in the high-frequency range. This clearly indicates that the effectiveness of striation is lost at high frequencies in the partially-coupled samples. The partially-coupled configuration can be still used in low-frequency applications. There is a nearly six-fold reduction in AC loss around 50 Hz. The loss behavior of the fully-coupled samples (M5 and M6) are almost identical except for the influence of stabilizer layer thickness in M6. This could be a result of eddy current contributions to the total AC losses at low frequencies. The losses of the fully-coupled samples increase quickly in the low frequency range and saturate close to the values for a non-striated sample at high frequencies.

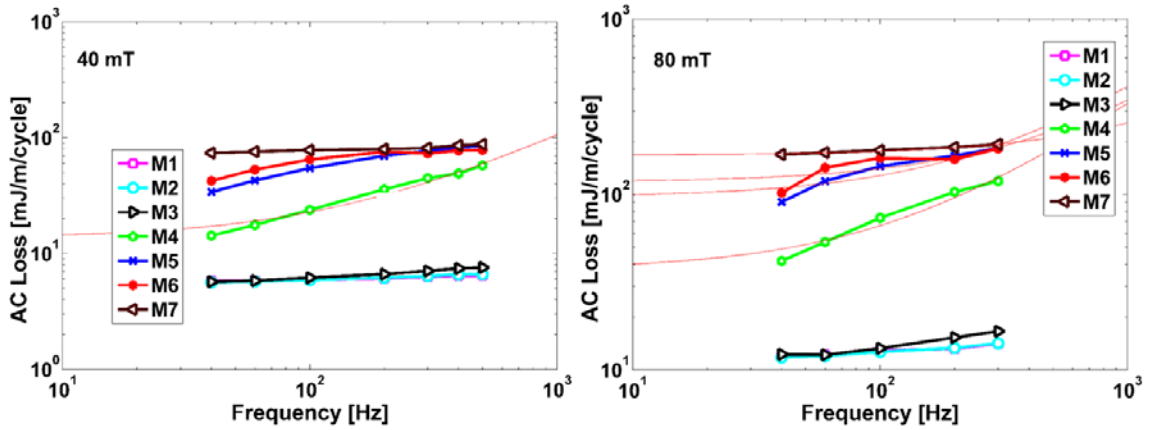

Figure 5-27. Magnetization AC loss as a function of frequency at three different field amplitudes, 40 and 80 mT.

The AC losses per cycle for the fully and partially-coupled samples are not linearly depend on frequencies. For this reason, the previous interpretation cannot be applied to these samples. Linear fit lines, shown in Figure 5-27 for 80 mT, were added to show the poor agreement between the fits and experimental data. In these samples, the eddy current contribution is probably significant and as a result does not obey the linear frequency dependency. Because of this, the loss ratios on these samples were investigated (Figure 5-28). The AC loss of the non-reference M7 sample is divided by M4, M5, and M6 in order to see the overall loss reduction. The loss ratios decrease with increasing frequency and at 500 Hz, the loss ratio for all three samples converges indicating that the loss performances of a striated and non-striated sample are equal. However, at 40 Hz there is still significant loss reduction in the case of the partially-coupled sample, M4. This sample can still be used in some cable applications even with the partially-coupled configuration. By examining the loss ratios for the completely-coupled M5 and M6 samples, the loss reduction is found not to be satisfactory even at low frequencies and these samples are unlikely to be used in any low AC loss applications.

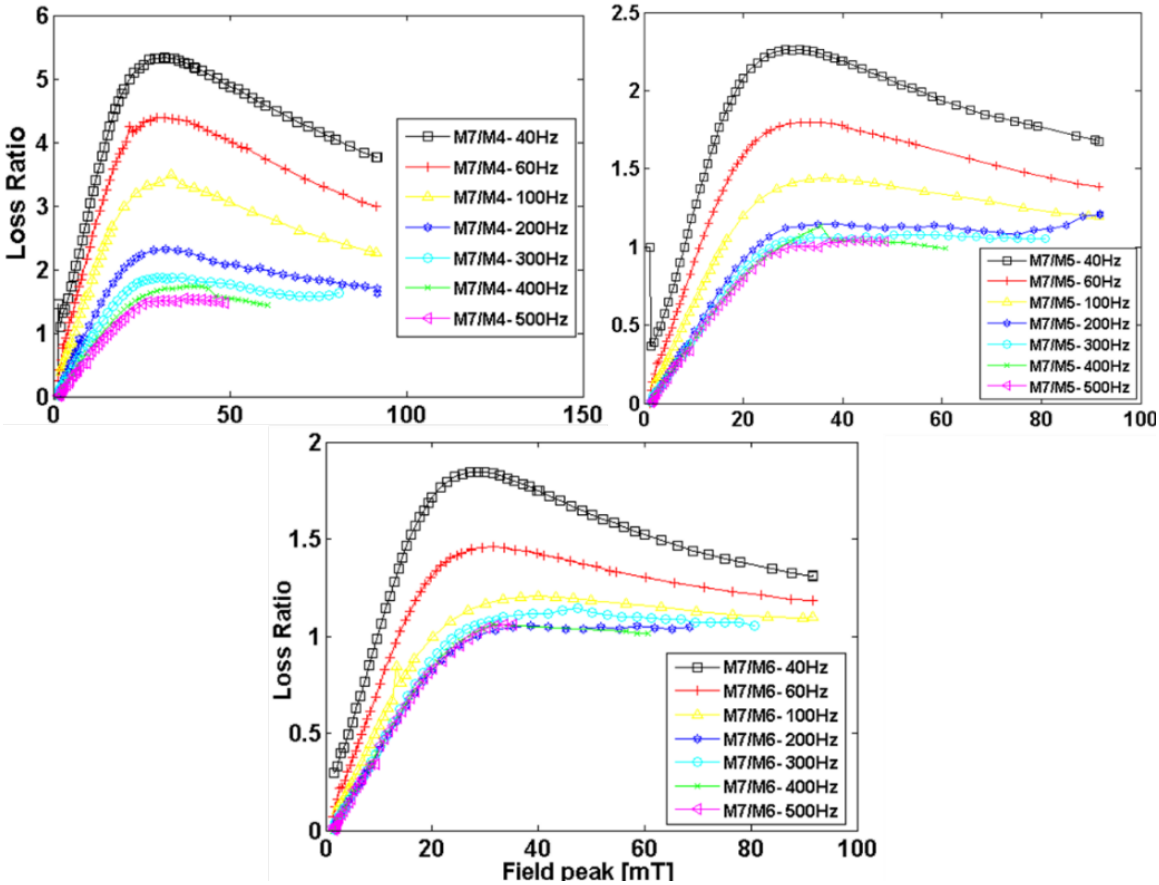

Figure 5-28. Loss ratios (the loss of non-striated reference sample is divided by M4, M5 and M6 respectively) versus applied field.

5.6. Effect of filament number on AC losses

The loss ratios represented by the inverse L3, L6 and L7 AC losses normalized to the L12 AC loss are provided in Figure 5-29 along with their respective B-I predictions. At ~60 mT and 100 Hz the losses are reduced by at least 80, 40 and 16-fold in the 48, 24 and 12-filament tapes respectively. These are the highest reported values of AC loss reduction in coated conductors fabricated with a thick copper stabilizer. The B-I calculations agree with these measured AC loss ratios indicating that the losses are hysteretic in nature with negligible contributions from other loss mechanisms above the penetration field. The magnitude of the AC loss reduction is larger than that expected from a width reduction and may be due to a reduction in the I_c of the multifilamentary tapes. In

B-I calculations the groove width and I_c reductions have been taken into account. Fluctuations in the loss ratio of L12 to L6 are due to the small loss magnitude measured in L6. For confirmation purposes, the frequency dependence loss ratios are presented in Figure 5-30 with similar loss reductions to those obtained from the field dependent loss ratios. Again the fluctuations in the loss ratio of L12 to L6 are due to the small loss magnitude measured in L6. At 80 mT, the loss ratio is slightly higher compared to 40 mT and it is independent of frequency. This is because of the slight magnetic coupling effect that presented at low field values.

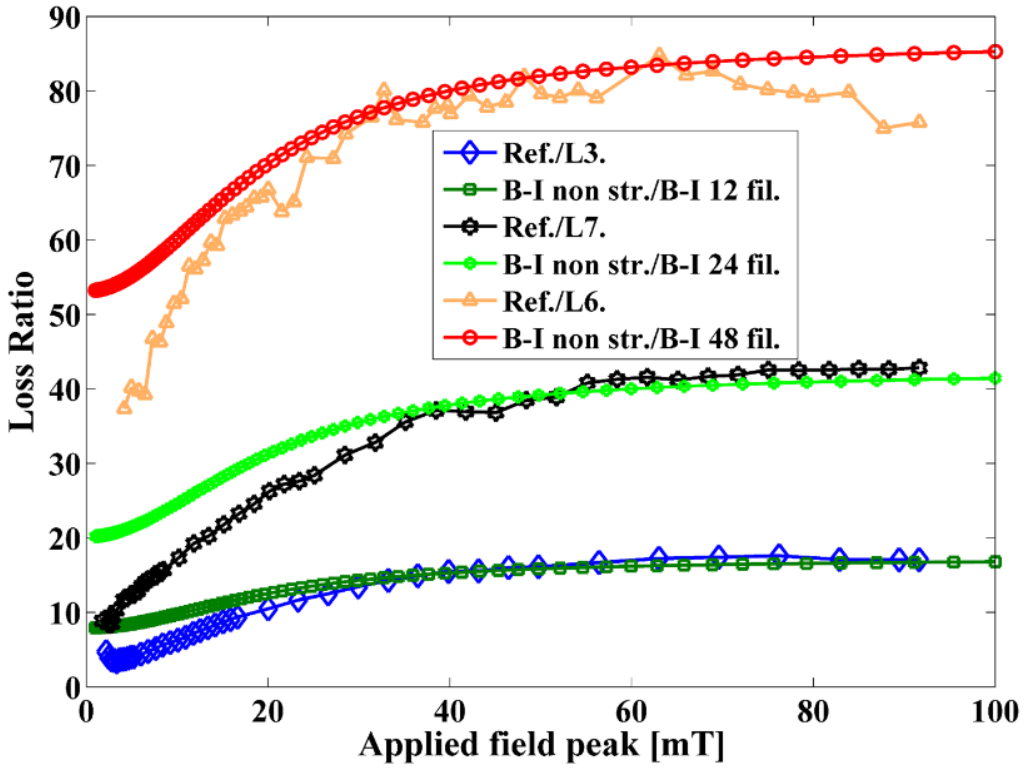

Figure 5-29. Loss ratios represented by the inverse of the AC losses of L2, L6 and L7 normalized to the AC loss of L1 in AC magnetic fields up to 100 mT at 100 Hz.

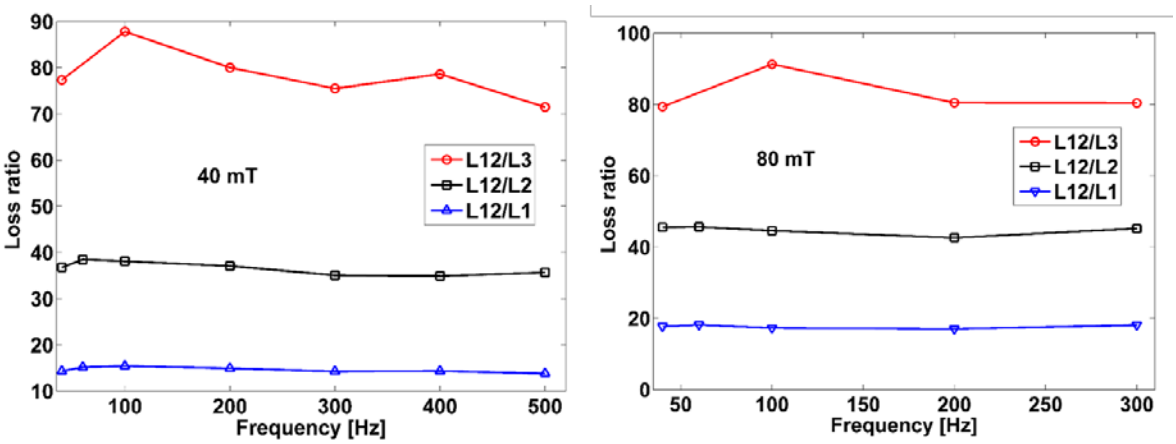

Figure 5-30. Frequency-dependent loss ratios for samples with different filament numbers at two particular fields.

The required filament width for AC loss applications should be found by considering a conventional wire in an actual application. Copper is most widely used conductor for electrical application. Current transfer through a conductor such as copper generates heat. This process is called Joule heating or resistive heating and can be written in power per current per length as

$$\frac{P_{\text{Joule}}}{IL} = \frac{IR}{L}. \tag{5-1}$$

By substituting $R = \frac{\rho L}{\text{Area}}$ into the equation

$$\frac{P_{\text{Joule}}}{IL} = \rho J. \tag{5-2}$$

The operational current for a copper wire is typically $1\text{x}10^6$–$3\text{x}10^6$ A/m^2 [206]. Taking the minimum value of 1 MA/m^2 and the copper resistivity of $2.97\text{x}10^{-8}\Omega$m (found in the section 2.2.2.2.) the resistive loss in this conductor can be calculated to be 29.7 W/kA/m. In the case of alternating current with an amplitude of I_{max}, the average power loss per length per current [P/ I_{max}/m] is ~15 W/kA/m with no cooling. Cooling efficiency can be taken as 1/15 for liquid nitrogen [60]. The equivalent loss for a superconductor cooled at liquid nitrogen

temperatures is ~1 W/kA/m. In order for HTS coated conductors to replace copper conductors in AC applications the losses in the former have to be limited to an acceptable level. Taking the resistive loss in a copper wire as a benchmark, an acceptable AC loss target in HTS coated conductors would be 1 W/kA/m. After normalizing the losses with respect to the I_c this target was met by several of the samples fabricated in this study: L12, L3, L7, and L6, up to field values of 0.01, 0.02, 0.035 and 0.075 T respectively at 100 Hz. This result indicates that only 48-filament coated conductors with a structure similar to L6 can meet an AC loss criterion of 1 W/kA/m in operational field values (100 mT). These findings indicate that substantially narrow filaments need to be fabricated for applications where AC losses are an important factor. Filaments ~100 μm wide would be required to meet the AC loss target of 1 W/kA/m in a field of ~0.2 T at 100 Hz. The reported process of laser scribing followed by selective electroplating can easily be adapted to fabricate these narrow filaments with a thick copper stabilizer.

5.7. Adhesion improvements

The mechanical properties of CCs along the c-axis are weak and have to be improved to incorporate CCs into applications. The REBCO layer has the weakest mechanical properties in 2G-HTS CCs, causing problems under stress. The results presented in this section are related to improving the mechanical properties (adhesion) of the conductors along the c-axis. The adhesion tests were performed using the T peel test configuration; therefore, the stress state was predominantly sheer in nature.

The adhesion of a thin film is affected by several factors. The most important factors are the film thickness, film composition, and processing temperature. In this part of the dissertation, the composition of the REBCO superconductor layer is modified to

obtain better adhesion strength. The goal was to modify the defective structures in the REBCO matrix. For this purpose, the standard REBCO composition of Y or Gd was replaced by Sm. Initially the REBCO samples with Sm were prepared to improve the in-field performance. However, it was realized that samples with Sm have profoundly fewer defects compared to samples with the standard composition. The precursor mole ratios of the samples are as follows: 0.075:1.2:0:0:2:2.5 and 0.075:0:0.6:0.6:2:2.3 of Zr:Sm:Gd:Y:Ba:Cu. A TEM cross-section of the samples with compositions of GdYBCO and SmBCO are shown in Figure 5-31a and b respectively. In the standard sample (GdYBCO) there are considerable in-plane defects such as RE_2O_3 and BZO nanorods while the sample with Sm (SmBCO) has few rods and almost no oxides.

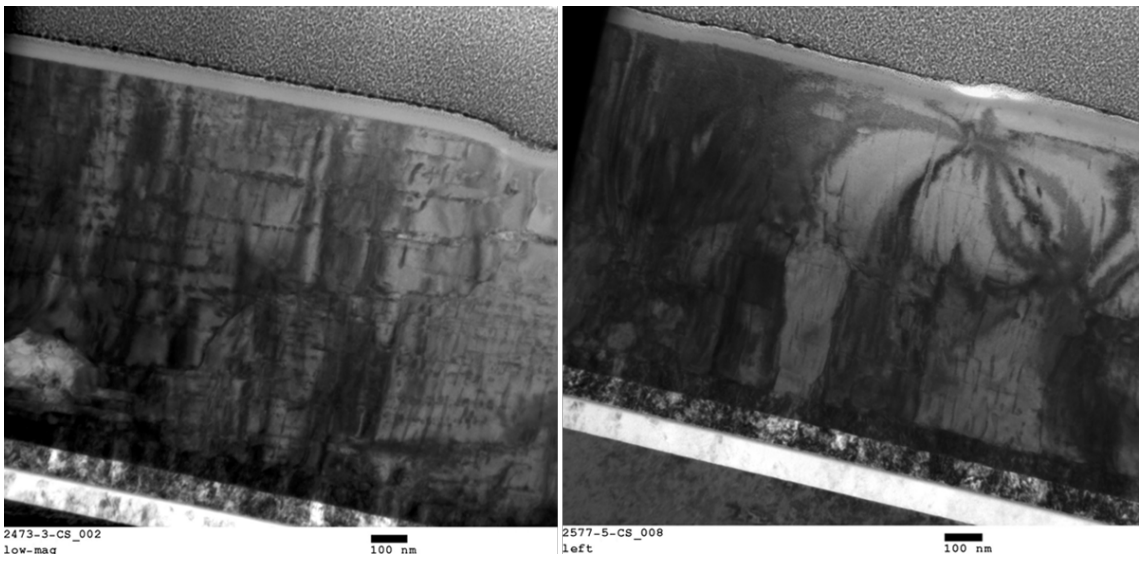

Figure 5-31. TEM cross-section of the samples GdYBCO (left) and SmBCO (right).

The sample without Sm also has huge CuO_x particles in the matrix (Figure 5-32). In order to identify these particles an EDX analysis was performed on the related regions. From the EDX the elements in the particles were identified to be CuO_x.

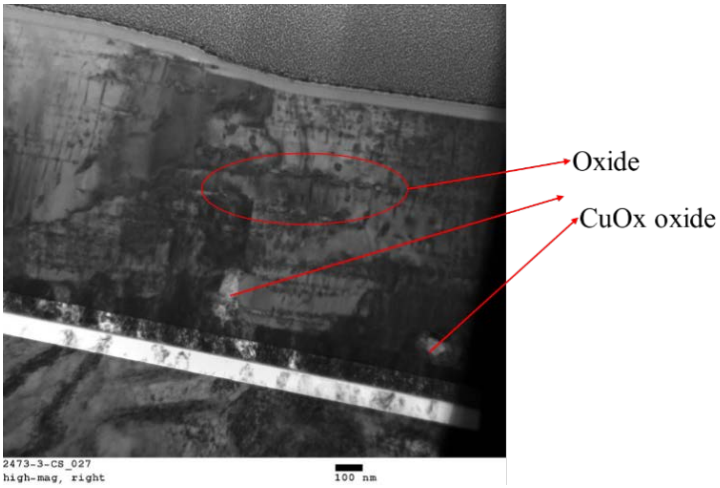

Figure 5-32. TEM cross-section and EDX analysis of a standard sample showing the defects including the CuO_x.

Higher magnification images of the samples with and without Sm showed that the Sm sample has fewer defects like stacking faults and $BaZrO_3$ (BZO) nano rods while the standard sample has many including RE_2O_3, BZO nano rods, and CuO_x (Figure 5-33).

Figure 5-34 shows the overall picture of the standard and Sm samples. It is very clear that the standard sample in-plane defects are dominant and also impede the growth of nano rods along the c-axis while in the Sm sample the nano rods along the c-axis grow longer and have fewer in-plane defects.

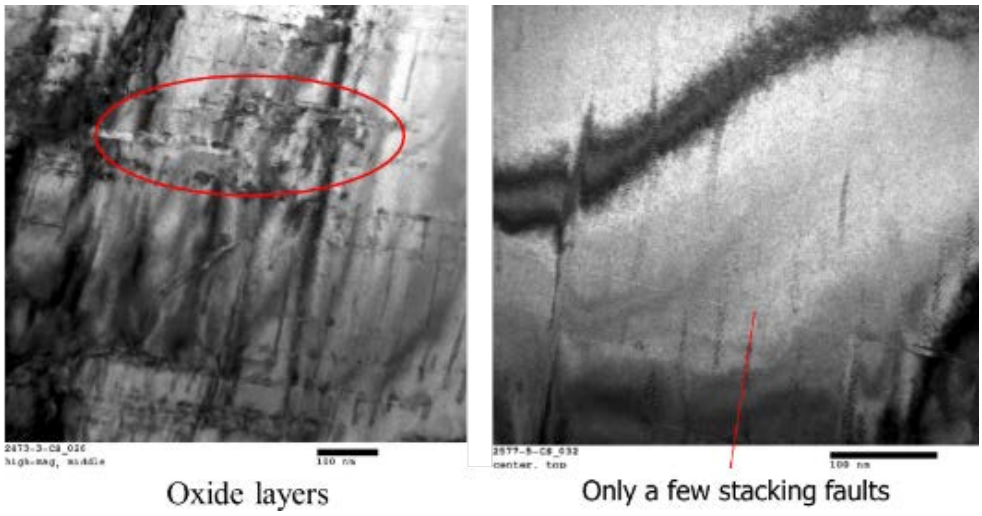

Figure 5-33. High magnification images of the (left) standard and (right) Sm samples.

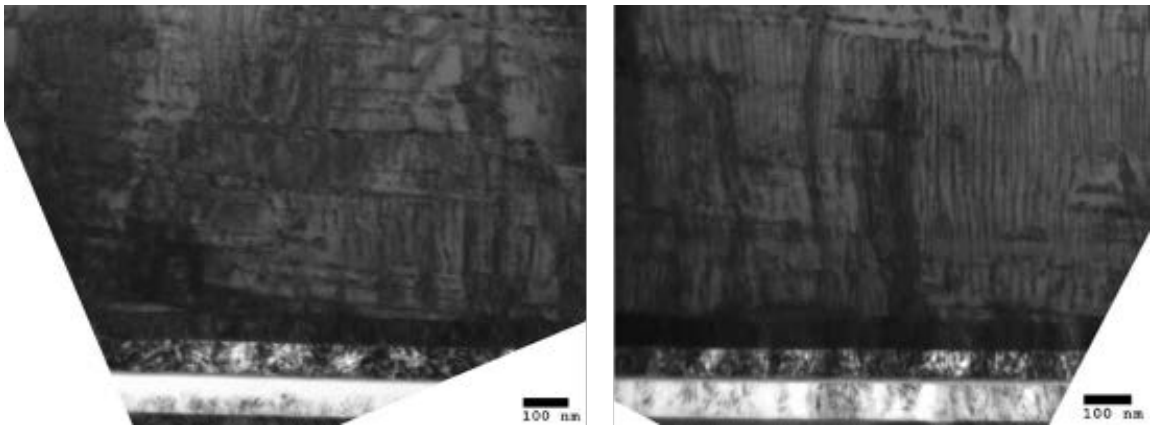

Figure 5-34. Low magnification TEM cross-sections of the (left) standard and (right) Sm samples.

T peeling tests were performed on samples with different mole ratios of Sm and a standard composition sample. The processing temperature is 975˚C for all the samples. The peeling test results are given in Figure 5-35a. A significant increase in adhesion strength is observed in Sm samples compared to the standard sample. The mean adhesion strength of the samples is shown in Figure 5-35b. The various Sm samples follow a similar trend while the standard sample has a considerably lower peeling strength.

Photographs of the samples with a 2.5 Cu mole ratio are shown in Figure 5-36. A very smooth surface following peeling can be seen clearly in Figure 5-36a. Unfortunately, the deposited copper for the second sample could not withstand the force exerted by bounding and was torn during the test (Figure 5-36b). For this reason, the peeling area became smaller with increased displacement and the peeling strength gradually reduced.

Optical microscope images are presented in Figure 5-37 for the standard sample, and the Sm samples with a 2.4 and 2.5 Cu mole ratio. Determination of the peeling locus for the standard composition sample is very complex. The peeling locus consists of buffer/REBCO interface regions and REBCO cohesive delamination. It is extremely difficult to identify whether the peeling mode is interfacial or cohesive because of the complexity. For this reason, this mode of de-cohesion is called a mixed-mode de-cohesion.

The samples with Sm have one predominant peeling locus. This peeling mode can be identified as interfacial de-cohesion or debonding and is purely related the interfacial bonding energy between the sputtered silver protective layer and the REBCO layer.

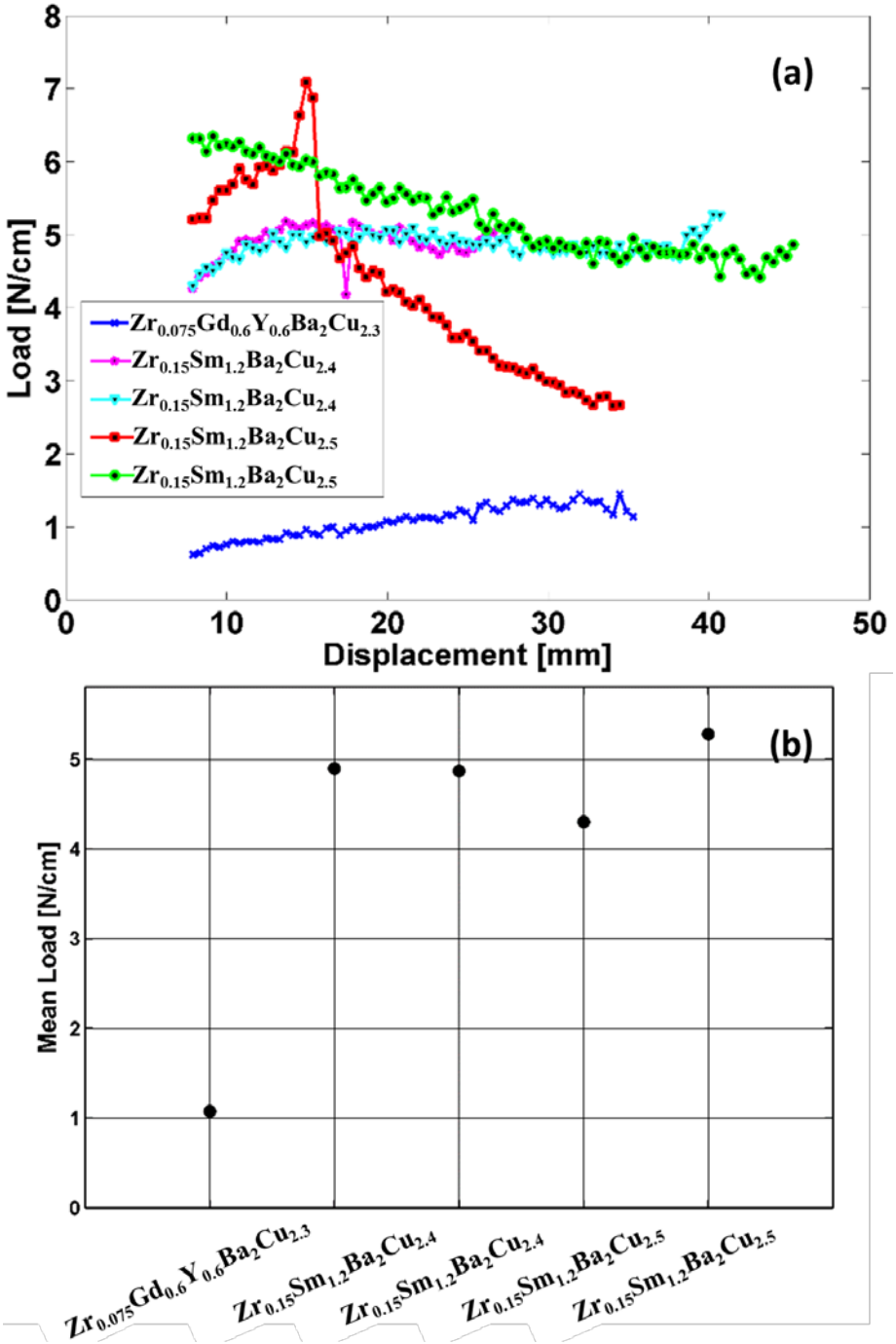

Figure 5-35. (a) Load-displacement curves for samples with different compositions and (b) mean peeling strength.

Figure 5-36. Photographs of the samples with a 2.5 Cu mole ratio. (b) Electroplated copper was torn in the second sample.

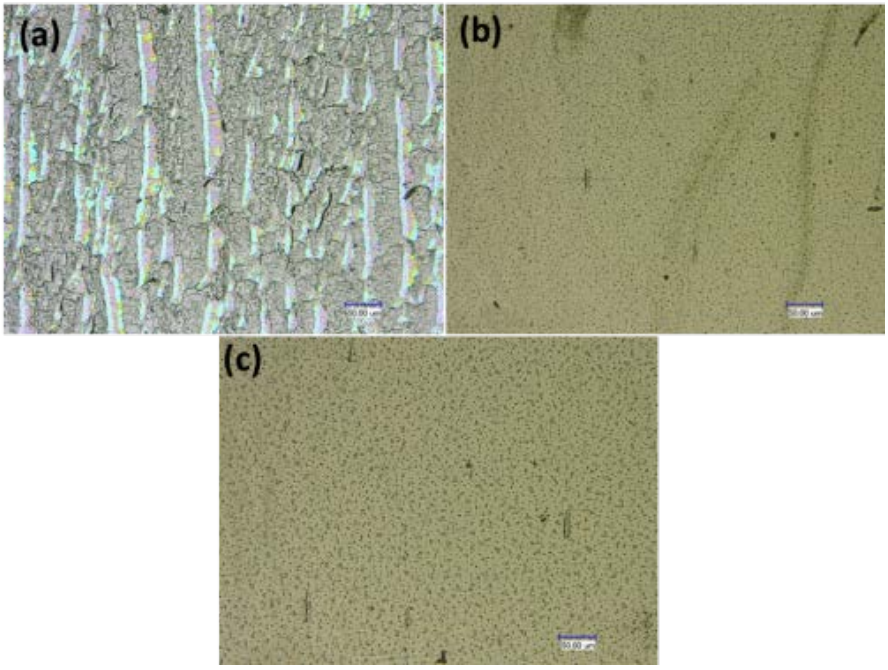

Figure 5-37. Optical images of the peeled samples with different compositions. (a) standard composition, (b) Sm sample with a 2.4 Cu mole ratio and (c) Sm sample with a 2.5 Cu mole ratio.

SEM images confirm same peeling modes (Figure 5-38). Based on these results, the silver to REBCO interfacial adhesion energy is higher than the mixed mode de-cohesion. By modifying the composition of the REBCO matrix, the interfacial adhesion of the REBCO/buffer was strengthened and yielded only interfacial de-cohesion.

To test the reproducibility of these results, another set of samples were prepared with the same composition and the same processing temperature. The results for these samples are provided in Figure 5-39.

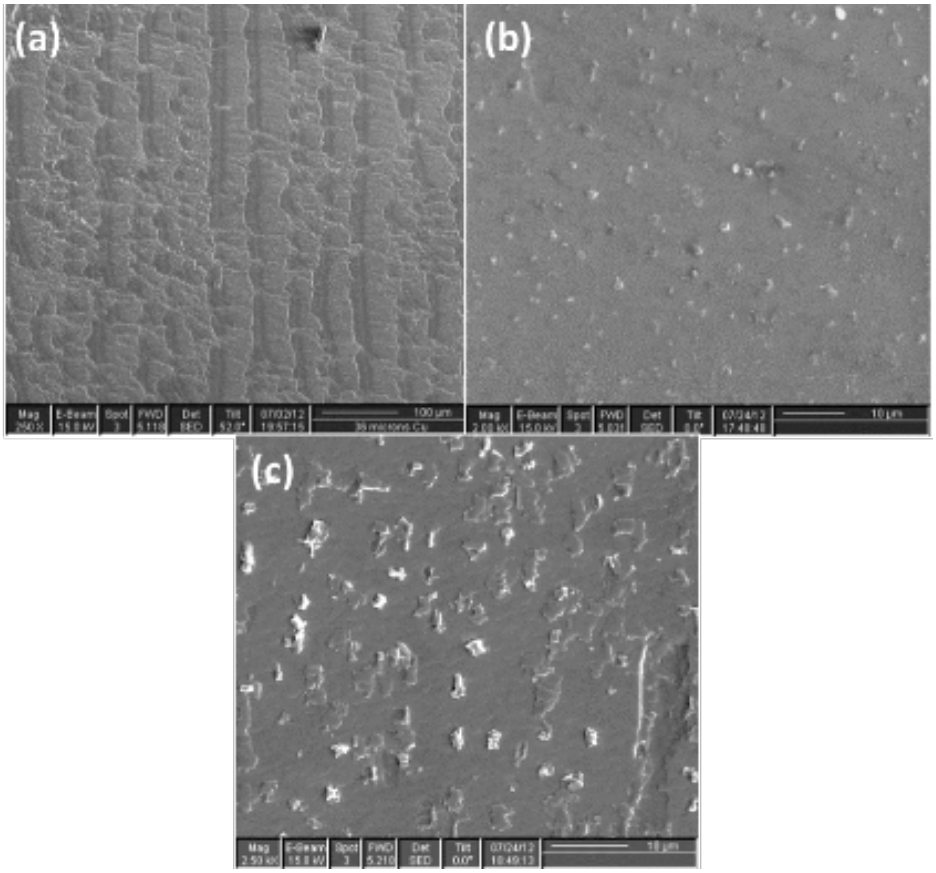

Figure 5-38. SEM images of the peeled samples with different compositions. (a) standard composition, (b) Sm sample with a 2.4 Cu mole ratio and (c) Sm sample with a 2.5 Cu mole ratio.

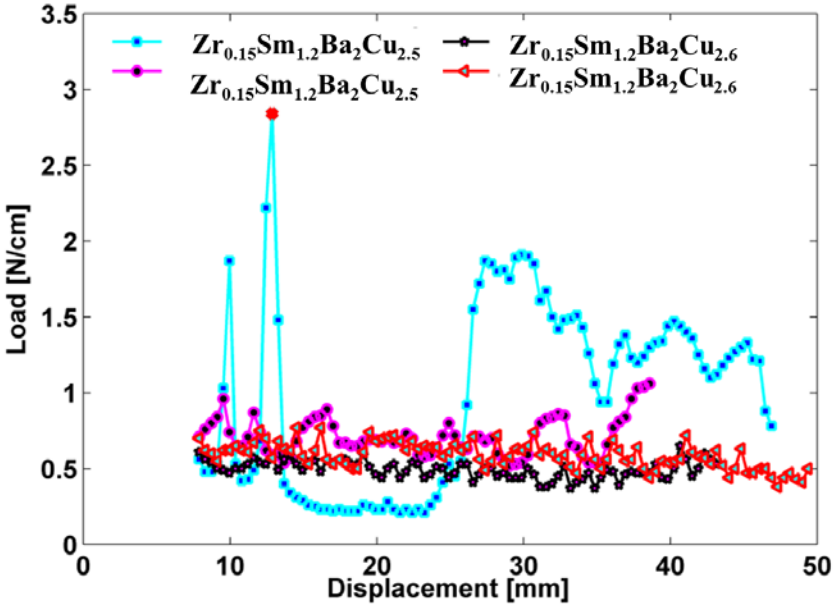

Figure 5-39. Load-displacement curves for the peeling strength confirmation samples.

Different adhesion performance was obtained from these samples. This behavior is explained by the photographs in Figure 5-40. Surprisingly, the upper and bottom half of the sample behaves differently. This might be related to MOCVD pre-processing, specifically the cleaning process, or a deformed buffer. The bottom half of the sample, shown in Figure 5-40a, has very strong adhesion while the upper half has relatively weak adhesion. The fluctuations in the sample plotted with the blue line in Figure 5-39 was caused by the peeling locus shifting between the Cu and REBCO matrix. These shifts correlate perfectly with the photographs shown in Figure 5-40a. The peel strength increase observed after 30 mm is due to the peeling locus shift to an Ag/Cu interfacial peeling at the bottom half. Although the ratio of silver/copper interface peeling is smaller, this provides an immense increase in the overall peel strength of the sample.

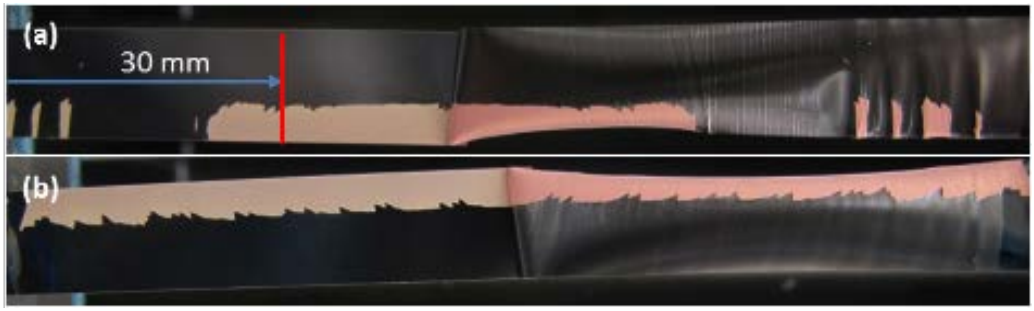

Figure 5-40. Photographs of the Sm samples with a 2.5 mole ratio Cu.

The bottom half of the sample (Figure 5-41b) shows a de-cohesion mode similar to the standard sample. It consists of a dominant mixed-mode de-cohesion and is similar to the one shown in Figure 5-38a. It is known that the peeling strength of a sample that has the mixed mode de-cohesion is about 1 [N/cm] from Figure 5-35a. Looking at these two differently peeled regions, the mixed mode occupies roughly 2/3 of the area while the Ag/Cu interfacial peeling occupies 1/3 (the line shown in Figure 5-40a). The Ag/Cu interfacial peeling should be about 4-5 [N/cm]. With a rough calculation the average

peeling force per unit width, $p_{avr} \approx 1/3*4 + 2/3*1 = 2\,\mathrm{N/cm}$ can be found. This is similar to the value obtained in Figure 5-39.

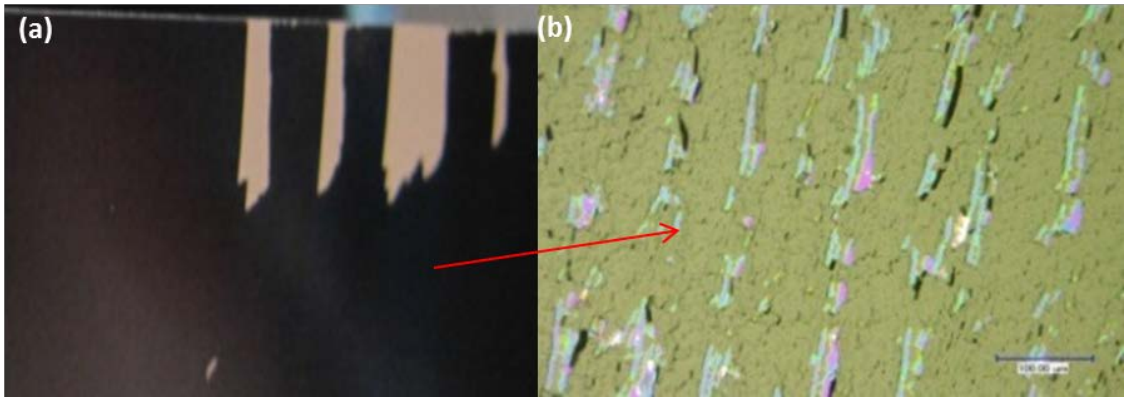

Figure 5-41. A section from the photograph in Figure 5-40b is provided in (a) the optical image from the bottom of (a) is shown in (b).

The mixed mode deformation microstructures differ between samples and provide different adhesion strength. Based on the defects formed within the REBCO matrix, the REBCO cohesive debonding might dominate the mixed mode peeling. However, this does not necessarily mean the peeling strength would be higher when compared with the mixed mode microstructures that dominate buffer/REBCO interfacial debonding. The microscopic defects present in the REBCO matrix might reduce the adhesion strength of the REBCO matrix less than the buffer/REBCO interfacial adhesion strength. In this case, the microstructures after peeling would include the dominant REBCO cohesive peeling.

Due to the fact that the results from the second sample set were not conclusive another set of samples was fabricated using the previous protocol and exposed to the same peeling experiments. The results are provided in Figure 5-42. Slightly lower peeling strengths were obtained for the Sm samples with a 2.5 Cu mole ratio compared to the peeling strength of the previous sample. In this set, an additional Sm sample with a 2.6

mole ratio was included. The peeling strength of this sample is a little higher than the peeling strength of the Sm sample with a 2.5 Cu mole ratio.

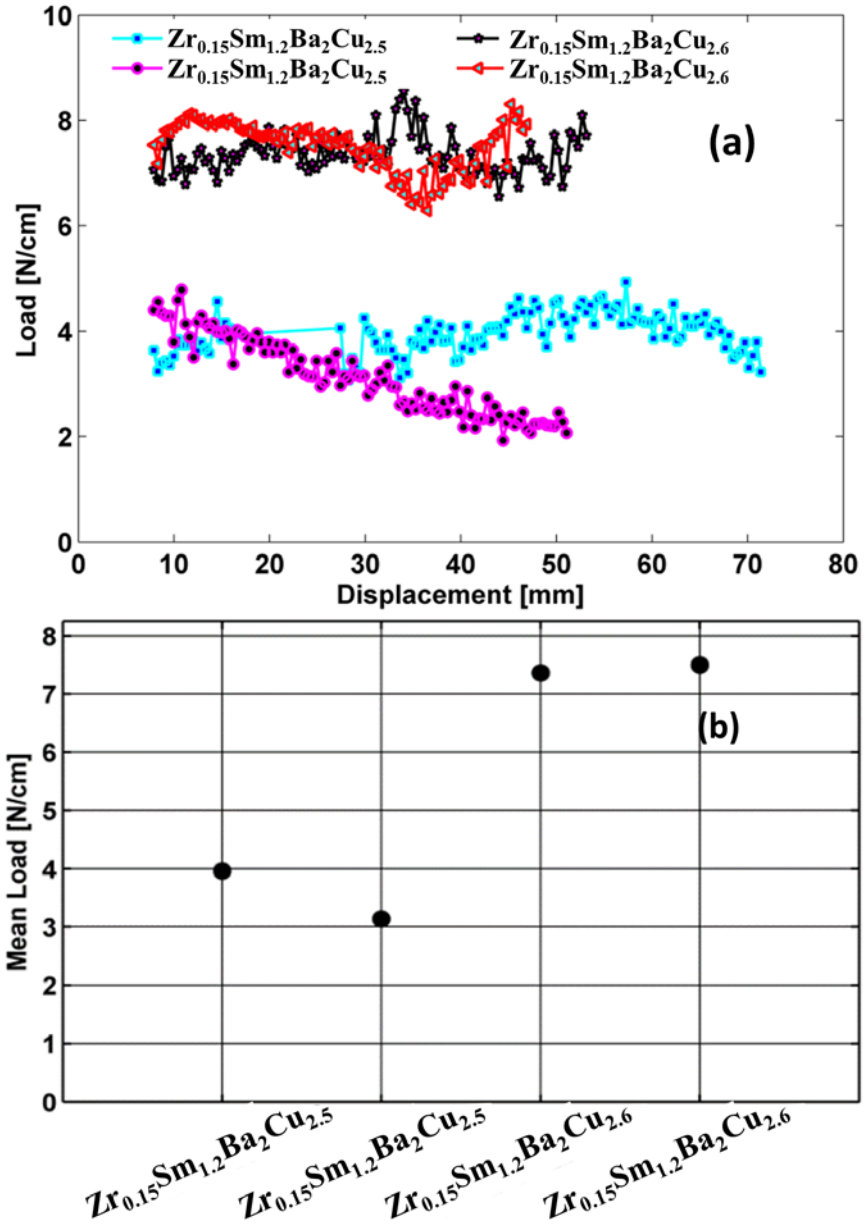

Figure 5-42. (a) Load-displacement curves for the repeated Sm samples with a 2.5 mole ratio and a 2.6 mole ratio of copper and (b) the mean peeling strengths.

With Sm substitution the adhesion strength was improved three-fold. The sample with a composition of $Zr_{0.15}Sm_{1.2}Ba_2Cu_{2.6}O_x$ provided a better peeling strength compared to the standard composition or the samples with lower Cu mole ratios. The Sm addition

reduced the defects inside the REBCO and the structure became more robust; therefore, the peeling strength is improved.

This preliminary T peeling test showed that modifying the defects in the REBCO superconducting layer matrix has a large impact on the mechanical properties of CCs along the c-axis. Growth conditions, cleaning of the buffer before processing, or defects on the buffer layer are also important factors since they determine the REBCO/buffer interfacial debonding. REBCO/buffer interfacial debonding results in the weakest peeling strength. Steps should be taken to improve the peeling strength of CCs by focusing on the interfacial bounding between the REBCO and buffer layer and the REBCO cohesive bonding. The strength level of the Ag/REBCO interfacial debonding was sufficient for almost all targeted applications.

Chapter 6. Conclusions

In this dissertation, the problems of filamentization of a thick stabilizer layer and the delamination of 2G-HTS CCs were addressed. A selective electroplating protocol was developed to achieve a fully-filamentized 2G-HTS with a thick copper stabilizer and small filaments. The adhesion strength of the 2G-HTS coated conductors was also improved.

Initially, the buffer layers were striated followed by a MOCVD-REBCO deposition and subsequent electroplating of a silver stabilizer layer. Magnetization AC loss measurements of the sample before electroplating showed the expected reduction, proportional to the width of the conductor. However, after electroplating, the silver deposited on both the superconducting filaments and the ill-textured REBCO trenches. This structure is undesirable because it couples the filaments increasing the loss drastically. For this reason, another method to fully-filamentize both the REBCO and stabilizer layers in HTS coated conductors was developed. This technique utilizes a combined top-down scribing process, striation oxidation, and bottom-up electroplating. In this method, the Ag shunt, REBCO layer, and buffer stack were removed by mechanical striation using a diamond tip. Eleven striations were made over the 12 mm tape width followed by post-annealing in an oxygen atmosphere to create a highly-resistive oxide layer on the grooves. A thick stabilizer copper layer was then selectively electroplated onto the filaments while the oxidized grooves remained free of electrodeposited copper. This is the first demonstration of a fully-filamentized 2G-HTS conductor with thick copper layer. The coupling losses have been significantly reduced due to the absence of electroplated copper on the grooves and the increased resistivity of the coupling path across the oxidized grooves. Eddy current losses were also significantly reduced due to the copper

filamentization. The AC loss reduction in the striated samples compared to the equivalent non-striated samples is ~11-fold prior to copper electroplating and at least ~13-fold following electroplating. The results were compared with the well-known B-I model and there was good agreement between the model and experimental results. This architecture resulted in a reduction of hysteretic, coupling, and eddy current losses while incorporating all the benefits of the stabilizer.

AC loss characterization of the fully-filamentized samples fabricated using the selective electroplating technique and with different stabilizer thicknesses was also conducted. The results showed that the selective electroplating technique is a viable way to reduce losses in AC field applications for a stabilizer thickness up to 30 μm with no additional magnetization loss contribution. AC loss measurements indicated an approximately 15-fold AC loss reduction in fully-filamentized or decoupled samples with 12 filaments in high field regardless of copper plating thickness. The measurements for partially and fully-coupled samples revealed that the lack of stabilizer filamentization resulted in higher losses in high field due to the electrical coupling and an increase in the total losses beyond those seen in a non-striated sample due to the additional influence of magnetic coupling. In the partially-coupled configuration there was still a 5-fold loss reduction observed. This structure could be utilized in some cable applications that can tolerate larger AC losses compared to others.

The material agglomeration at the diamond tip front during the semi top-down mechanical striation was found to be problematic and might be solved by incorporating high frequency vibrational loading into the tip. Instead, a unique laser striation technique was implemented for filamentization. Selective-electroplating was applied successfully to

the laser striated conductors incorporating different stabilizer layer thickness and filament number. These results indicated that the developed technique can be incorporated successfully into the well-known laser ablation filamentary process without compromising the AC loss reductions while still benefiting from the thick stabilizer layer. The loss ratios with are the loss of a reference control sample divided by the losses of multifilamented samples, were calculated and compared with B-I models respective to their filament number. The loss ratios were found to match well with the B-I model at field values above the penetration field revealing that the losses are hysteretic in nature with negligible contributions from the other loss mechanisms such as coupling and eddy current. With increasing filament numbers, the AC losses are reduced. The data shows a loss reduction of 80, 40 and 16-fold at ~60 mT and 100 Hz in the 48, 24 and 12-filament tapes respectively. These are the highest reported AC loss reduction values in coated conductors fabricated with a thick copper stabilizer. Taking the resistive loss of copper wire as a benchmark, an acceptable AC loss target in HTS coated conductors was calculated to be 1 W/kA/m. This indicates that only 48-filament coated conductors can meet this AC loss criterion. These findings also indicate that very narrow filaments need to be fabricated for CC applications where AC losses are an important factor. By extrapolating the results, it was found that ~100 μm wide filaments would be required to meet the AC loss target of 1 W/kA/m in a field of ~0.2 T at 100 Hz. The reported process of laser scribing followed by selective electroplating can be adapted to fabricate these narrow filaments with a thick copper stabilizer.

The effective widths of the filaments were calculated from the AC loss measurements and compared to the widths obtained from the SEM and optical microscopy.

These values were nearly identical indicating that the developed technique is very successful. Oxygenation temperature effects on the samples were investigated. The calculated filament widths were found to be smaller after high temperature oxygenation due to the diffusion of elements from the Hastelloy substrate, making the filament edge non-superconducting. Overall the coupling loss was substantially decreased after the oxygenation step in the laser-striated samples and almost completely suppressed in the mechanically-striated samples.

I_c degradation is a crucial problem in multifilamentary tape manufacturing and it has been scrutinized in this dissertation as well. There is an expected decrease in I_c due to the reduced cross section resulting from the HTS material removal. Although the critical current of the mechanically striated tape with post oxygenation did not degrade appreciably beyond the expected value from the material removal, the oxygenation temperature was found to have a profound effect on I_c degradation in the laser-striated samples. The mechanically-striated samples showed a 9% I_c degradation compared to the calculated 6%. This degradation increased to 11% when etching was involved. The experimental and calculated I_c degradation for the laser-striated samples were 27% and 7% respectively. By reducing the oxygenation temperature to 550ºC, the I_c degradation was minimized and became comparable to the calculated degradation in the laser-striated samples. The degradation following oxygenation at 550°C was ~8 % compared to the 6-7 % calculated from the material removal. Surprisingly the laser striation process itself did not have a significant effect on I_c degradation. The measurement of individual filament I_cs revealed that the I_c is relatively low at the tape edges compared to the middle, which indicates that the I_c is not uniform along the width of the tape.

The coupling losses in the samples with different oxygenation temperatures do not affect the total loss performance drastically in 12-filament tapes; however, this loss component becomes extremely important when the hysteretic losses are comparable to the coupling losses. The sample oxygenated at lower temperatures had the highest coupling component and the coupling component decreased by increasing the oxygenation temperature. This could be the result of the reduced groove oxide resistivity at low temperatures and the formation of a different oxide compound on the grooves.

Testing methods were developed to evaluate and improve the adhesion strength of the conductors. The composition of the REBCO conductors was modified to alter matrix defects inside the REBCO. T-peel tests were performed on the samples because of its simplicity and it was found that in-plane defects were drastically reduced by substituting Y or Gd with Sm . The sample with Sm showed at least 3-fold enhancement of the adhesion strength along the c-axis.

6.1. Future studies

The ultimate goal of this project is to scale up multifilamentary conductor manufacturing for long lengths, to wind a coil using the conductor, and to demonstrate the viability of these wire structures in AC loss reduction, even in coil configurations. This requires a reel-to-reel setup for the striation and electroplating process. The development of a reel-to-reel laser striation technique is in progress and a conceptual design is provided in Figure 6-1.

The current electroplating cell is not capable of providing long-length electroplating. For this purpose, a reel-to-reel electroplating system was set up at the University of Houston. A picture of this system is provided in Figure 6-2.

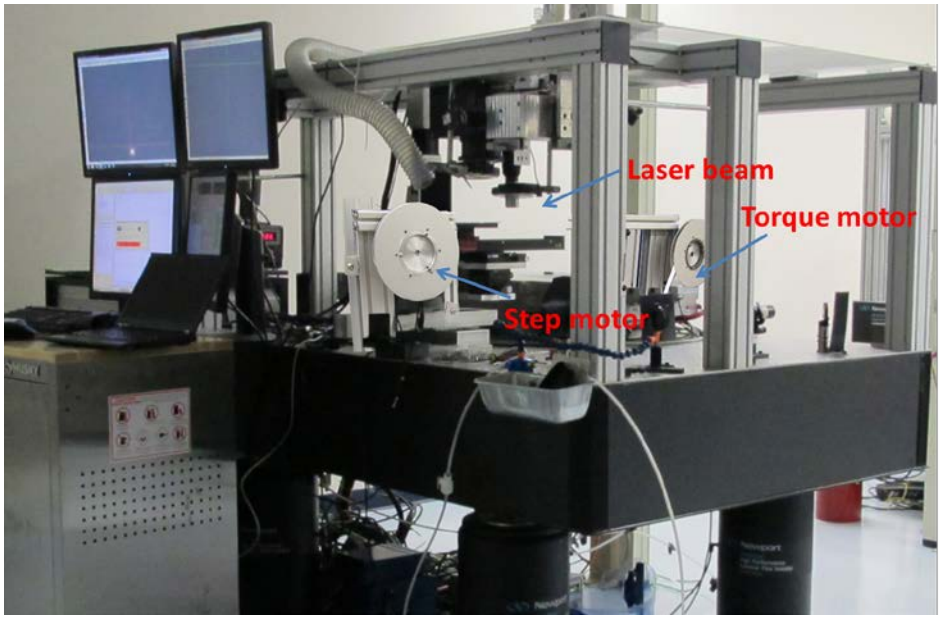

Figure 6-1. Reel-to-reel laser scribing system.

Figure 6-2. Reel-to-reel electroplating system.

After fabricating long multifilamentary tapes and winding a coil, a testing system for evaluating AC loss performance needs to be developed. An identical non-striated coil also needs to be manufactured for comparison purposes.

In this thesis, only the T-peeling test configuration was investigated since it was the easiest one to start with and different peeling test methods and configurations need to be evaluated. The stress state differs for each test configuration and it is still not clear which of these test configurations have a better correlation with coil performance. A 90° test needs to be performed to characterize the sample peeling behavior. In this test, the stress state is dominantly tensile and this configuration duplicates almost identically the forces under thermal cycling in an actual coil. Additionally, 180° peeling test configuration should also be tested since this test also has different stress state. After these tests, the conductors need to be wound into a coil. The improved mechanical properties have to be confirmed in an actual coil performance test to check if the short sample adhesion tests can be correlated with coil performance.

There is still work to be done before these processes can be implemented in real world applications. However, these studies have made significant inroads into developing a viable strategy for the commercial manufacturing of low AC loss 2G-HTS REBCO CCs.

References

[1] H.K. Onnes, *The Resistance of Pure Mercury at Helium Temperatures*, Commun. Phys. Lab. Univ. Leiden, 12 (1911) 120.

[2] J.R. Gavaler, *Superconductivity in Nb-Ge Films Above 22 K*, Appl. Phys. Lett., 23 (1973) 480-482.

[3] J.G. Bednorz, K.A. Muller, *Possible High-Tc Superconductivity in the Ba-La-Cu-O system*, Z. Phys. B-Condens. Mat., 64 (1986) 189-193.

[4] M.K. Wu, J.R. Ashburn, C.J. Torng, P.H. Hor, R.L. Meng, L. Gao, Z.J. Huang, Y.Q. Wang, C.W. Chu, *Superconductivity at 93-K in a New Mixed-Phase Y-Ba-Cu-O Compounds System at Ambient Pressure*, Phys. Rev. Lett., 58 (1987) 908-910.

[5] H. Maeda, Y. Tanaka, M. Fukutomi, T. Asano, *A New High-Tc Oxide Superconductor Without Rare-Earth Element*, Jpn. J. Appl. Phys. Part 2 - Lett., 27 (1988) L209-L210.

[6] R.M. Hazen, C.T. Prewitt, R.J. Angel, N.L. Ross, L.W. Finger, C.G. Hadidiacos, D.R. Veblen, P.J. Heaney, P.H. Hor, R.L. Meng, Y.Y. Sun, Y.Q. Wang, Y.Y. Xue, Z.J. Huang, L. Gao, J. Bechtold, C.W. Chu, *Superconductivity in the High-Tc Bi-Ca-Sr-Cu-O System-Phase Identification*, Phys. Rev. Lett., 60 (1988) 1174-1177.

[7] A. Schilling, M. Cantoni, J.D. Guo, H.R. Ott, *Superconductivity Above 130-K in the Hg-Ba-Ca-Cu-O System*, Nature, 363 (1993) 56-58.

[8] J. Nagamatsu, N. Nakagawa, T. Muranaka, Y. Zenitani, J. Akimitsu, *Superconductivity at 39 K in Magnesium Diboride*, Nature, 410 (2001) 63-64.

[9] B.I. Zimmer, W. Jeitschko, J.H. Albering, R. Glaum, M. Reehuis, *The Rate Earth Transition Metal Phosphide Oxides LnFePO, LnRuPO and LnCoPO with ZrCuSiAs Type Structure*, Journal of Alloys and Compounds 229 (1995) 238-242.

[10] *Coalition for the Commercial Applications of Superconductivity* (CCAS) (Available online): http://www.ccas-web.org/superconductivity/).

[11] D. Larbalestier, A. Gurevich, D.M. Feldmann, A. Polyanskii, *High-T-c Superconducting Materials for Electric Power Applications*, Nature, 414 (2001) 368-377.

[12] W. Meissner, R. Ochsenfeld, *Ein Neuer Effekt bei Eintritt der Supraleitfähigkeit*, Naturwissenschaften 21 (1933) 787-788.

[13] M.N. Wilson, Superconducting Magnets, Oxford University Press, New York, 1983.

[14] A.C. Rose-Innes, E.H. Rhoderick, Introduction to Superconductivity, Second ed., Pergamon press, New York, 1978.

[15] M. Tinkham, Introduction to Superconductivity, Robert .E. Krieger Publishing Co., Inc., Florida, 1975.

[16] G. Blatter, M.V. Feigelman, V.B. Geshkenbein, A.I. Larkin, V.M. Vinokur, *Vortices in High-Temperature Superconductors*, Reviews of Modern Physics, 66 (1994) 1125-1388.

[17] J.E. Kunzler, J.H. Wernick, F.S.L. Hsu, E. Buehler, *Supercondcutivity in Nb3Sn at High Current Density in a Magnetic Field of 88 kgauss*, Phys. Rev. Lett., 6 (1961) 89.

[18] S. Jin, R.C. Sherwood, R.B. Vandover, T.H. Tiefel, D.W. Johnson, *High-Tc Superconductors-Composite Wire Fabrication*, Appl. Phys. Lett., 51 (1987) 203-204.

[19] I.W. Chen, X. Wu, S.J. Keating, C.Y. Keating, P.A. Johnson, T.Y. Tien, *Texture Development in YBa2Cu3Ox by Hot Extrusion and Hot-Pressing*, J. Am. Ceram. Soc., 70 (1987) C388-C390.

[20] M. Hong, S.H. Liou, J. Kwo, B.A. Davidson, *Superconducting Y-Ba-Cu-O Oxide-Films by Sputtering*, Appl. Phys. Lett., 51 (1987) 694-696.

[21] R.B. Laibowitz, R.H. Koch, P. Chaudhari, R.J. Gambino, *Thin Superconducting Oxide-Films*, Phys. Rev. B, 35 (1987) 8821-8823.

[22] J. Kwo, T.C. Hsieh, R.M. Fleming, M. Hong, S.H. Liou, B.A. Davidson, L.C. Feldman, *Structural and Superconducting Properties of Orientation-Ordered Y1Ba2Cu3O7-x Films Prepared by Molecular-Beam Epitaxy*, Phys. Rev. B, 36 (1987) 4039-4042.

[23] M.E. Gross, M. Hong, S.H. Liou, P.K. Gallagher, J. Kwo, *Versatile New Metalorganic Process for Preparing Superconducting Thin-Films*, Appl. Phys. Lett., 52 (1988) 160-162.

[24] D. Dijkkamp, T. Venkatesan, X.D. Wu, S.A. Shaheen, N. Jisrawi, Y.H. Minlee, W.L. McLean, M. Croft, *Preparation of Y-Ba-Cu Oxside Superconductor This-Film Using Pulsed Laser Evaporation from High-Tc Bulk Material*, Appl. Phys. Lett., 51 (1987) 619-621.

[25] A.D. Berry, D.K. Gaskill, R.T. Holm, E.J. Cukauskas, R. Kaplan, R.L. Henry, *Formation of High-Tc Superconducting Films by Orgaometallic Chemical Vapor-Deposition,* Appl. Phys. Lett., 52 (1988) 1743-1745.

[26] H. Yamane, H. Masumoto, T. Hirai, H. Iwasaki, K. Watanabe, N. Kobayashi, Y. Muto, H. Kurosawa, *YBCO Superconducting Films Prepared on $SrTi_3$ Substrates by Chemical Vapour-Deposition,* Appl. Phys. Lett., 53 (1988) 1548-1550.

[27] D.K. Fork, K. Char, F. Bridges, S. Tahara, B. Lairson, J.B. Boyce, G.A.N. Connell, T.H. Geballe, *YBCO Films on YSZ and Al_2O_3 by Pulsed Laser Depositions,* Physica C, 162 (1989) 121-122.

[28] P.C. McIntyre, M.J. Cima, J.A. Smith, R.B. Hallock, M.P. Siegal, J.M. Phillips, Effect of Growth Conditions on the Properties and Morphology of Chemically Derived Epitaxial Thin-Film of $YBa_2Cu_3O_{7-x}$ on (001) $LaAlO_3$, J. Appl. Phys., 71 (1992) 1868-1877.

[29] D. Dimos, P. Chaudhari, J. Mannhart, *Superconducting Transport Properties of Grain Boundaries in $YBa_2Cu_3O_7$ Bicrystals,* Phys. Rev. B, 41 (1990) 4038-4049.

[30] A. Goyal, D.F. Lee, F.A. List, E.D. Specht, R. Feenstra, M. Paranthaman, X. Cui, S.W. Lu, P.M. Martin, D.M. Kroeger, D.K. Christen, B.W. Kang, D.P. Norton, C. Park, D.T. Verebelyi, J.R. Thompson, R.K. Williams, T. Aytug, C. Cantoni, *Recent Progress in the Fabrication of High-J(c) Tapes by Epitaxial Deposition of YBCO on RABiTS,* Physica C, 357 (2001) 903-913.

[31] R. Gupta, A. Anerella, J. Cozzolino, J. Escallier, G. Ganetis, A. Ghosh, A. Harrison, A. Marone, J. Muratore, J. Schmalzle, W. Sampson, P. Wanderer, *Status of High*

Temperature Superconductor Magnet R&D at BNL, IEEE Trans. Appl. Supercond., 14 (2004) 1198-1201.

[32] Y. Iijima, K. Kakimoto, M. Kimura, K. Takeda, T. Saitoh, *Reel to Reel Continuous Formation of Y-123 Coated Conductors by IBAD and PLD Method*, IEEE Trans. Appl. Supercond., 11 (2001) 2816-2821.

[33] J.R. Groves, P.N. Arendt, S.R. Foltyn, Q.X. Jia, T.G. Holesinger, L.A. Emmert, R.F. DePaula, P.C. Dowden, L. Stan, *Improvement of IBAD MgO Template Layers on Metallic Substrates for YBCO HTS Deposition*, IEEE Trans. Appl. Supercond., 13 (2003) 2651-2654.

[34] C.P. Wang, K.B. Do, M.R. Beasley, T.H. Geballe, R.H. Hammond, Deposition of In-Plane Textured MgO on Amorphous Si_3N_4 Substrates by Ion-Beam-Assisted Deposition and Comparisons with Ion-Beam-Assisted Deposited Yttria-Stabilized-Zirconia, Appl. Phys. Lett., 71 (1997) 2955-2957.

[35] V. Selvamanickam, Y. Xie, J. Reeves, Y. Chen, *MOCVD-Based YBCO-Coated Conductors*, MRS Bull., 29 (2004) 579-582.

[36] V. Selvamanickam, H.G. Lee, X. Xiong, Y. Qiao, Y. Xie, J. Reeves, Y. Li, A. Knoll, K. Lenseth, *Recent Developments in Scale up of High Performance High Temperature Superconductors*, in: V. Matias, J. Talvacchio, X. Xi, Z. Han, H.W. Neumuller (Eds.) Frontiers in Superconducting Materials-New Materials and Applications, Materials Research Society, Warrendale, 2004, pp. 29-31.

[37] V. Selvamanickam, A. Guevara, Y. Zhang, I. Kesgin, Y. Xie, G. Carota, Y. Chen, J. Dackow, Y. Zuev, C. Cantoni, A. Goyal, J. Coulter, L. Civale, *Enhanced and Uniform In-Field Performance in Long (Gd, Y)-Ba-Cu-O Tapes with Zirconium*

Doping Fabricated by Metal-Organic Chemical Vapor Deposition, Supercond. Sci. Technol., 23 (2010).

[38] V. Selvamanickam, Y.M. Chen, X.M. Xiong, Y.Y.Y. Xie, M. Martchevski, A. Rar, Y.F. Qiao, R.M. Schmidt, A. Knoll, K.P. Lenseth, C.S. Weber, *High Performance 2G Wires: From R&D to Pilot-Scale Manufacturing*, IEEE Trans. Appl. Supercond., 19 (2009) 3225-3230.

39] S.S. Kalsi, *Installation and Operation of Superconducting Rotating Machines*, in: Transmission and Distribution Conference and Exposition, 2003 IEEE PES, 2003, pp. 1098-1101 vol.1093.

[40] C.T. Reis, S.P. Mehta, B.W. McConnell, R.H. Jones, *Development of High Temperature Superconducting Power Transformers*, in: Power Engineering Society Winter Meeting, 2002. IEEE, 2002, pp. 151-156 vol.151.

[41] M.W. Rupich, X.P. Li, S. Sathyamurthy, C.L.H. Thieme, K. DeMoranville, J. Gannon, S. Fleshler, *Second Generation Wire Development at AMSC*, IEEE Trans. Appl. Supercond., 23 (2013).

[42] P.N. Barnes, M.D. Sumption, G.L. Rhoads, *Review of High Power Density Superconducting Generators: Present State and Prospects for Incorporating YBCO Windings*, Cryogenics, 45 (2005) 670-686.

[43] J.F. Maguire, J. Yuan, W. Romanosky, F. Schmidt, R. Soika, S. Bratt, F. Durand, C. King, J. McNamara, T.E. Welsh, *Progress and Status of a 2G HTS Power Cable to Be Installed in the Long Island Power Authority (LIPA) Grid*, Applied Superconductivity, IEEE Transactions on, 21 (2011) 961-966.

[44] K.E. Gray, D.E. Fowler, *A Superconducting Fault-Current Limiter*, J. Appl. Phys., 49 (1978) 2546-2550.

[45] Y.Y. Xie, K. Tekletsadik, D. Hazelton, V. Selvamanickam, *Second Generation High-Temperature Superconducting Wires for Fault Current Limiter Applications*, IEEE Trans. Appl. Supercond., 17 (2007) 1981-1985.

[46] N. Mathias, S. Michael, *High-Temperature Superconductor Fault Current Limiters: Concepts, Applications, and Development Status*, Superconductor Science and Technology, 20 (2007) R15.

[47] L. Martini, M. Bocchi, R. Brambilla, R. Dalessandro, C. Ravetta, *Design and Development of 15 MVA Class Fault Current Limiter for Distribution Systems*, IEEE Trans. Appl. Supercond., 19 (2009) 1855-1858.

[48] C.A. Baldan, J.S. Lamas, C.Y. Shigue, E. Ruppert, *Fault Current Limiter Using YBCO Coated Conductor-The Limiting Factor and Its Recovery Time*, IEEE Trans. Appl. Supercond., 19 (2009) 1810-1813.

[49] J. Bock, A. Hobl, J. Schramm, *Superconducting Fault Current Limiters - a New Device for Future Smart Grids, in: Electricity Distribution (CICED)*, 2012 China International Conference on, 2012, pp. 1-4.

[50] S. Rich., *Development of Ultra Efficient Electrical Motor Systems*, in: DOE Annual Superconductivity Peer Review Meeting (2004), Washington, DC.

[51] D.U. Gubser, *Superconducting Motors and Generators for Naval Applications*, Physica C, 392–396, Part 2 (2003) 1192-1195.

[52] J.H. Zhu, W.J. Yuan, T.A. Coombs, Q. Ming, *Simulation and Experiment of a YBCO SMES Prototype in Voltage Sag Compensation*, Physica C, 471 (2011) 199-204.

[53] W.J. Yuan, W. Xian, M. Ainslie, Z. Hong, Y. Yan, R. Pei, Y. Jiang, T.A. Coombs, *Design and Test of a Superconducting Magnetic Energy Storage (SMES) Coil*, IEEE Trans. Appl. Supercond., 20 (2010) 1379-1382.

[54] U.P. Trociewitz, M. Dalban-Canassy, M. Hannion, D.K. Hilton, J. Jaroszynski, P. Noyes, Y. Viouchkov, H.W. Weijers, D.C. Larbalestier, *35.4 T Field Generated Using a Layer-Wound Superconducting Coil Made of (RE)$Ba_2Cu_3O_{7-x}$ (RE = rare earth) Coated Conducto*r, Appl. Phys. Lett., 99 (2011).

[55] W.D. Markiewicz, D.C. Larbalestier, H.W. Weijers, A.J. Voran, K.W. Pickard, W.R. Sheppard, J. Jaroszynski, A.X. Xu, R.P. Walsh, J. Lu, A.V. Gavrilin, P.D. Noyes, *Design of a Superconducting 32 T Magnet With REBCO High Field Coils*, IEEE Trans. Appl. Supercond., 22 (2012).

[56] R. Gupta, M. Anerella, G. Ganetis, A. Ghosh, H. Kirk, R. Palmer, S. Plate, W. Sampson, Y. Shiroyanagi, P. Wanderer, B. Brandt, D. Cline, A. Garren, J. Kolonko, R. Scanlan, R. Weggel, *High Field HTS R&D Solenoid for Muon Collider*, IEEE Trans. Appl. Supercond., 21 (2011) 1884-1887.

[57] T. Takematsu, R. Hu, T. Takao, Y. Yanagisawa, H. Nakagome, D. Uglietti, T. Kiyoshi, M. Takahashi, H. Maeda, *Degradation of the Performance of a YBCO-Coated Conductor Double Pancake Coil Due to Epoxy Impregnation*, Physica C, 470 (2010) 674-677.

[58] R. Gupta, M. Anerella, J. Cozzolino, G. Ganetis, A. Ghosh, G. Greene, W. Sampson, Y. Shiroyanagi, P. Wanderer, A. Zeller, *Second Generation HTS Quadrupole for FRIB*, IEEE Trans. Appl. Supercond., 21 (2011) 1888-1891.

[59] Y. Yanagisawa, H. Nakagome, T. Takematsu, T. Takao, N. Sato, M. Takahashi, H. Maeda, *Remarkable Weakness Against Cleavage Stress for YBCO-Coated Conductors and its Effect on the YBCO Coil Performance*, Physica C, 471 (2011) 480-485.

[60] G. Ries, M. Leghissa, J. Rieger, J. Wiezorek, M. Oomen, *High-Tc Superconductors and AC Loss in Electrotechnical Devices*, Physica C, 310 (1998) 283-290.

[61] A.M. Wolsky, AC Losses: *What is Being Done to Teduce Them and Why Success is Important*: in, International Energy Agency, 2009.

[62] F. London, H. London, *The Electromagnetic Equations of the Supraconductor*, Proceedings of the Royal Society of London. Series A - Mathematical and Physical Sciences, 149 (1935) 71-88.

[63] E.H. Brandt, *Thermal Depennin and Melting of the Flux-Line Lattice in High-Tc Supercoductors*, International Journal of Modern Physics B, 05 (1991) 751-795.

[64] E. Brandt, *Thermally Activated Depinning of Vortices in High-Tc Superconductors*, in: J. Ashkenazi, S. Barnes, F. Zuo, G. Vezzoli, B. Klein (Eds.) High-Temperature Superconductivity, Springer US, 1991, pp. 437-445.

[65] P.W. Anderson, *Theory of Flux Creep in Hard Superconductors*, Phys. Rev. Lett., 9 (1962) 309-311.

[66] E.H. Brandt, *Universality of Flux Creep in Superconductors with Arbitrary Shape and Current-Voltage Law*, Phys. Rev. Lett., 76 (1996) 4030-4033.

[67] J. Rhyner, Magnetic Properties and AC-losses of Superconductors with Power Law Current-Voltage Characteristics, Physica C, 212 (1993) 292-300.

[68] S. Stavrev, F. Grilli, B. Dutoit, N. Nibbio, E. Vinot, I. Klutsch, G. Meunier, P. Tixador, Y. Yifeng, E. Martinez, *Comparison of Numerical Methods for Modeling of Superconductors*, Magnetics, IEEE Transactions on, 38 (2002) 849-852.

[69] C.P. Bean, *Magnetization of Hard Superconductors*', Phys. Rev. Lett., 8 (1962) 250-253.

[70] C.P. Bean, *Magnetization of High-Field Superconductors*, Reviews of Modern Physics, 36 (1964) 31-39.

[71] T. Hayashi, S. Nakamura, M. Iwakuma, K. Funaki, A. Ibi, Y. Yamada, T. Izumi, Y. Shiohara, T. Saitoh, Y. Iijima, *AC Loss Properties of Laser-Scribed Multi-Filamentary GdBCO Coated Conductors with Artificial Pinning Centres*, Physics Procedia, 36 (2012) 1522-1527.

[72] K.V. Namjoshi, P.P. Biringer, *Low-Frequency Eddy-Current Loss Estimation in Long Conductors by Using the Moment of Inertia of Cross-Sections*, IEEE Trans. on Magnetics, 24 (1988) 2181-2185.

[73] W.J. Carr, *Loss in a Striated Coated Conductor*, Supercond. Sci. Technol., 20 (2007) 168-175.

[74] L.S. Lakshmi, M.P. Staines, K.P. Thakur, R.A. Badcock, N.J. Long, *Frequency Dependence of Magnetic AC Loss in a Five Strand YBCO Roebel Cable*, Supercond. Sci. Technol., 23 (2010).

[75] K.H. Müller, *AC Power Losses in Flexible Thick-Film Superconducting Tapes*, Physica C, 281 (1997) 1-10.

[76] M. Marchevsky, E. Zhang, Y.Y. Xie, V. Selvamanickam, P.G. Ganesan, *AC Losses and Magnetic Coupling in Multifilamentary 2G HTS Conductors and Tape Arrays*, IEEE Trans. Appl. Supercond., 19 (2009) 3094-3097.

[77] I. Kesgin, G. Majkic, V. Selvamanickam, *Fully Filamentized HTS Coated Conductor Via Striation and Selective Electroplating*, Physica C, 486 (2013) 43-50.

[78] I. Kesgin, G. Majkic, V. Selvamanickam, *Effect of Selectively Electrodeposited Stabilizer Thickness on AC Loss Behavior of Fully-Filamentized HTS Wire*, IEEE Trans. Appl. Supercond., 23 (2013) 5900505-5900505.

[79] W.J. Carr, C.E. Oberly, *Filamentary YBCO Conductors for AC Applications*, IEEE Trans. Appl. Supercond., 9 (1999) 1475-1478.

[80] W.J. Carr, C.E. Oberly, *Transverse Resistivity of a Filamentary Coated Conductor*, Supercond. Sci. Technol., 19 (2006) 64-67.

[81] E.H. Brandt, M. Indenbom, *Type-II-Superconductor Strip with Current in a Perpendicular Magnetic Field*, Phys. Rev. B, 48 (1993) 12893-12906.

[82] X. Cai, I. Kesgin, R. Schmidt, Y. Chen, V. Selvamanickam, *Completely Etch-Free Fabrication of Multifilamentary Coated Conductor Using Inkjet Printing and Electrodeposition*, IEEE Trans. Appl. Supercond., PP (2013) 1-1.

[83] K. Suzuki, J. Matsuda, M. Yoshizumi, T. Izumi, Y. Shiohara, M. Iwakuma, A. Ibi, S. Miyata, Y. Yamada, *Development of a Laser Scribing Process of Coated Conductors for the Reduction of AC Losses*, Supercond. Sci. Technol., 20 (2007) 822-826.

[84] G.A. Levin, P.N. Barnes, N. Amemiya, S. Kasai, K. Yoda, Z. Jiang, *Magnetization Losses in Multifilament Coated Superconductors*, Appl. Phys. Lett., 86 (2005).

[85] G.A. Levin, P.N. Barnes, N. Amemiya, S. Kasai, K. Yoda, Z.A. Jiang, A. Polyanskii, *Magnetization Losses in Multiply Connected $YBa_2Cu_3O_{6+x}$-Coated Conductors*, J. Appl. Phys., 98 (2005).

[86] Y. Mawatari, *Critical State of Periodically Arranged Superconducting-Strip Lines in Perpendicular Fields*, Phys. Rev. B, 54 (1996) 13215-13221.

[87] N. Amemiya, S. Kasai, K. Yoda, Z.N. Jiang, G.A. Levin, P.N. Barnes, C.E. Oberly, *AC Loss Reduction of YBCO Coated Conductors by Multifilamentary Structure*, Supercond. Sci. Technol., 17 (2004) 1464-1471.

[88] G. Majkic, I. Kesgin, Y. Zhang, Y.F. Qiao, R. Schmidt, V. Selvamanickam, *AC Loss Filamentization of 2G HTS Tapes by Buffer Stack Removal*, IEEE Trans. Appl. Supercond., 21 (2011) 3297-3300.

[89] W.T. Norris, *Calculation of Hysteresis Losses in Hard Superconductors Carrying AC: Isolated Conductors and Edges of Thin Sheets*, Journal of Physics D: Applied Physics, 3 (1970) 489.

[90] Y.B. Kim, C.F. Hempstead, A.R. Strnad, *Magnetization and Critical Supercurrents*, Physical Review, 129 (1963) 528-535.

[91] M. Polak, J. Kvitkovic, P. Mozola, E. Usak, P.N. Barnes, G.A. Levin, *Frequency Dependence of Hysteresis Loss in YBCO Tapes*, Supercond. Sci. Technol., 20 (2007) S293-S298.

[92] C.E. Oberly, L. Long, G.L. Rhoads, W. James Carr Jr, *AC Loss Analysis for Superconducting Generator Armatures Wound with Subdivided Y–Ba–Cu–O Coated Tape*, Cryogenics, 41 (2001) 117-124.

[93] J.G. Weisend, Handbook of Cryogenic Engineering, Taylor & Francis Group, 1998.

[94] T. Flynn, Cryogenic Engineering, Second Edition, Revised and Expanded, Taylor & Francis, 2004.

[95] O. Tsukamoto, H. Nakayama, S. Odaka, M. Ciszek, S. Hahakura, M. Ueyama, K. Ohmatsu, D. Miyagi, *Transport Current Losses in HoBaCuO-123 Coated Conductors with a Ni-Alloy Substrate*, Physica C, 426–431, Part 2 (2005) 1290-1294.

[96] D.N. Nguyen, P. Sastry, D.C. Knoll, J. Schwartz, *Electromagnetic and Calorimetric Measurements for AC losses of a YBa2Cu3O7-delta Coated Conductor with Ni-Alloy Substrate*, Supercond. Sci. Technol., 19 (2006) 1010-1017.

[97] R.C. Duckworth, M.J. Gouge, J.W. Lue, C.L.H. Thieme, D.T. Verebelyi, *Substrate and Stabilization Effects on the Transport AC Losses in YBCO Coated Conductors*, IEEE Trans. Appl. Supercond., 15 (2005) 1583-1586.

[98] E. Martínez, Y. Yang, C. Beduz, Y.B. Huang, *Experimental Study of Loss Mechanisms of AgAu/PbBi-2223 Tapes with Twisted Filaments Under Perpendicular AC Magnetic Fields at Power Frequencies*, Physica C, 331 (2000) 216-226.

[99] S.P. Ashworth, M. Suenaga, *Experimental Determination of the Losses Produced by the Interaction of AC Magnetic Fields and Transport Currents in HTS tapes*, Physica C, 329 (2000) 149-159.

[100] S.P. Ashworth, M. Suenaga, *The Calorimetric Measurement of Losses in HTS Tapes Due to AC Magnetic Fields and Transport Currents*, Physica C, 315 (1999) 79-84.

[101] J.P. Murphy, M.J. Mullins, P.N. Barnes, T.J. Haugan, G.A. Levin, M. Majoros, M.D. Sumption, E.W. Collings, M. Polak, P. Mozola, *Experiment Setup for Calorimetric*

Measurements of Losses in HTS Coils Due to AC Current and External Magnetic Fields, IEEE Trans. Appl. Supercond., 23 (2013).

[102] D.N. Nguyen, *Alternating Current Loss Characteristics in (Bi,Pb)$_2$Sr$_2$Ca$_2$Cu$_3$O$_{10}$ and YBa2Cu3O7-delta Superconducting Tapes*, Departmenyt of Physics, The Florida State University, 2007.

[103] Z. Jiang, N. Amemiya, *An Experimental Method for Total AC Loss Measurement of High Tc Superconductors*, Superconductor Science & Technology, 17 (2004) 371-379.

[104] S. Fukui, Y. Kitoh, T. Numata, O. Tsukamoto, J. Fujikami, K. Hayashi, *Transport Current AC Losses of High-Tc Superconducting Tapes Exposed to AC Magnetic Field-Study on a New Measurement Method*, Advances in Cryogenic Engineering Materials, Vol 44, Pts a and B, 44 (1998) 723-730.

[105] T. Ogasawara, Y. Takahashi, K. Kanbara, Y. Kubota, K. Yasohama, K. Yasukochi, *Alternating Field Losses in Superconducting Wires Carrying dc Transport Currents*: Part 1 single core conductors, Cryogenics, 19 (1979) 736-740.

[106] C. Schmidt, E. Specht, *AC Loss Measurements on Supercondcutors in the Microwatt Range*, Review of Scientific Instruments, 61 (1990) 988-992.

[107] S. Zannella, L. Jansak, M. Majoros, V. Selvamanickam, K. Salama, *AC Energy Dissipation in high-Tc Superconductors*, Physica C, 205 (1993) 14-20.

[108] S.P. Ashworth, *Measurements of AC Losses Due to Transport Currents in Bismuth Superconductors*, Physica C, 229 (1994) 355-360.

[109] M.P. Oomen, J. Rieger, M. Leghissa, H.H.J. ten Kate, *Magnetic AC Loss in Multi-Filamentary Bi-2223 / Ag tapes*, Physica C, 290 (1997) 281-290.

[110] J.J. Rabbers, B. ten Haken, H.H.J. ten Kate, *Measuring Transport Current Loss of BSCCO/Ag Tapes Exposed to External AC Magnetic Field*, Physica C, 310 (1998) 101-105.

[111] K.H. Muller, K.E. Leslie, *Self-Field AC Loss of Bi-2223 Superconducting Tapes*, IEEE Trans. Appl. Supercond., 7 (1997) 306-309.

[112] J.J. Rabbers, B. ten Haken, H.H.J. ten Kate, *Advanced AC Loss Measurement thods for High-Temperature Superconducting Tapes*, Review of Scientific Instruments, 72 (2001) 2365-2373.

[113] J. W. J. Carr, *Loss in a Striated Coated Conductor*, Supercond. Sci. and Technol., 20 (2007) 168.

[114] J.J. Rabbers, O. van der Meer, W.F.A. Klein Zeggelink, O.A. Shevchenko, B. ten Haken, H.H.J. ten Kate, *Magnetisation Loss of BSCCO/Ag Tape in Uni-Directional and Rotating Magnetic Field*, Physica C, 325 (1999) 1-7.

[115] M. Majoros, M.D. Sumption, M.A. Susner, E.W. Collings, J. Souc, F. Gomory, M. Vojenciak, L.M. Fisher, A.V. Kalinov, I.F. Voloshin, *AC Magnetization Loss of a YBCO Coated Conductor Measured Using Three Different Techniques*, IEEE Trans. Appl. Supercond., 21 (2011) 3293-3296.

[116] S. Foner, *Versatile and Sensitive Vibrating-Sample Magnetometer*, Review of Scientific Instruments, 30 (1959) 548-557.

[117] J.-H.P.a.R. Stilwell, PPMS VSM NHMFL Summer School Training Presentation, 2012.

[118] K.W. See, *Experimental and Theoretical Approached for AC Losses in Practical Superconducting Tapes for Engineering Applications*, Faculty of Engineering, University of Wollongong, 2012.

[119] J. Souc, F. Gomory, M. Vojenciak, *Calibration Free Method for Measurement of the AC Magnetization Loss*, Supercond. Sci. Technol., 18 (2005) 592-595.

[120] S. Takács, *Properties of Superfine Superconducting Filaments Embedded in Normal Matrix*, Czech J Phys, 36 (1986) 524-536.

[121] K. Yasohama, K. Morita, T. Ogasawara, *Superconducting Properties of Cu-NbTi Composite Wires with Fine Filaments*, IEEE Trans. on Magnetics, 23 (1987) 1728-1731.

[122] P. Dubots, A. Fevrier, J. Renard, J. Tavergnier, J. Goyer, K. Hoang Gia, *NbTi Wires with Ultra-Fine Filaments for 50 - 60 Hz use: Influence of the Filament Diameter Upon Losses*, IEEE Trans. on Magnetics, 21 (1985) 177-180.

[123] I. Hlasnik, S. Takacs, V.P. Burjak, M. Majoros, J. Krajcik, L. Krempasky, M. Polak, M. Jergel, T.A. Korneeva, O.N. Mironova, I. Ivan, *Properties of Superconducting NbTi Superfine Filament Composites with Diameters < 0.1 μm*, Cryogenics, 25 (1985) 558-565.

[124] Y.B. Huang, R. Flukiger, *Reducing AC Losses of Bi(2223) Multifilamentary Tapes by Oxide Barriers*, Physica C, 294 (1998) 71-82.

[125] Y.B. Huang, M. Dhalle, G. Witz, F. Marti, E. Giannini, E. Walker, R. Passerini, A. Polcari, S. Clerc, K. Kwasnitza, R. Flukiger, *Development of Bi(2223) Multifilamentary Tapes with Low AC Losses*, J. Supercond., 11 (1998) 495-505.

[126] A.M. Campbell, *Coupling Losses in Filamentary Superconductors with a Resistive Barrier*, Supercond. Sci. Technol., 10 (1997) 932-935.

[127] S.P. Ashworth, B.A. Glowacki, M. Ciszek, E.C.L. Chesneau, P. Haldar, *Connectivity Between Filaments in BSCCO-2223 Multi-Filamentary Tape*, IEEE Trans. Appl. Supercond., 7 (1997) 1662-1665.

[128] M.P. Oomen, J. Rieger, M. Leghissa, B. ten Haken, *Effective Transverse Resistivity in Superconducting Tapes with Various Filament Shapes and Structures*, Supercond. Sci. Technol., 13 (2000) 1101-1106.

[129] A.M. Campbell, *A General Treatment of Losses in Multifilamentary Superconductors*, Cryogenics, 22 (1982) 3-16.

[130] V. Selvamanickam, Y. Chen, X. Xiong, Y.Y. Xie, J.L. Reeves, X. Zhang, Y. Qiao, K.R. Lenseth, R.M. Schmidt, A. Rar, D.W. Hazelton, K. Tekletsadik, *Recent Progress in Second-Generation HTS Conductor Scale-Up at SuperPower*, IEEE Trans. Appl. Supercond., 17 (2007) 3231-3234.

[131] Q.Y. Ma, P. Dosanjh, J.F. Carolan, W.N. Hardy, *Inhibition of Superconductivity in Y-Ba-Cu-O Films by Si Ion-Implantation*, Appl. Phys. Lett., 63 (1993) 3633-3635.

[132] R.H. Koch, C.P. Umbach, G.J. Clark, P. Chaudhari, R.B. Laibowitz, *Quantum Interference Devices Made from Superconducting Oxide Thin-Films*, Appl. Phys. Lett., 51 (1987) 200-202.

[133] D.P. Kern, K.Y. Lee, R.B. Laibowitz, A. Gupta, *High-Resolution Paterning of High-Tc Superconductors*, J. Vac. Sci. Technol. B, 9 (1991) 2875-2878.

[134] G.J. Clark, A.D. Marwick, R.H. Koch, R.B. Laibowitz, *Effects of Radiation-Damage in Ion-Implanted Thin-Films of Metal-Oxide Superconductors*, Appl. Phys. Lett., 51 (1987) 139-141.

[135] M.E. Gross, W.L. Brown, S.B. Dicenzo, E.H. Hartford, J.J. Yeh, M. Hong, *Ion-Beam Patterning of Spin-on Metalorganics Precursors and Formation of High Tc-Superconductors*, Appl. Phys. Lett., 53 (1988) 802-804.

[136] M. Kuhn, B. Schey, R. Klarmann, W. Biegel, B. Stritzker, J. Eisenmenger, P. Leiderer, *Patterning of YBCO Thin Films by Ion Implantation and Magneto-Optical Investigations*, Physica C, 294 (1998) 1-6.

[137] Q.Y. Ma, E.S. Yang, G.V. Treyz, C.A. Chang, *Novel Method of Paterning YBaCuO Superconducrting Thin-Films*, Appl. Phys. Lett., 55 (1989) 896-898.

[138] Q.Y. Ma, P. Dosanjh, A. Wong, J.F. Carolan, W.N. Hardy, *Inhibition Patterning of Oxide Superconducting Filmd with Si Ion-Implantation*, Supercond. Sci. Technol., 7 (1994) 294-297.

[139] M. Gurvitch, A.T. Fiory, *Preparation and Substrate Reactiontions of Superconducting Y-Ba-Cu-O Films*, Appl. Phys. Lett., 51 (1987) 1027-1029.

[140] Y. Yoshizako, M. Tonouchi, T. Kobayashi, *Chemical Etching of High-Tc Superconducting Y-Ba-Cu-O Films in Phosphoric-Acid Solution*, Jpn. J. Appl. Phys. Part 2 - Lett., 26 (1987) L1533-L1534.

[141] I. Shih, C.X. Qiu, *Chemical Etching of Y-Cu-Ba-O Thin-Films*, Appl. Phys. Lett., 52 (1988) 1523-1524.

[142] A. Inam, X.D. Wu, T. Venkatesan, S.B. Ogale, C.C. Chang, D. Dijkkamp, *Pulsed Laser Etching of High-Tc Superconducting Films,* Appl. Phys. Lett., 51 (1987) 1112-1114.

[143] M. Scheuermann, C.C. Chi, C.C. Tsuei, D.S. Yee, J.J. Cuomo, R.B. Laibowitz, R.H. Koch, B. Braren, R. Srinivasan, M.M. Plechaty, *Magnetron Sputtering and Laser Paterning of High Tranition-Temperature Cu Oxide-Films,* Appl. Phys. Lett., 51 (1987) 1951-1953.

[144] J. Mannhart, M. Scheuermann, C.C. Tsuei, M.M. Oprysko, C.C. Chi, C.P. Umbach, R.H. Koch, C. Miller, *Micropaterning of HigH-Tc Films with Excimer Laser,* Appl. Phys. Lett., 52 (1988) 1271-1273.

[145] A. Gupta, G. Koren, *Direct Laser Writing of Superconducting Patterns of* $YBa_2Cu_3O_{7-delta}$, Appl. Phys. Lett., 52 (1988) 665-666.

[146] L.R. Harriott, P.A. Polakos, C.E. Rice, *High-Resolution Patterning of High-Tc Superconductors,* Appl. Phys. Lett., 55 (1989) 495-497.

[147] G.C. Hilton, E.B. Harris, D.J. Vanharlingen, *Growth, Paterning, and Weak-Link Fabrication of Superconducting YBa2Cu3O7-x Thin-Films,* Appl. Phys. Lett., 53 (1988) 1107-1109.

[148] B. Hauser, M. Diegel, H. Rogalla, *Preparation of Thin-Film YBaCuO Quantum Interference Devices with a Ligt-Off Technique,* Appl. Phys. Lett., 52 (1988) 844-846.

[149] C.B. Cobb, P.N. Barnes, T.J. Haugan, J. Tolliver, E. Lee, M. Sumption, E. Collings, C.E. Oberly, *Hysteretic Loss Reduction in Striated YBCO,* Physica C, 382 (2002) 52-56.

[150] M.D. Sumption, E. Lee, C.B. Cobb, P.N. Barnes, T.J. Haugan, J. Tolliver, C.E. Oberly, E.W. Collings, *Hysteretic Loss vs. Filament Width in Thin YBCO Films Near the Penetration Field*, IEEE Trans. Appl. Supercond, 13 (2003) 3553-3556.

[151] K.M. Metkus, M.S. Osofsky, N.A. Charipa, A. Piqué, *Laser Direct-Write for Low AC Loss High Temperature Superconductor*, Journal of Laser Micro/Nanoengineering, 8 (2012) 19-23.

[152] S.P. Ashworth, F. Grilli, *A Strategy for the Reduction of AC Losses in YBCO Coated Conductors*, Supercond. Sci. Technol., 19 (2006) 227-232.

[153] D.W. Hazelton, Y.Y. Xie, Y. Qiao, E. Zhang, V. Selvamanickam, *Superpower's Second Generation HTS Conductor Design for Stability and Low AC Losses*, in: U. Balachandran (Ed.) Advances in Cryogenic Engineering, Vol 52A & 52B, Amer Inst Physics, Melville, 2006, pp. 859-868.

[154] O. Tsukamoto, M. Ciszek, *AC Magnetization Losses in Striated YBCO-123/Hastelloy Coated Conductors*, Supercond. Sci. Technol., 20 (2007) 974-979.

[155] R.C. Duckworth, M.P. Paranthaman, M.S. Bhuiyan, F.A. List, M.J. Gouge, *AC Losses in YBCO Coated Conductor with Inkjet Filaments*, IEEE Trans. Appl. Supercond., 17 (2007) 3159-3162.

[156] F.A. List, T. Kodenkandath, M.W. Rupich, *Fabrication of Filamentary YBCO Coated Conductor by Inkjet Printing*, IEEE Trans. Appl. Supercond., 17 (2007) 3355-3358.

[157] M.D. Sumption, E.W. Collings, P.N. Barnes, *AC Loss in Striped (filamentary) YBCO Coated Conductors Leading to Designs for High Frequencies and Field-Sweep Amplitudes*, Supercond. Sci. Technol., 18 (2005) 122-134.

[158] G.A. Levin, P.N. Barnes, J.W. Kell, N. Amemiya, Z. Jiang, K. Yoda, F. Kimura, *Multifilament YBa2Cu3O6+x-Coated Conductors with Minimized Coupling Losses*, Appl. Phys. Lett., 89 (2006).

[159] N. Amemiya, K. Yoda, S. Kasai, Z.N. Jiang, G.A. Levin, P.N. Barnes, C.E. Oberly, *AC Loss Characteristics of Multifilamentary YBCO Coated Conductors*, IEEE Trans. Appl. Supercond., 15 (2005) 1637-1642.

[160] M. Majoros, B.A. Glowacki, A.M. Campbell, G.A. Levin, P.N. Barnes, *Transport AC Losses in Striated YBCO Coated Conductors*, in: H.W. Weber, F.M. Sauerzopf (Eds.) 7th European Conference on Applied Superconductivity, Iop Publishing Ltd, Bristol, 2006, pp. 564-567.

[161] K. Suzuki, M. Yoshizumi, T. Izumi, Y. Shiohara, M. Iwakuma, A. Ibi, S. Miyata, Y. Yamada, *Development of Scribing Process of Coated Conductors for Reduction of AC Losses*, Physica C, 468 (2008) 1579-1582.

[162] G.A. Levin, J. Murphy, T.J. Haugan, J. Souc, J. Kovac, P. Kovac, *AC Losses of Copper Stabilized Multifilament YBCO Coated Conductors*, IEEE Trans. Appl. Supercond., 23 (2013).

[163] R.C. Duckworth, F.A. List, Y.F. Zhang, *Effect of Interfacial Resistance on AC Loss as a Function of Applied AC Field in YBCO Filamentary Conductors*, IEEE Trans. Appl. Supercond., 19 (2009) 3327-3331.

[164] Y. Zhang, *Electrodepositon of silver stabilizer layer for second generation superconducting tapes*, University of Houston, 2011.

[165] M. Majoros, B.A. Glowacki, A.M. Campbell, G.A. Levin, P.N. Barnes, M. Polak, *AC losses in striated YBCO coated conductors, Applied Superconductivity*, IEEE Transactions on, 15 (2005) 2819-2822.

[166] M. Iwakuma, H. Hayashi, H. Okamoto, A. Tomioka, M. Konno, T. Saito, Y. Iijima, Y. Suzuki, S. Yoshida, Y. Yamada, T. Izumi, Y. Shiohara, *Development of REBCO Superconducting Power Transformers in Japan*, Physica C, 469 (2009) 1726-1732.

[167] H. Okamoto, H. Hayashi, A. Tomioka, M. Konno, M. Owa, A. Kawagoe, F. Sumiyoshi, M. Iwakuma, K. Suzuki, T. Izumi, Y. Yamada, Y. Shiohara, *AC Loss Properties in YBCO Model Coils for Loss Reduction*, Physica C, 468 (2008) 1731-1733.

[168] J.H. Park, L. Chen, K.C. Goretta, R.E. Koritala, U. Balachandran, *Oxidation of Hastelloy C276*, in: B. Balachandran, D. Gubser, K.T. Hartwig (Eds.) Adv. Cryog. Eng., Vols 48A and B, Amer Inst Physics, Melville, 2002, pp. 495-502.

[169] R. Bhattacharya, Y. Qiao, V. Selvamanickam, *Electrodeposited Cu-Stabilization Layer for High-Temperature Superconducting Coated Conductors*, J Supercond Nov Magn, 24 (2011) 1021-1026.

[170] W. Goldacker, A. Frank, R. Heller, S.I. Schlachter, B. Ringsdorf, K.P. Weiss, C. Schmidt, S. Schuller, *ROEBEL Assembled Coated Conductors (RACC): Preparation, Properties and Progress*, IEEE Trans. Appl. Supercond, 17 (2007) 3398-3401.

[171] K. Yasukochi, *Large Coil Task of IEA in the Development of Superconducting Magnets for Fusion*, IEEE Trans. on Magnetics, 17 (1981) 1720-1725.

[172] M. Leghissa, B. Gromoll, J. Rieger, M. Oomen, H.W. Neumüller, R. Schlosser, H. Schmidt, W. Knorr, M. Meinert, U. Henning, *Development and Application of Superconducting Transformers*, Physica C, 372–376, Part 3 (2002) 1688-1693.

[173] J. Šouc, F. Gömöry, J. Kováč, R. Nast, A. Jung, M. Vojenčiak, F. Grilli, W. Goldacker, *Low AC loss Cable Produced from Transposed Striated CC Tapes*, Supercond. Sci. and Technol., 26 (2013) 075020.

[174] S. Terzieva, M. Vojenčiak, F. Grilli, R. Nast, J. Šouc, W. Goldacker, A. Jung, A. Kudymow, A. Kling, *Investigation of the Effect of Striated Strands on the AC Losses of 2G Roebel Cables*, Supercond. Sci. and Technol., 24 (2011) 045001.

[175] M.R.Z. Victor, G. Francesco, S. Frederic, *A full 3D Time-Dependent Electromagnetic Model for Roebel Cables*, Supercond. Sci. and Technol., 26 (2013) 052001.

[176] F. Grilli, V. Zermeno, M. Vojenciak, E. Pardo, A. Kario, W. Goldacker, *AC Losses of Pancake Coils Made of Roebel Cable*, IEEE Trans. Appl. Supercond, 23 (2013) 5900205-5900205.

[177] J. Zhenan, R.A. Badcock, N.J. Long, S. Mike, K.P. Thakur, L.S. Lakshmi, A. Wright, K. Hamilton, G.N. Sidorov, R.G. Buckley, A. Naoyuki, A.D. Caplin, *Transport AC Loss Characteristics of a Nine Strand YBCO Roebel Cable*, Supercond. Sci. and Technol., 23 (2010) 025028.

[178] J. Zhenan, S. Mike, A.B. Rod, N.J. Long, A. Naoyuki, *Transport AC loss Measurement of a Five Strand YBCO Roebel Cable*, Supercond. Sci. and Technol., 22 (2009) 095002.

[179] R. Apsey, D.E. Baynham, P. Clee, D. Cragg, N. Cunliffe, R. Hopes, R. Stovold, *Design of a 5.5 Metre Diameter Superconducting Solenoid for the Delphi Particle Physics Experiment at LEP*, IEEE Trans. on Magnetics, 21 (1985) 490-493.

[180] T. Hasegawa, N. Ohtani, T. Koizumi, Y. Aoki, S. Nagaya, N. Hirano, L. Motowidlo, R.S. Sokolowski, R.M. Scanlan, D.R. Dietderich, S. Hanai, *Improvement of Superconducting Properties of Bi-2212 Round Wire and Primary test Results of Large Capacity Rutherford Cable*, IEEE Trans. Appl. Supercond, 11 (2001) 3034-3037.

[181] E.W. Collings, M.D. Sumption, R.M. Scanlan, D.R. Dietderich, L.R. Motowidlo, R.S. Sokolowski, Y. Aoki, T. Hasegawa, *Bi:2212/Ag-based Rutherford Cables: Production, Processing and Properties*, Supercond. Sci. and Technol., 12 (1999) 87.

[182] S.I. Schlachter, W. Goldacker, F. Grilli, R. Heller, A. Kudymow, *Coated Conductor Rutherford Cables (CCRC) for High-Current Applications: Concept and Properties*, IEEE Trans. Appl. Supercond, 21 (2011) 3021-3024.

[183] A. Kario, M. Vojenciak, F. Grilli, A. Kling, B. Ringsdorf, U. Walschburger, S.I. Schlachter, W. Goldacker, *Investigation of a Rutherford Cable Using Coated Conductor Roebel Cables as Strands*, Supercond. Sci. and Technol., 26 (2013) 085019.

[184] M. Majoros, M.D. Sumption, E.W. Collings, *Transport AC Loss Reduction in Striated YBCO Coated Conductors by Magnetic Screening*, IEEE Trans. Appl. Supercond, 19 (2009) 3352-3355.

[185] P. Kruger, F. Grilli, M. VojenCiak, V.M.R. Zermeno, E. Demencik, S. Farinon, *Superconductor/Ferromagnet Heterostructures Exhibit Potential For Significant Reduction of Hysteretic Losses*, Appl. Phys. Lett., 102 (2013) 202601-202604.

[186] M. Majoros, B.A. Glowacki, A.M. Camppbell, *Modelling of the Influence of Magnetic Screening on Minimisation of Transport AC Losses in Multifilamentary Superconductors*, IEEE Trans. Appl. Supercond, 11 (2001) 2780-2783.

[187] M. Vojenčiak, J. Šouc, F. Gömöry, *Critical Current and AC Loss Analysis of a Superconducting Power Transmission Cable with Ferromagnetic Diverters*, Supercond. Sci. and Technol., 24 (2011) 075001.

[188] Y.F. Zhang, R.C. Duckworth, T.T. Ha, F.A. List, M.J. Gouge, Y.M. Chen, X.M. Xiong, V. Selvamanickam, A. Polyanskii, *AC Loss Reduction in Filamentized YBCO Coated Conductors With Virtual Transverse Cross-Cuts*, IEEE Trans. Appl. Supercond., 21 (2011) 3301-3306.

[189] V. Arp, *Stresses in Superconducting Solenoids*, Journal of Applied Physics, 48 (1977) 2026-2036.

[190] J.E.C. Williams, E.S. Bobrov, *Magnet System of the 500 MHz NMR Spectrometer at the Francis Bitter National Magnet Laboratory: II. Disturbances, Quenches, and Training*, Rev. Sci. Instrum., 52 (1981) 657-661.

[191] Y. Zhang, D.W. Hazelton, A.R. Knoll, J.M. Duval, P. Brownsey, S. Repnoy, S. Soloveichik, A. Sundaram, R.B. McClure, G. Majkic, V. Selvamanickam, *Adhesion Strength Study of IBAD–MOCVD-Based 2G HTS Wire Using a Peel Test*, Physica C, 473 (2012) 41-47.

[192] D.C. van der Laan, J.W. Ekin, C.C. Clickner, T.C. Stauffer, *Delamination Strength of YBCO Coated Conductors Under Transverse Tensile Stress*, Supercond. Sci. Technol., 20 (2007) 765-770.

[193] N. Cheggour, J.W. Ekin, C.L.H. Thieme, Y.Y. Xie, V. Selvamanickam, R. Feenstra, *Reversible Axial-Strain Effect in Y–Ba–Cu–O Coated Conductors*, Supercond. Sci. and Technol., 18 (2005) S319.

[194] J.W. Ekin, S.L. Bray, N. Cheggour, C.C. Clickner, S.R. Foltyn, P.N. Arendt, A.A. Polyanskii, D.C. Larbalestier, C.N. McCowan, *Transverse Stress and Fatigue Effects in Y-Ba-Cu-O Coated IBAD Tapes*, IEEE Trans. Appl. Supercond., 11 (2001) 3389-3392.

[195] M. Sugano, K. Osamura, W. Prusseit, R. Semerad, T. Kuroda, K. Itoh, T. Kiyoshi, *Reversible Strain Dependence of Critical Current in 100 a Class Coated Conductors*, IEEE Trans. Appl. Supercond., 15 (2005) 3581-3584.

[196] G. Majkic, E. Galstyan, Z. Yifei, V. Selvamanickam, *Investigation of Delamination Mechanisms in IBAD-MOCVD REBCO Coated Conductors*, IEEE Trans. Appl. Supercond., 23 (2013) 6600205-6600205.

[197] Y. Yanagisawa, H. Nakagome, T. Takematsu, T. Takao, N. Sato, M. Takahashi, H. Maeda, *Remarkable Weakness Against Cleavage Stress for YBCO-Coated Conductors and its Effect on the YBCO Coil Performance*, Physica C, 471 (2011) 480-485.

[198] T. Miyazato, M. Hojo, M. Sugano, T. Adachi, Y. Inoue, K. Shikimachi, N. Hirano, S. Nagaya, *Mode I Type Delamination Fracture Toughness of YBCO Coated Conductor with Additional Cu Layer*, Physica C, 471 (2011) 1071-1074.

[199] N. Sakai, S. Lee, N. Chikumoto, T. Izumi, K. Tanabe, *Delamination Behavior of Gd123 Coated Conductor Fabricated by PLD*, Physica C, 471 (2011) 1075-1079.

[200] J.R. Reeder, J.H. Crews, *Mixed-Mode Bending Method for Delamination Testing*, AIAA Journal, 28 (1990) 1270-1276.

[201] K.L. Mittal, *Adhesion Measurement of Thin Films*, ElectroComponent Science and Technology, 3 (1976) 21-42.

[202] K.S. Kim, J. Kim, *Elasto-Plastic Analysis of The Peel Test for Thin-Film Adhesion*, J. Eng. Mater. Technol.-Trans. ASME, 110 (1988) 266-273.

[203] T.R. Hull, J.S. Colligon, A.E. Hill, *Measurement of Thin Film Adhesion*, Vacuum, 37 (1987) 327-330.

[204] N. Fujiwara, H. Hayashi, S. Nagaya, Y. Shiohara, *Development of YBCO Power Devices in Japan*, Physica C, 470 (2010) 980-985.

[205] N. Amemiya, S. Kasai, K. Yoda, Z. Jiang, G.A. Levin, P.N. Barnes, C.E. Oberly, *AC Loss Reduction of YBCO Coated Conductors by Multifilamentary Structure*, Supercond. Sci. and Technol., 17 (2004) 1464.

[206] A.P. Malozemoff, W. Carter, S. Fleshler, L. Fritzemeier, Q. Li, L. Masur, P. Miles, D. Parker, R. Parrella, E. Podtburg, G.N. Riley, Jr., M. Rupich, J. Scudiere, W. Zhang, *HTS Wire at Commercial Performance Levels*, IEEE Trans. Appl. Supercond., 9 (1999) 2469-2473.

Appendix A

Due to the resistanceless electron motion, electric field, **E**, is continuously used to accelerate the electrons as

$$m\dot{\mathbf{v}}_s = e\mathbf{E}, \tag{A-1}$$

where v_s is the velocity of super−electrons, and *m* and *e* are their mass and charge respectively. Super-current density can be written as

$$\mathbf{J}_s = n_s e\mathbf{v}_s, \tag{A-2}$$

where n_s is super-electron density. By substitution Equation (A-1) into (A-2), rate of increase in current density continuously increase by electrical field as

$$\dot{\mathbf{J}}_s = \frac{n_s e^2}{m}\mathbf{E}. \tag{A-3}$$

The Meissner effect suggests that inside a superconductor the magnetic flux density is not only constant but also its value is zero. So both derivative of magnetic field, $\dot{B}$, and magnetic field, *B* must be zero. By employing Maxell's equations, two basic electromagnetic properties can be defined – one is given with (A-3 and the second one is

$$\mathbf{B} = -\frac{m}{n_s e^2}\nabla \times \mathbf{J}_s. \tag{A-4}$$

Equations (A-3) and (A-4) are called London Equations and these give the relations between $\mathbf{J_s}$, **E** and **B** of a superconductor. With applying Ampere's circuital law, $\nabla \times \mathbf{B} = \mu_0 \mathbf{J}$ one can be obtained that magnetic field obeys the following equation [14]

$$\nabla \times \nabla \times \mathbf{B} = \frac{-\mu_0 n_s e^2}{m}\mathbf{B},$$
$$\nabla(\nabla \cdot \mathbf{B}) - \nabla^2 \mathbf{B} = -\frac{\mu_0 n_s e^2}{m}\mathbf{B}, \text{and} \tag{A-5}$$
$$\nabla^2 \mathbf{B} = \mathbf{B} / \alpha.$$

For 1D geometry magnetic field $B = (0, 0, B_0)$ and above equation reduced to

$$\frac{d^2 B}{dx^2} - \frac{B}{a} = 0. \tag{A-6}$$

Using the boundary conditions $B(0) = B_0$ and $B(\infty) = 0$, a solution can be found

$$B(x) = B_a e^{-x/\sqrt{\alpha}}. \tag{A-7}$$

Similarly for 1D case $Js = (0, Js, 0)$ can be found by

$$J_s(x) = \frac{B_a}{\sqrt{\alpha}} e^{-x/\sqrt{\alpha}}. \tag{A-8}$$

Appendix B

Hysteretic AC loss can be calculated for a simple one dimensional geometry, as shown in Figure B-1, using CS model. The slab is comparably long in y and z directions, it can be considered to be infinitely long in these two directions in order to eliminate edge effects. Magnetization generated by a current loop I enclosed an area is $m = Al$ and with CS assumption, $J = J_c$, the magnetic moment, M, can be described for the given problem in Figure B-1 (a) as

$$M = \int_{a-p}^{a} J_c x dx = \frac{\mu_0 J_c}{2}\left(p^2 - 2ap\right) \text{for } p < a, \tag{B-1}$$

$p = B_0 / 2\mu_0 J_c$ is the field penetration depth. B_a changes from 0 to its peak, B_0 and a is the half width of the slab. A plot for magnetization versus applied field is provided in Figure B-1 (b). The dashed line is for magnetization below penetration field and solid continuous line is for above penetration field.

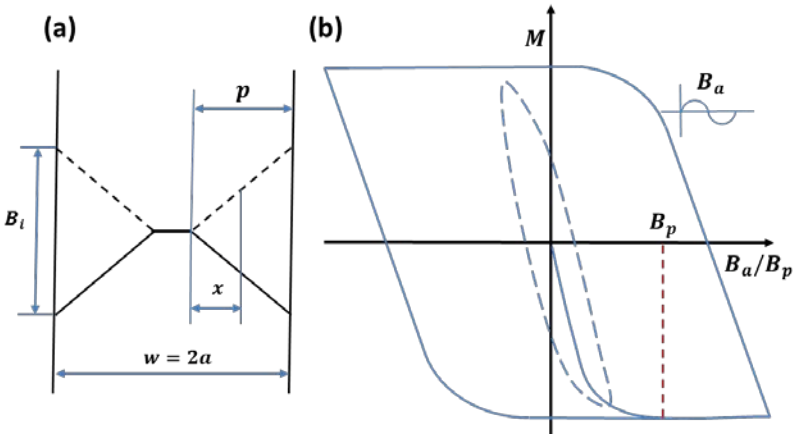

Figure B-1. Geometry for hysteresis calculations by CSM (a), magnetic moment curves before (dashed line) and after (solid line) penetration field reached (b).

Below penetration field the superconductor is in the Meissner state and the magnetization from *dB/dt* corresponds to pure energy storage with no energy lost as heat.

Above penetration field flux pinning generates hysteretic behavior. The area enclosed by the *B(H)* curve through a *dB/dt* cycle represents the thermal loss.

The time-varying electric field induces screening current according to Faraday's law. This implies that hysteretic loss either can be found by finding the area of the *M-B* loop ($\int MdB = \int BdM$) or by integrating $\mathbf{J}\cdot\mathbf{E}$ over the volume since the screening currents are bound currents that correspond to sample magnetization. Thus, the loss term can be written as

$$P = \int \mathbf{J_c}\cdot\mathbf{E}dV = \int J_c \frac{\partial \phi}{\partial t}. \tag{B-2}$$

In the current problem, $\Delta\phi(x) = \int_0^x \Delta\phi(\kappa)\,d\kappa = \mu_0 J_c x^2/2$. Then, loss per unit volume per cycle from CS

$$P_{\text{mh-sb}} = \frac{1}{a}\int_0^p J_c \mu_0 J_c x^2 dx = \frac{\mu_0 {J_c}^2 p^3}{3a}, \text{ for } p < a. \tag{B-3}$$

Sometimes it is convenient to present this results in terms of normalized field, $\beta = B_0 / B_{p0} = B_0 / 2\mu_0 J_c a$. By substitution into and doubling the losses to include the other half of the loop, the loss per cycle per volume can be obtained for below penetration field as

$$P_{\text{mh-sb}} = \frac{{B_0}^2 \beta}{2\mu_0 3} = \frac{{B_0}^2}{2\mu_0}\Gamma(\beta), \text{ for } \beta < 1. \tag{B-4}$$

The losses for above penetration field as

$$P_{\text{mh-sb}} = \frac{{B_0}^2}{2\mu_0}\left\{\frac{1}{\beta} - \frac{2}{3\beta^2}\right\} = \frac{{B_0}^2}{2\mu_0}\Gamma(\beta), \text{ for } \beta > 1. \tag{B-5}$$

Appendix C

Faraday's first and second law of electrolysis state that the amount of a material deposited on an electrode is proportional to the amount of electricity used. Thus the following equation gives the charge required to reduce *m* moles of atom,

$$Q = mnN_a Q_e \text{ or } m = \frac{Q}{nF}, \tag{C-1}$$

where *n* is number of moles of electrons required to reduce one mole of metal during plating or the number of electrons taking part in the reduction, *m* is the number of gram moles of metal deposited, N_a is Avogadro's number or number of atoms in a mol, Q_e is electrical charge per electron and *F* in Faraday's constant. Charge used in the deposition can be obtained by,

$$Q = \int \text{Idt}. \tag{C-2}$$

I is the current in ampere. If the current during deposition holds constant, this equation can be simplified as product of current by the deposition time, *t*, therefore, the thickness of plated material can be found by following equation,

$$\delta = \frac{M_w It}{nFAD}, \tag{C-3}$$

where M_w is atomic weight of the plated material, *A* is area, and *D* is density of the plated material.